Field Induced Motions of Microparticles and Fluids for Mixing, Dye-degradation, Energy Harvesting

A thesis submitted

in partial fulfillment of the requirements for the degree of

Doctor of Philosophy

Submitted

by

Shirsendu Mitra

Under the Guidance

of

Prof. Dipankar Bandyopadhyay

Department of Chemical Engineering

Indian Institute of Technology Guwahati

March 2020

STATEMENT

- **Title of Thesis:** Field Induced Motions of Microparticles and Fluids for Mixing, Dye-degradation, Energy Harvesting
- **The thesis is submitted for the Degree of** Doctor of Philosophy (Ph.D.)
- The results reported is research carried out by myself in the Department of Chemical Engineering, Indian Institute of Technology Guwahati, India under the supervision of Prof. Dipankar Bandyopadhyay.
- Specifications regarding thesis format have been closely followed.
- The contents of the thesis have been organized based on the guidelines.
- The thesis has been prepared without resorting to plagiarism.
- All sources have been acknowledged appropriately wherever the work derived is based on the findings of other sources, in accordance with the general practice of reporting scientific observations.
- The thesis has not been submitted elsewhere for a degree.

March 2020 **Shirsendu Mitra**

Department of Chemical Engineering **Ph.D. Student**

Indian Institute of Technology Guwahati **Roll No:** 146107009

CERTIFICATE

This is to certify that the research works performed in the thesis entitled, "Field Induced Motions of Microparticles and Fluids for Mixing, Dye-degradation, Energy Harvesting" by **Shri Shirsendu Mitra**, have been carried out under my supervision and this work has not been submitted elsewhere for a degree.

Prof. Dipankar Bandyopadhyay

Supervisor

Professor

Department of Chemical Engineering

Indian Institute of Technology Guwahati

March 2020

Acknowledgment

I express sincere gratitude to my supervisor *Prof. Dipankar Bandyopadhyay* for guidance, teaching, and support throughout my thesis execution. It is indeed an honor for me to work with a person with full enthusiasm, attitude. I have seen myself growing both personally and professionally under his guidance. I am grateful to him to introduce myself with state-of-art research and giving me the opportunity to carry out my thesis work under his supervision.

I thank *Prof. Saptarshi Manjumdar*, IIT Hyderabad for the guidance during the formulation of my PhD problems. I am grateful to all the doctoral committee members, *Prof. Ganesh Natarajan, Prof. Amaresh Dalal, Prof. Partho Sarathi Gooh Pattader,* and *Prof. Tamal Banerjee*, for their unconditional support in every aspect of my thesis. I wish to thank all the faculty members in the Department of Chemical Engineering. I owe a lot to my teachers, *Mr. Rajat Shaw, Mrs. Anjushree Dhara, Prof. P Ray, Prof. P. De, Prof. Debasis Sarkar*, and *Prof. Shampa Chakraborty*.

My sincere gratitude to my lab senior *Dr. Abir Ghosh* for support and help in the formative stage of my thesis, which has significantly helped in improving the quality of the studies presented in the thesis.

I can never forget to thank my Lab mates. During my PhD, I have carried out my research work in the SMAART Lab, which has provided me the platform to explore the world of micro and nanotechnologies. I am thankful for all the past and the present members of the laboratory to create such a lab environment where innovations are always in stepping distance. I have enjoyed working with *Mr. Nilanjan Mandal, Mr. Rupam Sinha, Mr. Nirmal Roy, Mr. Saikat Biswas, Mr. Joydip Chaudhury, Mr.*

Siddharth Thakur, Mr. Harsh, Mr. Anvesh Dixit, Mr. Sagnik Midya, Mr. Sunil Kumar Singh, Mr. Kanishka Murmu, Mr. Anirudhha Deb, Mr. Ankur Pandey, Mr. Shaon Sutradhar, Mr. Anshuman Pashupalak, Mr. Mohit Sachan, Mr. Vinod Vanarse, Mr. Jiwajyoti Mahanta, Mr. Sahil Jagnani, Mr. Ankit Chaudhury, Mr. Chintak Parashar, Mr. Nayan Jyoti Kakoti, Ms. Samitha Kancharla, Ms. Shreya Mukherjee, Ms. Tamanna Bhuyan, Ms. Tanushree Ghosal, Ms. Aishwarya S, Ms. Satarupa Dutta, Ms. Mitali Basak, Dr. Abir Ghosh, Dr. Sunny Kumar, Dr. Saptak Rarotra, Dr. Mitradip Bhattacharjee, Dr. Amit Kumar Singh, Dr. Nayan Mani Das, Dr. Seim Timung, Dr. Boleddu Ravi, Dr. Binita Nath, and Dr. Manash Borthakur at IIT Guwahati. I also thank *Shailesh ji and Dip*, for their efforts to help me out in the official matters and conduct lab maintenance works smoothly.

I am really fortunate to have a great company outside the lab too, which has made the campus life enjoyable at IIT Guwahati. The memories will certainly be associated with me all of my life. I am thankful to *Rupam, Nirmal, Saikat, Sunil, Kanishka, Anirudhha, Ankur, Nilanjan Da, Ritesh, Kuldeep, Debashis da, Supriyo Da, Piyal, Abhik, Gaurab, Satadru, Kuldeep, Bitang, Saptarshi, and Mitali* to be there during all ups and downs. I cherish the sweet moments, the evening/late-evening never-ending discussion and arguments, organizing conferences or departmental programs, and playing sports.

There are few friends who become inseparable from your life and their presence gives you joy and strength. I am delighted to acknowledge *Mr. Sujit Bose, Mr. Abhijeet Das, Mr. Raja Mondal,* and *Mr. Saswata Roy*. They are beyond any ‘thanks or sorry’ and they probably know me the best. Any kind of acknowledgment is really unnecessary for them. I am really fortunate that I met you guys.

I thank CIF instruments facilities of IIT Guwahati and the supercomputing PARAM Ishan facilities of IIT Guwahati, without which my work would not have completed. I am also thankful to all the staff members of the Department of Chemical Engineering, IIT Guwahati for their timely help regarding all the administrative issues.

I also acknowledge the Department of Science and Technology (DST), Ministry of Human Resource Development (MHRD), and Ministry of Electronics and Information Technology (MeitY), IMPRINT MHRD for the financial supports. Especially, I also thank few of the projects funded by aforementioned funding agencies bearing project identification numbers, DST SERB, Grant no. EMR/2016/001824, MeitY - grant no. 5(9)/2012-NANO, and the MHRD IMPRINT Project 8058.

Finally, I would like to take this opportunity to thank my beloved parents for being the strongest support not only during my PhD career but also throughout my life. Ishani, my elder sister, what should I say about you! All three of you are my source of inspiration. I am also indebted to my nephew and nieces, Ishita, Raisa and Riyan, for their invaluable affection and care. I am equally overwhelmed by all the support I get from my other family members.

I dedicate this thesis to my family.

SHIRSENDU MITRA

Contents

Synopsis 1
S1. INTRODUCTION 1
S2. TECHNICAL CHAPTERS 3
S2.1. Chapter 2 3
S2.2. Chapter 3 5
S2.3. Chapter 4 6
S2.4. Chapter 5 7
S2.5. Chapter 6 8
S3. Summary and Future Scope 10
Chapter 1 11
Chapter 2 11
ABSTRACT 17
2.1. INTRODUCTION 19
2.2. PROBLEM FORMULATION 21
2.2.1. Governing Equations: 21
2.2.2. Boundary Conditions: 23
2.2.3 Analytical Solution: 24
2.2.4. Numerical Solution Methodology: 25
2.3. VALIDATION 26
2.4. RESULTS AND DISCUSSION 27
2.5. CONCLUSIONS 41
Chapter 3 43
ABSTRACT 43
3.2. PROBLEM FORMULATION 46
3.3. SOLUTION METHODOLOGIES 49
3.3.1. Analytical Solution: 49
3.3.2. Numerical Methodology: 50
3.3.3. Validation: 51
3.4. RESULTS AND DISCUSSION 51
3.4.1. Homogeneous Channels: 51
3.4.2. Mixing in Heterogeneous Channels: 54

Contents

3.4.3. Mixing in Flexible Channels:.....60
3.5. CONCLUSIONS.....65
Chapter 4.....67
ABSTRACT.....67
4.1. INTRODUCTION.....69
4.2. MATERIALS.....71
4.3. METHODS.....72
4.3.1. Preparation of Active Material:.....72
4.3.2. Electrode fabrication:.....72
4.3.2. Preparation and characterization of SC:.....73
4.3.3. Design of Separators:.....74
4.3.4. Electrochemical analysis:.....74
4.3.5. Supercapacitor Arrangement:.....74
4.4. CHARACTERIZATIONS.....75
4.5. THEORETICAL FORMULATION.....76
4.6. RESULTS AND DISCUSSION.....79
4.6.1. Electrode geometry and distance:.....79
4.3.2. Frequency dependent PPS performance:.....81
4.3.3. Charge storage mechanism:.....88
4.4.4. Capacitance from TCM and CV analysis:.....92
4.4. CONCLUSIONS.....95
Chapter 5.....97
ABSTRACT.....97
5.1. INTRODUCTION.....98
5.2. RESULTS AND DISCUSSION.....101
5.2.1. CNT-bot Locomotion:.....101
5.2.2. Fuel Cell Application:.....106
5.2.3. Dye Degradation Application:.....107
5.3. EXPERIMENTAL SECTION.....109
5.3.1. Materials and methods:.....109
5.3.2. Characterization:.....111
5.3.2.1. FESEM and Raman Spectroscopy of MWCNT-COOH and Fe^{+2} doped MWCNT-COOH.....111
5.4. CONCLUSIONS.....122
Chapter 6.....125

Contents

ABSTRACT 125
INTRODUCTION 126
6.2. PROBLEM FORMULATION 129
6.2.1. Governing Equations: 129
6.2.2. Boundary Conditions: 131
6.3. NUMERICAL METHODOLOGY 131
6.4. VALIDATION 132
6.4.1. Analytical Model: 132
6.4.2. Boundary Conditions: 132
6.4.3. Comparison of Semi-Analytical and Simulation Results: 133
6.5. RESULTS & DISCUSSION 135
6.5.1. Influence of Shape: 135
6.5.2. Influence of External concentration gradient: 136
6.5.3. Influence of Zero concentration gradient: 140
6.6. CONCLUSIONS 148
Chapter 7 150
LIST OF PUBLICATIONS 155
1. Journal Publications 155
2. Conference Publications 156
3. Patents 157

List of Figures

Figure 2.1: Schematic representation of a charged particle of diameter, d_p, experiencing electrophoretic motion inside an electrolyte under an externally applied electric field potential, ϕ_1, inside a microfluidic channel of diameter d and length l. Distribution of co-ions and counter-ions has been shown by the respective signs around a positively charged particle. **21**

Figure 2.2: Plot (a) shows the variation in up with external potential (ϕ_1). The triangular symbols with a solid line are obtained from the nonlinear CFD simulations and the square symbols with dashed line are form the proposed analytical model. Particle diameter (d_p), surface potential (ϕ_2), channel length (l_c), channel confinement (d/dp), initial concentration of ions (c_{i0}) are kept as 2 μm, -50 mV, 15 μm , 5, 0.001 mM/lt respectively. Plot (b) shows the comparison of particle speeds in a microchannel experimental results with CFD simulation for a particle ~10 μm diameter and other parameters as taken by experimental article. **26**

Figure 2.3: Plot (a) shows the nonlinear distribution of co-ion (c_2, red broken line), counter-ion (c_1, traffic green dash dot line), and difference of co- and counter-ions (Δc, blue solid line) around the charged particle of diameter 2 μm with a surface charge of -50 mV. Other simulation parameters involved are listed in **Table.2.2**. Plot (b) shows the profile of ζ-potential around the charged particle of diameter 1 μm and surface potential -50 mV. The solid line represents the profile obtained by solving PNP equation and the red dotted line shows the Debye Hückel profile. **28**

Figure 2.4: Image set (a) shows the contours of the co-ion concentration (c_2), image set (b) shows distribution of counter-ion concentration (c_1), and image set (c) shows distribution of the difference of concentration (Δc) around a microparticle of 2 μm diameter undergoing electrophoretic migration inside a microchannel of 5 μm width and 15 μm length. The contours are plotted at different time intervals as shown on the images. The viscosity coefficient, relative permittivity of the electrolyte, ζ-potential at the EDL, and externally applied field are, 0.023 Pa s, 80, 0.05 V, and 1 V, respectively. **29**

Figure 2.5: Frames (i) to (vi) in the image set (a) show the position of the moving particle at different time intervals when the diameter (d_p) is 2 μm and surface potential is -50 mV. Frames (i) to (vi) in the image set (b) show the respective distribution of stress on the solid particle undergoing electrophoresis. Plots (c) – (e) show the variations in the displacement (s), velocity (u_p), and acceleration (a) with time (t) of the particle undergoing electrophoresis under the influence of the externally applied electric field. The other parameters employed in the simulations are enlisted in the **Table 2.2**. **30**

List of Figures

Figure 2.6: Shows the development of the potential distribution, hence the EDLs, around the charged particle from unsteady to the steady state. The potential distribution surrounding the particle is plotted at different time steps, as mentioned in the figure legend. The particle having diameter 1 μm is kept inside a microfluidic channel of diameter 5 μm and length 15 μm. The bulk electrolyte concentration is kept at 0.001 mol/m^3. **31**

Figure 2.7: Image (a) shows the velocity contours around a charged microparticle of diameter 2 μm and a ζ-potential of -50 mV, undergoing electrophoretic motion. Image (b) shows the typical electric field potential (ϕ_2) contour around the charged particle while the particle is in motion. Image (c) shows the fluid velocity (u_f) surrounding the particle along the sections 11', 22', 33', and 44', as shown in the image (a) through the solid cut lines. Image (d) shows variation in the electric field potential (ϕ_2) in the fluid surrounding the particle along the cut lines 11', 22', 33', and 44'. Solid line in pink color shows the Debye Hückel profile for electric field potential (ϕ_2) . The other parameters employed for the simulations are listed in **Table.2.2**. **33**

Figure 2.8: The frames (i) – (vii) in the image set (a) show displacement of particles of varying size, 0.2 μm, 0.6 μm, 1.0 μm, 1.4 μm, 1.8 μm, 2.2 μm, and 2.6 μm having surface potential of – 50 mV. The frames (i) – (vii) in the image set (b) show the stress on the moving particle. The plot (c) shows the steady state velocity (u_p) of the particles of different diameter (d_p). The plot (d) represents the contribution of viscous drag, electrophoretic force and the resultant of two forces. All other parameters used for the calculations are enlisted in the **Table.2.2**. **34**

Figure 2.9: Schematic images (a) to (d) show different kinds of chemical heterogeneity on the surface of the particle of diameter 1 μm. The surface potentials for different color codes are also shown on the figures. The image (e) shows the steady state velocity (u_p) of the particles (a) to (d) with the variation in the ϕ_2 on the red-lobe. **35**

Figure 2.10: The plots (a) – (f) show the variation in u_p with surface potential (ϕ_2), external electric field potential (V_{ext}), the viscosity of the electrolyte (μ), and initial molar concentration of the solute (c_0), diameter of the particle (d_p), and the confinement in the microchannel (d/d_p), respectively. The triangular symbols are obtained from the nonlinear CFD simulations, the solid box symbols are calculated from Henry law, the square symbols are form the Smoluchowski's equation, and the circular symbols are from the proposed analytical model. The necessary dimensional parameters used in the simulations are enlisted in **Table 2.2**. **37**

Figure 2.11: The plot shows the variation in u_p when d = 5 μm and l is changed from 15 μm to 50 μm. The ϕ_p, d_p, and c_0 considered in these simulations are, -0.05 V, 1 μm, and 0.001 mol/m^3, respectively. All other simulation parameters are enlisted in **Table 2.2**. **39**

Figure 2.12: Plot (a) shows the position of a particle under electrophoretic migration after 0.006 s when surface potentials at the confining walls are, ϕ_w = - 0.01 V while the surface potential on the particle is, ϕ_p = - 0.05 V. The colour map shows the contours of the fluid velocity surrounding the particle. The plots (b) and (c) show the spatial contours of the electric field potential (ϕ) near the particle surface and the confining wall when ϕ_p = - 0.05 V and ϕ_w = - 0.01 V. Plot (d) shows the variation in the particle speed (u_p) with ϕ_w. The ϕ_p, d_p, d, l, and c_0 considered in these simulations are, -0.05 V, 0.6 μm, 5 μm, 15 μm, and 0.001 mol/m^3, respectively. All other simulation parameters are enlisted in the Table 2.2. **40**

Figure 3.1: Schematically shows an EO flow inside a microchannel of diameter d and length l_c. The surface charges on the channel walls are shown by encircled negative sign. The channels with chemical patches on the walls are shown by yellow (lighter shade) marks and associated symbols, 'ζ' with positive and negative signs. The groves directing inward of the channel walls represent physical patterns. The groves having yellow (lighter shade) marks and associated symbol 'ζ' represent physicochemical patterns. The flexibility of the channel walls is shown by inward curvature on the walls with the arrows signifying the direction of flexibility. The directions of the driving EO force ($\rho_e \mathbf{E}$) and the resistive viscous force are shown by the arrows. The notations X and Y (x and y) represent dimensionless (dimensional) Cartesian coordinates. **47**

Figure 3.2: Shows comparison between dimensionless velocity profiles (Y vs. U) obtained from analytical (solid blue line) and CFD simulations (dotted red line) solutions. Diameter of channel (d), length of the channel (l_c), Debye length (λ), viscosity of the fluid (μ), density of the fluid (ρ), ζ-potential are kept as 10 μm, 50 μm, 305 nm, 0.001 Pa s, 1000 kg m^{-3}, – 100 mV, respectively. **51**

Figure 3.3: Plot (a) shows unsteady EO flow profiles for developing flows at time intervals 0 s (dash-dot-dot), 0.04 s (dash-dot), 0.08 s (broken), 0.1 s (dash dot dot with black) and 0.2 s (solid) for λ = 0.1 μm. Plot (b) shows steady EO flow profiles (Y vs. U) in the channels of diameters, 4.5 μm (dash-dot), 9.7 μm (broken), and 30 μm (solid). Plot (c) shows steady EO flow profiles for Debye lengths, λ = 0.1 μm (dash-dot-dot), 0.2 μm (dash-dot), and 0.3 μm (solid). Plot (d) shows the variation in the electric field

potential (ϕ_ζ) along the vertical direction of the channel (Y vs. ζ) for the channels in the plot (b). The channel diameter (d), length (l_c), surface charge ϕ_ζ at wall, applied external voltage (V), Debye length (λ) are kept as, 30 μm, 150 μm, – 50 mV, 5 V, and 300 nm, respectively. **52**

Figure 3.4: Plot (a) shows the variation in the average velocity (u_{avg}) with the diameter of the channel (d) at a fixed ϕ_ζ. Plot (b) shows the subsequent variation in the volumetric flow rate (Q). The walls are kept at, ϕ_ζ^w = – 25 mV with applied external potential of 5 V. The aspect ratio of the channels (l_c /d) is kept same for all the simulations. **53**

Figure 3.5: Plot (a) shows a chemically heterogeneous microchannel with alternating positive and negative ϕ_ζ^w on the walls. The zones A, B, C, and D show the places where the velocity and pressure gradient profiles are reported. The contour shows the variation in ϕ_ζ across the channel. Plot (b) shows the variation in the pressure gradient ($-dp/dx$) along the x-direction across the cut-line D. Plot (c) shows the contour of 'u' with streamlines and arrows symbolizing fluid velocity. Plots (d), (e), and (f) show the velocity profiles at the cut-lines A (heterogeneity with positive ϕ_ζ^w), B (heterogeneity with negative ϕ_ζ^w), and C (homogeneous positive ϕ_ζ^w), respectively, as shown in the plot (a). The solid, dash, dash-dot, and dash-dot-dot represent profiles at 1 V – 4 V, respectively. The d_p, l_c, ϕ_ζ^w, V, λ, μ, and ρ are kept as, 30 μm, 150 μm, –25 mV, 4.25 V, 300 nm, 0.001 Pa s, and 1000 kg m^{-3}, respectively. The width of each patch is kept as 15 μm. **55**

Figure 3.6: Plot (a) shows a physicochemically heterogeneous microchannel. The cut-lines A, B, C, and D show the zones where the velocity and pressure profiles are reported. The contour shows the variation in ϕ_ζ across the channel. Plot (b) shows the variation in – dp/dx along the x-direction across the cut-line D. Plot (c) shows streamlines at the middle of the channel (heterogeneous portion) overlaid on x directional velocity (u) and the arrows signify velocity vector. Plots (d) – (f) show the velocity profiles at the cut-lines A (physicochemical heterogeneity with positive ϕ_ζ^w), B (physicochemical heterogeneity with negative ϕ_ζ^w), and C (physicochemical heterogeneity with negative ϕ_ζ^w). Solid, dash, dash-dot, and dash-dot-dot represent profiles at 1 V – 4 V, respectively. The d_p, l_c, ϕ_ζ^w, V, λ, μ, and ρ are kept as, 30 μm, 150 μm, – 25 mV, 4.25 V, 300 nm, 0.001 Pa s, 1000 kg m^{-3}, respectively. The width of each patch is kept as 15 μm and the height of the physical patterns is 3 μm. **58**

Figure 3.7: Plots (a) and (c) show the variations in the vorticity (ω) of the recirculation patterns near the chemical patches shown in the **Fig. 3.5(d)** (cut-line A in **Fig. 3.5(a)**) and near the physicochemical patches shown in the **Fig. 3.6(d)** (cut-line A in **Fig. 3.6(a)**). The plots (b) and (d) show the corresponding velocity profiles across the microchannel. The other parameters such as d_p, l_c, ϕ_ζ^w, and λ are kept as, 30 μm, 150 μm, – 25 mV, and 100 nm, respectively. **59**

Figure 3.8: Shows the EO velocity profile at the middle of a flexible microchannel compressing and expanding periodically with a sinusoidal wave motion. **60**

Figure 3.9: Image set (i) – (vi) in the plot (a) show streamlines overlaid on velocity contours at different time intervals 0, 2, 4, 6, 8, and 10 s for a physicochemically patterned flexible channel having a full contraction ((i) – (iii)) and expansion cycle ((iv) – (vi)). Plots (b) and (c) show velocity profiles at the cut-line taken in zones A and B in plot (a) and subsequent variation in vorticity (ω) with time have been shown in the plots (d) and (e). The solid (broken) lines represent compression (expansion) cycle. The channel diameter and length are kept as 10 μm and 50 μm. The magnitudes of ϕ_ζ^w at the walls and external applied field are, 25 mV and 5 V, respectively. **62**

Figure 3.10: The plots (a), (b), and (c) show the variations in the total electric field potential (ϕ), current density (J), and x-component of velocity (u), respectively. The variables are plotted along the cut-line of a chemically heterogeneous microchannel at, y = 29.75 μm, similar to the line D shown in **Fig. 3.5(a)**. The plots (d), (e), and (f) show the same for a physicochemically heterogeneous microchannel. The d, l_c, ϕ_ζ^w, ρ, μ, V, are kept at 30 μm, 150 μm, +/– 25 mV, 1000 kg/m^3, 0.001 Pa s, 4.2 V, respectively. The solid, broken, dash-dot, dash-dot-dot represent the parametric study of applied external voltage (1, 2, 3, and 4 V). **63**

Figure 3.11: Plot (a) shows schematic representation of the proposed potential measurement set up. Plot (b) shows relative current density (J/J_0) profiles near the wall at a cut-line of, y = 29.75 μm, similar to the line D shown in **Fig. 3.5(a)**. Plot (c) shows a calibration curve (J/J_0 vs. ϕ_ζ) to determine unknown potential of the test object. **64**

Figure 4.1: Image (a) shows the profile for the net electric field potential (ψ_{net}) between a pair of electrodes representing a Helmholtz electrical double layer (EDL). Image (b) illustrates the equivalent circuit derived from the system shown in the image (a) using two capacitor model (TCM). Image (c) shows the distribution of ions in a diffuse layer following the Gouy-Chapman model. Image (d) represents the Gouy-Chapman-Stern

(GCS) model consisting of an immobile Stern layer and mobile diffuse layer in the EDL. **69**

Figure 4.2: The steps to assemble the supercapacitors (SCs) are shown schematically. Images (a) and (b) show the pre-processing of a Cu electrode wherein the plate was roughened using a sand paper. The insets in the images (a) and (b) show the FESEM micrographs of the surface before and after roughening. Thereafter, the roughened plate was sputter-coated with Pt, as shown in the image (c). Image (d) shows the masking of a part of the Pt coated Cu plate using a commercially available tape. The drop casting of the active material – slurry of rGO mixed with carbon black and PTFE, its coating on the Pt coated Cu plate, and subsequent drying have been shown in the images (e) and (f). Image (g) shows the removal of the mask and subsequent surface morphology at the FESEM inset. Image (h) shows the final PPS arrangement wherein a pair of electrodes shown in the image (g) was assembled with a separator in the middle as shown. The separator was composed of a filter paper or a tissue paper, or PVDF (SEM) soaked with electrolytes such as aqueous solutions of KOH and H_2SO_4 having different ionic strengths. Images (i) and (j) show the cross-sectional schematic images of the parallel (PPS) and curved (CPS) plate SCs. The scales shown on the FESEM images are of 20 μm. **73**

Figure 4.3: Raman spectra of active material deposited on the Cu surface. **75**

Figure 4.4: The FESEM images of different separators used in PPS. Image (a) – (d) show filter paper (FP), tissue paper, electro-spun PVDF fibres, and perforated filter paper (PFP), respectively. The scale bars on the images (a) and (b) are of 20 μm while the scale bars on the images (c) and (d) are 5 μm and 500 μm, respectively. **76**

Figure 4.5: Shows the schematic representation of the (i) PPS and (ii) CPS, including its parameters and initial boundary conditions used during the simulations. **77**

Figure 4.6: Cyclic voltammetry (CV) measurements associated with the different supercapacitor arrangements such as PPS and CPS, as shown in the previous figure. Images (Ia) and (Ib) show the variations in the specific current, I_S, with the applied electric field potential, φ, when the electrode separation distance was, d_e = 100 μm. Here, $I_S = I_0/m$, where I_0 is the measured current from CV and m is the mass of the active material. The images (Ia) and (Ib) correspond to the scan rates, v = 50 mV/s and 100 mV/s, respectively. The radius of curvature (κ) were measured, as shown in the inset of the image (Ia) where κ = 0 m^{-1} represents PPS while κ = 0.035 m^{-1}, 0.123 m^{-1}, and 0.2 m^{-1} show different CPS configurations. **Images (IIa)** and **(IIb)** show the CV when κ = 0.035 for d_e = 100 μm and 500 μm, and scan rates, v = 50 mV/s and 100

mV/s, respectively. The separator used for all the experiments was filter paper (FP) soaked in 4M KOH. **79**

Figure 4.7: Electrochemical impedance spectroscopy (EIS) measurements associated with the PPS having different electrolytes and separator materials. Image (a) shows the high-frequency region (> 10 kHz) of Nyquist plots (real (Z') versus imaginary impedance (-Z")) obtained from EIS analysis of PPSs with two different electrolytes 4M KOH (circular symbols) and 1M H_2SO_4 (square symbols). Image (b) illustrates the same for different separators, namely, filter paper (FP), tissue paper (TP), perforated filter paper (PFP), and polyvinylidene fluoride (PVDF). In all the experiments, d_e = 100 µm. **81**

Figure 4.8: Images (Ia) and **(IIa)** represent the Nyquist and Bode (imaginary impedance (-Z") versus frequency (f)) plots obtained from the EIS of a PPSs with different KOH concentrations (4M, 2M, 1M, and 0.5M) in which d_e = 100 µm. Images (Ib) and (IIb) represent the Nyquist and Bode plots for d_e = 100 µm - 500 µm when the electrolyte was 4M KOH. **Images (Ic)** and **(IIc)** represent the Bode plots for the PPS when 4M KOH and 1M H_2SO_4 were used as electrolytes and d_e =100 µm. In all the experiments FP was used as the separator material. **84**

Figure 4.9: The schematic diagram in image (a) shows the directions of the electric fields, E_p – the applied field leading to the polarization of electrodes and E_h – electric field generated due to the formation of EDL. The diagram also shows the variation in net electric field potential, ψ_{net} (solid line) across the SC and the thicknesses of the EDLs (d_{h1} and d_{h2}) near the electrodes. Images (b)-(f) represents the results obtained using simulation studies. Image (b) shows the time-dependent variation in E_h along d_e during the formation of EDL at their respective electrodes in PPS, image (c) shows profiles of concentration of cations (ξ_+) and anions (ξ_-), and ψ_{net}, with the electrode distance (x_e). Image (d) shows the variation in capacitance (C_0) with time (t). The inset image shows the gradient of the electric potential due to ions (ψ_1) at x = 0 µm, taken for calculating the capacitance according to Eq. 4.10.. Image (e) shows the variation in C_0 with KOH concentration (ξ_{KOH}) obtained from experiments and simulations (lines) for ε = 3, 4, and 5. Image (f) shows the variation in C_0 with radius of curvature (κ) of CPS from experiments (symbols, **Fig. 4.6**) and simulations (lines) for ε = 3, 4, and 5. **89**

Figure 4.10: Comparison between theoretical and experimental specific capacitance (C_S) values. Image (a) shows the comparison among the experimentally calculated C_S from CV curves of **Fig. 4.2** and the theoretically calculated C_S from TCM using Eqs. Eqs. (4.16) and (4.17). The line with asterisk symbols represents the values calculated from TCM and the two lines having triangular and box symbols represent experimental

values at two different scan rates, 50 mV/s, and 100 mV/s, respectively. The experimental values of C_S were obtained for angles, κ = 0.035 m^{-1}, 0.123 m^{-1}, and 0.2 m^{-1} at scan rates, v = 50 mV/s and 100 mV/s. Image (b) represents a similar comparison for κ = 0.034 m^{-1} and electrode separations, d_e = 100 μm and 500 μm. **93**

Figure 4.11: Images shows profiles of E_p, E_h, and E_{net} (E_p- E_h) in (a) PPS, and (b) CPS (for κ = 0.035) configurations. The normalized distance between the electrodes in the x-axis is, $x_N = x/d_e$, where x is the distance from the electrode. The separation distance is 100 μm for PPS and 25 μm for CPS. Image (c) shows the variation in dielectric constant (ε) with time (t) for the PPS. **94**

Figure 5.1: Schematically shows a CNT-bot composed of a –COOH functionalized MWCNT cluster doped with a ferrous (Fe^{2+}) salt and magnetite nanoparticle (FeONPs) before coated with a Mg film. The CNT-bot was capable of undergoing two reactions in acidic and alkaline water (e.g. $Mg + H_2O \rightarrow Mg(OH)_2 + H_2$, $Mg + HCl \rightarrow MgCl_2 + H_2$ and $NaHCO_3$ + MWCNT-COOH → MWCNT-COONa+ $H_2O + CO_2$) and Fenton reaction (in absence of light) and Photo Fenton reaction (in presence of UV light) in the peroxide fuel ($Fe^{+2} + H_2O_2 \rightarrow Fe^{+3} + H_2O + O_2$), as shown on the image. Subsequently, the motor moved by the ejection of hydrogen bubbles in acidic water, carbon-dioxide propulsion in the alkaline water, and oxygen bubbles in the peroxide fuel. The motors could show directionality in the motion under acid and alkali gradients leading to acid- and alkali-taxes, as shown on the images. The scheme also shows that hydrogen and oxygen serve as fuels of PEM Fuel cell and the CNT-bot can also perform dye degradation function. **99**

Figure 5.2: Shows the particle locomotion under varied conditions. Image sets (a) – (c) show the trajectory of the random motions of the CNT-bot at different time intervals (shown on the image) in a hydrogen peroxide bath (12%, v/v), water, and 0.5M hydrochloric acid bath, respectively. Image set (d) shows trajectory of the CNT-bot inside a 0.5M aqueous solution of sodium bicarbonate. Image sets (e) - (g) show the trajectory of the directional motion of the CNT-bot at different time intervals when a concentration gradient was established by dripping acid in a water bath, alkali in a peroxide bath, and bicarbonate dripping in a bath of water, respectively. The arrow heads in these images indicate the direction of the movement of the motor. The concentration gradient is indicated by the bromophenol blue, phenolphthalein, and indicators in the image sets (e) – (g), respectively. Image set (h) shows particle trajectory at different time intervals driven by an externally applied magnetic field. In these experiments, the motor size was of ~180 μm to ~300 μm. **101**

Figure 5.3: Shows the speeds of CNT-bots of size range ~180 to 300 μm under different conditions. Plot (a) shows the variation in the speed of the CNT-bot (u_P) in the aqueous

peroxide bath for which the concentration of peroxide (C_{Per}) was increased from 1% (v/v) to 12% (v/v). Plot (b) shows the variation in u_P in a 5% (v/v) peroxide bath when the pH of the bath was varied. Plot (c) shows the variation in u_P when the pH of the water bath was varied. Plot (d) shows the variation in u_P of at different $NaHCO_3$ loading, in pure water, and for a Mg free swimmer. Plot (e) shows variation in u_P with different applied magnetic field strength (H) for a particle of size 220 μm. Plot (f) shows variation in u_P with the intensity of UV LEDs for photo-active CNT-bots. **104**

Figure 5.4: Image (a) shows PEM fuel cell set up for electricity generation using the CNT-bots. The containers 1 (filled with CNT-bots and peroxide) and 2 (filled with acidic water and CNT-bots) generated pure O_2 and H_2 gases in real time, which were supplied to the fuel cell (3) through gas tubing (4), as shown. The current generated was measured by a digital multimeter (5). Images (a) and (b) show progressive increase in the potential with time. Image (c) shows the potential developed against amount of CNT-bots fed in the fuels and image (d) shows transient potential output across PEM fuel cell. **106**

Figure 5.5: Plot (a) shows the UV-Vis absorption of methylene blue solutions of different known concentrations, from 0.01 mM to 0.10 mM. Image (b) shows color of 0.1 mM methylene blue solution before and after degradation using CNT-bot. Image (c) shows the decay of methylene blue solution in the presence of CNT-bots (red triangular symbols), and Photo-active CNT-bots (traffic green diamond symbols). **108**

Figure 5.6: Schematically shows different steps of CNT-bot fabrication. **111**

Figure 5.7: Images (a) and (c) show the Raman spectroscopy and FESEM images of pristine –COOH substituted MWCNT. The images (b) and (d) show the same of Fe^{2+} doped –COOH substituted MWCNTs. **112**

Figure 5.8: The FESEM images of CNT-bot at different stages. Image (a) shows the pristine –COOH functionalized MWCNT at 100 k magnification with the inset showing the same at a higher magnification. Image (b) shows the Fe^{2+} doped MWCNT at 30 k magnification with the inset showing the same at 10^5x. Image (c) shows the FeONP doped MWCNT at 30 k magnification with the inset showing the same at 10^5x. Image (d) shows the FeONP and Fe^{2+} doped MWCNT at 30 k magnification with the inset showing the same at 10^5x. Images (e) and (f) show, at lower magnification, the morphology of the Janus-CNT-bot in which one side was FeONP/Fe^{2+} doped MWCNT while the other side was magnesium coated FeONP/Fe^{2+} doped MWCNTs. **113**

Figure 5.9: Plots (a) – (c) show the gas-chromatographs (GC) of the gases issued out when the CNT-bot reacted with 5% aqueous hydrogen peroxide, 0.05M aqueous HCl, and 0.5M aqueous sodium bicarbonate, respectively. **114**

Figure 5.10: Image (a) shows the UV-Vis spectra of different known iodine solutions in the presence of excess iodide. Image (b) shows calibration curve, absorbance vs. peroxide concentration (C_0) for peroxide concentration ranging from 1% (v/v) to 10% (v/v) aqueous peroxide solutions. Plot (c) shows UV-Vis spectra of different iodine solutions generated at different time intervals of reaction. Plot (d) shows C_0 vs. time (t) plot for reaction between ferrous sulphate present in CNT bot and hydrogen peroxide solution. **116**

Figure 5.11: The plot shows the variation in the concentration of hydrochloric acid in water (C_{acid}) with time (t) during the reaction of aqueous acid solution with the CNT-bots. **117**

Figure 5.12: Shows magnetic hysteresis loops from vibrational scanning magnetometry (VSM) of pure magnetite (red line) and CNT-bots (blue line), respectively. **117**

Figure 5.13: Plots (a) to (c) show Raman shifts of pristine MWCNT-COOH, TiONP, and the composite TiONP-$FeSO_4$ doped MWCNT-COOH. **118**

Figure 5.14: Images (a) and (d) show FESEM images of pristine –COOH substituted MWCNT, TiO_2, TiO_2 and ferrous sulphate doped MWCNT-COOH, and the ultimate photo-active CNT-bots after magnesium deposition. **119**

Figure 5.15: Shows the cyclic voltammetry plots of an electrochemical cell having ~ 10% H_2O_2 taking Ag/AgCl and Pt as the reference and counter electrodes while the CNT-bots on carbon tape as the working electrode. The black curve indicates CV of carbon tape electrode without CNT-bots and red curve signifies CV with carbon tape electrode with CNT-bots. **120**

Figure 5.16: Images (a) – (d) show the EDXS spectra of pristine carboxylated MWCNT, magnetite doped MWCNTs, ferrous sulphate treated and magnetite doped MWCNTs, and CNT-bots after final magnesium coating, respectively. **121**

Figure 5.17: Image (a) shows XRD spectra of pristine magnetite nanoparticles. Image (b) shows magnetite doped and ferrous sulphate treated MWCNTs. Image (c) shows XRD spectra of the CNT-bots after the deposition of magnesium layer. **121**

Figure 6.1: Schematically shows chemophoretic movement of an elliptical particle inside a liquid filled microchannel as a result of local osmotic pressure imbalance. An assymetric catalytic chemical reaction is taking place on the particle surface with different reaction kinetics at the two different halves of the particle. There are two reactants, which give two products following reaction stoichiometry, $aA+bB\rightarrow cC+dD$. **129**

Figure 6.2: Image (a) shows the comparison of concentration profile, at the left side of the moving particle, obtained from CFD numerical simulation and analytical solution. Image (b) shows a similar comparison for the right side of the moving particle. A first-order reaction is undergoing having rate constants k_L = 1.75 and k_R = 8.9 s^{-1} in the left and right halves of the particle, respectively. **134**

Figure 6.3: Shows automated chemophoretic motions of particles with different shapes inside a channel of diameter (d) 250 μm and length (l_c) 500 μm. For all the cases perimeter of the particle is kept 56 μm. Plot (a) shows developed average osmotic pressure difference across the particle, taking the average along with a line extended u_p to 10 μm both sides from the particle surface. Plot (b) compares and contrasts the speed of the particles with different shapes. **135**

Figure 6.4: Shows the chemophoretic motion of a Janus particle moving inside a microfluidic channel of diameter (d_p) 5 μm and length of the channel (l) 15 μm in presence of a constant concentration Dirichlet condition at the left side of the channel. The semi-major and semiminor axis length of the elliptical particle is *1* μm and 0.7 μm, respectively. Image set (i) to (vi) of column A show the position of the particle inside the channel at different time intervals. Image sets of column B show a reactant concentration (c_{r1}) at all the respective frames. Image set of column C represents the concentration profile of a product (c_{p1}) around the particle at respective time intervals. Images (i) to (vi) of column D show the osmotic pressure profile around the particle, across the channel. **137**

Figure 6.5: shows the concentration profile along the channel axis of reactants taken in the right and left-hand side of the particle. Blue lines (lighter shade) represent concentration of the reactant A, whereas grey (darker shade) denotes concentration of reactant B. Image (b) shows the concentration of the products, again blue (lighter shade) represents the concentration of product C and grey (darker shade) shows concentration

of product D. Plot (c) shows the osmotic pressure profiles in the right and left half of the particle. Particle surfaces are taken as the starting point and from the particle $-l$, and $+l$ represents left and right distance along the axis. Solid lines denote for left side profiles and the dotted lines denote the right side profiles. **138**

Figure 6.6: Image set (i) to (vii) of plot (a) represent motion of the particle inside a microchannel having diameter (d_p) 5 μm with varying length (l) 20, 24, 28, 30, 32, 36, 46 μm respectively. Plot (b) shows average pressure drop (Δp) across the particle for different channel lengths. Plot (c) shows particle velocity for different channel lengths. Image set (i) to (vi) of column (d) shows the motion of a particle of diameter having different rate kinetics at the left side of the particle as shown in the figure keeping rate constant of the right-hand side and all other physical parameters unchanged. **140**

Figure 6.7: Shows the average concentration vs time profile (taken across a line along the axis away from the particle surface) of the reactants (c_{ri}) and products (c_{pi}) at the left-hand side of the particle. Plot (b) shows the same average concentration of reactants (c_{ri}) and products (c_{pi}) at the right-hand side of the particle. Plots (c) and (d) show the developed osmotic pressure (π) vs time profile for the left and right side of the particle respectively. **141**

Figure 6.8: Shows the contour of the osmotic pressure, surrounding a particle having a higher reaction rate (k_1) at the right-hand side, with a particle moving from right to the left hand side. Images (b) and (c) show contours of concentration of a reactant and a product for the situation as shown in Fig. 6.7(a). Plot (d) shows the contour of osmotic pressure, surrounding a particle having a higher reaction rate (k_1) at the left-hand side, with a particle moving left to right. Plots (e) and (f) show the concentration of contours of a reactant and a product surrounding the particle, respectively. **143**

Figure 6.9: Images (a) to (c) show the reactant concentration, product concentration, and osmotic pressure vs distance from the particle surface (l) plots for a particle having a higher reaction kinetics on the right half of the particle. Images (d) to (f) show the reactant concentration, product concentration, and osmotic pressure vs distance from the particle surface (l) profiles for a particle having higher reaction rate constant on the left half of the particle. **144**

Figure 6.10: Images (a) to (d) show the osmotic pressure distribution taken on a line along the axis of the channel near the particle. The distance 'l' is measured from the surface of the particle. Images (a) and (c) have higher diffusivity of product components (D_{pi}) than reactant components (D_{ri}) with alternating reaction rates at both sides as

commented in the images. Images (b) and (d) have higher diffusivity of the reactant components (D_{ri}) than product components (D_{pi}) with alternating higher and lower reaction rates as indicated in the diagrams. **145**

Figure 6.11: Plot (a) and (b) show the particle velocity against the ratio of (D_p/D_r) and (D_r/D_p) respectively. The right-hand side of the particle has a higher reaction rate (k_R = 8.80 $M^{-1}s^{-1}$) compared to the left-hand side (k_L = 0.88 $M^{-1}s^{-1}$) of the particle. Image (c) shows the particle velocity against a coefficient defined as ($[k_L\text{-}k_R]/[D_r\text{-}D_p]$). Image (d) shows the variation of particle velocity for a reaction where there is an increase of entropy with respect to stoichiometric coefficient *c*. The stoichiometry of the reaction is $aA+bB \rightarrow cC+dD$. **147**

Abbreviation	Full Name
EDL	Electrical Double Layer
EO	Electroosmotic
CFD	Computational Fluid Dynamics
2D	Two Dimensional
3D	Three Dimensional
FEM	Finite Element Method
GLS	Galerkin Least Square
PNP	Poisson Nernst Planck
DH	Debye Hückel
SCs	Super Capacitors
PPS	Parallel Plate Super Capacitor
CPS	Curved Plate Super Capacitor
GCS	Gouy Chapman Stern
GO	Graphene Oxide
rGO	Reduced Graphene Oxide
TCM	Two Capacitor Model
FP	Filter Paper
TP	Tissue Paper
EIS	Electrochemical Impedance Spectroscopy
CV	Cyclic Voltametry
PVDF	polyvinylidene difluoride
FeONPS	Magnetite Nanoparticles
TiONPS	Titanium Dioxide Nanoparticles
PEM	Proton Exchange Membrane
CNT	Carbon Nanotubes
MWCNT	Multi-Walled Carbon Nanotubes

Synopsis

Field Induced Motions of Microparticles and Fluids for Mixing, Dye-degradation, Energy Harvesting

S1. INTRODUCTION

The research on autonomously moving particles and fluid motions at the micro and nanoscale have gained considerable importance owing to their futuristic applications in nanotechnology, biotechnology, medical science, microfluidics, and many more. In such small-scale confinements, the flow of liquids and particles is often hindered by severe resistance due to the frictional forces. Hence, the flows inside such environments are mostly laminar and require augmented external force field for a faster movement. Thus, motions of fluids or particles at the micro or nanoscale are largely engendered by various external fields like a magnetic field, electric field, light intensity, chemical gradient, Marangoni force, and capillary force, among others.

In particular, the motions of microparticles or fluids inside microfluidic channels are also important because of various advantages such as availability of high surface to volume ratio, the proximity of interactions, and enhanced transport capabilities. For example, the microfluidic motions find multifarious applications in fields like microreactors, micropumps, microseparation, or hosting of various flows in biological systems. On the other hand, microscale particle movements, especially the self-propulsions, have diverse applications in the futuristic fields of micro-surgery, drug delivery, cargo transport, energy harvesting, chemical and biological sensing, and environmental remediation.

Among the various kinds of motions, over the years the electrokinetic flows of the fluids and particles have gained a lot of interest owing to its frequent appearance in various living and non-living systems. The thesis emphasizes on a host of electrokinetic motions of both microscale particles and fluids targeting directional transport, delivery, mixing, and energy storage applications. The electrokinetic phenomena are always concurrent with the formation of electrical double layer (EDL), which is a preferential

distribution of ions surrounding a charged surface. A charged surface in an electrolyte often attracts counter-ions due to electrostatic interaction leading to the formation of an immobile Stern layer. The mobile counter-ions ions near the immobile Stern layer form a diffuse layer, which is together termed as the EDL. Helmholtz was the first to report the presence of the same while Gouy introduced the concept of the diffuse layer surrounding the particle. Later, Chapman gave Maxwell-Boltzmann statistics before Stern combined the propositions from Helmholtz and Gouy-Chapman to elucidate the 'inner' immobile Stern layer and 'outer' mobile Gouy-Chapman diffuse layer in EDL. More recently, the Bockris-Devanathan-Müller (BDM) model for EDL included the influence of the solvent while the electrochemical behavior of the EDLs as capacitors has been extended further with the discoveries of the supercapacitor and pseudo-capacitance.

Among the other electrokinetic flows, electroosmosis is the motion of EDL near a charged surface under an externally applied electric field to engender movement in the bulk electrolyte. On the other hand, electrophoresis is the motion of charged particles under an externally applied electric field due to the formation of the EDLs surrounding the same. Both the phenomena are very frequently observed in most of the various biological systems undergoing *in vivo* and *in vitro* motions. Apart from the electrokinetic motions, the microparticles also show bubble propulsion, diffusophoresis, magnetophoresis, chemotaxis, phototaxis, or sonotaxis under the influence of chemical potential gradient, magnetic field, electric field, light or acoustic fields. Such self-propulsions often emulate the motility of many living species such as amoeba, bacteria, or sperm. The future vision in this regard is to translate the artificial self-propelling micro or nanobots for targeted drug delivery or surgical applications under in vivo condition.

In view of this background, the present thesis focuses on deciphering some fundamental aspects of the movements of microparticles under electric field, chemical potential gradient, and light sources. In this regard, the thesis explores the roles of surface heterogeneity and finds suitable applications in the area of transportation, dye-degradation, and energy harvesting. The thesis also explores the fundamental aspects of an electroosmotic flow inside a microfluidic channel before exploring its capability in micromixing applications. Further, an EDL based energy storage application has also

been attempted while exploring the fundamentals of the charging and discharging of a supercapacitor. During this exploration, all three important handles such as the analytical, computational, and experimental have been used. The objectives of the present thesis are summarized chapter wise as follows,

(i) modulations in the speed and direction of the electrophoretic motion of a 'Janus' micro or nanoparticle with the variation in the chemical heterogeneities on the surface.; (ii) micromixing in the electroosmotic flows inside rigid to flexible channels having physical and physicochemical patterns; (iii) charge storage abilities inside EDL of parallel and curved supercapacitors; (iv) fabrication of multifunctional and multimodal 3G CNT bots capable of showing chemo-, magneto- and photo-taxis along with the capability of energizing a fuel cell and environmental remediation; (v) the origin of the chemotactic motion of a Janus particle undergoing a differential chemical reaction across the surface. The thesis is composed of following five technical chapters with an introductory Chapter 1 in the beginning and a tight summery as Chapter 7 at the end.

S2. TECHNICAL CHAPTERS

S2.1. Chapter 2

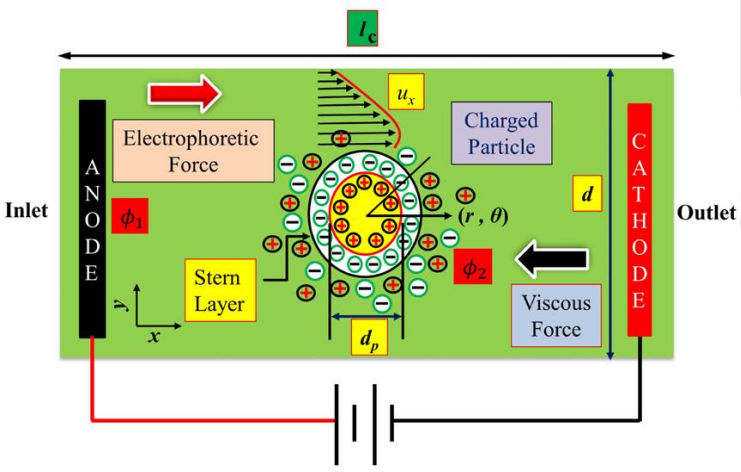

Figure S1: Schematic representation of a charged particle of diameter (d_p), experiencing electrophoretic motion inside an electrolyte under an externally applied electric field potential (ϕ_a), inside a microfluidic channel of diameter d and length l_c. Distribution of co-ions and counter-ions (cations and anions) has been shown by the respective signs around a positively charged particle.

In this chapter, a comprehensive theoretical model has been proposed to analyze the electrophoresis of a charged microparticle under the influence of an externally applied

electric field in an electrolyte filled microchannel. **Figure S1** schematically describes the theoretical set up. The Poisson-Nernst-Planck equations for ion-transport are coupled with the mass and momentum balances before solving them numerically employing finite element method with appropriate boundary conditions. The numerical model includes the efficacies of the moving-deforming-mesh and fluid-structure interaction to uncover the most accurate picture of such motions. A simple analytical model has been developed alongside the Smoluchowski's equation to compare and contrast the numerical results. The simulations reveal that the electrical double layer (EDL) develops dynamically surrounding the particle when it is immersed in an electrolyte and exposed to the external electric field. During the development stage of the EDL, an unsteady motion of the particle is observed before a steady electrophoretic migration is established. Even during the steady migration, an asymmetric EDL surrounding the particle is observed. The electrophoretic velocity obtained from the simulations is found to be consistently lower than the existing and proposed analytical models. The influence of the formation of the asymmetric EDL, the fluid-structure interaction, and particle-inertia are found to be some of the major reasons for the deviations. The particle size, fluid viscosity, applied field intensity, and surface potential is found to influence significantly the speed of the particles. The drag around the particle, the wall-drag near the confinement, and the variation in the electrophoretic thrust owing to the variation in the size of the particle are found to be some other influential parameters in this regard. Interestingly, the speed and direction of the electrophoretic motion of the 'Janus' particles can be tuned with the variation in the chemical heterogeneities on the surface.

This chapter focuses on the comprehensive numerical simulations of a single-phase electroosmotic flow in the patterned and flexible microfluidic channels. **Figure S2** schematically shows different kinds of channel heterogeneities along with theoretical setup taken for present electroosmotic work. A finite element based solver has been employed to solve the Poisson equation in the limit of Debye-Hückel approximation, which is coupled with momentum and continuity equations for fluid flow and the Laplace equation for the external field to uncover the detailed flow features. The study shows the variations in the nature of the base-state velocity profiles with the, (i) physical and chemical heterogeneities on the walls, (ii) the ratio of the Debye length to the

channel diameter, (iii) physical properties of the fluid in microfluidic channels of diameter ranging from 1 μm to 30 μm, and (iv) the effects of the channel deformability.

S2.2. Chapter 3

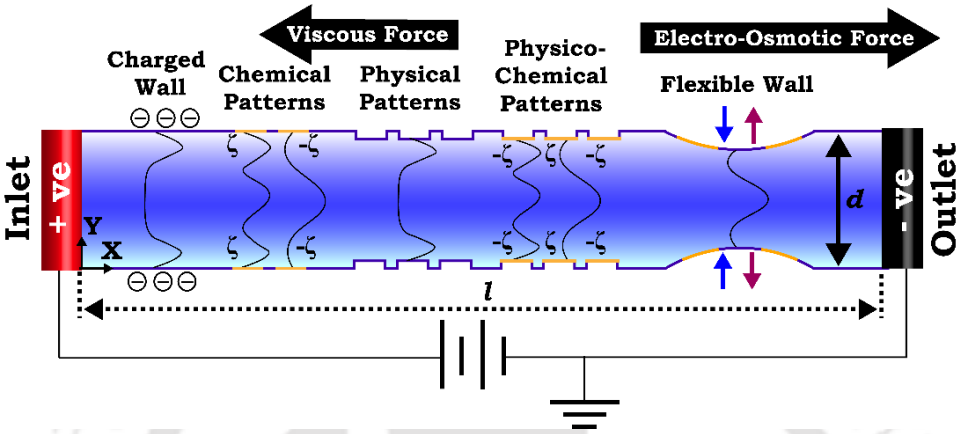

Figure S2: Schematically shows an EO flow inside a microchannel of diameter d and length l_c. Surface charges on the channel walls are shown by an encircled negative sign. Channels with chemical patches on the walls are shown by yellow marks and associated symbols, 'ζ' with positive and negative signs. The groves directing inward of the channel walls represent physical patterns. The grooves having yellow marks and associated symbol 'ζ' represent physico-chemical Patterns. The flexibility of the channel walls is shown by inward curvature on the walls with two arrows signifying to and fro motion. The directions of the driving EO force and the resistive viscous force are shown by arrows. X and Y represent dimensionless coordinates, whereas x and y represent dimensional Cartesian coordinates.

Interestingly, the study reveals that the flow rates and the flow patterns are closely related to the flexibility and deformability of the channel walls owing to the deformation of the EDLs near the channel walls. On the other hand, the chemical heterogeneity present on the channel wall facilitates the variation in the ζ-potential of the channel wall, which in turn locally modulate the flow rate inside the channel to cause intermixing of the layers during the fluid flow. The physical patterns present on the walls also influence the flow patterns leading to the formation of the mixing patterns in the microchannel. Stream lines for different situations have been analyzed to evaluate the extent of internal mixing due to the deformability and physicochemical heterogeneity of the microchannel. The results presented decipher various unknown flow profiles that are possible in case of an electroosmotic flow, which can be employed for augmented fluid mixing inside the microfluidic devices. The variation of current

density along the channel having heterogeneous channel walls has also been explored mentioning its probable application in the field of ζ-potential measurements.

S2.3. Chapter 4

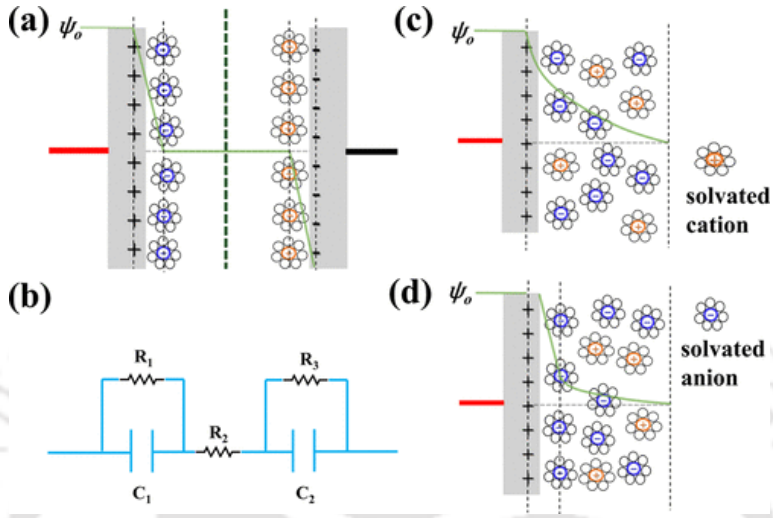

Figure S3: Plot (a) shows profile for the net electric field potential (ϕ_{net}) between a pair of electrodes representing a Helmholtz electrical double layer (EDL). Plot (b) shows equivalent circuit derived from the system shown in (a) using two-capacitor model (TCM). Plot (c) shows distribution of ions in a diffuse layer following the Gouy−Chapman model. Plot (d) shows the Gouy−Chapman−Stern (GCS) model consisting of an immobile Stern layer and mobile diffuse layer in the EDL.

In the fourth chapter, the study reveals various unexplored pathways to energy storage in parallel and curved plate supercapacitors (SCs). Plot (a) to (d) of **Fig. S3**, schematically represents Helmholtz layer on SC plates, model circuit diagram of the SCs set up, distribution of solvated ions following Gouy-Chapman, and following Gouy-Chapman-Stern theory. The spatiotemporal variations in the electric field intensity of such SCs were found to have a significant influence on their performance. The observations unearth the limitations associated with the previous theoretical models, which are routinely employed to analyze the performance of SCs by considering electrical double layers (EDLs) as capacitors near the electrodes. The time-dependent electrochemical behaviors of SCs obtained from the Nyquist and Bode diagrams of electrochemical impedance spectroscopy showed (i) electrode polarization at the higher-frequency sweeps, (ii) immobile Helmholtz layer formation at the mid-frequency zone, and (iii) formation of diffuse layer of EDL in the low-frequency regime.

The results suggest that charge storage of SCs heavily depends on electrode geometry, type of electrolyte, electrolyte concentration, electrode separation, separator type, and dielectric relaxation of the electrolyte. A theoretical model composed of Poisson−Nernst−Planck equations for the electric field in electrolyte and Laplace equation for the electric field in electrodes coupled with Navier-Stokes equations for the fluid flow was numerically solved with appropriate boundary conditions to uncover the pathways to supercapacitance during the experiments. The experimental and theoretical studies together reveal that the use of the potential drop across the EDL originating from the opposing electric fields due to electrode polarization and EDL formation could provide more accurate pathways to supercapacitance of such SCs.

S2.4. Chapter 5

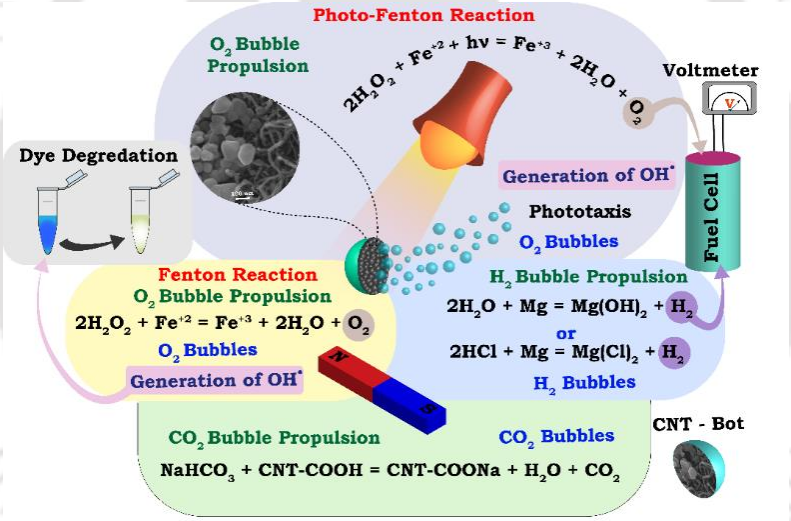

Figure S4: Schematically shows a CNT-bot composed of a –COOH functionalized MWCNT cluster doped with a ferrous (Fe^{2+}) salt and magnetite nanoparticale (FeONPs) before coated with a Mg film. The CNT-bot was capable of undergoing two reactions in acidic and alkaline water (e.g. $Mg + H_2O \rightarrow Mg(OH)_2 + H_2$, $Mg + HCl \rightarrow MgCl_2 + H_2$ and $NaHCO_3$ + MWCNT-COOH → MWCNT-COONa+ $H_2O + CO_2$) and Fenton reaction (in absence of light) and Photo Fenton reaction (in presence of UV light) in the peroxide fuel ($Fe^{2+} + H_2O_2 \rightarrow Fe^{3+} + H_2O + O_2$), as shown on the image. Subsequently, the motor moved by the ejection of hydrogen bubbles in acidic water, carbon-dioxide propulsion in the alkaline water, and oxygen bubbles in the peroxide fuel. The motors could show directionality in the motion under acid and alkali gradients leading to acid- and alkali-taxes, as shown on the images. The scheme also shows that hydrogen and oxygen serve as fuels of PEM Fuel cell and the CNT-bot can also perform dye degradation function.

In this chapter, we report the development of a 3G microswimmer, namely CNT-bot, capable of undergoing acid-, alkali-, magneto- and photo-taxis inside the acidic or alkaline baths of peroxide fuel and/or water. In **Fig. S4**, we schematically describe the summary of the entire work. The use of carboxyl functionalized multi-walled-carbon-nanotubes (MWCNT) facilitated a propulsion of the CNT-bot in the alkaline water by ejecting of carbon-dioxide bubbles. Further, the doping of magnetite nanoparticles (FeONPs), ferrous ions (Fe^{2+}), and titanium dioxide nanoparticles (TiONPs) instigate the magnetic, chemical, and photonic handles for propulsions. While the FeONPs stimulated magneto taxis as high as ~10 body lengths per second under the influence of a bar magnet, the chemotaxis in the peroxide fuel of similar speed was achieved by bubble-propulsion of oxygen gas originating from the Fenton reaction.

In addition, light stimulated Photo-Fenton reaction led to the phototaxy of the CNT-bot. A thin coating of magnesium imparted a half-faced Janus look to the CNT-bot, which helped in the motions inside normal or acidic water mediums through the ejection of hydrogen gas bubbles. The chemotaxes could be transformed into pH stimulated directional motion by establishing a concentration gradient of acid or alkali across the peroxide and/or water baths. The capacity of the CNT-bots to produce oxygen (hydrogen) bubbles in the peroxide (acidic water) fuel was exploited to power a PEM fuel cell to generate electricity. The pure oxygen and hydrogen gases generated by the CNT-bots in separate chambers were fed directly to the fuel cell in which the incessant motions of the particle facilitated the creation and release of the pure gases for the on-demand electricity generation. The motor could also perform dye degradation through advanced oxidation owing to production of intermediate hydroxyl radicals from Fenton's reaction.

S2.5. Chapter 6

This chapter deciphers motion of a Janus particle, which undergoes catalytic reaction on its surface showing two different rate kinetics at its two ends inside a liquid medium containing suitable reactants. **Figure S5** schematically represents the summary of this chapter. A second order reaction, with the stoichiometric equation, $aA + bB = cC + dD$, has been considered. The particle is driven by chemical potential gradient across it and the same is occurred either as a result of differential rate kinetics around the particle

or because of the application of external concentration gradient. The problem is modeled using hydrodynamics, reaction-convection-diffusion equations, and fluid-structure interaction equations.

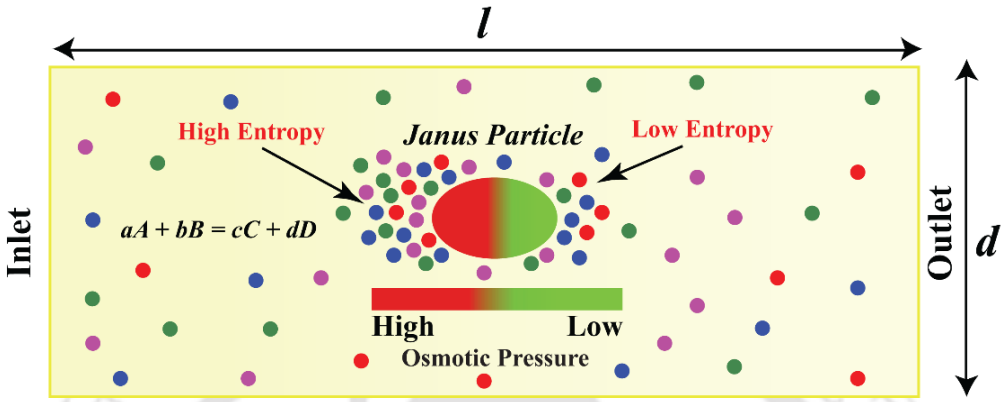

Figure S1: Schematically shows that an elliptical particle undergoing chemotaxis motion inside a microchannel of diameter d and length l_c. A catalytic chemical reaction, which develops a local osmotic pressure gradient, is taking place on the particle surface, which has different reaction kinetics at different halves of the particle.

Finite element based CFD simulations have been used to solve the governing equations and acquire numerical solutions. Owing to different reaction kinetics and also because of the difference in diffusivities of the constituent reactants and products, an osmotic pressure gradient appears across the particle. Despite a very small osmotic pressure build-up across the particle, the micro-sized particle can actually exhibit motion under the influence of this developed osmotic pressure. Diffusivities of the components play a crucial role in determining the speed and direction of motion of the particle. For reactions with no entropy change with respect to stoichiometry, diffusivities of the components actually determine the fate of the particle motion and reaction rate accelerates the motion of the particle. Components surrounding the particle having equal diffusivities for both reactants and products, with no stoichiometric change, cannot exhibit any motion as no osmotic pressure builds up in this particular situation. However, it has been shown that if there is an entropy change with respect to the stoichiometry of the reaction, the particle can actually exhibit motion with or without any difference in diffusivity of the constituent reactants and products. Conditions for particle motion directions have also been summarized and reported in this chapter.

S3. Summary and Future Scope

In summary, this thesis focuses on the fundamentals and applications of the, (i) modulations in the speed and direction of a 'Janus' motor under electric field.; (ii) micromixing in the electroosmotic flows inside rigid, flexible, and physicochemically heterogeneous microchannels; (iii) charge storing EDL of supercapacitors; (iv) multifunctional and multimodal 3G CNT bots capable of showing chemo-, magneto- and photo-taxis; (v) chemotactic motion of a Janus particle undergoing a differential chemical reaction across the surface. In the process, various applications are shown related to directional transport, mixing, energy harvesting, energy storage, and dye degradation. During this exploration, all three important handles such as the analytical, computational, and experimental have been used. The phenomena uncovered in the present work can be extended to the following works as future scopes:

- Experimental studies on the electroosmotic flow inside rigid, flexible, and physicochemically heterogeneous microchannels
- Theoretical and experimental studies on the electroosmotic flow inside rigid, flexible, and physicochemically heterogeneous nanotubes
- Use of micro/nanobots for drug delivery under *in vivo* and *in vitro* conditions
- Improvement of the efficiency and power density of the charge storing EDL of supercapacitors and microbot based fuel cells.

Chapter 1

Introduction

INTRODUCTION

The motions of the mesoscale particles[1-6] or fluids[7-10], especially inside low dimensional channels, conduits, and confinements, have fascinated a large group of scientists and technologists in the recent years owing to their emergence in a variety of interdisciplinary areas of research, which include nanotechnology, biotechnology,[11] medical science,[12, 13] or microfluidics.[14, 15] With the advent of nanotechnology and microfluidics the use of particle and fluid motion in the presence of external fields have become an important phenomenon. In one direction, the studies related to the micro or nanofluidic motions are elementary in the design and development of state-of-art microreactors,[16] micropumps,[17] micromixers,[18, 19] microseparator,[20, 21] or biomicrofluidics.[22] All these devices/instruments mentioned here have found frequent applications in pharmaceutical, healthcare, fine chemicals, biomedical, environmental and food technology related fields. On the other hand, motions of micro or nanoscale particles find diverse applications in the futuristic fields of micro surgery,[23] drug delivery,[24-26] cargo transport,[27-29] energy harvesting,[30-32] chemical and biological sensing,[33-35] and environmental remediation[36, 37] among many others. Targeted drug delivery, micro-surgery using robots, artificial wound healing, and instant environmental remediation are few of the future generation. Scientists and technologists are in the process of improving these fields to come up with innovative solutions. All those applications are discussed in more detail in the upcoming chapters of this thesis. Interestingly, at the mesoscale, the motions of liquids and particles are often dictated by the intermolecular, surface tension, or frictional forces while the forces due to inertia[38-40] or gravity become increasingly unimportant. Importantly, flows inside such environments are mostly in the low speed diffusion dominated laminar regime and thereby require the additional external fields to expedite the same.[7, 41, 42] For example, the prior-art suggests motions of fluids or particles at the micro or nanoscale engendered by an electric field,[43-46] magnetic field,[47-49] chemical potential gradient,[50, 51] acoustic vibrations,[52, 53] photonic excitation,[54] surface tension gradient[55-57] or capillary force.[58, 59] Thus, in the past few decades, extensive research efforts have been observed in exploring the fundamentals and applications of the motions of the fluids and particles, especially at the micro to nano length scales. In all the

aforementioned literatures a chronological development of field driven flows were observed targeting simple to complicated applications with the progress of time.

In particular, the motions of microparticles or fluids inside microfluidic channels are also found to be important because of various advantages such as availability of high surface to volume ratio,[60-62] the proximity of interactions,[63-65] and enhanced transport capabilities.[66, 67] Droplet splitting, specific surface area enhancement in various unit operations with the help of micro and nanotechnology has become recent generations' trends for targeting enhanced efficiencies of processes like micro heat and mass transfers, enhanced reaction rate kinetics, fast response of sensors, and actuators. In this direction, among the various other kinds of motions, the electrokinetic flows of the fluids and particles have gained a considerable interest owing to their applicability at the mesoscale. One of the major objectives of the present thesis is to explore a few novel features of the electrokinetic motions of both microscale particles and fluids targeting directional transport,[68-71] delivery, mixing,[72] and energy storage[71, 73] applications. A detailed explanation of electrokinetics are further given in the introduction sections of the second and third chapters of this thesis.

The electrokinetic phenomena are always concurrent with the formation of electrical double layer (EDL), which is a preferential distribution of ions surrounding a charged surface. The formation of EDL happens when a charged surface is immersed inside a weak electrolyte, which helps in electrostatically attracting counter-ions to form an immobile Stern layer. Subsequently, a layer of mobile counter-ions ions near the immobile Stern layer form a diffuse layer, which is together termed as the EDL.[74-77] Helmholtz was the first to report the presence of the same while Gouy introduced the concept of the diffuse layer surrounding the particle. Later, Chapman gave Maxwell-Boltzmann statistics before Stern combined the propositions from Helmholtz and Gouy-Chapman to elucidate the 'inner' immobile Stern layer and 'outer' mobile Gouy-Chapman diffuse layer in EDL.[78-80] More recently, the Bockris-Devanathan-Müller (BDM) model for EDL included the influence of the solvent while the electrochemical behavior of the EDLs as capacitors has been extended further with the discoveries of the supercapacitor and pseudocapacitance.[80-82]

Among the other electrokinetic flows, electroosmosis (EO) is the motion of EDL near a charged surface under an externally applied electric field to engender movement in the bulk electrolyte.[83, 84] On the other hand, electrophoresis (EP) is the motion of

charged particles under an externally applied electric field due to the formation of the EDL surrounding the same.[85] Both the phenomena are very frequently observed in various *in vivo* and *in vitro* biological systems.[86-89] In recent days, application of electrokinetic phenomena to target some *in vivo* applications are being thought of. Most of the biological cells and tissues have surface potential and the same have the potential to form EDL around the same with the ions which are present in intra or extra cellular matrix of the cells. In the presence of inherent or external electric fields those EDL can show movements along with the movements of cells and cellular matrix. Further, the EO flows have recently been employed for diverse applications, which include micropumps,[17] flow microcontrollers,[90] or flow FETs.[91, 92] In addition, various fundamental aspects of the EO flows have been extensively studied employing the theoretical[93-97] and experimental[98-100] frameworks since the discovery of the phenomenon in the early 19th century by Reuss[101, 102] and Porrett.[103, 104] A number of recent developments have shown the usage of state-of-art experimental and theoretical tools at the micro to nanoscale in exploring the unknown features of EO flows,[30-40] like the exploration of the details of the steady,[96] unsteady,[97] and temperature[105] profiles. The EP flows have also been employed extensively over the years in protein separation,[106, 107] gel electrophoresis,[108, 109] ζ-potential analysis,[110-113] particle size analysis,[109, 114, 115] or dynamic light scattering[116-118] applications.

Apart from the EP motions, the microparticles also show diverse field driven motions such as induced electrophoresis,[119-122] dielectrophoresis,[123, 124] magnetophoresis,[125, 126] sonotaxis,[52, 53] phototaxis,[54] marangoni flow[55-57] under the influence of electric field, magnetic field, light or acoustic fields. All those kinds of motions of the particles and charged objects have applications in various chemical, biological, and biotechnology related applications. Separation of proteins, blood cells, nucleus are few of the applications. On the other hand, for the self-propellers, a weak driving force is inherently generated in the vicinity of the micro or nanobots owing to various reasons, like development of ζ-potential,[127-129] chemical potential,[130, 131] surface tension[55-57]or temperature gradients,[132-134] to mention a few. Such self-propulsions often emulate the motility of many living species such as amoeba, bacteria, or sperm. The prior-art suggests that the chemically-powered self-propellers achieve motility by the conversion of chemical energy into the mechanical one. They acquire motion by

ejecting a stream of gas microbubbles for bubble-recoil propulsion[135-138] or from a differential fuel concentration gradient.[4, 139, 140]

Among other chemical propulsions, the hydrogen peroxide (H_2O_2) fuel based[141, 142] bubble propulsion has been the most extensively reported system for the motility of artificial micro or nano systems. Of late, along with the peroxide fuel, many of such kind of bots have also been fabricated, which are capable of showing self-propulsion in water,[143, 144] hydrazine,[145] inorganic acids, alkali, citric acid, sodium borohydride, acetylene, urea,[146] glucose,[147] halogens, and alcohol.[148] Notably, the self-propelling objects have gained importance over field driven flow due to their capability of autonomous motion.[149] Conversely, the field driven propulsion gained considerable interest because of their capability to remotely control the self-propelling motions.[150, 151] In particular, these remotely controlled self-propelling objects are envisioned to be deployed as chemical and biological sensing agents as drug/gene drug delivery,[24-26] fuel cell energy harvester,[59, 61] surface patterning bots, non-invasive surgery tools, cell manipulation to environmental remediation[36, 37] agents, among many other applications. One of the long-standing future visions in this regard has been to translate these artificial field driven or self-propelling micro or nanobots for targeted drug delivery or surgical applications under *in vivo* condition.[152, 153]

Besides the motions of the particles, the charge storage exploiting EDL formation on highly porous surface-active materials is one of the very attractive research topics. Such EDL based capacitors (EDLCs) are expected to mitigate the future energy storage challenge with the vision of a greener world[154-156] using high quality renewable energies replacing the popular fossil or nuclear fuels.[157, 158] EDL capacitor is an arrangement where a large amount of charge can be stored exploiting the active material that is present on the electrode surface which has high porosity and tortuosity and the same facilitates charge storage. In this direction, the renewable power generators are often integrated with the supercapacitors (SCs).[159] Among the many other types of SC available, the most popular choice has been the usage of the EDL based SCs. According to the current understanding of charge storage mechanism of the SCs, the energy is stored at the electrode-electrolyte interface due to the accumulation of opposite charges in the electrode surface and EDL. In this situation, the capacitance per unit square area of the charge separation at the electrode-electrolyte interface is defined as the intrinsic capacitance of an SC.

In view of this background, the present thesis focuses on exploring some uncharted fundamental aspects of the movements of microparticles under electric field, chemical potential gradient, and light sources. In this regard, the thesis uncovers the roles of surface heterogeneity and finds suitable applications in the area of self-propelling motions, dye-degradation, and energy harvesting. The thesis also unearths some of the fundamental aspects of an electroosmotic flow inside a microfluidic channel before exploiting their capability in micromixing applications. Further, an EDL based energy storage application has also been attempted while studying the fundamentals of the charging and discharging of a SC. During this exploration, all three important handles such as the analytical, computational, and experimental have been used.

The thesis is composed of following five technical chapters with an introductory Chapter 1 in the beginning and a tight summery as Chapter 7 at the end. The technical objectives of the present thesis are summarized chapter wise as follows, Chapter – 2: modulations in the speed and direction of the electrophoretic motion of a 'Janus' micro or nanoparticle with the variation in the chemical heterogeneities on the surface; Chapter – 3: micromixing in the electroosmotic flows inside rigid to flexible channels having physical and physicochemical patterns; Chapter – 4: charge storage abilities inside EDL of parallel and curved supercapacitors; Chapter – 5: fabrication of multifunctional and multimodal 3G CNT bots capable of showing chemo-, magneto- and photo-taxis along with the capability of energizing a fuel cell and environmental remediation; and Chapter – 6: the origin of the chemotactic motion of a Janus particle undergoing a differential chemical reaction across the surface.

Chapter 2

Effects of Fluid-Structure-Interaction and Surface Heterogeneity on the Electrophoresis of Microparticle

ABSTRACT

A theoretical model is proposed to analyze the electrophoresis of a charged microparticle in an electrolyte filled microchannel. The Poisson-Nernst-Planck equations are coupled with the mass and momentum balances before solving them numerically with appropriate boundary conditions. The model includes the efficacies of moving-deforming-mesh and fluid-structure interaction to uncover the accurate picture of such motions. An analytical model has also been developed to compare with the numerical results. The simulations reveal that the electrical double layer (EDL) develops dynamically surrounding the particle when it initiates electrophoresis. An unsteady motion of the particle is observed during the development stage of the EDL before a steady electrophoretic migration is established. Even during the steady migration, an asymmetric EDL surrounding the particle is observed. The electrophoretic velocity obtained is found to be consistently lower than the existing models. The influences of formation of the asymmetric EDL, the fluid structure interaction, and particle-inertia are found to be some of the major reasons for the deviations. The particle size, fluid viscosity, applied field intensity, and surface potential is found to influence significantly the speed of the particles. The drag around the particle, the wall-drag near the confinement, and the variation in the electrophoretic thrust owing to the variation in the size of the particle are found to be some other influential parameters. Interestingly, the speed and direction of the electrophoretic motion of the ‘Janus’ particles can be tuned with the variation in the chemical heterogeneities on the surface.

Name	Symbol
Diameter of channel	d
Length of channel	l_c
Diameter of particle	d_p
Distance from particle surface	L
Surface potential	ζ_w
External potential	V
Diffusivity of cation	D_+
Diffusivity of anion	D_-
Density of fluid	ρ
Viscosity of fluid	μ
Permittivity of the vacuum	ε
Faraday constant	F
Bulk concentration	c_0
Charge of ions	z_+ / z_-
Relative permittivity	ε_r
Universal gas constant	R
Absolute temperature	T
Nernst-Einstein mobility	u_{mi}

Table 2.1: Nomenclature of the symbols used in this chapter.

Chapter 2

2.1. INTRODUCTION

The physics associated with various electrokinetic processes[21, 120, 160-162] such as electroosmosis,[96, 163, 164] diffuisophoresis,[165, 166] electrophoresis,[119-122] or streaming[167-170] ,and sedimentation[171, 172] potentials have fascinated the researchers for ages owing to their links with various naturally occurring phenomena. Arguably, the understanding of them has become more important in the various domains of microfluidic applications with the advancements in mesoscale fabrication and characterization techniques. For example, the electroosmotic pumps[17, 173] and gel or capillary electrophoretic devices[174] are now commercially available. Further, dielectrophoresis has been widely used for cell sorting[175-177] and membrane control.[178] The streaming potential has also been employed for energy harvesting[30-32] while electroosmosis has been employed for micromixing applications.[179, 180] In particular, the electrophoretic migrations[181-183] of the colloidal objects are found to be of utmost importance in super-capacitors[184], analysis of nucleic acids[21, 185-188] and proteins,[189-191] self-propulsion[192-194] migrations of proteins across cell membrane,[195-197] and testing of drugs.[198, 199] Thus, in the recent years, a lot of research activity has been observed to identify the finer aspects of the electrophoretic migrations of different types of micro to nanoscale particles.

The theoretical understanding of the electrophoretic migration has also evolved progressively during the past few centuries.[200-202] For example, Smoluchowski balanced the viscous and electric field forces to analytically evaluate the electrophoretic speed of a particle as, $U_0 = (\varepsilon\zeta/\mu)E$ [203], wherein ζ, ε, μ, and E represent ζ-potential of the EDL, the dielectric constant of the electrolyte, dynamic viscosity fluid medium, and the electric field, respectively. While the Smoluchowski's equation was found to be appropriate for the situations where the thickness of the EDL was much smaller than the particle dimension,[204] the expression provided by Hückel, $\lambda = \sqrt{RT\varepsilon/2c_0F^2}$ was found to be far more appropriate for the situations with thicker EDL. These expressions have widely been used in the past few decades to characterize the various properties of the micro or nanoscale particles such as size, size-distribution, ζ-potential, mobility, and electrostatic forces of attraction.[205] Importantly, these formulations neglected the effects of particle inertia, fluid structure interaction, dynamics of the formation of the EDL around the particle during migration, surface heterogeneities, and effects of confinement.[206]

Thus, of late, extensive research activities have been observed to integrate these aspects into the theoretical formalisms. For example, Dukhin and co-workers, showed the effect of high surface charge density in determining the electrophoretic speed while Schnitzer and co-workers[207] studied the effect of Dukhin number on electrophoretic mobility integrating the effects of the related nonlinearities. The distortion of ionic equilibrium and EDL due to the high surface charge density was numerically simulated by O'Brien and White[208] to obtain an electrophoretic speed much smaller than the same predicted by Smoluchowski's model. Subsequently, the expressions for electrophoretic mobility for a dielectric charged particle having a finite but polarized double layer surrounding the particle were derived. The studies on the effects of proximity[122, 209-213] or channel confinement[210] predicted very different electrophoretic velocity than the same predicted by Smoluchowski.

However, there are a number of questions that remain still unaddressed. For example, most of the previous studies ignore the, (i) effects of the movement of particle on the flow of the electrolyte and EDL; (ii) fluid-structure interaction; (iii) development of charge distributions in the EDL; (iv) distortion of the EDL; (v) size and the shapes of the particles; and (vi) presence of chemical or physical heterogeneities on surface. In view of this background, we perform computational fluid dynamic (CFD) simulations to analyze the aforementioned attributes of the electrophoretic migrations of a charged particle. The unsteady transitions of the EDL have been considered in the model through the widely accepted Poisson-Nernst-Planck (PNP) equations,[214-216] which are numerically solved along with the mass and momentum balance equations to uncover the detailed spatiotemporal dynamics of the EDL surrounding a charged particle. The uses of the moving deforming mesh along with the fluid structure interactions have helped in uncovering the influence of these aspects on the electrophoretic mobility of the charged particle. In particular, we focus on electrolytes with lower salt loading,[5, 217-220] which gives rise to thick EDLs in the limit of 0.1 to 0.3 μm under infinite dilution.[221-223] The study uncovers that the size of the particle, confinement effects, surface heterogeneities, and the dynamics of the EDL formation have significant influences on the electrophoretic mobility of a charged particle, which leads to significant deviations from the predictions made by previous theoretical models.

2.2. PROBLEM FORMULATION

2.2.1. Governing Equations:

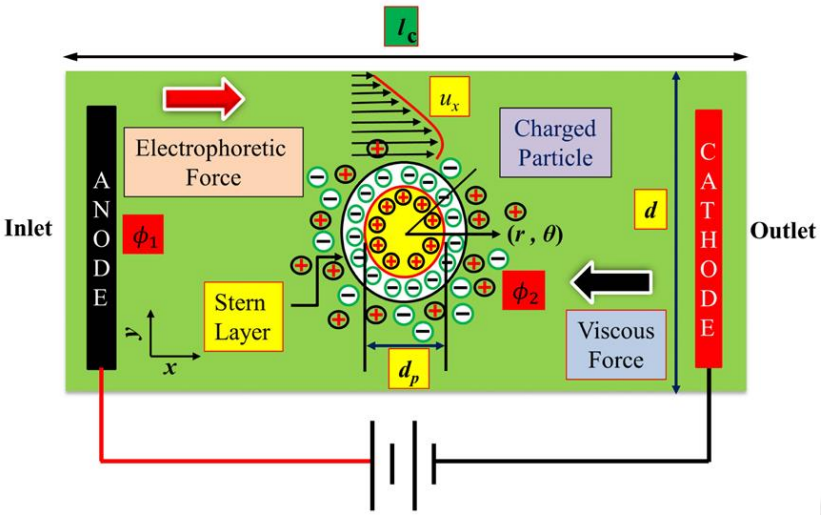

Figure 2.1: Schematic representation of a charged particle of diameter, d_p, experiencing electrophoretic motion inside an electrolyte under an externally applied electric field potential, ϕ_1, inside a microfluidic channel of diameter d and length l. Distribution of co-ions and counter-ions (cations and anions) has been shown by the respective signs around a positively charged particle.

Figure 2.1 schematically shows the two-dimensional (2-D) geometry employed for the numerical and analytical modeling of the electrophoretic movement of a charged particle inside an electrolyte under the influence of an external electric field. The figure indicates that the effects of the flow of the electrolyte, the electric field around the charged particle, the externally applied field and subsequent transport of ions from bulk to the particle surface or vice versa are mutually coupled. In what follows, we present a theoretical model, which comprehensively considers all these aspects. A mixed coordinate system has been employed to solve the governing equations with the boundary conditions. The region surrounding the particle is modeled in the polar coordinate system (r, θ) considering the center of the particle as, $r = 0$, as shown on the image. However, the hydrodynamic equations and the equations for the ionic concentrations are solved in the entire channel employing a Cartesian coordinate system (x, y), as shown on the figure.

In this formulation, the bold variables are vectors, the bold variables with double overbar are tensors, partial derivative is denoted as ∂, ∇ represents gradient operator, D is material derivative, $\mathbf{I}$ is identity tensor, and the superscript T is transpose. The

bracketed variables denote components, e.g., **u**(u,v) and **v**(u_s,v_s) represent fluid velocity and displacement of the solid particle, respectively. The concentration of i^{th} ion is denoted by c_i. The notations, ϕ_1 and ϕ_2 denote externally applied electric field potential and the ζ-potential around the charged particle surface, respectively. The total electric field potential is the algebraic sum of the pair of aforementioned potentials represented as, $\Phi = \phi_1 + \phi_2$.

The governing equation for the externally applied electrostatic field on the bulk electroneutral electrolyte has been obtained from the Gauss's law as $\nabla \cdot \mathbf{E} = 0$, where **E** is the electric field vector. The irrotational ($\nabla \times \mathbf{E} = 0$) nature of such fields helps in obtaining the electric field in terms of the potential as, $\mathbf{E} = -\nabla\Phi$, which eventually leads to the following Laplace equation,

$$\nabla^2 \phi_1 = 0. \tag{2.1}$$

The electrostatic field and the ions distribution in the EDL surrounding the charged particle surface is governed by the following PNP equation,

$$\varepsilon \nabla^2 \phi_2 = -\sum z_i c_i . \tag{2.2}$$

The distribution of the ions surrounding the charged particle is governed by the following scalar transport equations,

$$\partial c_i / \partial t + u_i \cdot \nabla c_i = D_i \nabla^2 c_i + z_i F u_{mi} \nabla \cdot c_i \nabla\Phi . \tag{2.3}$$

In this equation, the last term appears due to the ion migration under electric field. The term u_{mi} represents Nernst-Einstein mobility[224], and this is equal to $u_{mi} = (D_i / RT)$. In Eq. (2.3), the last term incorporates the effects of the electrophoretic migration. The electrolyte is considered to be incompressible, immiscible, and Newtonian while flowing inside the microchannel. It may be noted here that since the applied direct current (DC) electric field on the particle is overwhelmingly strong, we neglect the force arising from the dielectric mismatch between the particle and electrolyte.

The Laplace and Poisson equations for the electric, as shown in the Eqs. (2.1) and (2.2) along with the scalar transport equations for the co- and counter-ions in the Eq. (2.3) have been coupled with the continuity and Navier-Stokes equations of motion to comprehensively model the electrophoretic migration of a charged particle inside an electrolyte under the influence of an externally applied electric field,

$$\nabla \cdot \mathbf{u} = 0, \tag{2.4}$$

$$\rho \frac{D\mathbf{u}}{Dt} = -\nabla p + \mu\left(\nabla^2 \mathbf{u}\right) + \rho_e \mathbf{E}. \tag{2.5}$$

Here, $\rho_e = -\varepsilon \nabla^2 \phi_2$ is the charge density in the EDL. The electrophoretic force in the momentum equation originates from the Maxwell stresses, ($\mathbf{M} = \varepsilon_0 \left(\mathbf{E}_i \mathbf{E}_i - 0.5\mathbf{E}_i^2\right)$ due to the combination of external electric field and potential around the charged particle. The formalism used here has been followed by a number of previous theoretical works.[225]The inertial effect of the particle migration has been taken into account through the implementation of the fluid structure interaction,

$$\rho_s \left(\partial^2 \mathbf{v}_s / \partial t^2\right) - \nabla \cdot \bar{\bar{\boldsymbol{\sigma}}} = 0, \tag{2.6}$$

$$\bar{\bar{\boldsymbol{\sigma}}} = -p\bar{\bar{\mathbf{I}}} + \mu\left(\nabla \mathbf{u} + \nabla \mathbf{u}^T\right). \tag{2.7}$$

Here the symbols, ρ_s, $\bar{\bar{\boldsymbol{\sigma}}}$, p, and μ represent the density of the solid, hydrodynamic stress tensor, fluid pressure, and viscosity of the electrolyte, respectively.

2.2.2. Boundary Conditions:

In order to solve the Eq. (2.1) constant potential boundary conditions have been applied across the channel length as, $\phi_1 = V_{ext}$ at x = 0 and $\phi_1 = 0$ at $x = l$. The electric field for EDL is obtained by solving the Eq. (2.2) with the boundary conditions as the surface potential, $\phi_2 = \zeta$ at $r = R$. The Eq. (2.3) is solved with a constant inflow condition, $c_i = c_{i0}$, at the inlet of the channel, x = 0, and normal flux condition, $-\mathbf{n} \cdot \nabla D_i c_i = 0$, at the outlet, $x = l$. The initial condition to solve the Eq. (2.3) is, $c_i = c_{i0}$ at t = 0. In order to solve the continuity and Navier-Stokes equations, no slip (u = 0) and impermeable (v = 0) boundary conditions are enforced at the walls. The pressure is kept constant at inlet and outlet of the channel to arrest the fluid flow except for electrophoretic migration. For the fluid structure interaction, the two-way coupling is enforced along with the particle. For this purpose, continuity of velocity boundary condition, $\mathbf{u} = \dot{\mathbf{u}}_s$, have been enforced on the particle surface while a no-slip condition is enforced along the inner wall of the tube. Zero displacement ($\mathbf{u_s}$ = 0) and zero speed ($\dot{\mathbf{u}}_s$ = 0) of the particle at initial time (t = 0) have been enforced to meet the two boundary conditions necessary two solve the Eq. (2.6). The hydrodynamic stress, which is being imparted on the particle surface is taken from the coupled momentum equations. Thus,

the fluid flow applies force on the particle while the particle displacement also enforces the fluid movement. A moving deforming mesh with dynamic refinement and regeneration of the mesh-elements has been used to track the particle migration.

Table 2.2: Parameters used in the Simulations

Name	Symbol	Value	Unit
Diameter of channel	d	5	μm
Length of channel	l	15	μm
Diameter of particle	d_p	2.0	μm
Surface potential	ζ_w	50	mV
External potential	V	0.5	V
Diffusivity of cation	D_+	2×10^{-9}	m^2/s
Diffusivity of anion	D_-	4×10^{-9}	m^2/s
Density of fluid	ρ	1000	Kg/m^3
Viscosity of fluid	μ	0.0023	Pa s
Bulk concentration	c_0	0.001	mM/lt
Charge of ions	z_+ / z_-	1/-1	-
Relative permittivity	ε_r	78.3	-

2.2.3 Analytical Solution:

A simple analytical model has been proposed here to complement the CFD results. For this purpose, a spherical coordinate system has been chosen. A charged particle of radius *r* has been taken in an electrolytic solution having cations and anions. The electric field, which is generated near the particle surface owing to the surface charge, and the formed electrical double layer near the charged surface, is governed by the Poisson equation,

$$\nabla^2\phi_2 = \kappa^2\phi_2 . \tag{2.8}$$

Here, $\phi_2 = \phi_2(r,\theta,\phi)$, i.e. the potential is function of radial, angular and azimuthal directions. For the simplicity of the model, we neglected the dependence of the potential on angular and azimuthal directions. Here, *k* is the reciprocal of the Debye length. In this analytical model, we have incorporated the Debye-Hückel approximation where

$\kappa^{-1} = \sqrt{RT\varepsilon/2c_0F^2}$. The symbols used in this expression and their typical values employed for the calculations have been provided in the **Table 2.2**. The Eq. (2.8) has been solved by using Wolfram Mathematica™ subject to the boundary conditions, at *r* = *R*, $\phi_2 = \zeta$; and at *r* = *R*+ λ, $\phi_2 = 0$. The obtained solution is very cumbersome and for the sake of brevity, the expression is not shown here.

The analytical method employed to obtain the electrophoretic speed has been employed in a number of previous works [205, 226] wherein the Stokes drag force is equated with the electric field force. The electrophoretic force is evaluated by doing a volume integral around the particle from the surface (*R*) until the EDL thickness ($R+\lambda$) as,

$$F_E = \varepsilon\varepsilon_0\kappa^2 E \int_0^{2\pi}\int_0^{\pi}\int_R^{R+\lambda} \phi_2 r^2 \sin\theta d\theta d\phi dr \,. \tag{2.9}$$

Where the externally applied electric field intensity, $E = V_m/l$ and V_m is the average potential of the applied field,

$$V_m = (1/l)\int_0^l \phi_1 dx \,. \tag{2.10}$$

It may be noted here that while the solution for the potential near the particle is done by taking spherical polar coordinate system, the solution for the external field has been done by taking a Cartesian reference frame as the channel in 2D has a shape of a rectangle. Equating the electrophoretic body force with the drag force for a spherical particle we obtain the analytical electrophoretic speed of the particle as,

$$u_p = \frac{\varepsilon\varepsilon_0\kappa^2 E \int_0^{2\pi}\int_0^{\pi}\int_R^{R+\lambda} \nabla^2\phi_2 r^2 \sin\theta d\theta d\phi dr}{6\pi\mu R} \,. \tag{2.11}$$

The above integration is performed using the commercial package Mathematica™.

2.2.4. Numerical Solution Methodology:

The most accurate finite element method (FEM) has been employed to numerically discretize and solve the coupled set of Eqs. (2.1) – (2.7) with the mentioned boundary conditions employing the COMSOL Multiphysics™ software. The software uses Galerkin least-square (GLS) method along with the second order elements for velocity and first order elements to discretize the equations. The segregated predictor-corrector

method with incremental pressure correction led to the velocity and pressure profiles for the flow. A second-order backward difference method led to consistent initialization and time-marching with an optimal time step size of ~10^{-4} s. The data obtained from the solver file is extracted and after appropriate post processing are reported as the results. Numerical convergence for this finite element based solution has been reached at ~ 50000 mesh elements with additional refinements of the meshes near particle surfaces, where EDLs are formed.

2.3. VALIDATION

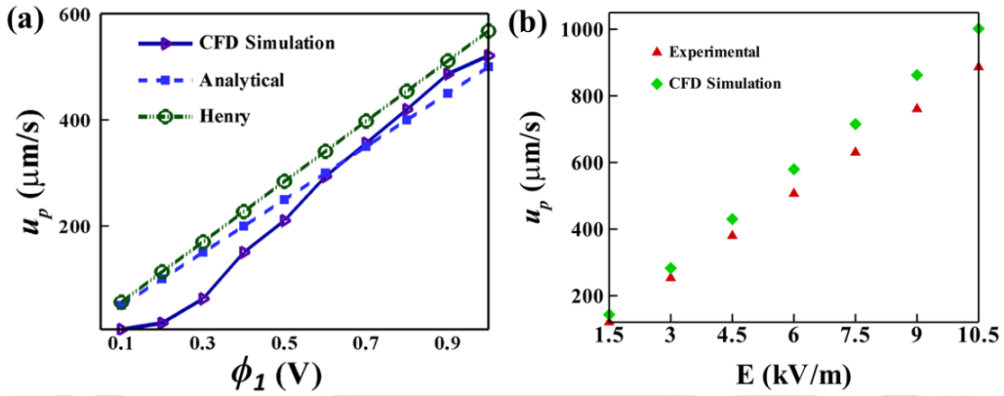

Figure 2.2: Plot (a) shows the variation in u_p with external potential (ϕ_1). The triangular symbols with a solid line are obtained from the nonlinear CFD simulations and the square symbols with dashed line are form the proposed analytical model. Particle diameter (d_p), surface potential (ϕ_2), channel length (l), channel confinement (d/d_p), initial concentration of ions (c_{i0}) are kept as 2 μm, -50 mV, 15 μm, 5, 0.001 mM/lit respectively. Plot (b) shows the comparison of particle speeds in a microchannel when the experimental results are compared with CFD simulations for a particle ~10 μm diameter and other parameters as taken by an experimental article.

The Eq. (2.11) is employed to validate the simulated results obtained from this work. Further, we also have validated the simulated results with the existing analytical methods in order to prove the accuracy of the simulated results. We validated the order of magnitude of particle velocity, moving under the electrophoretic force, obtained from the finite element based computational fluid dynamics results against the analytical particle velocity as obtained from the Eq. (2.11) and other methods. **Figure 2.2** shows particle velocity plotted against different external potential having considerable match between analytical and numerical profile and hence validates the authenticity of the numerical simulation. However, with a very small external potential, the particle cannot undergo any motion not being able to overcome the particle inertia

to have a motion. Moreover, with increasing velocity we find a considerable match in both the velocities obtained numerically and analytically.

The deviation of the simulated to the analytical velocity is found because of particle inertia, non-uniform profile of ζ-potential surrounding the particle, and channel confinement. However, in the asymptotic limit, with less channel confinement, small particle size, and electrolyte with lower solute concentration, we observe a considerable match between analytical and CFD simulation results. Moreover, we also compare the particle speed with the Henry model available in literature. Although there is no one to one map of the particle speeds obtained by CFD simulation with both proposed analytical and the Henry model[69], the simulation can give nearly match at said asymptotic limits. The reasons for deviation are elaborately discussed in the results and discussion of this chapter. Moreover, we compared the simulation results with a similar experimental work. The parameters given in the plot are taken for the simulation and all other parameters are kept equal as much as practicable. In such a scenario, although we did not get exact match between experimental and simulation results the comparison is quite good as we get a complete order of magnitude similarity and an equal trend.

2.4. RESULTS AND DISCUSSION

When a charged particle is placed in a solution, it preferentially develops an EDL around the surface because of differential affinity towards the cations and anions in the solution. Thus, the attraction and repulsion of counter- and co-ions helps in developing concentration profiles of the cations and anions surrounding the particle. **Figure 2.3(a)** shows the concentration profiles of the co-ions (c_1), counter-ions (c_2), and the difference of concentration between co- and counter-ions (Δc) with the distance away from the particle (l). The unevenly (evenly) broken line suggests that in the EDL the counter-ion (co-ion) concentration diminishes (increases) gradually away from the charged surface before asymptotically reaching bulk concentration after a finite distance away from the particle. The solid line shows the profile of the Δc, which shows a diminishing trend away from the particle surface.

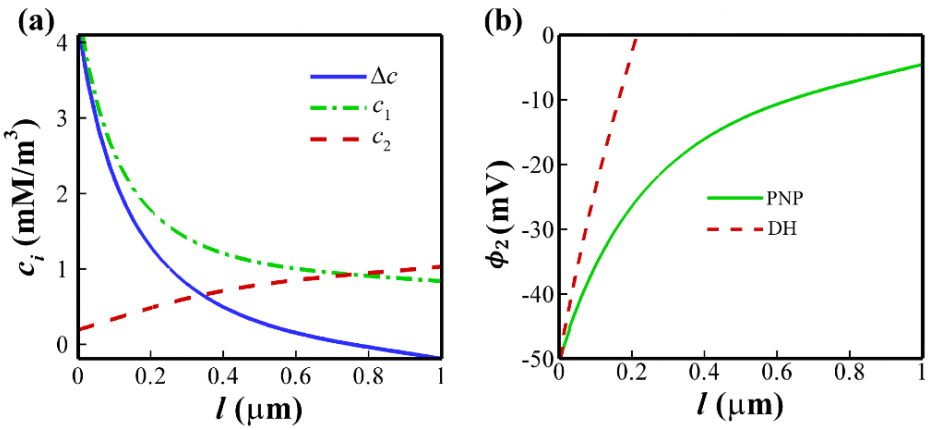

Figure 2.3: Plot (a) shows the nonlinear distribution of co-ion (c_2, red broken line), counter-ion (c_1, traffic green dash dot line), and difference of co- and counter-ions (Δc, blue solid line) around the charged particle of diameter 2 μm with a surface charge of -50 mV. Other simulation parameters involved are listed in **Table 2.2**. Plot (b) shows the profile of ζ-potential around the charged particle of diameter 1 μm and surface potential -50 mV. The solid line represents the profile obtained by solving PNP equation and the red dotted line shows the Debye Hückel profile.

As mentioned in the previous section, the PNP equation has been solved to obtain the electric field potential developed around the charged particle owing to the charge distribution of the ions in the electrolyte, as shown in the **Fig. 2.3(a)**. **Figure 2.3(b)** shows that the distribution of the ions in the EDL, which eventually develops a variation in the electrical potential around the particle. The figure shows the development of the ζ-potential profile (solid green line) in the EDL, which is the effective potential of the charged microparticle in the electrolyte. In this plot, we also have provided a comparison by analytically evaluating the electric field potential from the Poisson equation under the Debye Hückel approximation, as shown by the broken line. In this regard, the Debye length (λ) is calculated from the expression, $\lambda = \sqrt{RT\varepsilon / 2c_0F^2}$ for which the magnitudes of the variables employed are listed in **Table 2.2.** The plots in the **Fig. 2.3(b)** suggests that the PNP profile shows considerable non-linear characteristics of the electric field potential across the particle as compared to the profile obtained from the analytical model with Debye Hückel approximation. Further, the values obtained under the Debye Hückel matches with the PNP profile only near the surface of the particle while they deviate significantly away from the particle. The profile for the electric field potential obtained from the PNP equations is expected to be more accurate and has a significant influence on the particle velocity, as can be observed in the later part of the chapter. Importantly, when the particle is in

electrophoretic motion the charges may redistribute around the particle with time. In what follows, we show such variations of the ionic concentration profiles around a particle undergoing electrophoresis with the help of comprehensive CFD simulations. The use of moving deforming mesh and fluid structure interaction in the CFD model helps in the analysis of the spatiotemporal variation in the particle position and subsequent change in the ions in the electrolyte during its migration.

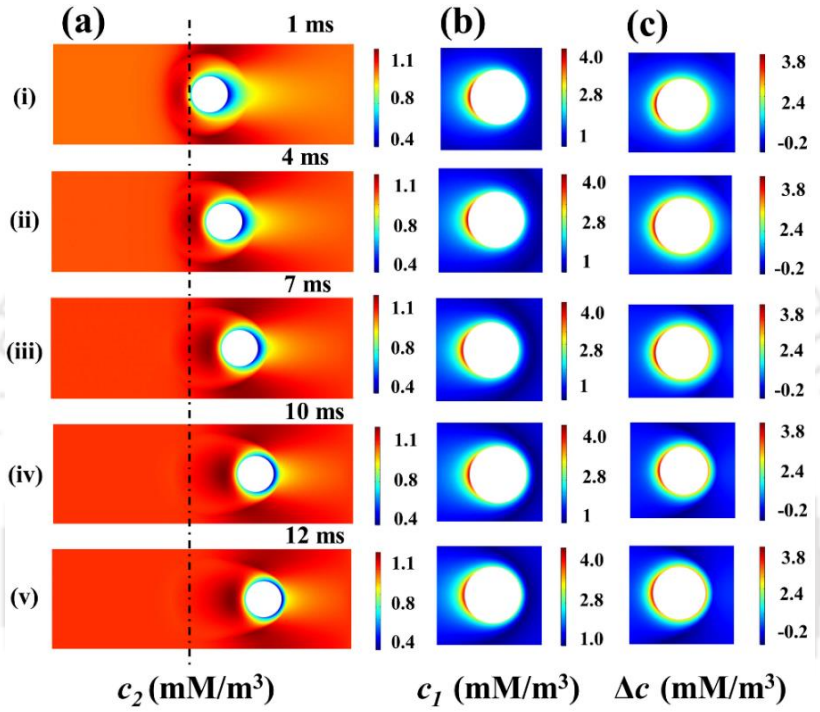

Figure 2.4: Image set (a) shows the contours of the co-ion concentration (c_2), image set (b) shows distribution of counter-ion concentration (c_1), and image set (*c*) shows distribution of the difference of concentration (Δc) around a microparticle of 2 μm diameter undergoing electrophoretic migration inside a microchannel of 5 μm width and 15 μm length. The contours are plotted at different time intervals as shown on the images. The viscosity coefficient, relative permittivity of the electrolyte, ζ-potential at the EDL, and externally applied field are, 0.023 Pa s, 80, 0.05 V, 1 V, respectively.

Figure 2.4(a) shows the contours of the concentration of the co-ions in the EDL surrounding the microparticle with time as the particle migrates toward the downstream of the microchannel under the influence of the external electrostatic field. Subsequently, the **Figs. 2.4(b)** and **2.4(c)** show contours of the concentration of the counter-ions (c_1) and Δc around the particle at different time intervals. The concentration profiles shown in this figure uncover that the proposed computational model can accurately predict the dynamic change in the distributions of the co- and counter-ions during the movement of the particle. This phenomenon is found to have a serious influence on the electric

field potential surrounding the particle and subsequently on the electrophoretic mobility.

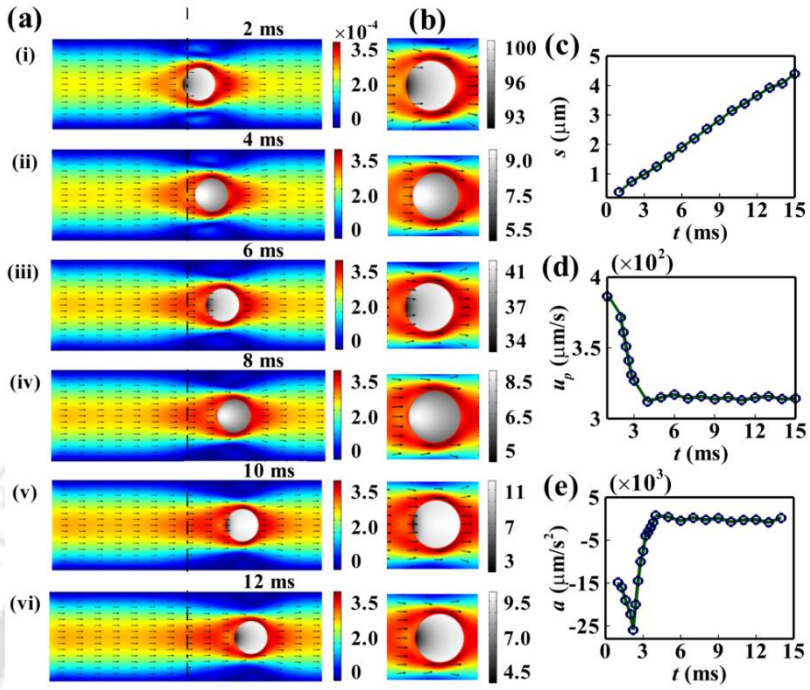

Figure 2.5: Frames (i) to (vi) in the image set (a) show the position of the moving particle at different time intervals when the diameter (d_p) is 2 μm and surface potential is -50 mV. Frames (i) to (vi) in the image set (b) show the respective distribution of stress on the solid particle undergoing electrophoresis. Plots (c) – (e) show the variations in the displacement (s), velocity (u_p), and acceleration (a) with time (t) of the particle undergoing electrophoresis under the influence of the externally applied electric field. The other parameters employed in the simulations are enlisted in the **Table 2.2**.

Figure 2.5 shows dynamics of the microparticle undergoing electrophoresis in a microchannel under the influence of an externally applied electric field. The stress developed due to the fluid-particle interaction during the motion of the particle is shown in the image set (b). Plots (c) – (e) show the variations in the displacement (s), velocity (u_p), and acceleration (a) with time (t) of the particle undergoing electrophoresis under the influence of the externally applied electric field. The figure suggests that any electrophoretic migration initiates with an unsteady motion with the variations in the velocity and acceleration before reaching a steady state value, as shown on the plots (c) – (e). At the onset, there are fluctuations in the velocity and acceleration, which become constant after a time interval. Further, the figure uncovers that the fluid velocity surrounding the particle is rather non-uniform, which generates a non-uniform stress on

the particle owing to the fluid-particle interaction. Interestingly, the particles take about a few milliseconds to reach the steady state velocity, which suggests that the transient time scale is governed by the time of formation of the EDL. In general, EDLs are developed as a result of diffusion of counter-ions towards the charged particles, which leads to a diffusion time scale, $\tau_D = d_p^2 / D_i$. The **Table 2.2** suggests that τ_D ~millisecond up to which the particle velocity increases before assuming the steady state velocity. Now, the following part shows the detail of EDL formation with time by showing the potential distribution profile against distance from the particle surface at different time intervals until it reaches equilibrium.

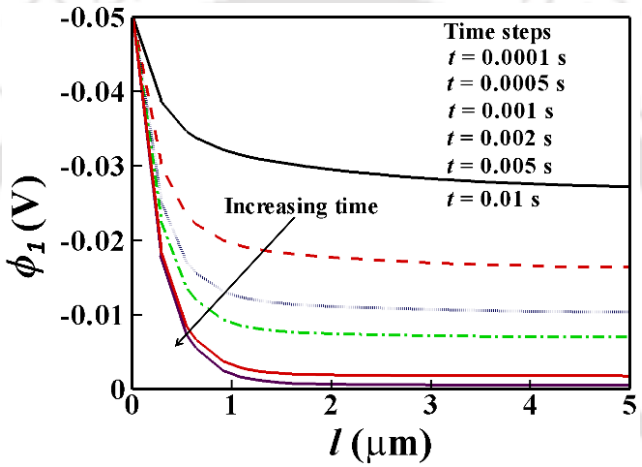

Figure 2.6: Shows the development of the potential distribution, hence the EDLs, around the charged particle from unsteady to the steady state. The potential distribution surrounding the particle is plotted at different time steps, as mentioned in the figure legend. The particle having diameter 1 μm is kept inside a microfluidic channel of diameter 5 μm and length 15 μm. The bulk electrolyte concentration is kept at 0.001 mol/m^3.

We have done a transient analysis on the current physical phenomenon. As discussed in the discussion of the **Fig. 2.3** tells the particle acquires steady state motion after around ~0.01 s. The time scale of the process is governed by the EDL formation time scale of the process and the same is quantified by, $\tau_D = d_p^2 / D$. Using the present physical parameters, the time scale has been found to fall in the range of 1-20 ms, and the transient time scale for EDL formation has also found to be falling in the same range. **Figure 2.6** shows the profiles of ζ-potential plotted at different time steps. It is found that there is no significant change of potential as we change the time step from 0.005 to 0.01 s. Hence, the EDL formation saturates at a time somewhere between 5ms

to 10 ms. The same transient is also observed in the particle motion transient phenomenon.

The dynamic development of the concentration profiles of the co- and counter-ions surrounding the particle undergoing electrophoresis (as shown in the **Fig. 2.3**) causes the initial fluctuations of velocity in the unsteady regime. After a time-interval, once the distribution of the co- and counter-ions surrounding the particle attains a steady profile, the velocity and acceleration become constant. Interestingly, most of the previous studies [213] report the steady state electrophoretic velocity and unable to predict the time dependent fluctuations of the concentration of the ions, velocity, and acceleration owing to the limitations associated with the theoretical model and solution technique. The use of the PNP and ion transport equations with the mass and momentum balance equations help us in uncovering the entire spectrum of the motion undergone by a microparticle during electrophoresis. Further, the use of moving deforming mesh and the fluid-particle interaction in the computational model helps in revealing the real picture associated with the electrophoresis of a particle moving under the influence of the externally applied electric field. In the following sections, we focus on the steady state concentration of the ions and velocity evaluated from the CFD simulations to uncover a host of interesting aspects associated with the electrophoresis of a particle.

Figures 2.7(a) and **2.7(b)** show the typical contours of fluid velocity (u_f) and the electric field potential (ϕ_2) surrounding the particle when it is under a steady electrophoretic migration after the unsteady part is over. The contours clearly suggest that both of these parameters are rather asymmetrically distributed around the microparticle undergoing electrophoresis inside a microchannel, which is unlike most of the analytical models proposed so far. [46, 227, 228] In order to elaborate on this issue, the **Fig. 2.7(a)** shows different cut lines around the particle taken at different angles along with the variations in profiles of the fluid velocity (u_f) and the electric field potential (ϕ_2) surrounding the particle has been plotted in the **Figs. 2.7(c)** and **2.7(d)**.

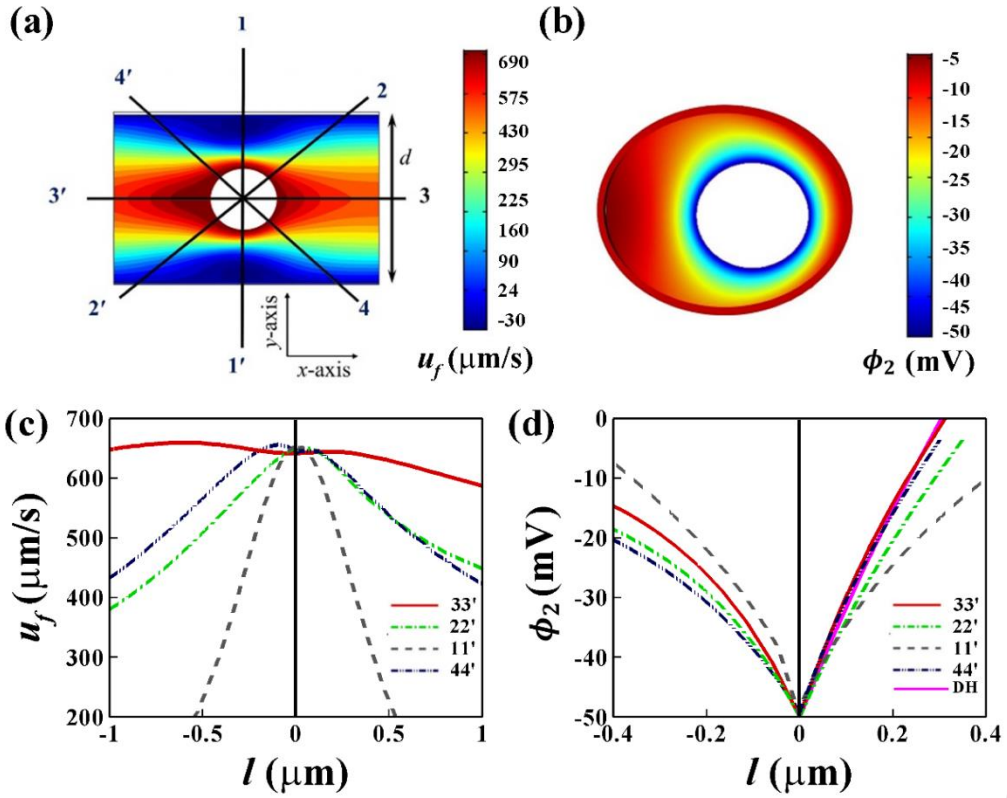

Figure 2.7: Image (a) shows the velocity contours around a charged microparticle of diameter 2 μm and a ζ-potential of -50 mV, undergoing electrophoretic motion. Image (b) shows the typical electric field potential (ϕ_2) contour around the charged particle while the particle is in motion. Image (c) shows the fluid velocity (u_f) surrounding the particle along the sections 11', 22', 33', and 44', as shown in the image (a) through the solid cut lines. Image (d) shows variation in the electric field potential (ϕ_2) in the fluid surrounding the particle along the cut lines 11', 22', 33', and 44'. Solid line in pink color shows the Debye Hückel profile for electric field potential (ϕ_2). The other parameters employed for the simulations are listed in **Table.2.2**.

Figure 2.7(c) shows that although the fluid velocity near the particle is almost nearly same in every direction, away from the particle, u_f diminishes faster in the vertical direction (cut line 11') than in the axial direction (cut line 33'). The fluid velocity surrounding the particle is found to be around 200 to 700 μm/s for a microparticle of diameter 2 μm when the surface potential is about –50 mV and an applied external potential of 1 V. Subsequently, the **Fig. 2.7(d)** shows the variation in ϕ_2, which also confirms the non-uniformity of the ion concentration in the direction of the particle migration and normal to the same. While the simpler Debye Hückel (solid pink line) predicts a linear uniform distribution of the ions surrounding the particle, the theoretical model presented here shows a non-linear trend of the same with the variation in different directions of the particle. Certainly, the formalism proposed in this study

shows a more realistic picture of the development of the EDL surrounding the electrophoresis of a microparticle inside a microchannel, the subsequent fluid velocity surrounding the same, and the ion concentrations in the electrolyte.

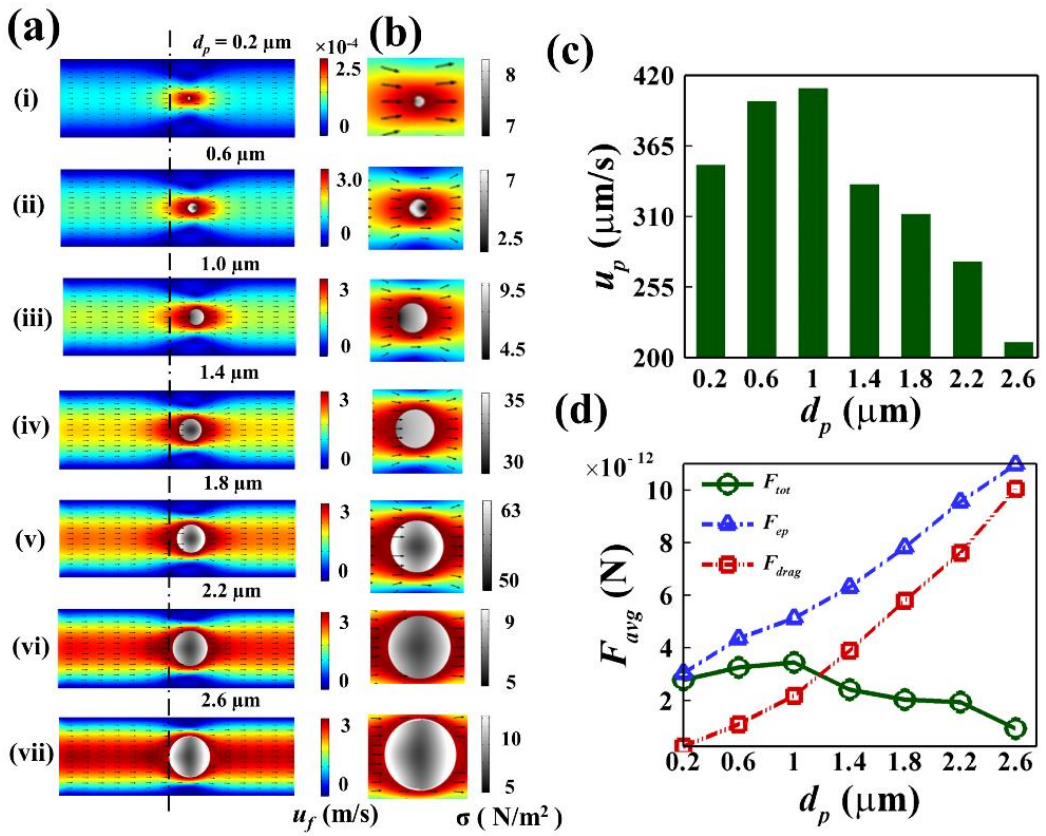

Figure 2.8: The frames (i) – (vii) in the image set (a) show displacement of particles of varying size, 0.2 µm, 0.6 µm, 1.0 µm, 1.4 µm, 1.8 µm, 2.2 µm, and 2.6 µm having surface potential of – 50 mV. The frames (i) – (vii) in the image set (b) show the stress on the moving particle. The plot (c) shows the steady state velocity (u_p) of the particles of different diameter (d_p). The plot (d) represents the contribution of viscous drag, electrophoretic force and the resultant of two forces. All other parameters used for the calculations are enlisted in the **Table.2.2**.

Importantly, most of the previous theoretical studies could not include the effect of the size of a particle on its electrophoretic migration. We calculated different average body forces (F_{avg}) over the entire region of the channel in order to show the contribution of the electrophoretic force (F_{ep}) and the viscous drag force and the resultant total force (F_{tot}) acting on the particle. In the **Figs. 2.8(a)** and **2.8(b)**, we show the migrations of the particles after 5 ms of diameter ranging from 0.2 µm to 2.6 µm and subsequent stress (σ) developed on the surface of the particles. **Figure 2.8(c)** shows the variation in the steady state electrophoretic velocity (u_p) of the particle with the diameter (d_p). The plots suggest when the electric field intensity is kept constant, the increase in d_p

leads to the enhancement of body force due to the electric field, as shown by the triangular symbols in the plot (d). However, the drag force also increases simultaneously with d_p, as shown by the square symbols in the **Fig. 2.8(d)**. The drag force eventually prevails over the electrophoretic force to cause a decline in the net force (F_{tot}) acting on the bigger sized particles, as shown by the filled circular symbols in the plot (d). Electrophoretic body force and the resistive inertial force of the particle are contrasting and both depends on particle size following different functions. As a result, the net force passes through a maxima at a critical particle size resulting a maxima in particle speed as well. The electrophoretic force is calculated numerically, across the EDL from the obtained CFD simulation results, whereas the drag force is calculated from the formula, $6\pi\eta u_{avg} R$. Again u_{avg} signify the average fluid speed along horizontal direction calculated along a line, which remains inside EDL and the same is obtained from CFD simulation results. In a way, for smaller size nanoparticles F_{tot} increases with size owing to the increase in the electrophoretic body force leading to an increase in u_p. However, if we further increase the size of the particle the particle speed again starts decreasing after passing through a maxima due to the dominance of drag force in that domain.

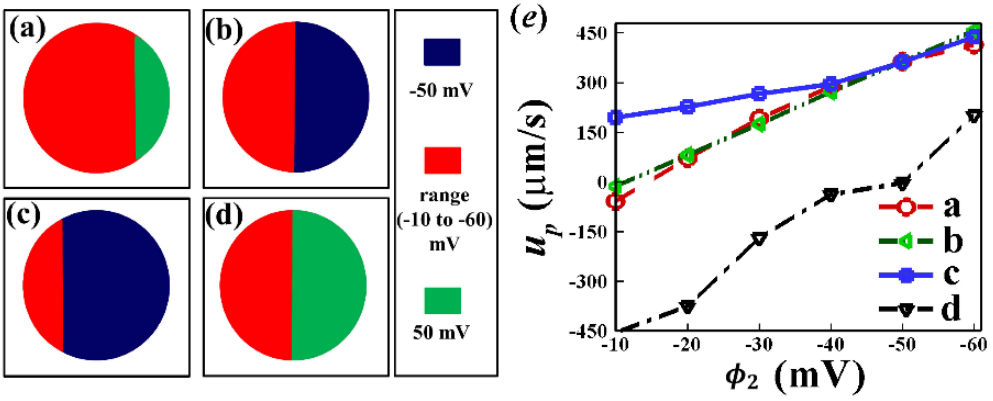

Figure 2.9: Schematic images (a) to (d) show different kinds of chemical heterogeneity on the surface of the particle of diameter 1 μm. The surface potentials for different color codes are also shown on the figures. The image (e) shows the steady state velocity (u_p) of the particles (a) to (d) with the variation in the ϕ_2 on the red-lobe.

Further, we investigate the variation in the steady state electrophoretic velocity with the heterogeneity in the charge, ϕ_2, on the particle surface. **Figures 2.9(a)** to **2.9(d)** schematically show some typical 'Janus' particles having different ϕ_2 on the side-lobes of the particle as mentioned on the image. For example, image (a) shows a particle with a negative charge (red portion) at the 75% surface and rest 25% positive (green portion).

Further, images (b) and (c) show the variation in the surface fraction of the red to blue lobes from 50% until 25%. Image (d) shows a Janus particle with hemispherical lobes and opposing charges. A set of simulations are performed with these chemically heterogeneous Janus particles wherein we vary the surface potential of the red colored zone from – 10 mV to – 60 mV and plotted the variation in the steady state electrophoretic speed (u_p) with the same, as shown in the **Fig. 2.9(e)**.

For the (a) – (c) type particles we observe that u_p increase with the increase in the ϕ_2 of the red lobe. These plots also show that when in the red part ϕ_2 is smaller than the blue one, the u_p increases with the increase in the surface fraction of the blue part from 50% and 75% for the particles (b) – (c). However, when both the red and blue zones have similar potential the u_p becomes nearly same. Particle (a) starts with a negative velocity and then changes its direction to positive velocity, as 25% of the particle has +50 mV whereas rest changes from +10 to +60 mV. Interestingly, type (d) particle moves in the opposite direction ($u_p < 0$) owing when the red-lobe has –10 mV and the green-lobe has 50 mV of surface charge. However, when the red-lobe attains a – 60 mV of surface charge the particle again shows $u_p > 0$. The figure suggests that the speed and directionality of the electrophoretic migration can be tuned by changing the surface potentials of a Janus particle.

Plots (a) – (f) in the **Fig. 2.10** show a parametric study of the variation in u_p with surface potential (ϕ_2), external electric field potential (V_{ext}), the viscosity of the electrolyte (μ), and initial molar concentration of the solute (c_0), diameter of the particle (d_p), and the clearance area in the microchannel (d/d_p), respectively. In the plots, the results obtained from the nonlinear CFD simulations, Smoluchowski's equation, Henry's law, and the analytical model proposed in the section 2.3 are compared and contrasted. The particle speed is calculated and compared with the simulation result from Henry's law [205] as the region we are operating is low to high 'ka'. Here 'k' is the reciprocal of the Debye length and 'a' is the characteristic length, which is the diameter of the particle. The plots (a) – (c) show that u_p increased with increase in ϕ_2 and V_{ext} and reduction in μ.

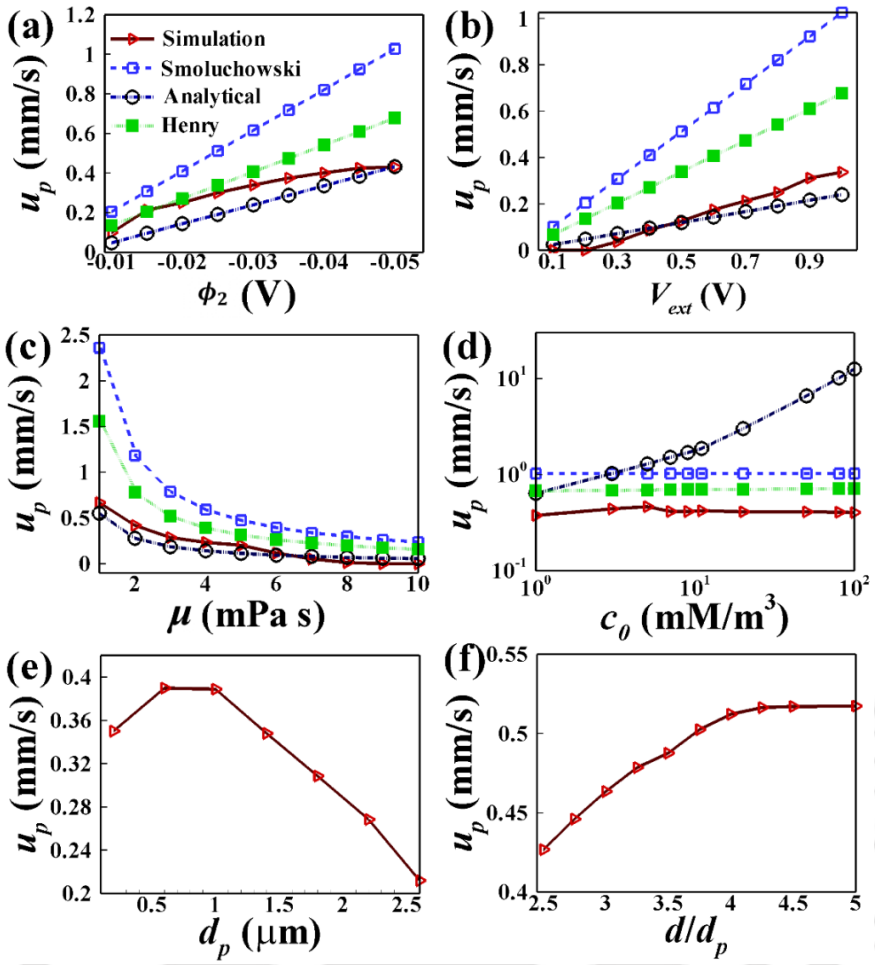

Figure 2.10: The plots (a) – (f) show the variation in u_p with surface potential (ϕ_2), external electric field potential (V_{ext}), the viscosity of the electrolyte (μ), and initial molar concentration of the solute (c_0), diameter of the particle (d_p), and the confinement in the microchannel (d/d_p), respectively. The triangular symbols are obtained from the nonlinear CFD simulations, the solid box symbols are calculated from Henry law [205], the square symbols are form the Smoluchowski's equation, and the circular symbols are from the proposed analytical model. The necessary dimensional parameters used in the simulations are enlisted in **Table 2.2**.

Interestingly, although the analytical models predict a linear increase in u_p with ϕ_2 and V_{ext}, the CFD simulations uncover a nonlinear increase. Further, the plot (d) shows that although the proposed analytical model predicts an increase in u_p with c_0, however the Smoluchowski's model and the CFD results predict very less variation in this regard. It is well known that the Debye length is highly sensitive to the bulk concentration because, $\kappa^{-1} = \sqrt{RT\varepsilon/2c_0F^2}$. Thus, the particle speed obtained from the analytical profile is effected by the change of Debye length. However, the CFD

simulations show the formation of a much mode diffused EDL, which is affected marginally with the variation in the initial concentration of the solute in electrolyte.

More importantly, the electrophoretic velocity obtained from the CFD simulations is consistently found to be lower than the Smoluchowski's and the proposed analytical model. The influence of the dynamic development of EDL, formation of the asymmetric EDL surrounding the particle, the fluid structure interaction during the particle motion, inertial force of the particle, and the difference in the drag force surrounding the particle while it is under motion are some of the important reasons for these deviations from the analytical models, which have been more accurately captured by the CFD simulations. The plots (e) and (f) show that even the size of the particle and the clearance inside the channel due to the confinements can also influence the electrophoretic mobility of a particle, which has been theoretically uncovered by very few previous works. The interplay of the drag around the particle and the wall drag due to confinement with the electrophoretic body force plays a major role in these variations. For example, a smaller particle in a channel with bigger diameter may undergo a smaller wall and surface drag, however, may also experience a smaller electrophoretic thrust. In comparison, a bigger particle in a narrower channel may experience both surface and wall drag at a much higher scale although it may experience a larger electrophoretic thrust. Concisely, the **Figs. 2.9 and 2.10** together uncover that the particle size, fluid viscosity, applied external field intensity, surface potential, heterogeneity in the surface potential, and confinement effects are some very important parameters to influence the electrophoretic migrations of the micropartiles, which have not been explored theoretically so far employing a comprehensive model.

It may be noted here that, for all the simulations shown here, we have neglected the surface potential of the channel wall owing to the assumption that the walls bear insignificant amount of charge. At the same time, the channel length was taken very small in order to reduce the computational cost. Dielectric mismatch of the particle and the fluid has also been neglected. Here, in the next part, we justify all the assumptions taken for the simulation along with their contribution to changing the electrophoretic migration inside microfluidic channels. Point wise justifications of all the assumptions are as given in the following section.

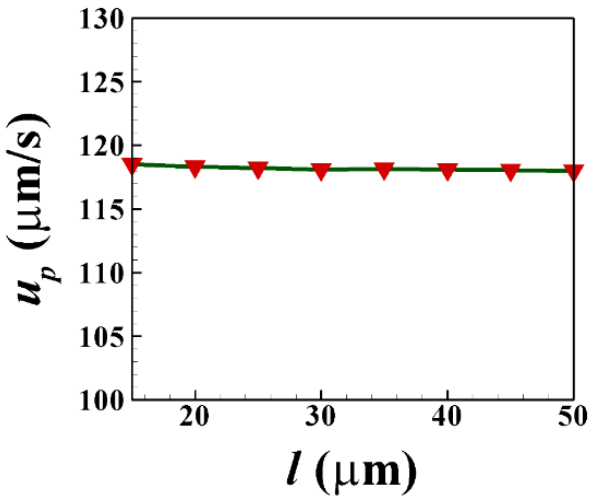

Figure 2.11: The plot shows the variation in u_p when d = 5 μm and l is changed from 15 μm to 50 μm. The ϕ_p, d_p, and c_0 considered in these simulations are, -0.05 V, 1 μm, and 0.001 mol/m^3, respectively. All other simulation parameters are enlisted in **Table 2.2**.

Channel length is one of the parameters that may affect the particle speed and hence a parametric study is made changing the channel length. **Figure 2.11** shows that when we vary the channel length (l) maintaining other parameters constant there is hardly any influence on u_p. Thus, in all the simulations, we have kept the channel length three times of the channel diameter in order to lower computational time at an acceptable mesh resolution.

In the present study, we assume that the electric field potential on the confining walls (ϕ_w) is very less compared to the same on the particle (ϕ_p). Thus, the effects of ϕ_w have been neglected in all the results. **Figure 2.12** shows effects of ϕ_w on the electrophoretic speed of the particle (u_p). The plot (a) in this figure shows the position of the particle after 0.006 s when ϕ_w = - 0.01 V and ϕ_p = - 0.05 V. The color map shows the contours of fluid velocity. The plots (b) and (c) show the variations in the electric field potentials (ϕ) across the EDLs near the confining walls and particle surface. These figures suggest that, while the EDL on the particle surface is responsible for the electrophoretic migration under the influence of the externally applied electric field, the EDL near the confining walls can cause electroosmotic flows across the channel under similar circumstances.

It is well known that when the charges of the EDLs are similar (dissimilar) for the particle surface and the confining wall, the electroosmotic flow is expected to facilitate (retard) electrophoretic velocity (u_p). For example, when the particle has a surface

potential of, ϕ_p = - 0.05 V, a similar potential at the confining wall, ϕ_w = - 0.01 V engender an electroosmotic flow towards the direction of the electrophoresis, as shown in the plot (a).

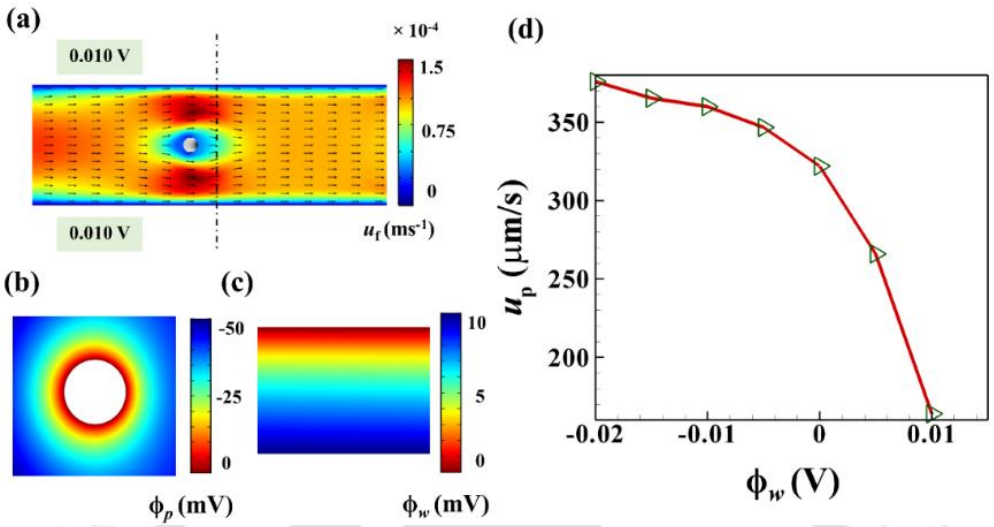

Figure 2.12: Plot (a) shows the position of a particle under electrophoretic migration after 0.006 s when surface potentials at the confining walls are, ϕ_w = - 0.01 V while the surface potential on the particle is, ϕ_p = - 0.05 V. The color map shows the contours of the fluid velocity surrounding the particle. The plots (b) and (c) show the spatial contours of the electric field potential (ϕ) near the particle surface and the confining wall when ϕ_p = - 0.05 V and ϕ_w = - 0.01 V. Plot (d) shows the variation in the particle speed (u_p) with ϕ_w. The ϕ_p, d_p, d, l, and c_0 considered in these simulations are, -0.05 V, 0.6 μm, 5 μm, 15 μm, and 0.001 mol/m^3, respectively. All other simulation parameters are enlisted in the **Table 2.2**.

Plot (d) shows that when ϕ_w is varied from 0 V to -0.02 V a progressively stronger electroosmotic flow surrounding the particle led to a larger u_p when ϕ_p = - 0.05 V. Interestingly, when ϕ_s > 0, the u_p drops sharply because now the direction of the electroosmotic flow is against the direction of the particle motion. A larger length of the walls ensures that the drop in u_p with increase in ϕ_s is sharper when ϕ_s > 0. The simulations uncover that the length, and the type and magnitude of ϕ_w can affect the particle speed only when ϕ_w > 0.1 ϕ_s, otherwise it can be neglected. The analysis reveals that same potential on particle and wall may accelerate the particle motion whereas an opposite charge can retard or eventually reverse the motion of the particle. A detailed analysis of the same we keep as a future scope of research work.

The dielectric mismatch at the solid-fluid interface often leads to dielectrophoresis under the influence of a non-uniform electric field surrounding a particle. In particular,

when an AC field is applied on a particle, this aspect becomes more pronounced owing to the generation of the additional force due to the mismatch in dielectric constant [123, 229],

$$F_{DEP} = 2\pi r^3 \varepsilon_m Re\left[\frac{\varepsilon_p - \varepsilon_m}{\varepsilon_p + 2\varepsilon_m}\right]\nabla\left|\vec{E}_{rms}\right|^2 .$$

Here r, ε_p, ε_m, Re, E_{rms} represent particle radius, particle dielectric constant, medium dielectric constant, Reynolds Number, and root mean square electric field, respectively. In the present study, since we have DC field and also since we assume the dielectric mismatch between the particles is not large, we have neglected this effect. However, under a DC field, the gradient of dielectric constant at the solid-liquid interface due to the dielectric mismatch between the particle (ε_p) and the electrolyte (ε_m) can also lead to the force, $\mathbf{F}_\varepsilon = 0.5\varepsilon_0\left(|\mathbf{E}|\right)^2\nabla\varepsilon$, alongside the electrophoretic body force, $\mathbf{F}_{ep} = \rho_e\nabla\Phi$. The simulations uncover that the body force ($\mathbf{F}_{ep}$ ~ 10^8 N/m^3) is a few orders of magnitude stronger than the force due to dielectric mismatch ($\mathbf{F}_\varepsilon$ ~ 10^5 -10^6 N/m^3) because of which we neglect the inclusion of this force too.

2.5. CONCLUSIONS

In this chapter, we develop an all-inclusive theoretical model to analyze the electrophoresis of a charged microparticle under the influence of an externally applied electric field in an electrolyte filled microchannel. The major conclusions are,

(i) The Poisson-Nernst-Planck equations for ion-transport coupled with the mass and momentum balances have been solved numerically employing finite element method with appropriate boundary conditions including the efficacies of the moving-deforming-mesh and fluid-structure interaction. The numerical results obtained from the proposed theoretical model uncover the most accurate picture of such motions. A simple analytical model has been developed alongside the Smoluchowski's equation to compare and contrast the numerical results. The electrophoretic velocity obtained from the simulations are found to be consistently

lower than the existing and proposed analytical models, which is presently employed to explain the experimental results.

(ii) The simulations reveal that the EDL develops dynamically surrounding the particle at the initial stages of the electrophoretic motion leading to an unsteady motion of the particle. Later, although a steady electrophoretic migration is established under the externally applied electric field, an asymmetric EDL surrounding the particle is observed. The influence of formation of the asymmetric EDL, the fluid structure interaction, and particle-inertia are found to be some of the major reasons for the deviations of the results from the existing analytical models.

(iii) The particle size, fluid viscosity, drag on the particle and the fluid, applied field intensity, and surface potential are found to influence significantly the speed of the particles, which has not been explored so far. The drag around the particle, the wall drag near the confinement, and the variation in the electrophoretic thrust owing to the variation in the size of the particle are found to be some other influential parameters. For example, a smaller particle in a wider channel with bigger diameter may undergo a smaller wall and surface drag, however, may also experience a smaller electrophoretic thrust. In comparison, a bigger particle in a narrower channel may experience both surface and wall drag at a much higher scale although it may experience a larger electrophoretic thrust.

(iv) Examples are shown where the speed and direction of the electrophoretic motions of the 'Janus' particles can be tuned with the variation in the chemical heterogeneities on the surface. The magnitude of the surface charge on the lobes of the Janus particle, the surface fraction of the lobes, and the type of the surface charge on the lobes are found to be some important parameters in this regard.

Concisely, the study reports some very interesting aspects of micro or nanoscale electrophoretic migrations, which can be useful in improving the understanding and applications in a variety of fields such as DNA or protein migration, sedimentation, super-capacitors and batteries, self-propulsion of microrobots, and testing of vaccines or antibiotics, among others.

Chapter 3

Electroosmosis with Augmented Mixing in Rigid to Flexible Microchannels with Surface Patterns

ABSTRACT

We explore the salient features of a single-phase electroosmotic flow inside patterned and flexible microfluidic channels. A finite element based simulator has been developed to solve the coupled system of, Poisson equation in the limit of Debye-Hückel approximation for the electrolyte, Laplace equation for the externally applied electric field, and continuity and momentum equations for fluid flow, with appropriate boundary conditions. The study uncovers some exceptional unsteady and steady flow profiles with the variations in the, (i) ratio of the Debye length to the channel diameter, (ii) dimensions and locations of the physical and chemical heterogeneities decorated on the walls, (iii) the strength of the external field and (iv) the extent of deformability of the channel walls. Interestingly, the flow profiles are found to be closely related to the deformability of the channel walls owing to the deformation of the electrical double layers. Further, the surface heterogeneities present on the channel walls are found to facilitate the variation in the ζ-potential, which in turn can locally modulate the flow rate inside the channel to cause intermixing of the layers. The extent of mixing due to the deformability and physicochemical surface heterogeneity of the microchannel has been critically analyzed to decipher the usage of these electroosmotic flows for the augmented microfluidic mixing in the laminar flow regime. The variations of current densities along the channel walls with diverse surface patterns have also been explored for the probable application in the field of differentiating ζ-potentials of bio-surfaces.

Stands for	Symbol
Cartesian coordinate directions	x, y
x component speed of fluid	u
Diameter of channel	d
Length of channel	l_c
Chemical patch width	p_w
Physical patch thickness	h
Viscosity	μ
Density	ρ
ζ-potential	ϕ_ζ
External potential	ϕ_a
Total potential	ϕ
Debye length	λ
Displacement of flexible channel	s
Amplitude of sinusoidal displacement	a_0
Initial amplitude of sinusoidal displacement	a_{i0}

Table 3.1: Nomenclature of the symbols used in this chapter.

Chapter 3

3.1. INTRODUCTION

The studies related to the microfluidic devices have gained considerable momentum over the past few decades owing to their diverse applications in the areas of medical diagnostics,[230-233] biotechnology,[234-236] analytical sciences,[237, 238] and separation processes.[176, 239, 240] In particular, the usage of diverse microscale electrokinetic flows such as electroosmosis,[95, 241, 242] electrophoresis,[243, 244]diffusiophoresis,[245] streaming[246, 247] or sedimentation[248, 249] potentials have become one of the major foci because they have opened up the possibility of remotely guided transport of electrolytes,[250] energy harvesting, and storage,[251, 252] separation of bio molecules[253, 254] among others. In addition, over the years, the researchers have also been intrigued by the complex fundamental aspects of electrokinetic flows.[255, 256] For example, the details of the dynamics of the formation of the electrical double layers (EDLs) in the electrolyte near the electrodes,[202, 257-264] their movement under the externally applied electric field,[265, 266] the consequences of the formation and movement of the EDLs in the transport of fluids or particles,[96, 244, 245, 253, 260, 261, 267] or influence of the various electrolytic, fluidic, or particle properties in these phenomena are among the areas where a number of fundamental aspects are still not very well understood. Especially, the multiscale nature of the problem starting from the ionic movement in an electrolyte under an electric field to the formation of nanoscale EDL and then to the emergence of the various microscale electrokinetic phenomena pose a lot of difficulties in setting up the theoretical and experimental frameworks for an exact scientific analysis. Thus, of late, extensive efforts have been invested to uncover the salient unexplored features of the microscale electrokinetic flows.

The characteristics of the Electroosmotic (EO) flows have been extensively studied employing diverse theoretical[93-97] and experimental[98-100] frameworks since its discovery in the early 19th century by Reuss[101, 102] and Porrett.[103, 104] However, since the literature is very large we only discuss the relevant works, which are attempted in this chapter. For example, a lot of recent developments have shown the usage of state-of-art experimental and theoretical tools at the micro to nanoscale in exploring the unknown features of EO flows.[30-40] In the process, the details of the steady,[96] unsteady,[97] and temperature[105] profiles of EO flows have been theoretically explored. Further, the influence of the interfacial Maxwell Stresses on the single[268] and two-

phase[269-273] EO flow profiles have also been reported recently. A few attempts have also been made to achieve micromixing at the highly confine low Reynolds number systems undergoing EO flows.[164, 274] A few experimental works[267, 275, 276] have studied the effects of surface roughness on the EO flows inside microchannels. Importantly, patches of changing surface potential are found to create a significant amount of mixing in EO microflows.[93] Interestingly, although there are a number of studies related to mixing inside flexible microfluidic channels,[277] there is hardly any study, which extends the same towards the domain of EO flows.

In view of this background, the current study focuses on a rigorous theoretical analysis on micromixing of EO flows inside the microfluidic channels with physicochemical heterogeneity and flexibility at the boundaries. For this purpose, a computational fluid dynamics (CFD) simulator has been developed to solve the coupled, Poisson equation for the electrolyte and Laplace equation for the external electric field along with the continuity equations and equations of motion for the fluid flow with appropriate boundary conditions. The simulations uncover interesting and unexplored steady and unsteady EO flow profiles inside the microfluidic channels with heterogeneous and flexible channel walls. Subsequently, the simulations show the formation of local vortices inside such channels, which opens up the possibility of designing micromixers employing the EO flows. We also report the variation in the current density inside such EO flows having different kinds of physical and chemical patterns on the flexible walls. Such systems emulate the flow of electrolytes through the flexible biological micropores having a charged surface with physicochemical heterogeneities. Thus, the results reported here are not only important for futuristic applications like micromixing or microreactors but also may improve the understanding of electrokinetic flows inside the various biological systems.

3.2. PROBLEM FORMULATION

The single phase EO flow in a microchannel has been modeled assuming the fluid to be isothermal, Newtonian, and incompressible. **Figure 3.1** schematically shows different kinds of patterns on various microchnanels that are considered in this study such as homogeneous, chemically heterogeneous, physically heterogeneous physicochemically heterogeneous, and channels with flexible walls. The figure also

shows the direction of the electric field applied for the flow and the charges at the walls for the respective geometries.

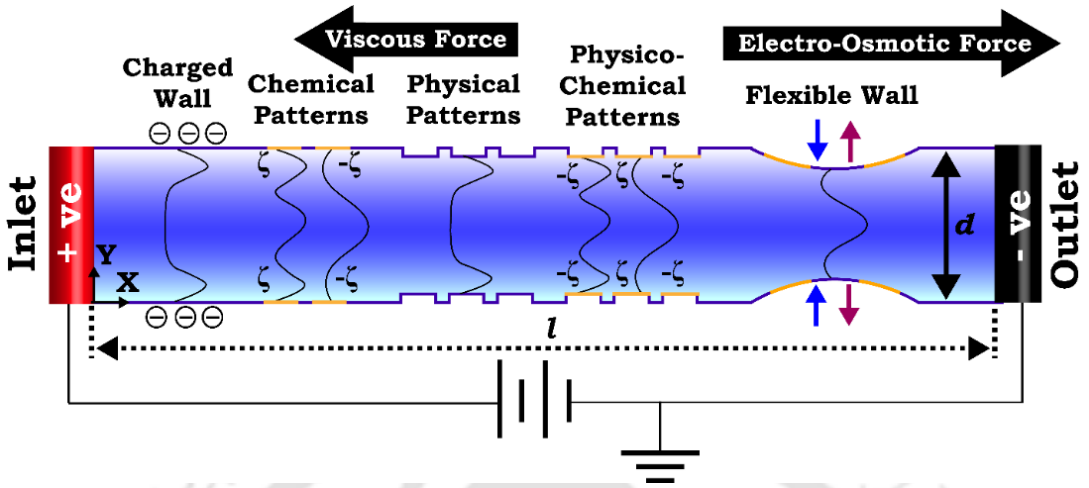

Figure 3.1: Schematically shows an EO flow inside a microchannel of diameter d and length l_c. The surface charges on the channel walls are shown by encircled negative sign. The channels with chemical patches on the walls are shown by yellow (lighter shade) marks and associated symbols, 'ζ' with positive and negative signs. The groves directing inward of the channel walls represent physical patterns. The groves having yellow (lighter shade) marks and associated symbol 'ζ' represent physicochemical patterns. The flexibility of the channel walls is shown by inward curvature on the walls with the arrows signifying the direction of flexibility. The directions of the driving EO force ($\rho_e \mathbf{E}$) and the resistive viscous force are shown by the arrows. The notations X and Y (x and y) represent dimensionless (dimensional) Cartesian coordinates.

A two-dimensional (2D) Cartesian coordinate system has been used to model the physical problem in which the velocity components along x- and y-directions are represented by the symbols, u and v. The variables represented in uppercase signify dimensionless parameters while any parameter in bold represents a vector quantity. The dimensionless diameter is represented by the notation, D_c, in order to avoid confusion with the notation, D, which stands for material derivative operator. Any variable with a suffix 'avg' represents spatial average of the parameter. The density, viscosity, dielectric permittivity, zeta-potential, and externally applied potential are represented by the symbols, ρ, μ, ε, ζ, and V, respectively. The electric field potentials due to the surface charge and applied potential are denoted by ϕ_ζ and ϕ_a, respectively. The overall potential is assumed to be the algebraic sum of these two and is represented by ϕ. The operator, D, stands for material derivative and the gradient operator is represented by

the standard symbol, ∇. It may be noted here that for all the simulations the length of the channel is kept 2.5 times the channel diameter. The patch length of heterogeneity is always kept as half of the channel diameter.

In this formulation, there are two types of electric field potentials in which one is due to the charged boundaries confining the channel while the other is due to the applied electric field along the direction of the flow. The former is governed by the Poisson equation as,

$$\varepsilon \nabla^2 \phi_\zeta = \rho_e . \tag{3.1}$$

Where, ρ_e is the charge density of the electrolyte near the channel wall. Applying the Debye-Hückel approximation, Eq. (3.1) has been reduced to the following form, which has an analytical solution,

$$\nabla^2 \phi_\zeta = \phi_\zeta / \lambda^2 . \tag{3.2}$$

Here, λ is the Debye length. The external field in the direction of the EO flow has been governed by Laplace equation,

$$\nabla^2 \phi_a = 0 . \tag{3.3}$$

Thus, the total electric field potential (ϕ) is modeled as the algebraic sum of the pair of individual potentials as,

$$\phi = \phi_\zeta + \phi_a . \tag{3.4}$$

The overall electric field has been obtained as the gradient of the total electrical potential as,

$$\mathbf{E} = -\nabla \phi . \tag{3.5}$$

The electric field equations are coupled with the continuity and Navier-Stokes equations as,

$$\nabla \cdot \mathbf{u} = 0, \tag{3.6}$$

$$\rho \frac{D\mathbf{u}}{Dt} = -\nabla p + \mu \nabla^2 \mathbf{u} + \rho_e \mathbf{E} . \tag{3.7}$$

The boundary conditions employed to solve the Eq. (3.2) are, at $y = 0$, $\phi_\zeta = \zeta$, and at $y = \lambda$, $\phi_\zeta = 0$. The Eq. (3.3) has been solved by enforcing the boundary conditions, at x

= 0, $\phi_a = \phi_{a\max}$ and at $x = l_c$, $\phi_a = \phi_{a\min}$. In order to solve the set of Eqs. (3.6) and (3.7) we use no-slip and impermeable boundary conditions at the walls of the channel **u** (u, v) = 0 while the pressure is kept at atmospheric pressure at both the inlet (x = 0) and outlet ($x = l_c$) of the channel.

3.3. SOLUTION METHODOLOGIES

3.3.1. Analytical Solution:

In this section, initially, we convert the equations for the EO flow into their dimensionless forms before solving them analytically. For this purpose, time, t, pressure, p, velocity, **u**, and electric field potential, ϕ are made dimensionless employing the parameters d^2/ν, $\rho\nu^2/d^2$, ν/d and $E_{el}d$, respectively, where ν is the kinematic viscosity and $E_{el}d = V/l_c$. Following this, Debye-Hückel approximation has been made to reduce Poisson equation in the following form,

$$\frac{d^2\Phi_\xi}{dY^2} = \frac{\Phi_\xi}{De^2}. \tag{3.8}$$

The following solution of the Eq. (3.8) is obtained by enforcing the boundary conditions, $\Phi_\zeta = Z_\zeta$ at $Y = -D_c/2$ and $D_c/2$

$$\Phi_\zeta = Z_\zeta Cosh\left[\frac{Y}{De}\right] Sech\left[\frac{D_c}{2De}\right]. \tag{3.9}$$

Similarly, the following solution of the Laplace equation for the applied field is obtained by enforcing the boundary conditions, at $X = 0$, $\Phi_a = \Phi_{am}$ and at $X = L_c$, $\Phi_a = 0$

,

$$\Phi_a = \Phi_{am}\left(1 - X\right). \tag{3.10}$$

The set of Eqs. (3.6) and (3.7) can be reduced to the following forms under lubrication approximation after making them dimensionless,[179]

$$d^2U/dY^2 = \left(E_0/E_R De^2\right)\nabla^2\Phi\nabla\Phi, \tag{3.11}$$

where $E_0 = (\epsilon E_{el} d \zeta_s)/(\rho\nu^2)$ and $E_R = \zeta_s/(E_{el}d)$ are a pair of dimensionless numbers. Eq. (3.11) has the following analytical solution wherein the no-slip and impermeability

boundary conditions are enforced at confining walls, which is the analytically obtained EO flow profile,[179]

$$U = \frac{\left(E_0/E_R\right) Z_\varsigma \Phi_{am} Sech\left[\frac{D_c}{2De}\right]\left(2ZSinh\left[\frac{D_c}{2De}\right] - D_c Sinh\left[\frac{Z}{De}\right]\right)}{D_c De}. \quad (3.12)$$

3.3.2. Numerical Methodology:

Finite element based CFD software COMSOL Multiphysics™ has been employed to solve the dimensional Eqs. (3.2) – (3.7) with the boundary conditions mentioned previously. The Galerkin least-square (GLS) method, 2nd order elements for velocity, and 1st order elements for pressure gradient calculations have been employed to discretize the set of coupled nonlinear partial differential equations. The segregated predictor-corrector method with incremental pressure correction led to the velocity and pressure profiles for the flow wherein an adaptive physics controlled mesh is employed for increased accuracy. The Multiphysics solver PARDISO has been used for a faster computing power. A second-order backward difference method is chosen for time-marching with an optimal time step size of ~10^{-4} s. A mesh size of 50,000 elements provides grid independent solution while convergence of the solutions has been ensured through the monitoring of process parameters. Standard inlet, outlet, wall, and pressure boundary conditions are chosen for the CFD models to obtain the unique solutions. For the deforming channel simulation, the deforming geometry module of COMSOL Multiphysics™ has been employed. In this module, the channels are made to deform following a sinusoidal geometrical function, which depends on both space and time. For this purpose, we have taken a complex sinusoidal function, $s(x, t) = a_0 \sin(2\pi\ 100\ t)$ where a_0 is the amplitude of the sinusoidal displacement, $a_{i0} \sin(\pi x/l_c)$.

3.3.3. Validation:

The steady state velocity profiles obtained from the analytical and CFD models are compared in the **Fig. 3.2**. The figure shows a significant match between the numerical and analytical results. Conditionally, the numerical results are found to be within the range of 99% accuracy of the analytical results, which also suggests the accuracy of the numerical methodology. Thus, the CFD model has been extended for further work with heterogeneous and flexible microchannels, which cannot be done employing the analytical tools.

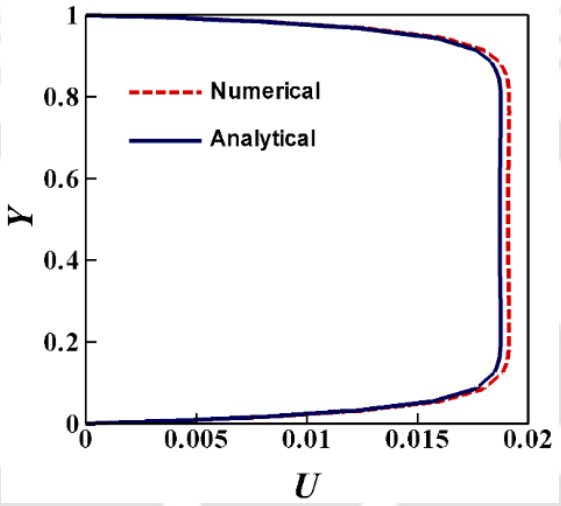

Figure 3.2: Shows comparison between dimensionless velocity profiles (Y vs. U) obtained from analytical (solid blue line) and CFD simulations (dotted red line) solutions. Diameter of channel (d), length of the channel (l_c), Debye length (λ), viscosity of the fluid (μ), density of the fluid (ρ), ζ-potential are kept as 10 µm, 50 µm, 305 nm, 0.001 Pa s, 1000 kg m^{-3}, – 100 mV, respectively.

3.4. RESULTS AND DISCUSSION

3.4.1. Homogeneous Channels:

When an electrolyte undergoes an EO flow inside a microfluidic channel with confining charged surfaces, the development of the EDL and the fluid flow takes place simultaneously. Thus, in the initial stages of the evolution, an unsteady developing EO flow profile is expected before attaining the steady state. **Figure 3.3(a)** shows one such incidence where an initial plug flow is progressively converted into a steady state EO flow profile. It may be noted here that the flow profiles shown here are taken at the far

downstream of the channel to avoid the entrance effects in the CFD simulations. The unsteady profiles suggest that, in short time, the EDLs near the channel walls move faster than the bulk fluid at the central part of the channel under the externally applied electric field. Subsequently, a pair of parabolic 'cup' shaped flow profiles near the channel wall proximity is observed. However, with the progress in time, the flow profile tends to become more like a parabolic profile with a flat front, as observed in the pressure driven turbulent flows.[278] Importantly, the unsteady[279, 280] and steady[281, 282] state EO flow profiles have already been predicted previously by a host of analytical and experimental works.[283, 284] Arguably, this may be the first report wherein these flow profiles are obtained by comprehensively solving the coupled equations for the electric field and motions.

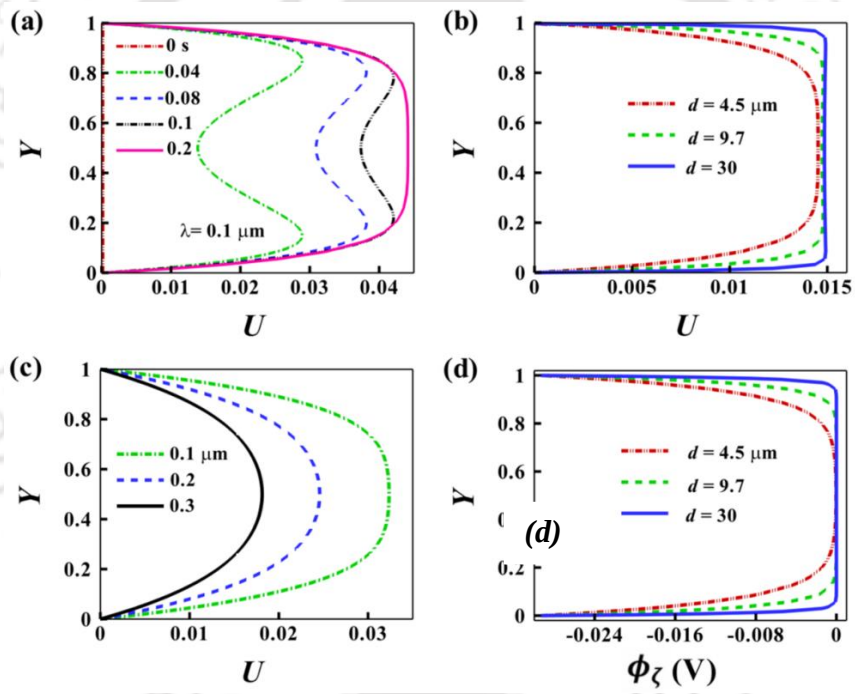

Figure 3.3: Plot (a) shows unsteady EO flow profiles for developing flows at time intervals 0 s (dash-dot-dot), 0.04 s (dash-dot), 0.08 s (broken), 0.1 s (dash dot dot with black) and 0.2 s (solid) for λ = 0.1 μm. Plot (b) shows steady EO flow profiles (Y vs. U) in the channels of diameters, 4.5 μm (dash-dot), 9.7 μm (broken), and 30 μm (solid). Plot (c) shows steady EO flow profiles for Debye lengths, λ = 0.1 μm (dash-dot-dot), 0.2 μm (dash-dot), and 0.3 μm (solid). Plot (d) shows the variation in the electric field potential (ϕ_ζ) along the vertical direction of the channel (Y vs. ζ) for the channels in the plot (b). The channel diameter (d), length (l_c), surface charge ϕ_ζ at wall, applied external voltage (V), Debye length (λ) are kept as, 30 μm, 150 μm, – 50 mV, 5 V, and 300 nm, respectively.

Previous studies suggest that in the EO flows, the steady profile has significant influence on the thickness of the EDL to the diameter of the channel.[285, 286] The **Fig. 3.3(b)** depicts different steady EO flow profiles with the variation in the diameter of the channel at a fixed EDL thickness or Debye length (λ) while **Fig. 3.3(c)** shows steady EO flow profiles with the variation in the Debye length at a fixed channel diameter. **Fig. 3.3(d)** shows the subsequent variation in the electric field potential (ϕ_ζ) corresponding to the **Fig. 3.3(b)**.The plots suggest that with the increase in d and reduction in λ (i.e, decrease in Debye length to diameter ratio, λ/d) the EO flow profile flattens towards the center of the microchannel. Concisely, the plots in the figure suggest that the unsteady nature of the EDL development and λ/d have significant influence on the EO flow profiles and hence on the throughput. Thus, these parameters can be important in the design and the development of EO pumps in near future.

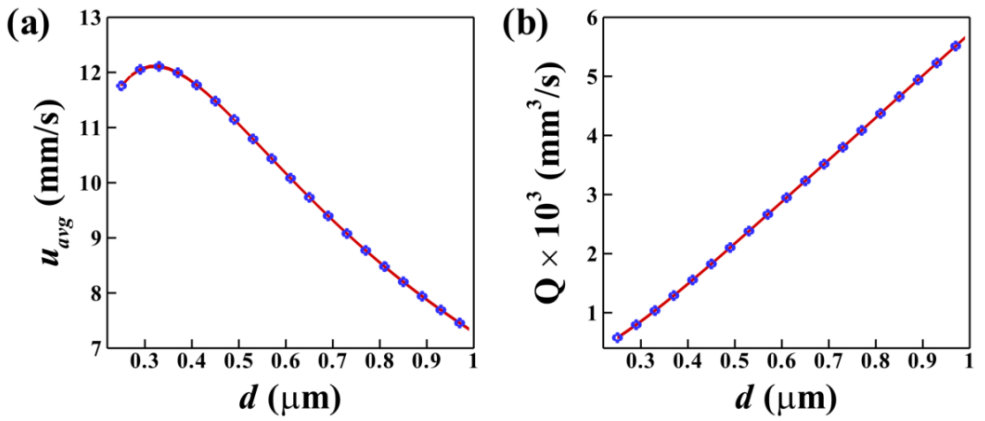

Figure 3.4: Plot (a) shows the variation in the average velocity (u_{avg}) with the diameter of the channel (d) at a fixed ϕ_ζ. Plot (b) shows the subsequent variation in the volumetric flow rate (Q). The walls are kept at, ϕ_ζ^w = – 25 mV with applied external potential of 5 V. The aspect ratio of the channels (l_c /d) is kept same for all the simulations.

In this line, the plots (a) and (b) in the **Fig. 3.4** shows the variations in the average velocity (u_{avg}) and flow rate (Q) of the EO flow with d. It may be noted here that in these simulations we have kept the aspect ratio of the channels (l_c/d) to be same, which ensures that the electric field intensity reduced (V/l_c) with the increase in the diameter of the channel. Interestingly, the plots highlight that for the thinner channels a predominant viscous force leads to a smaller u_{avg} while for a thicker channel a

progressively weaker field intensity (V/l_c) again leads to a smaller u_{avg}. The maximum u_{avg} is found to happen at some intermediate d when the channel diameters are essentially in the submicron regime.

For example, **plot 3.4 (a)** shows that, under the given conditions, up to ~ 400 nm channel diameter the u_{avg} of the EO flow increases with d with the reduction in viscous influence. However, with further increase in d, u_{avg} reduces as the field intensity also reduces with the increasing length of the channel for a given applied voltage. Importantly, in such a scenario, the flow rate (Q) is always found to monotonically increase as the cross-sectional area of the channel increases by the magnitude proportional to d^2. Concisely, the simulations suggest that the strength of the EO flows has been decided by lots of factors such as the electrolyte strength, surface charge, applied field intensity, viscosity of the fluid, channel dimensions, and the thickness of the EDL, which may be important for the design and development of EO pumps or mixers in near future. **Figures 3.3** and **3.4** together help in inferring the variations in the flow profiles and throughput with the EDL thickness and channel diameter. Further, it is well known that flow reversal is an easy possibility in the EO flows either by reversal of the electric field or by the reversal of the surface charge.[95, 287, 288] Interestingly, these concepts can be brought in together for the fabrication of an EO channel with periodic physical and chemical patches of positive and negative surface potentials, which can manifest facile mixing inside the microfluidic channels. Surprisingly enough, although the use of surface patterns for micromixing has been tried for the pressure driven flows, there is hardly any report on the same for the EO flows especially employing the theoretical tools.

3.4.2. Mixing in Heterogeneous Channels:

The following **Figs. 3.5** and **3.6** show a few example cases of such flows and possible flow profiles inside the microfluidic channels. In particular, **Fig. 3.5** shows an EO flow where the entrance and exit walls are patched with, $\phi_\zeta^w = -25$ mV, while in the middle of the channel a pair of alternate patches of $\phi_\zeta^w = -25$ mV and $\phi_\zeta^w = 25$ mV are made, as shown in **Fig. 3.5(a)**.

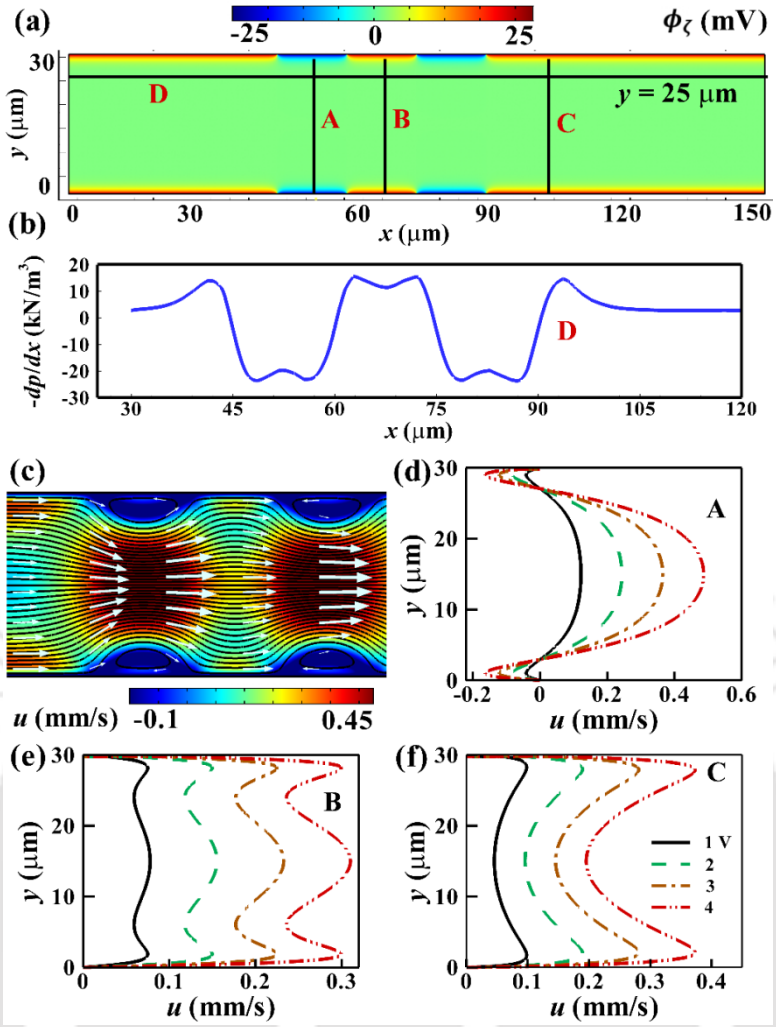

Figure 3.5: Plot (a) shows a chemically heterogeneous microchannel with alternating positive and negative ϕ_ζ^w on the walls. The zones A, B, C, and D show the places where the velocity and pressure gradient profiles are reported. The contour shows the variation in ϕ_ζ across the channel. Plot (b) shows the variation in the pressure gradient $(-dp/dx)$ along the x-direction across the cut-line D. Plot (c) shows the contour of 'u' with streamlines and arrows symbolizing fluid velocity. Plots (d), (e), and (f) show the velocity profiles at the cut-lines A (heterogeneity with positive ϕ_ζ^w), B (heterogeneity with negative ϕ_ζ^w), and C (homogeneous positive ϕ_ζ^w), respectively, as shown in the plot (a). The solid, dash, dash-dot, and dash-dot-dot represent profiles at 1 V – 4 V, respectively. The d_p, l_c, ϕ_ζ^w, V, λ, μ, and ρ are kept as, 30 μm, 150 μm, –25 mV, 4.25 V, 300 nm, 0.001 Pa s, and 1000 kg m^{-3}, respectively. The width of each patch is kept as 15 μm.

In such a channel, when an EO flow takes place from left to right, we observe a spatial variation in ϕ_ζ, as shown by the contours in the **Fig. 3.5(a)**. In general, the EDL

assumes the opposite charge to that of the wall. The direction of the applied electric field used for all the simulations has already been shown in the **Fig. 3.1**. Thus, the external field drives the positively charged EDL near the negatively charged wall (ϕ_ζ^w < 0) towards the positive *x*-direction whereas a reverse flow is observed in the locations of the negatively charged EDL near the positively charged wall ($\phi_\zeta^w > 0$). The plot (b) shows the variation in, $-dp/dx$, along the *x*-direction across the cut-line D, which suggests that the major reason behind the flow reversal, has been the variation of pressure gradient from negative to zero to positive in the locations of heterogeneities.

The plots (d) – (f) show the velocity profiles at the cut-lines A (a patch with ϕ_ζ^w = 25 mV), B (a patch with ϕ_ζ^w = – 25 mV), and C (downstream with ϕ_ζ^w = – 25 mV), respectively, as depicted in the plot (a). The plots show that the EO flow in the EDL enhances with the increase in the field intensity, as shown by the different solid, broken, dash-dot, and dash-dot-dot lines. Interestingly, different kinds of velocity profiles are observed owing to the presence of the chemical patterns on the channel walls. In a way, the patterns create a non-uniform variation in the pressure across the channel, which leads to a variation in the pressure gradient across the locations with chemical patches, as shown in the plot (b). The streamlines overlaid on velocity contour is plotted in the **Fig. 3.5(b)** suggest that such variations in the pressure gradient lead to localized recirculation flow patterns near the patches, which can be suitable for micromixing applications.

The zone A in the **Fig. 3.5(c)** shows a back flow near the walls while the fluid flow near the center of the channel is towards the direction of the flow. In contrast, the flow profiles of the zone B in the **Fig. 3.5(d)** shows a unique EO flow profile with three humps with a profoundly higher velocity near the bulk. In this case, a higher velocity near the center of the channel in the zone where the wall is patched with a positive ζ-potential is rather counterintuitive. This happens due to the back flows at the EDLs in the surrounding patches with negative ζ-potential. **Fig. 3.5(e)** shows the velocity profile at cut-section C where the flow profiles resemble the unsteady developing one shown previously in the figure 3 for the homogeneous channels. The results suggest that the

strength of the vortices can be modulated by tuning the patch length, periodicity of the patches, patch locations, and the charge on the patches, among other parameters.

Figure 3.6 shows another interesting EO flow pattern where the entrance and exit walls are patched with a surface charge of ϕ_ζ = –25 mV (i.e. positive ζ-potential near the wall) while in the middle of the channel a pair of alternate patches of positive and negative ϕ_ζ are made, as shown in the image (a) of **Fig. 3.6**. Further, in contrast to **Fig. 3.5**, physical patterns pointing inward to the channel walls are put with a thickness of 10 percent of the channel diameter, d_p = 30 μm. Subsequently, an applied external field drives the positively charged EDL near the negatively charged walls along the positive *x*-direction whereas a revere flow is observed in the location of the negatively charged EDL near the positively charged walls. The contours of ϕ_ζ have also been shown in the **Fig. 3.6(a)**. Further, near the constricted spaces of the channel, the velocity profile is supposed to change than the space where the cross-section is higher. In such a scenario, the plot (b) shows the variation in $-dp/dx$ along the *x*-direction across the cut-line D, which suggests that the major reason behind the flow reversal has been the change in the sign of the pressure gradient. The plots (d) – (f) show the velocity profiles show at the cut-lines A – physicochemical patch with a negative ζ-potential in a constricted zone, B – physicochemical patch with a positive ζ-potential in an expanded zone, and C – a physicochemical patch with a positive ζ-potential in a constricted zone, respectively, as depicted in the plot (a).

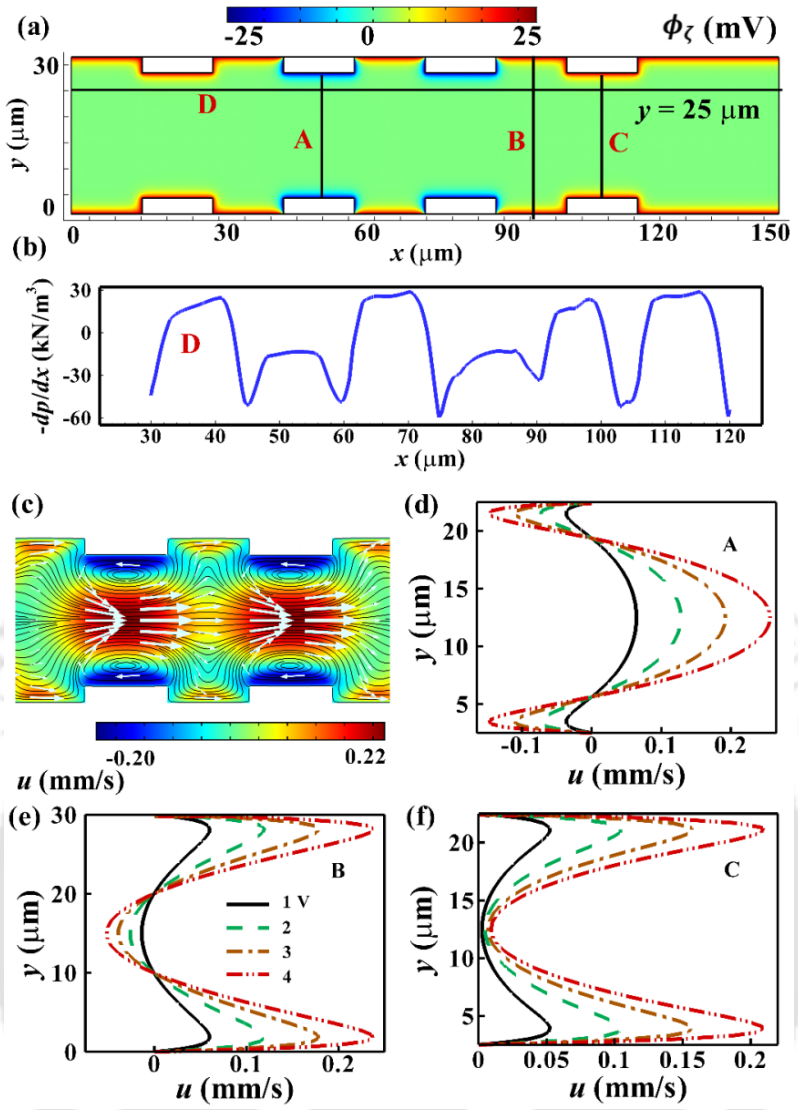

Figure 3.6: Plot (a) shows a physicochemically heterogeneous microchannel. The cut-lines A, B, C, and D show the zones where the velocity and pressure profiles are reported. The contour shows the variation in ϕ_ζ across the channel. Plot (b) shows the variation in $-\ dp/dx$ along the x-direction across the cut-line D. Plot (c) shows streamlines at the middle of the channel (heterogeneous portion) overlaid on x directional velocity (u) and the arrows signify velocity vector. Plots (d) – (f) show the velocity profiles at the cut-lines A (physicochemical heterogeneity with positive ϕ_ζ^w), B (physicochemical heterogeneity with negative ϕ_ζ^w), and C (physicochemical heterogeneity with negative ϕ_ζ^w). The solid, dash, dash-dot, and dash-dot-dot represent profiles at 1 V – 4 V, respectively. The d_p, l_c, ϕ_ζ^w, V, λ, μ, and ρ are kept as, 30 μm, 150 μm, – 25 mV, 4.25 V, 300 nm, 0.001 Pa s, 1000 kg m^{-3}, respectively. The width of each patch is kept as 15 μm and the height of the physical patterns is 3 μm.

The **Figs. 3.6(c)** and **3.6(d)** show the velocity profiles at the constricted and expanded cut-sections A and B where the flow profiles resemble the unsteady developing as shown previously in the **Fig. 3.3** for the homogeneous channels. The plot also shows that the flow in the EDL enhances with the increase in the field intensity. The zone C in the **Fig. 3.6(d)** shows a back flow near the walls while the fluid flow near the center of the channel is towards the direction of the flow. In contrast to the flow profiles of the zones A and B, again **Fig. 3.6(d)** shows a unique EO flow profile with back flow near the walls and a forward flow neat the central portion of the channel. Interestingly, in the upstream and downstream of the channel also we observe formation of the recirculation near the central part of the microchannel owing to the change in the diameter of the physically heterogeneous channel during the EO flows.

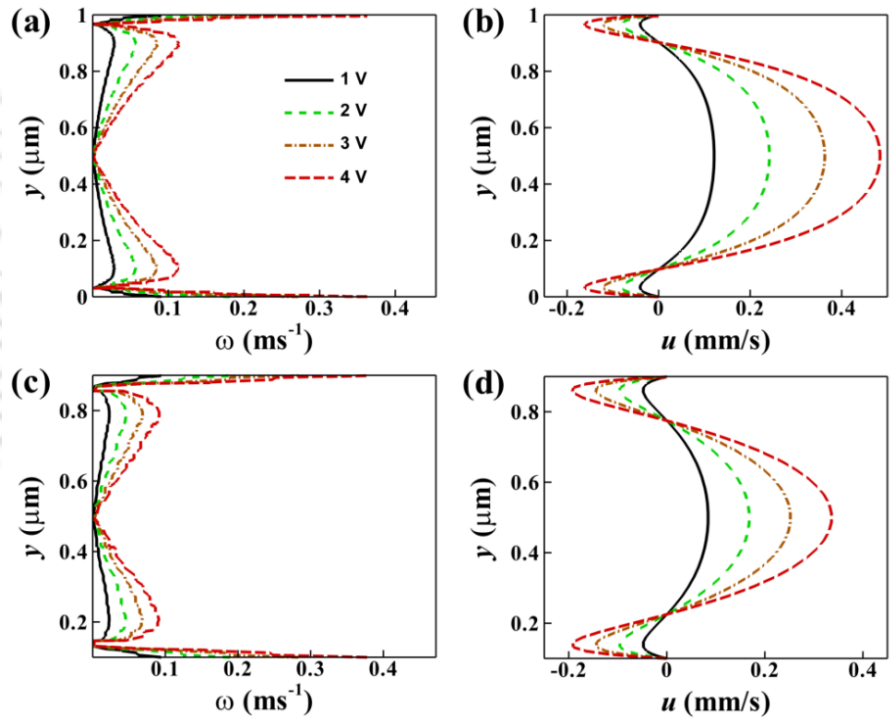

Figure 3.7: Plots (a) and (c) show the variations in the vorticity (ω) of the recirculation patterns near the chemical patches shown in the **Fig. 3.5(d)** (cut-line A in **Fig. 3.5(a)**) and near the physicochemical patches shown in the **Fig. 3.6(d)** (cut-line A in **Fig. 3.6(a)**). The plots (b) and (d) show the corresponding velocity profiles across the microchannel. The other parameters such as d_p, l_c, ϕ_ζ^w, and λ are kept as, 30 μm, 150 μm, – 25 mV, and 100 nm, respectively.

The results suggest that the strength of the vortices can be modulated by tuning the patch length, periodicity of the patches, patch locations, and the charge on the patches,

which may lead to more efficient mixing. The plots (a) and (c) in the **Fig. 3.7** shows the variations in the vorticity (ω) of the recirculation patterns near the chemical patches shown in the **Fig. 3.5(d)** (cut-line A in **Fig. 5(a)**) and near the physicochemical patches shown in the **Fig. 3.6(d)** (cut-line A in **Fig. 6(a)**). The plots (b) and (d) show the corresponding velocity profiles. The vorticity plots suggest the presence of adequate recirculation for mixing near the patches and walls, which increase with the reduction in the diameter of the channel and increase in the intensity of the applied electric field. Briefly, the **Figs. 3.5** – **3.7** show some exciting non-invasive pathways to promote recirculation and mixing inside the microfluidic channels, which are not explored so far from both theoretical and experimental perspectives.

3.4.3. Mixing in Flexible Channels:

Alongside the decoration of chemical or physicochemical patterns on the charged surface, constructing flexible microchannels for the EO flows can be another alternative to enhance mixing. The EO flows inside flexible biological capillaries are also an emerging and exciting field of research.[289, 290]

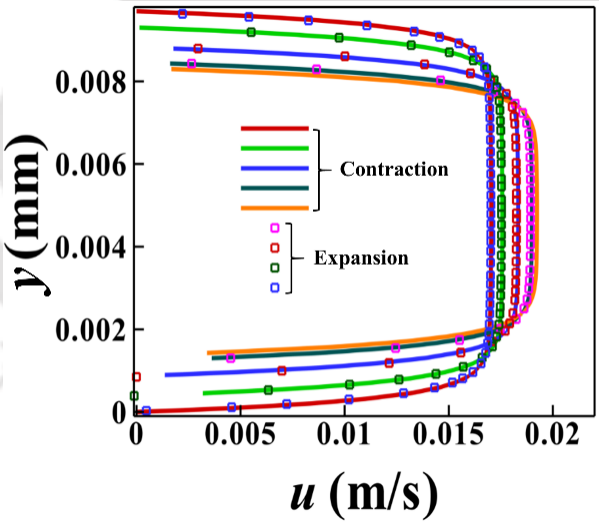

Figure 3.8: Shows the electroosmotic velocity profile at the middle of a flexible microchannel compressing and expanding periodically with a sinusoidal wave motion.

In this case, we consider a microchannel of diameter 10 µm undergoing a sinusoidal compression and expansion following a wave, s (x, t) = a_0 sin($2\pi nt$), where a_0 is the amplitude of the wave evaluated as, a_{i0} sin($\pi x/l_c$). Here, a_{i0} and n are taken to be, 1 µm and ($2\pi/10$) s^{-1}, respectively, which ensures that the middle of the channel to undergo

maximum deflection. The **Fig. 3.8** shows the velocity profile at the middle of the channel at different time instances when the position of the channel walls is different based on deformation. The solid lines in the figure legend show velocity profiles during compression cycle of the walls whereas the symbols show the profiles during the expansion cycle of the channel.

We have provided the details of the EO flows inside a flexible channel alongside showing the steady EO flow profiles in a flexible but homogeneous microchannel. The study suggests an enhancement (reduction) in the maximum velocity near the center of the channel with the contraction (expansion) of the homogeneous channels walls. This phenomenon can further be exploited for the enhancement of mixing. The image set (a) in the **Fig. 3.9** shows the velocity contours and streamlines of an EO flow inside a physicochemically patterned microfluidic channel with flexible walls. The images (i) – (iii) show the variation in the streamlines and velocity contours during the contraction cycle while the same for the expansion cycle is shown in the images (iv) – (vi). The plots (b) and (c) show the variations of EO flow profiles with time during the contraction (solid line) and expansion (broken line) of the channel in the zones A and B, as depicted in **Fig. 3.9(a)**. The plot (b) clearly shows the variation in EO flow profile with time during the contraction of the channel, which is reflected in the increase in the strength of the recirculation contour with the contraction of the channel walls due to localized reverse flow.

The subsequent variation in vorticity (ω) with time at the zones A and B in the plots (d) and (e) confirms an augmented mixing due to the flexibility of the channels having physicochemical patterns. In a way, the EO flow reported here is very similar to the one discussed with **Fig. 3.9** with one exception of having flexible walls. The results shown here highlight the importance of channel flexibility in the micromixing of fluids in the EO flows with patterned and flexible surfaces.

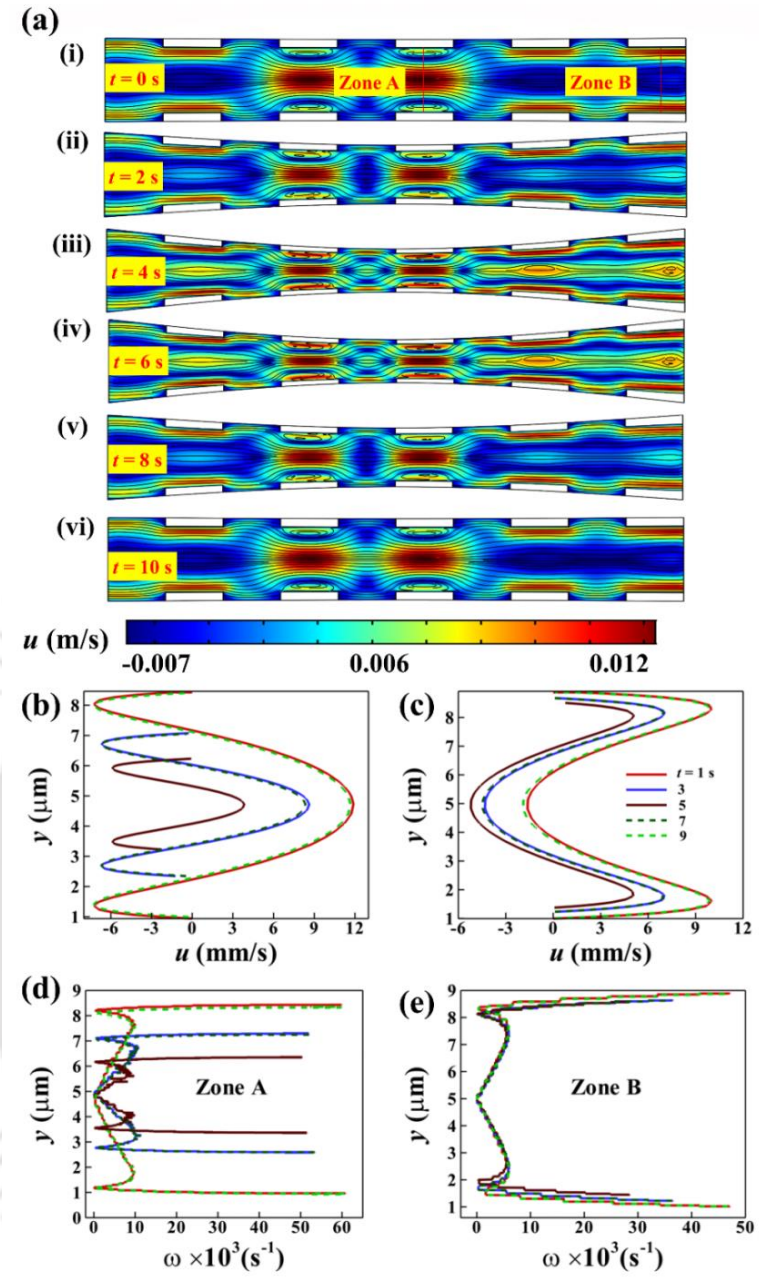

Figure 3.9: Image set (i) – (vi) in the plot (a) show streamlines overlaid on velocity contours at different time intervals 0, 2, 4, 6, 8, and 10 s for a physicochemically patterned flexible channel having a full contraction ((i) – (iii)) and expansion cycle ((iv) – (vi)). Plots (b) and (c) show velocity profiles at the cut-line taken in zones A and B in plot (a) and subsequent variation in vorticity (ω) with time have been shown in the plots (d) and (e). The solid (broken) lines represent compression (expansion) cycle. The channel diameter and length are kept as 10 μm and 50 μm. The magnitudes of ϕ_ζ^w at the walls and external applied field are, 25 mV and 5 V, respectively.

3.4.4. Current Density Profiles:

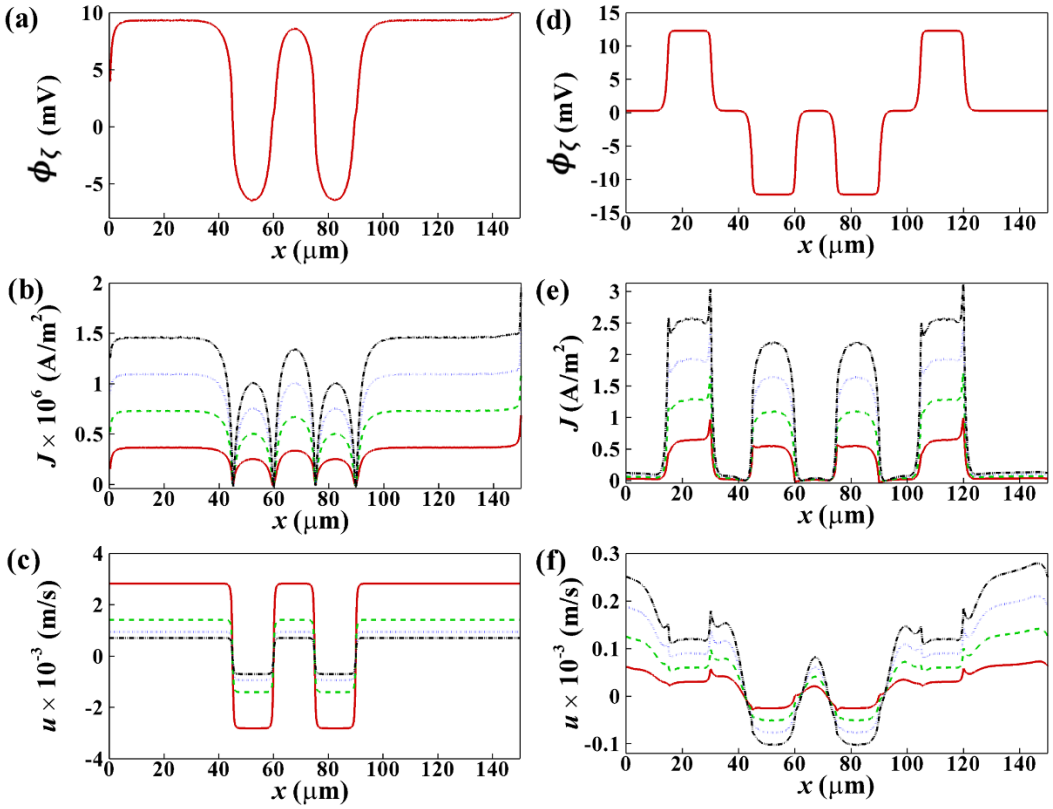

Figure 3.10: The plots (a), (b), and (c) show the variations in the total electric field potential (ϕ), current density (J), and x-component of velocity (u), respectively. The variables are plotted along the cut-line of a chemically heterogeneous microchannel at, y = 29.75 μm, similar to the line D shown in Fig. 3.5(a). The plots (d), (e), and (f) show the same for a physicochemically heterogeneous microchannel. The d, l_c, ϕ_ζ^w, ρ, μ, V, are kept at 30 μm, 150 μm, +/– 25 mV, 1000 kg/m3, 0.001 Pa s, 4.2 V, respectively. The solid, broken, dash-dot, dash-dot-dot represent the parametric study of applied external voltage (1, 2, 3, and 4 V).

The results discussed so far highlight that the physical, chemical or physicochemical patterns on the surface of an EO flow lead to the distortion of streamlines and forms local recirculation zones. This phenomenon can be also employed to map the charge density of the EDLs. For example, the plots (a), (b), and (c) in the **Fig. 3.10** shows the variations in ϕ_ζ, current density (J), and x-component of velocity (u) respectively, along the cut-line of a chemically heterogeneous microchannel at, y = 29.75 μm. Further, the plots (d), (e), and (f) show the same for a physicochemically heterogeneous microchannel. The plots suggest that the current density profiles follow the variation in the electric field potential near the channel walls

at the zone of EDL with chemical or physicochemical heterogeneity whereas they remain rather constant near the place where the channel is homogeneous. Such variations in the current density near the chemical and physicochemical patches can be employed to distinguish surfaces having different surface potentials.

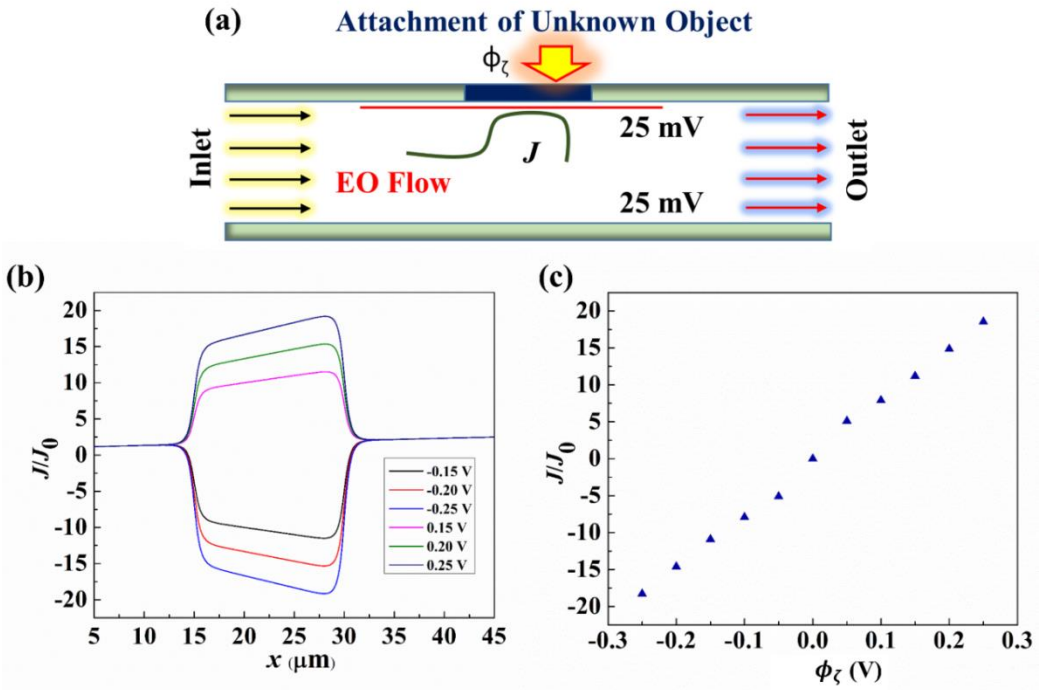

Figure 3.11: Plot (a) shows schematic representation of the proposed potential measurement set up. Plot (b) shows relative current density (J/J_0) profiles near the wall at a cut-line of, y = 29.75 μm, similar to the line D shown in **Fig. 3.5(a)**. Plot (c) shows a calibration curve (J/J_0 vs. ϕ_ζ) to determine unknown potential of the test object.

In fact, the biological cells with chemically heterogeneous surfaces are found to have variations in the ζ-potentials when immersed inside the diverse electrolytes.[111, 291, 292] Any disorder in the biological systems is also reflected as the variation in the surface charge, for example, the cancerous cells have a different surface potential than the healthy somatic cells. The numerical experiments shown in **Fig. 3.10** indicates that for such cell surfaces can be distinguished with an EO setup having chemically heterogeneous surface. In order to prove this hypothesis, we simulate a simple proof-of-concept to set up a device proposition in the **Fig.3.11**. **Figure 3.11(a)** schematically shows an arrangement where a microchannel with charged confining surfaces has been chemically patched in the location shown by the blue or dark color. **Figure 3.11(b)** shows the relative current density ($\boldsymbol{J}/\boldsymbol{J}_0$) profile near the patch and its variation with the

variation in ϕ_ζ of the patch. Here the actual current density ($\boldsymbol{J}$) is normalized by the current density of the homogenous channel ($\boldsymbol{J}_0$) to obtain the relative current density. **Fig. 3.11(c)** shows the calibration of $\boldsymbol{J}/\boldsymbol{J}_0$ with ϕ_ζ. In this setup, a pair of surfaces having different surface potentials, e.g. a healthy somatic and a cancerous cell, flowing with the EO flow may cause deviations of different extent from the calibration when they come near the patch. The extent of such deviations can be accounted for the sorting of the different types of cells.

3.5. CONCLUSIONS

In this study, a CFD simulator has been employed to solve coupled Poisson equation for the electrolyte, Laplace equation for the applied electric field, and continuity and momentum equations for fluid flow. The simulations uncover a host of steady and unsteady flow profiles of EO flow profiles inside homogeneous, chemically or physicochemically heterogeneous, and flexible microchannels. Importantly, the unsteady[279, 280] and steady[281, 282] state EO flow profile has already been predicted previously by a host of analytical and experimental works.[283, 284] Arguably, this may be the first report wherein these flow profiles are obtained by comprehensively solving the coupled equations for the electric field and fluid motion. Further, the strategic use of periodic patches of chemical and physicochemical patterns on the surface of the channel shows the emergence of the localized back flows which in turn facilitates the formation of the zone of recirculation inside the channel. The strength of the recirculation can be increased by enhancing the intensity of the applied field, changing the locations and dimensions of the patches, tuning the surface charge of the patches, reducing the channel diameter, and imparting flexibility to the channel walls. In the process, we show some simple and non-invasive pathways to promote recirculation and mixing inside the highly confined microfluidic channels employing the EO flows, which are not explored thus far. Once correlated and calibrated, the variation in the current density in the EDL near the chemical patches is found to be useful in the measurement of the variations in the ζ-potentials on the biologicalsurfaces.

Chapter 3

Chapter 4

Unexplored Pathways to Charge Storage in Supercapacitors

ABSTRACT

The study reveals various unexplored pathways to energy storage in the parallel and curved plate supercapacitors (SCs). The spatiotemporal variations in the electric field intensity of such SCs were found to have a significant influence on their performance. The observations unearth the limitations associated with the previous theoretical models, which are routinely employed to analyze the performance of SCs by considering electrical double layers (EDLs) as capacitors near the electrodes. The time-dependent electrochemical behaviors of SCs obtained from the Nyquist and Bode diagrams of electrochemical impedance spectroscopy showed, (i) electrode polarization at the higher frequency sweeps, (ii) immobile Helmholtz layer formation at the mid-frequency zone, and (iii) formation of diffuse layer of EDL at low-frequency-regime. The results suggest that charge storage of SCs heavily depend upon electrode geometry, type of electrolyte, electrolyte concentration, electrode separation, separator type, and dielectric relaxation of the electrolyte. A theoretical model composed of Poisson-Nernst-Plank equations for the electric field in electrolyte and Laplace equation for the electric field in electrodes were coupled with Navier-Stokes equations for the fluid flow was numerically solved with appropriate boundary conditions to uncover the pathways to supercapacitance during the experiments. The experimental and theoretical studies together reveal that the use of the potential drop across the EDL originating from the opposing electric fields due to electrode polarization and EDL formation could provide more accurate pathways to supercapacitance of such SCs.

Name	Symbol
Cartesian coordinates	x, y
Polar coordinates	r, θ
x component fluid speed	u
y component fluid speed	v
Distance between two plates	d_e
ζ-potential	ψ_1
External potential	ϕ
Total potential	ψ_{net}
Applied electric field	E_p
Resistive EDL electric field	E_h
Diffusivity of cation	D_+
Diffusivity of anion	D_-
Cation concentration	ζ_+
Anion concentration	ζ_-
Density of fluid	ρ
Viscosity of fluid	μ
Permittivity of the vacuum	ε
Faraday constant	F
Bulk concentration	c_0
Charge of ions	z_+ / z_-
Relative permittivity	ε_r

Table 4.1: Nomenclature of the symbols used in this chapter.

Chapter 4

4.1. INTRODUCTION

A number of recent works report that the integration of super capacitors (SCs) with energy generators can achieve higher device efficiency,[293, 294] suitable for futuristic portable[295] or large scale[296] applications. In particular, one of the major focus of research related to SCs has been directed towards the invention of materials for electrode preparation[297, 298], which possesses superior surface-to-volume ratio and electrical conductivity than the existing ones.[299-304] In this direction, among the other materials, graphene and its derivatives have been extensively used as the active material because they have the capacity to achieve a theoretical intrinsic capacitance up to 21 μF/cm^2. Further, extensive research efforts have been observed in optimizing the electrical conductivity and ion transport properties of the electrolyte between the SC electrodes.[305] The design of separators between the electrodes for more efficient ion transport is found to be another important aspect in this regard.[306]

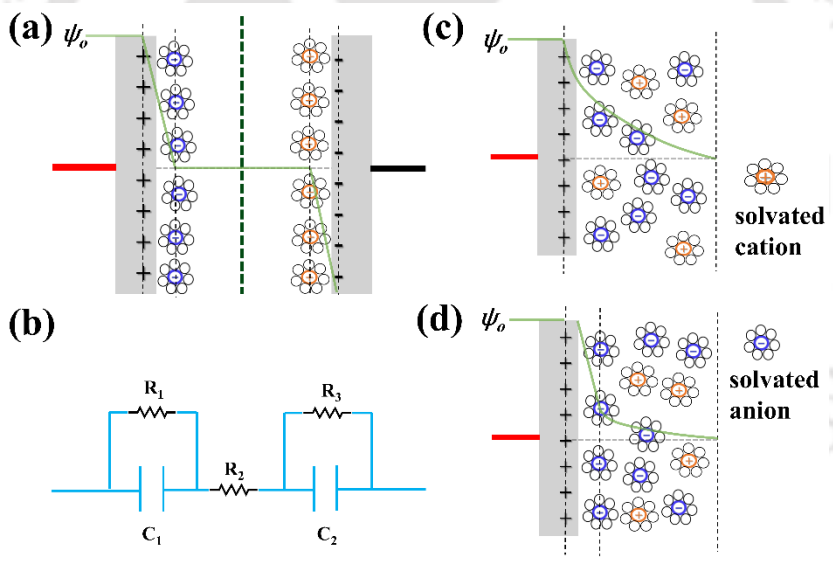

Figure 4.1: Image **(a)** shows the profile for the net electric field potential (ψ_{net}) between a pair of electrodes representing a Helmholtz electrical double layer (EDL). Image **(b)** illustrates the equivalent circuit derived from the system shown in the image (a) using two capacitor model (TCM). Image **(c)** shows the distribution of ions in a diffuse layer following the Gouy-Chapman model. Image **(d)** represents the Gouy-Chapman-Stern (GCS) model consisting of an immobile Stern layer and mobile diffuse layer in the EDL.

Importantly, efforts have also been made to uncover the underlying physics associated with the charging and discharging of the SCs, which may enable further improvements in their performance.[307] For example, according to the current understanding of charge storage mechanism of the SCs, the energy is stored at the

electrode-electrolyte interface due to the accumulation of opposite charges in the electrode surface and formation of electrical double layer (EDL).[308] In this situation, the capacitance per unit square area of the charge separation at the electrode-electrolyte interface is defined as the intrinsic capacitance of an SC. The performance of the SCs are experimentally characterized with the help of the electrochemical impedance spectroscopy (EIS), which helps in evaluating the equivalent series resistances, charge transfer resistance, Warburg resistance[309] alongside providing the real and imaginary capacitances.[310]

Traditionally, the charge separations at the electrodes are theoretically analyzed by the 'two capacitor model' (TCM), as schematically shown in **Fig. 4.1(a)** and in the equivalent circuit diagram in the **Fig. 4.1(b)**. The subsequent variation in the electric field potential (ψ) across the SC is also depicted in the figure. The TCM considers two immobile layers of opposite charges at the electrode-electrolyte interfaces, analogous to a solid state capacitor. The TCM also assumes the pristine Helmholtz model of EDL to be valid. Further, the TCM shows that the theoretical capacitance of an SC can only be the function of electrode surface area and Helmholtz layer thickness. However, experimental EIS studies in the prior-art[309] suggest that the capacitance of the SCs can also vary with scan rate, frequency of electric field, electric field potential, type of electrolyte, current discharge rates, and pressure between electrodes, among other parameters.[305, 311] Certainly, a better physical model interpreting the data obtained from the EIS during the charging and discharging cycles of SCs is the need of the hour.[312]

In this direction, the initial attempt was to use the Gouy-Chapman model for the EDL in the TCM having only one mobile layer of ionic distribution following the Maxwell-Boltzmann statistics near the electrodes, as shown in the **Fig. 4.1(c)**. The major drawback of this model was found to be the lack of ionic interactions, which is significant for the SCs using higher electrolyte concentration.[313, 314] The present understanding of the formation of EDL[85] around the electrodes is most comprehensively explained by the Gouy-Chapman-Stern (GCS) model,[315] as shown in the **Fig. 4.1(d)**. This model combines the Helmholtz and Gouy-Chapman models and suggests that the EDL consists of an immobile Stern layer near the electrode and a diffuse layer. Thus, the most recent works explain all the EIS data related to the SCs employing the details of the EDL through the GCS model while considering interactions between the solvated ions inside the electrolyte.[316] However, most of these

studies employ a parameter differential capacitance,[317] to account for most of the non-idealities associated with capacitance measurement. Clearly, a quantitative SC performance based on the time-dependent parameters is missing in the prior-art owing to the complexities associated with the dynamics of the ion transport near the electrode-electrolyte interface during charge-discharge cycles. A recent seminal theoretical work on the evaluation of the electrode, electrolyte and diffuse layer resistances from the Nyquist plot of EIS is directed toward this end.[318] Further, significant efforts have been made to study the characteristics of a metal-electrolyte interfaces in a SC and batteries using EIS.[319, 320] These studies underline the importance of time-dependent analysis to evaluate the performance of electrochemical devices.

In view of this background art, the present study uncovers the physical mechanisms of ion transport in parallel plate (PPS) and curved supercapacitors (CPS) with the help of EIS supplemented by a set of analytical and numerical models to describe these experimental behaviors. Initially, the EIS has been employed to uncover the charge storage mechanisms at different time-scales or frequencies[321] for different electrode geometries, electrode separation distances, electrolyte concentrations, types of electrolytes, and separators. The Nyquist and Bode diagrams obtained from EIS uncovered that the electrode polarization for SCs took place at smaller time scales, which was followed by the formation of the immobile Stern layer of the EDL at the intermediate time scales. Finally, the diffuse layer was formed at larger time scales. The time dependent ionic movements during the charge separation and subsequent dielectric relaxation of the electrolyte is found to play a significant role in the performance of the SC. The proposed analytical and numerical models evaluate the spatiotemporal escalation in the capacitance of the SCs based on difference between the electric fields due to, (i) polarization at the electrodes under the applied field and (ii) subsequent generation of the electric field in the electrolyte during the formation of the EDL during dielectric relaxation. The theoretical models proposed here is found reasonable to explain the experimental observations in a more comprehensive manner than previously reported ones.

4.2. MATERIALS

The graphite flakes (99.99%) were obtained from Alfa Aesar. The other necessary chemicals such as ethanol (C_2H_5OH, 99.99%), ethylene glycol ($C_2H_6O_2$),

dimethylformamide (DMF), potassium hydroxide (KOH) pellets, sulphuric acid (H_2SO_4), hydrochloric acid (HCl, 37%), hydrogen peroxide (H_2O_2, 50%), potassium permanganate ($KMnO_4$), ortho-phosphoric acid (H_3PO_4, 84%) poly-tetrafluoroethylene binder (60% (w/v) PTFE dispersion in water) and polyvinylidene difluoride (PVDF) were obtained from Merck, India. The chemicals were of analytical grade and used for the experiments without further purification. The Whatman filter paper (grade 1) and Kimtech tissue paper were used for the experiments while the Milli-Q grade water was used for varying the concentration of electrolytes.

4.3. METHODS

4.3.1. Preparation of Active Material:

Graphene oxide (GO) was synthesized following modified Hummer's method.[1,2] A 10 mg of dried GO was mixed with 50 ml of ethanol through ultrasonication (ASP, Telsonic) for ~2 h before adding another 50 ml of ethylene glycol in this solution. Thereafter, this mixture was heated under a sealed condition at 180°C and stirred continuously for thermal reduction. The uniform black mixture thus obtained was filtered to obtain the reduced graphene oxide (rGO). The rGO residue was then dried overnight under vacuum in a furnace (SNS, India) at 100°C before further use for electrode fabrication.

4.3.2. Electrode fabrication:

Figure 4.2 schematically demonstrates the fabrication steps of the proposed supercapacitors (SCs). In the first step, a 1 cm × 1.5 cm Cu substrate was cut before rubbing it with a sandpaper, as shown in the **Figs. 4.2(a)** and **4.2(b)**. The FESEM (JEOL 7610F, Japan) micrographs at the inset of images **(a)** and **(b)** show the typical surface morphologies of the initial and roughened Cu plates. Following this, a thin film (~5 Å) of Pt was deposited on the rough Cu plate using JEOL JEC-3000 FC sputtering system, as shown in the **Fig. 4.2(c)**. The thickness of the Pt layer was obtained from the calibration provided with the instrument. The Pt sputter coating on the Cu surface was performed to inhibit oxidation of Cu during cyclic voltammetry (CV) experiments.

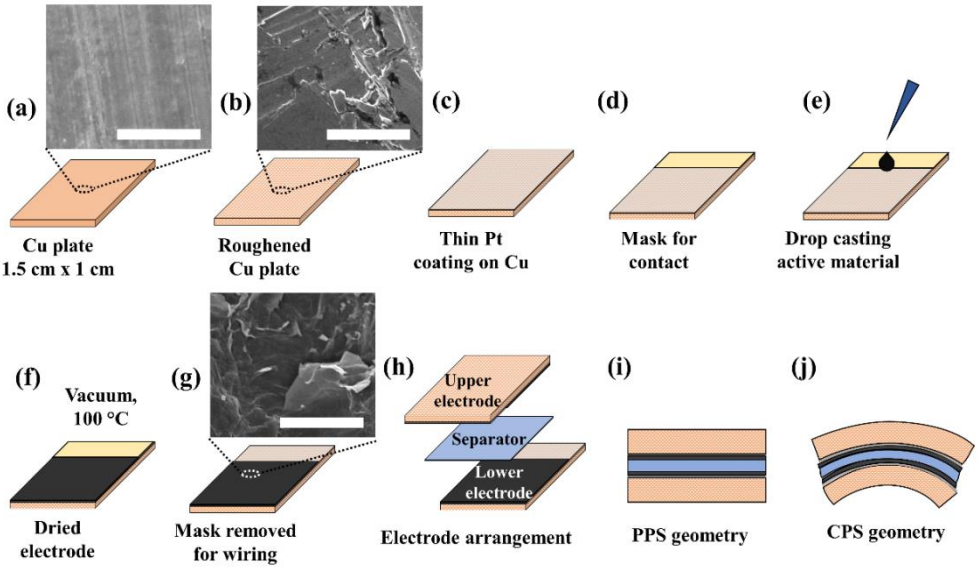

Figure 4.2: Shows the steps to assemble the supercapacitors (SCs) are shown schematically. Images (a) and (b) show the pre-processing of a Cu electrode wherein the plate was roughened using a sand paper. The insets in the images (a) and (b) show the FESEM micrographs of the surface before and after roughening. Thereafter, the roughened plate was sputter-coated with Pt, as shown in the image (c). Image (d) shows the masking of a part of the Pt coated Cu plate using a commercially available tape. The drop casting of the active material – slurry of rGO mixed with carbon black and PTFE, its coating on the Pt coated Cu plate, and subsequent drying have been shown in the images (e) and (f). Image (g) shows the removal of the mask and subsequent surface morphology at the FESEM inset. Image (h) shows the final PPS arrangement wherein a pair of electrodes shown in the image (g) was assembled with a separator in the middle as shown. The separator was composed of a filter paper or a tissue paper, or PVDF (SEM) soaked with electrolytes such as aqueous solutions of KOH and H_2SO_4 having different ionic strengths. Images (i) and (j) show the cross-sectional schematic images of the parallel (PPS) and curved (CPS) plate SCs. The scales shown on the FESEM images are of 20 μm.

4.3.2. Preparation and characterization of SC:

Graphene oxide (GO) was synthesized using modified Hummer's method. The detailed methodology of thermally reducing graphene oxide to produce reduced graphene oxide (rGO) and subsequently using it for preparing the active material. The active materials were coated on processed Cu plates, acting as the current collectors, to fabricate functional electrodes for parallel plate (PPS) and curved plate (CPS) supercapacitors. During the study, separators were soaked with an electrolyte, and then the electrode-separator-electrode configuration led to the formation of the proposed PPS. The edges of a PPS were bent against the graph paper to maintain a constant radius of curvature (κ) for the CPS.

4.3.3. Design of Separators:

Whatman filter paper (FP), Kimtech tissue paper (TP), and PVDF were used as the separator materials between the electrodes of PPS and CPS. PVDF nanofibers were prepared using electrospinning device (ESPIN NANOTECH - Super ES2) with 16% wt./vol. PVDF polymer in DMF and Acetone solvent (2:3 ratio). The operating voltage and distance between the ejection tip and collector drum were maintained at 20 kV and 15 cm respectively. The thicknesses of FP, TP, and PVDF surface after wetting with the electrolyte were found to be ~100 µm, ~45 µm, and 100 µm respectively, which were measured under optical microscope (Leica DM 2500). The variations in separation distance between the electrodes of the PPS and CPS were achieved by inserting different numbers (1-5) of wet FP layers. In order to keep the distance between the electrodes (d_e) similar for the PPS with different separators, we employed two layers of TP (d_e ~90 µm) for a PPS when compared with the PPS with one layer of FP or PVDF (d_e ~ 100 µm). Although, in most of the experiments we employed single layer of a separator or multilayers of the same separator, we also performed experiments with composite separators. For example, a comparative study was carried out with two TP layers or layers of FP, PFP, and PVDF as the composite separator.

4.3.4. Electrochemical analysis:

The electrochemical studies were performed using a potentiostat (CH-Instruments, 600C). Cyclic Voltammetry analysis was performed for the PPS and CPS with KOH electrolyte in the range of electric field potential (ϕ) of, 0 V to -0.3 V. The CV analysis was not performed in the high voltage range because there was a possibility of Cu-corrosion in the basic medium, which could lead to an excess current during charging cycle and an asymmetric CV curve. The Electrochemical Impedance Spectroscopy (ESI) was performed in frequency range from 100 kHz to 0.1 Hz with an electric field potential amplitude of 0.01 V.

4.3.5. Supercapacitor Arrangement:

A portion of the Pt coated Cu plate was masked before the active material was drop cast on the unmasked zone, as shown in the **Figs. 4.2(d) – (e)**. The mass loading of active material was kept ~2 mg/cm^2 on each electrode. The electrodes were dried

overnight under vacuum at 120°C, as shown in the **Fig. 4.2(f)**. The mask was removed subsequently (**Fig. 4.2(g)**) for making electrical connections (not shown here). The electrodes coated with active layer were pressed at 10 MPa pressure for a better adhesion of the active material before wiring of the circuits were initiated. A pair of electrodes were stacked in such a manner that the active regions faced each other, as shown in the **Fig. 4.2(h)**. Porous surfaces such as filter paper (FP), tissue paper (TP), or polyvinylidene difluoride (PVDF) soaked with electrolytes such as aqueous solutions of KOH and H_2SO_4 were used as a separator between the electrodes, as shown in the **Fig. 4.2(h)**. The planar SCs are termed as parallel plate supercapacitors (PPS) while the PPS were pressed from the sides to obtain the curved plate supercapacitors (CPS). The cross sectional views of the PPS and CPS are shown in **Figs. 4.2(i)** and **4.2(j)**, respectively.

4.4. CHARACTERIZATIONS

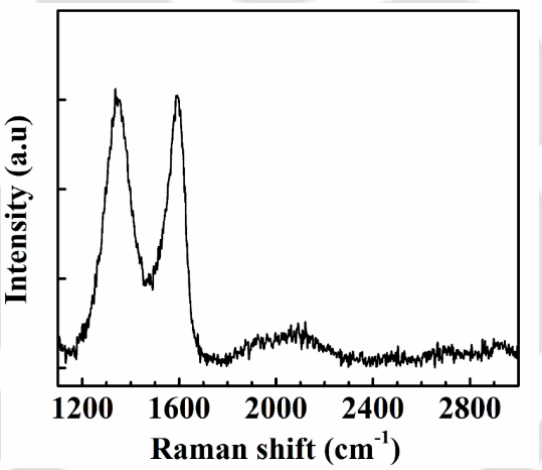

Figure 4.3: Raman spectra of active material deposited on the Cu surface.

4.4.1. Raman Spectroscopy:

Characterization of the active material deposited on Cu electrode was done using Raman spectroscopy, as shown in the **Fig. 4.3.** The characteristic D and G bands (at 1584 and 1352 cm^{-1}) in the Raman spectra show the presence of rGO in the active material.

4.4.2. Surface Morphology:

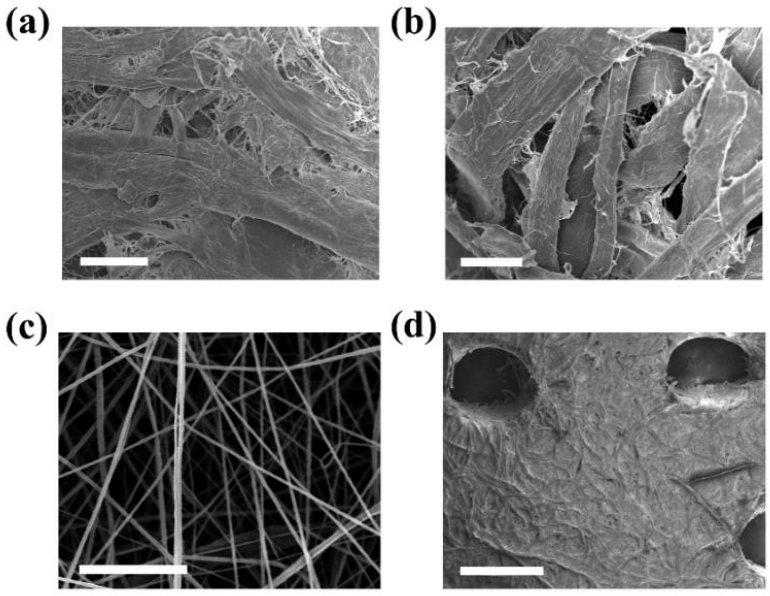

Figure 4.4: The FESEM images of different separators used in PPS. Image (a) – (d) show filter paper (FP), tissue paper, electro-spun PVDF fibres, and perforated filter paper (PFP), respectively. The scale bars on the images (a) and (b) are of 20 µm while the scale bars on the images (c) and (d) are 5 µm and 500 µm, respectively.

The surface morphology of different separator materials, namely filter paper (FP), tissue paper (TP), perforated filter paper (PFP) and electro-spun polyvinylidene fluoride fibres (PVDF) was investigated by FESEM. The images are illustrated in **Fig. 4.4** and a summary of their particle retention or porosity values are provided in **Table 4.2**.

Table 4.2. Properties of different electrolytes and separators

No.	Properties	Values
1	Ionic **c**onductivity of 4M KOH (2.244 mg/l)	570 mS/cm
2	Ionic conductivity of 1M H_2SO_4 (0.98 mg/l)	372 mS/cm
3	Particle retention of Whatman filter-paper (Grade-1)	11 µm
4	Particle retention of Kimtech tissue paper	~30 µm
5	Particle retention of electro-spun PVDF membrane	~2 µm
6	Particle retention of perforated filter-paper	500 µm
7	Average diameter of the nanofiber	158 nm

4.5. THEORETICAL FORMULATION

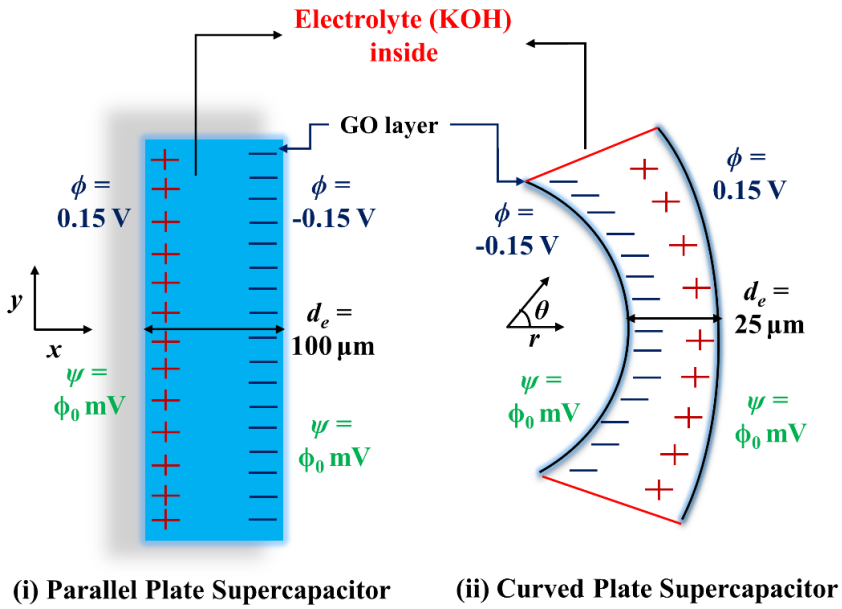

Figure 4.5: Shows the schematic representation of the (i) PPS and (ii) CPS, including its parameters and initial boundary conditions used during the simulations.

In this section, a theoretical model was developed and numerically solved to analyze the experimental results. In this formulation, we used two-dimensional (2D) Cartesian coordinate (x, y) system for the PPS configuration while for the CPS, we employed polar coordinate system (r, θ). We assumed that the applied surface potentials on the electrodes enable the formation of the EDL near the electrode-electrolyte interface. The dynamics of the formation of the EDL in the electrolyte was simulated by solving the Poisson-Nernst-Planck (PNP) equation coupled with the Navier-Stokes and ion transport equations for the fluid flow with appropriate boundary conditions. Further, the external electric field applied on the electrodes is obtained solving the Laplace equation with appropriate boundary conditions. In this formulation, we have assumed the electrolyte to be incompressible and Newtonian. All the variables in bold represent a vector, a bold variable with double overbar represents a tensor. Components placed inside bracket after a bold variable represent the components of that vector, e.g. in the expression $\boldsymbol{u}$ (u,v) the components of the vector u are denoted by u and v. The physical parameters viscosity, density, Faraday constant, concentration of the i^{th} ion, diffusivity of the i^{th} ion, relative dielectric permittivity of the medium is represented by the symbols μ, ρ, F, ξ_i, D_i, ε, respectively. Here 'i' represents different ions (cations and anions). The symbols, ∇ , D/Dt , ∇^2 represent gradient, material derivative, and Laplacian operators, respectively. Time is represented by the variable 't'.

The Navier-Stokes equations,

$$\rho D\mathbf{u}/Dt = -\nabla p + \mu\nabla^2\mathbf{u} + \rho_e\mathbf{E}\,, \qquad (4.1)$$

along with the continuity equation, $\nabla\cdot\mathbf{u} = 0$, were solved for the flow field in between the electrodes for both PPS and CPS. The last term in the Navier-Stokes equations, $\rho_e\mathbf{E}$, represents the body force owing to the electric field. The symbols ρ_e and E represent charge density and the electric field vector, respectively. The electric field is expressed as, $\mathbf{E} = -\nabla\psi$, where ψ is the electric field potential. No slip ($u = 0$) and impermeable ($v = 0$) boundary conditions were enforced at both the electrodes. The transport of the ions in the salt solution to develop the EDL was governed by Poison Nernst Planck (PNP) equation,

$$\varepsilon\nabla^2\psi_1 = -\sum z_i\xi_i\,. \qquad (4.2)$$

Here the term ξ_i represents the concentration of the i^{th} ion in the medium, which was obtained by solving the ion transport equation,

$$\partial\xi_i/\partial t + \mathbf{u}_i\cdot\nabla\xi_i = D_i\nabla^2\xi_i + z_i F\left(D_i/RT\right)\nabla\cdot\xi_i\nabla\psi\,. \qquad (4.3)$$

We employed constant surface potential boundary conditions to solve the PNP equation. The external field was obtained by solving the Laplace equation,

$$\nabla^2\phi = 0\,, \qquad (4.4)$$

with constant potential boundary conditions at the electrodes. The overall potential is taken as the algebraic sum, $\psi_{net} = \psi_1 + \phi$, of these potentials. The ion transport equations,

$$\partial\xi_i/\partial t + \mathbf{u}_i\cdot\nabla\xi_i = D_i\nabla^2\xi_i + z_i F\,\mathbf{u}_i\nabla\cdot\xi_i\nabla\psi_{net}\,, \qquad (4.5)$$

were solved with the help of the initial concentration, ξ_{i_bulk}, constant in the entire solution domain while zero-flux boundary conditions,

$$-\mathbf{n}\cdot\nabla D_i\xi_i = 0\,, \qquad (4.6)$$

for the ions enforced at the electrodes. Here, *n* is the unit vector normal to the surface of the capacitor plate, along *x*-direction as shown in the **Fig. 4.5**.

It is to be noted that the numerical simulations for this chapter is made taking initial guess values for a few parameters like specific surface area of the active material, electrode surface area, diffusivities of the ions, along with other related parameters as

the exact values are difficult to obtain. As a result, exact quantification of errors with respect to the results obtained from experiment is difficult to judge and has not been mentioned in the current study.

4.6. RESULTS AND DISCUSSION

4.6.1. Electrode geometry and distance:

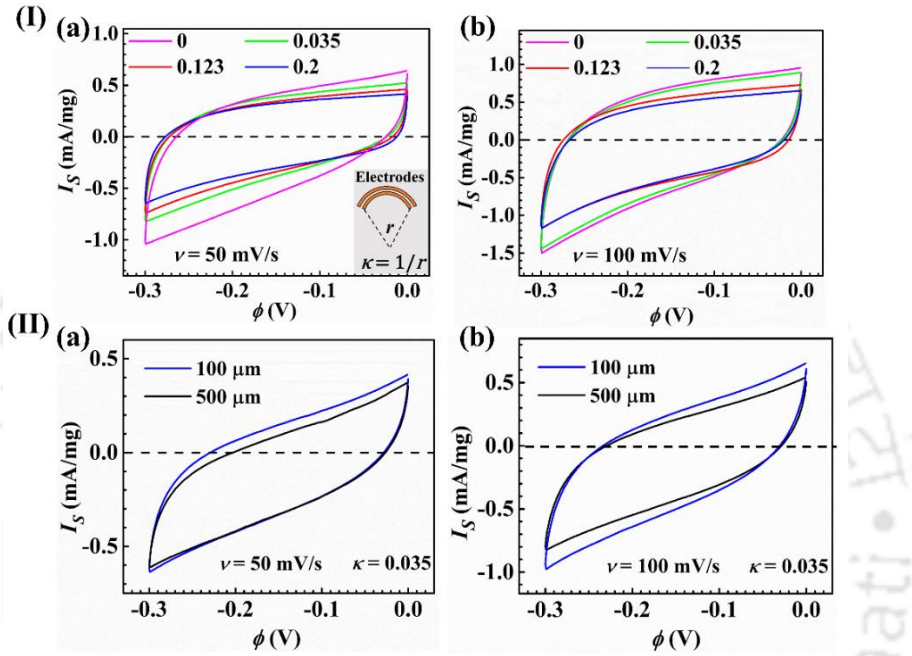

Figure 4.6: Shows cyclic voltammetry (CV) measurements associated with the different supercapacitor arrangements such as PPS and CPS, as shown in the previous figure. Images **(Ia)** and **(Ib)** show the variations in the specific current, I_S, with the applied electric field potential, φ, when the electrode separation distance was, d_e = 100 µm. Here, $I_S = I_0/m$, where I_0 is the measured current from CV and m is the mass of the active material. The images **(Ia)** and **(Ib)** correspond to the scan rates, ν = 50 mV/s, and 100 mV/s, respectively. The radius of curvature (κ) were measured, as shown in the inset of the image **(Ia)** where κ = 0 m^{-1} represents PPS while κ = 0.035 m^{-1}, 0.123 m^{-1}, and 0.2 m^{-1} show different CPS configurations. Images **(IIa)** and **(IIb)** show the CV when κ = 0.035 for d_e = 100 µm and 500 µm, and scan rates, ν = 50 mV/s and 100 mV/s, respectively. The separator used for all the experiments was filter paper (FP) soaked in 4M KOH.

At the beginning of this section, we discuss the effects of the electrode geometry and distance on the capacitance of the PPS and CPS. Towards that end, a series of CV analysis was performed for the supercapacitors (SCs) with different radius of curvatures (κ), ranging from 0 m^{-1} (PPS) to 0.2 m^{-1} (CPS) with same mass loading (2 mg/cm^2) of active material and electrode separation distance, d_e = 100 µm. **Figures 4.6(Ia)** and

4.**6(Ib)** display the typical CV characteristics, that is the variations in specific current, $I_s = I_0/m$, with the applied electric potential, ϕ. The results were obtained at two separate scan rates, ν = 50 mV/s and 100 mV/s, respectively, for the different PPS and CPS configurations. A smaller area under the discharge current curve in the positive *y*-axis confirmed a significant decrease in capacitance as κ increased from 0 m^{-1} (PPS) to 0.2 m^{-1} (CPS). This observation was true for both the number of scan rates out of which two are reported in this work.

It may be noted here that previously employed two-capacitor model (TCM) is in general unable to predict this reduction in capacitance as the curvature of the SCs increase from PPS to CPS. This is because, in TCM, the EDLs near the electrodes are modeled like a pair of infinitely long parallel plate capacitors. In this regard, the areas and thicknesses of the EDLs correspond to the surface areas of electrodes and the thicknesses of the Helmholtz layers, respectively.[322] This assumption also holds good in the case of CPS, since the Helmholtz layer thickness is of the order of micro to nanometer[323] while the electrode dimensions are in centimeter. Subsequently, the TCM assumes the same surface area and Helmholtz layer thickness for both PPS and CPS, which is the major reason behind its limitation to differentiate the capacitance of these configurations. However, the experiments shown in the **Fig. 4.6** uncovered that the capacitance in the PPS and CPS were different. We anticipated that the electric field in the different SC configurations varied with the change in the geometry of the electrodes which in turn influenced the variation in the capacitance.

In order to identify the other limitations of the TCM model, we further explored the effects of d_e for the CPS. As anticipated, the **Figs. 4.6(IIa)** and **4.6(IIb)** uncovered that for all scan rates the capacitance of the CPS decreased when d_e was increased. Again, the reduction in the capacitance of the CPS with increase in d_e could not be explained by the TCM because it did not account for d_e in the calculations of capacitance. The experiments corroborated that the TCM was insufficient to provide a comprehensive understanding of the charge storage of the SCs considered. In the PPS configuration, the electric field and its intensity were not expected to vary significantly across the electrodes owing to their planar geometry and constant separation distance. In contrast, for the CPS, the electric field intensity in between curved electrodes was expected to vary for a given applied electric field potential, φ (inset of **Fig. 4.11** in the later part).

Thus, the theoretical model proposed later consider the electric field and its intensity to evaluate the capacitance of the SCs.

4.3.2. Frequency dependent PPS performance:

In order to prove our hypothesis further, we attempted to understand electrochemical performance of the SCs more comprehensively. For this purpose, the key mechanisms at the molecular scale during the charging process were explored in detail. In this regard, we anticipated that the polarization of the current collector electrodes and the formation of the EDL near the electrode-electrolyte interface were the two important events during charge storage process in the SC. Since these events happen at different time scales, it was also important to analyze them with respect to time. Thus, we employed EIS, which emulates a pair of sinusoidal charging-discharging cycles at different frequencies (time-scale) to uncover these spatiotemporal characteristics during charge storage.

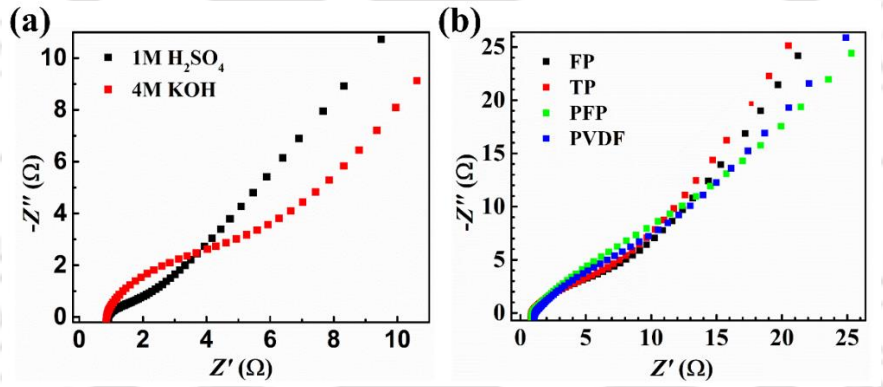

Figure 4.7: Electrochemical impedance spectroscopy (EIS) measurements associated with the PPS having different electrolytes and separator materials. Image **(a)** shows the high-frequency region (> 10 kHz) of Nyquist plots (real (*Z*') versus imaginary impedance (-*Z*")) obtained from EIS analysis of PPSs with two different electrolytes 4M KOH (circular symbols) and 1M H_2SO_4 (square symbols). Image **(b)** illustrates the same for different separators, namely, filter paper (FP), tissue paper (TP), perforated filter paper (PFP), and polyvinylidene fluoride (PVDF). In all the experiments, d_e = 100 µm.

A typical Nyquist plot obtained from the EIS of SCs consists of a semicircle at high-frequencies followed by a line with nearly 45° slope at the mid-frequency level and a vertical line at the lower frequencies[302]. In general, the EIS data obtained for various SCs are employed to evaluate the C_1, C_2, R_1, R_2, and R_3, as shown in the **Fig. 4.7(b)** after fitting the same with an equivalent circuit obtained from TCM. However, as we argued in this study that the TCM[303, 321] has limitations in predicting the capacitance in

the situations where the electric field intensity varies between the electrodes. The major reasons behind these variations in the electric field can be the polarization of the electrodes and subsequent formation of the EDL at molecular level during the charge storage cycle. The frequency dependent EIS analyzes shown in the following section gives a more accurate interpretation of those parameters.

4.3.2.1. High-frequency EIS (>10 kHz)

An EIS study of otherwise identical SCs having 1M H_2SO_4 and 4M KOH as electrolytes is shown in **Fig. 4.7(a)**. In this regard, the *x*-intercept, the real part of impedance (Z') at high-frequency, is traditionally termed as the equivalent series resistance (ESR) of the SCs.[16] **Figure 4.7(b)** shows that the *x*-intercept was similar for both the cases. However, it may be noted here that the ESR includes all the resistances due to the current collector, active material, binder, electrolyte, and separator.[24,26,35,50] Importantly, since we used two different electrolytes of different electrical resistivity, as shown in the **Table 4.2**, the ESR must be different for the two cases analyzed. A similar observation was made when different separator materials with different porosity were used keeping electrode separation, electrolyte, and other parameters constant as shown in **Fig. 4.7(b)**. Again, the figure suggests that the ESR was independent of the separator, which was quite unlikely owing to the use of different materials as separators. Surely, these experimental observations contradict the traditional method of estimating the ESR, which has been frequently employed to evaluate the electrochemical performance of SCs at high-frequency.

In this direction, we made an attempt to identify the origin of the SC parameters based on the high-frequency results of EIS after a careful analysis of the dynamics of the charging and discharging processes. It is well known that during the charging process, the observed current is a consequence of the accumulation of free charges on the metallic electrodes. Subsequently, an electric field is almost instantaneously established between the electrodes. However, the formation of EDL due to the drifting of ions of the electrolyte in response to this electric field is a much slower process. For example, the typical characteristic time-scale of charge relaxation for an electrolyte can be evaluated from, $\lambda_D d_e / D$, where λ_D is Debye length, d_e is electrode separation distance, and D is diffusivity.[54] Thus, for the experiments reported in the present work, the theoretical time scales for the aqueous electrolytes ($\lambda_D \sim 1 - 100$ nm, $D \sim 10^3$ μm^2/s,

and d_e ~ 100 μm)[54] we obtained the time scales in the range of, 10^{-4} to 10^{-2} s. The frequency at which the EIS intersect Z'-axis was 10^5 H< equivalent to 10^{-5} s, which was at least one order of magnitude smaller than the theoretically predicted ones.

Thus, a smaller experimental time scale in the high-frequency EIS analyzes charge relaxation time highlighted in the following mechanism. It is well known that the electrolyte resistance arises owing to the restriction in the movement of ions of an electrolyte under an electric field. At smaller time scales (i.e. at higher frequencies) these movements are minimal and contribute marginally to the effective electrical resistance. At the same time, the weakness of the ionic movement also rules out the ion-separator interaction. This again leads to the separator's meager contribution towards the net electrical resistance. Subsequently, we obtain identical electrical resistances at high-frequency EIS when the separator or the electrolytes were varied, as shown in the **Fig. 4.3**. In fact, the variations in the electrolyte strength (e.g. 0.5M to 4M KOH) led to marginal variations in the EIS response, as shown in the **Fig. 4.8(Ia)**.

However, the **Fig. 4.8(Ib)** shows that when d_e was increased while keeping other parameters same, the x-intercept of Z' in the EIS kept shifting towards higher electrical resistances. These experiments highlighted that indeed the electric field intensity between the electrodes had major influence in determining the real impedance (Z') or the electrical resistance of the PPS. In this situation, the increase in the electrical resistance of the PPS was attributed to the polarization of the electrodes due to lower electric field intensities. The EIS at the high-frequency zone corroborated that the electrical resistance of the PPS would depend on electrode resistance[318] and their polarization, which would vary with the applied electric field intensity. In fact, the mid-frequency region of EIS also showed the importance of electrode polarization charge storage mechanism, as discussed in the following section.

In a Nyquist plot, the semi-circular region in the mid-frequency zone indicates the concurrent dissipation (Z') and storage ($-Z''$) of electrical energy.[324] An equivalent circuit of such a system could be envisaged as a resistor and a capacitor connected in parallel.[325] While the resistor dissipates the electrical energy, the capacitors stores the same. For such a system, the magnitude of real impedance, $\Delta Z'$, equaling the horizontal spread (or diameter) of the semi-circular region (**Fig. 4.8(Ib)**), is in general termed as the charge transfer resistance.[300, 305, 326] Previous studies associated $\Delta Z'$ with the charge transfer resistance only when there is a redox reaction at the electrode-electrolyte

interface. For example, in the cases of pseudo-capacitors $\Delta Z'$ provides the information on the amount of electrical energy is dissipated during the redox reactions.[327]

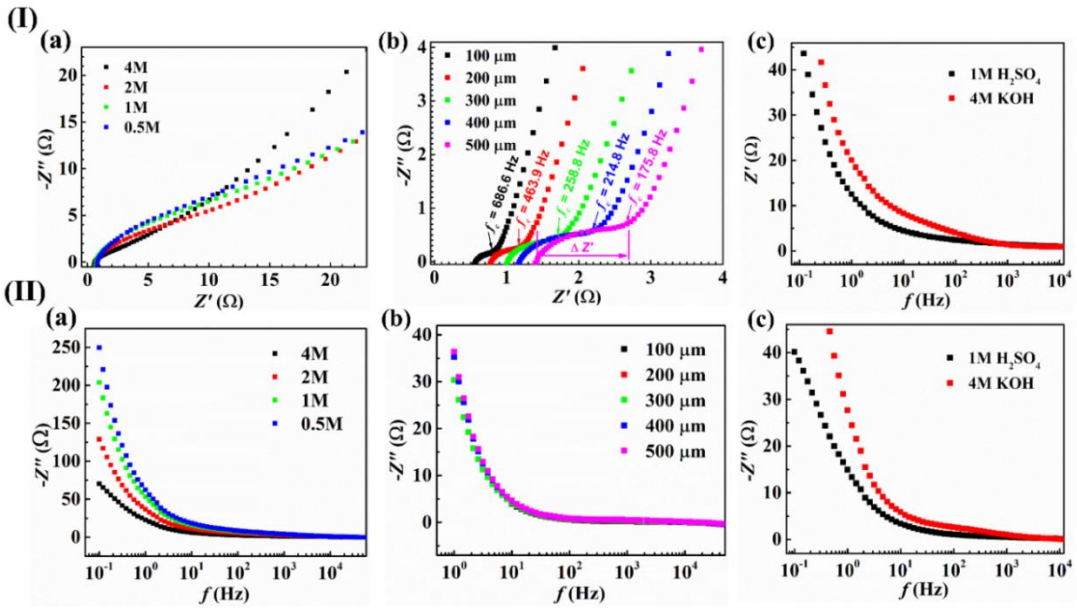

Figure 4.8: Images **(Ia)** and **(IIa)** represent the Nyquist and Bode (imaginary impedance (-Z˝) versus frequency (f)) plots obtained from the EIS of a PPSs with different KOH concentrations (4M, 2M, 1M, and 0.5M) in which d_e = 100 µm. Images **(Ib)** and **(IIb)** represent the Nyquist and Bode plots for d_e = 100 µm - 500 µm when the electrolyte was 4M KOH. Images **(Ic)** and **(IIc)** represent the Bode plots for the PPS when 4M KOH and 1M H_2SO_4 were used as electrolytes and d_e =100 µm. In all the experiments FP was used as the separator material.

4.3.2.2 Mid-frequency EIS (10 Hz-10 kHz):

Importantly, the charge storage in most of the SC configurations, such as the PPS shown here, is non-Faradaic type.[321] Thus, we expect that there is no redox reaction near the electrodes of a PPS, except during the dielectric breakdown or electrode corrosion. However, the experiments here uncover that Z' of the EIS spectra in the mid-frequency zone can also be an important parameter for the non-Faradaic SCs even in absence of any redox reactions between the electrodes and electrolyte. **Figure 4.8(1b)** shows that, although the electrolyte concentration and overpotential were kept similar, the width of semi-circular regions increased with d_e for a PPS. The experiments suggested that even in absence of a redox reaction between the electrodes and electrolyte the magnitude of $\Delta Z'$ increased. Certainly, the variation in the electrical resistance with d_e in the mid-frequency zone of the EIS had some other physical significance at ionic level.

In order to reveal the underlying mechanism of this phenomenon, we put up the following set of hypotheses: (i) during the electrode polarization, marginal ionic movements were observed in the PPS, which was previously established with the help of higher frequency results of EIS; (ii) the counter-ions in the electrolyte 'drifted' towards electrodes with the variation in the electric field to cause counter-charge accumulation near the polarized electrodes to initiate the formation of EDL with the progressive reduction in the frequency of the EIS; (iii) in the mid-frequency zone, a stronger ionic drift as compared to ionic diffusion ensured the formation of the Stern or immobile Helmholtz layer of EDL near the electrodes; (iv) subsequently, an electric field (E_h) was generated due to the formation of EDL near the electrodes, which was opposite to the one established due to electrode polarization (E_p); (iv) in the process, the bound charges and the ions present in the electrolyte underwent a frequency dependent dielectric relaxation, which led to a temporal increase in the frequency dependent dielectric constant of the electrolyte. In order to establish these arguments, we studied the resistive (Z' vs. f) and capacitive (-Z" vs. f) Bode plots of the EIS for the PPS considered in the **Fig. 4.8.(a)**. **Figures 4.8(Ic)** and **4.8(IIc)** show that in high-frequency region, as anticipated there was no ionic movement and the electrochemical responses were similar for both electrolytes. However, the responses started bifurcating for the different electrolytes in the mid-frequency range of 100-1000 Hz. The plots show that different ionic mobility and charge densities of 4M KOH and 1M H_2SO_4 led to different resistive and capacitive properties, respectively. In fact, the Bode plots uncovered that the experimentally observed dielectric relaxation starts in the time range of 10^{-3}-10^{-2}s, which was of the same order of the theoretically calculated characteristic time-scale for charge relaxation, which is discussed in **Fig 4.11(a)** in the later part of this chapter. [328]

Importantly, the bifurcation of the resistive and capacitive Bode plots also indicated a variation in the intrinsic property of the electrolytes after ~10^{-3}-10^{-2}s. For example, as the counter-ions move towards the electrodes, the dissipation and storage of electrical energy initiated owing to the movement of ions and subsequently the formation of the EDL. These two processes can be thought of as a resistor and capacitor in parallel, which resulted in the semi-circular nature of the Nyquist plot shown in the **Fig. 4.8(Ib)**. [324, 325] As a result of this ionic movement, **Fig. 4.8(Ic)** shows an increase in resistance

due to energy dissipation while **Fig. 4.8(IIc)** illustrates the energy storage due to the EDL formation.

The plots in the **Fig. 4.8(Ib)** also indicates that, at the initial stages of the charge storage of the PPS, the concentration gradient of the counter ions near the unshielded electrode surface was rather insignificant. For example, when d_e = 100 µm the plot shows, Z' = 0.5 Ω while $-Z''$ ~ 0. With the progress in time, the applied field drifted the counter-ions in the electrolyte more towards polarized electrodes. At this stage, the drift of the ions was expected to be stronger than the diffusion, which enabled the formation of a compact and immobile counter-ionic layer on the electrodes. The end of the semi-circular region of the Nyquist plot signified the completion of the immobile Helmholtz or Stern layer formation due to ion drift. For example, when d_e = 100 µm the plot shows that the formation of the immobile layer of EDL was complete at 686.6 Hz (0.0014 s) when Z' = 0.75 Ω while $-Z''$ ~ 0.3 Ω. Following this, the formation of the diffuse layer of the EDL started, which are analyzed by the Warburg element in EIS plots at the low-frequency range where diffusional ionic movements are significant, as discussed later. [329]

Importantly, before analyzing the low-frequency data of EIS, we investigated the effects of applied electric field intensity (E_p) and electrolyte concentration on the dynamics of EDL formation, in the mid-frequency range of EIS. Previously, **Fig. 4.8(Ib)** pointed out that the width of semi-circular region increased when the electric field intensity between the electrode reduced. This observation is similar to the case for Li-ion batteries where diffusional resistance of electrolyte increases with electrode separation distance. [320] The frequencies of the inflection points (f_c) at which semi-circular region completed are indicated by arrows on the figure. The plot suggests that f_c reduced from 686.6 Hz for d_e = 100 µm to about 175.8 Hz for d_e = 500 µm. As completion of semi-circular region marks the end of the Stern layer formation, decreasing frequency of inflection points suggested that the requirement of more time for the formation of Stern layer at a smaller E_p. This observation was in accordance with the predictions from the proposed theoretical model discussed later, [329, 330] which considered the flux of drifting ions to be the function of the applied electrostatic field. In a way, $\Delta Z'$ could be associated with the ionic resistance faced during the formation of Stern layer, which in turn would be the functions of electrolyte resistance and E_p.

Furthermore, the experimental observations in the Bode plot on the imaginary impedance (-Z'') in **Fig. 4.8(IIb)** suggests steady state concentration of counter-ions in the Stern layer did not vary with E_p. [329] In contrast, **Fig. 4.8(IIa)** suggests that the steady state concentration of counter-ions in the Stern layer increased with the concentration of KOH. Importantly, the **Figs. 4.8(Ia)** and **(IIa)** show that although the electrochemical responses were same for all electrolyte concentrations at the higher frequency EIS zone, the response varied with the molarity of the electrolyte KOH in the mid-frequency region. Thus, the capacitance increased with the concentration of KOH owing to the accumulation of the larger concentration of the counter-ions in the Stern layer. Concisely, the response of PPS in the mid-frequency EIS could uncover the dynamics of the formation of the Stern Layer in an EDL with the variations in the E_p and electrolyte strength.

4.3.2.3. Low-frequency EIS (<10 Hz):

After the completion of a semi-circular region of a Nyquist plot, the 45° line depicts the Warburg resistance observed in the frequency range of 1 Hz – 10 Hz.[16] In this regime, the plots in the **Fig. 4.8(Ib)** indicates that the real and imaginary impedances increased with equal magnitudes with the reduction in frequency. In this situation, previously, we identified that the formation of the immobile Helmholtz layer was complete. This ensured that there is a concentration gradient between the immobile Helmholtz layer and the bulk of the electrolyte. In such a situation, a dynamic equilibrium was expected to be established in the EDL where the ions would simultaneously diffuse out of the electrode as well as drift in towards the electrode. In Gouy-Chapman-Stern Model, this loosely bound mobile layer outside the immobile Helmholtz layer is termed as 'diffuse layer', which is also known as the 'space charge region'.[61] The equal increment in magnitude of real and imaginary impedances with frequency suggested drift and diffusional movements of ions in the equal and opposite directions at the low-frequency EIS. The drift (diffusion) movement during the EDL formation (shedding) also corresponded to the increased capacitance (resistance) across the polarized electrodes. The Nyquist plots shown in the **Fig. 4.8(Ib)** also show that after the formation of the diffuse layer, the capacitance of SC became constant, which was reflected in a nearly vertical line with increasing $|Z''| = 1/\omega C$ below 1 Hz where only, $\omega = 2\pi f$ was changing at C.

4.3.3. Charge storage mechanism:

The experiments shown above helped us in understanding the charge storage mechanisms of the SCs having PPS and CPS configurations. The experiments uncovered that at high-frequencies, the SCs behaves like a parallel plate capacitor because, in such a situation, only polarization of electrodes took place. This leads to an electric field of E_p, as shown later in the **Fig. 4.9(a)**. After the electrodes are polarized, in the mid-frequency domain, the charge relaxation of the electrolyte starts due to the drifting of ions. This led to the accumulation of the counter-charges on the polarized electrodes, leading to the formation of the immobile Helmholtz layer of the EDL. Further, in the low-frequency domain, the diffuse layer of the EDL forms owing to the simultaneous drifting and diffusion of the counter ions near the polarized electrode. The formation of the EDL develops an electric field E_h in the opposite direction of the E_p having nearly equal strength. At this stage, the dielectric relaxation of SC is expected to be completed. Subsequently, an exceptional increase in the capacitance ($C = Q/\Delta V$) of SCs was observed because for any given amount of charge on the electrodes (Q) reduction in the net electric field (E_p - E_h) led to reduction in the potential difference across the electrodes (ΔV). In such a scenario, the charge could be stored in the electrodes until they reach a ΔV at which charge leakage takes place due to dielectric breakdown.

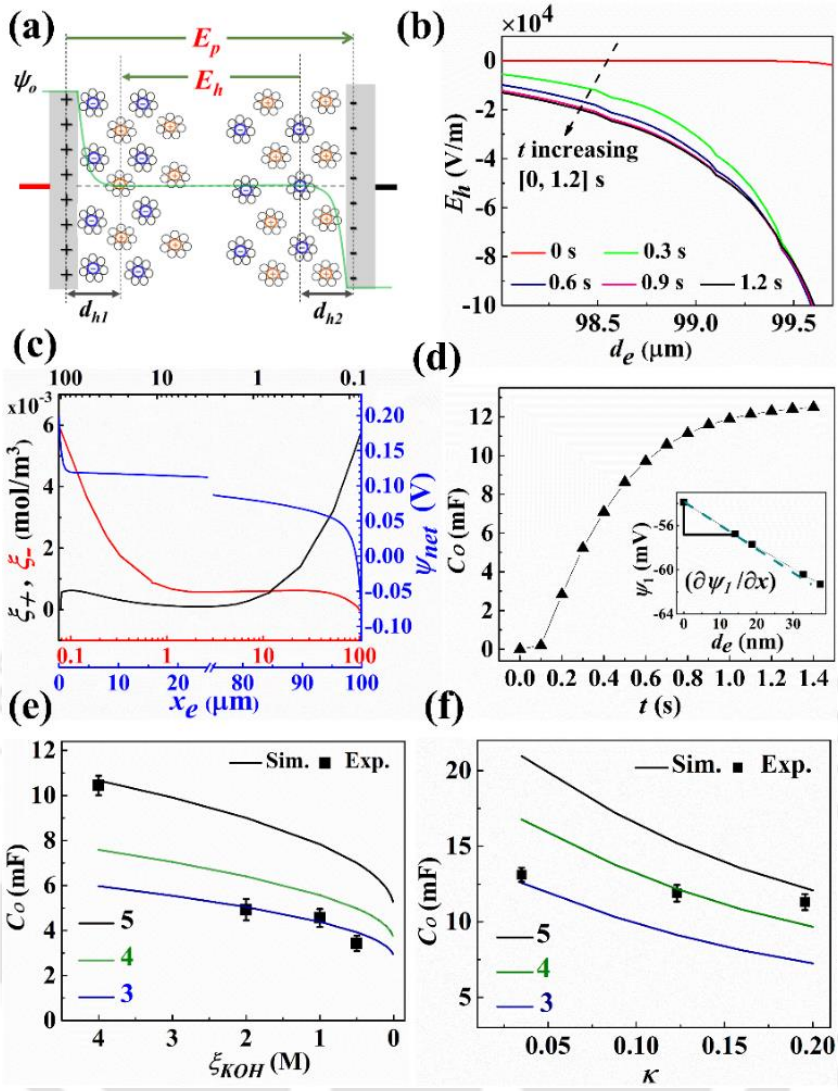

Figure 4.9: The schematic diagram in image **(a)** shows the directions of the electric fields, E_p – the applied field leading to the polarization of electrodes and E_h – electric field generated due to the formation of EDL. The diagram also shows the variation in net electric field potential, ψ_{net} (solid line) across the SC and the thicknesses of the EDLs (d_{h1} and d_{h2}) near the electrodes. Images **(b)**-**(f)** represents the results obtained using simulation studies. Image **(b)** shows the time-dependent variation in E_h along d_e during the formation of EDL at their respective electrodes in PPS, image **(c)** shows profiles of concentration of cations (ξ_+) and anions (ξ_-), and ψ_{net}, with the electrode distance (x_e). Image **(d)** shows the variation in capacitance (C_0) with time (t). The inset image shows the gradient of the electric potential due to ions (ψ_1) at x = 0 μm, taken for calculating the capacitance according to Eq. (4.10). Image **(e)** shows the variation in C_0 with KOH concentration (ξ_{KOH}) obtained from experiments and simulations (lines) for ε = 3, 4, and 5. Image (**f**) shows the variation in C_0 with radius of curvature (κ) of CPS from experiments (symbols, **Fig. 4.6**) and simulations (lines) for ε = 3, 4, and 5.

With this charge storage mechanism in mind, subsequently, we made an attempt to evaluate the experimentally measured capacitance of SCs with the help of analytical

and numerical models. For this purpose, in **Fig. 4.9(a)**, we show a typical geometry of a PPS in which an electric potential profile is drawn assuming EDL of thickness d_{h1} and d_{h2}, having charges equal and opposite to their respective electrodes. We assume that the EDL completely shields the charges at their respective electrodes, which establishes the electric field only due to EDL (E_h) of equal magnitude of electric field due to polarized electrodes (E_p). For such a system, the capacitance for a PPS can be analytically calculated as,

$$C = \frac{\sigma A}{\int E_{net} dx} = \frac{\sigma A}{\int (E_p - E_h) dx}. \tag{4.7}$$

For PPS:

$$\frac{\sigma A}{E_p L - E_h (L - d_{h1} - d_{h2})} = \frac{\sigma A}{E_h (d_{h1} + d_{h2})} = \frac{\varepsilon \varepsilon_o A}{(d_{h1} + d_{h2})}. \tag{4.8}$$

For CPS with inner plate radius (R_1) and outer plate radius (R_2):

$$\frac{\sigma A}{\int_{R_2}^{R_2} E_p dr - \int_{R_1 + d_{h1}}^{R_2 - d_{h2}} E_h dr} = \frac{\varepsilon \varepsilon_o A}{(R_1 + R_2) \ln \left[\frac{R_2 (R_1 + d_{h1})}{R_1 (R_2 - d_{h2})} \right]}. \tag{4.9}$$

Although Eq. (4.8) holds a resemblance with the widely employed TCM, however, from Eq. (4.9) we observe that in the case of CPS, capacitance would vary with the change in curvature radius, as experimentally observed in the **Fig. 4.6**. Therefore, physical interpretation of charge storage should not be drawn using TCM because it fails to account for the variation in E_p and E_h with electrode geometry. This is due to the reason that TCM considers electrodes having separate existence and calculates specific capacitance (C_S) of individual electrodes. [331]

In contrast, we propose that the charge storage initiates with the polarization of electrodes and then the electric field between the electrodes plays a crucial part in determining the performance of the SC. Hence considering separate capacitance for each electrode for symmetric electrolytic SC would not be prudent. To experimentally calculate the capacitance of an SC, widely used method for capacitance calculation using CV and Galvanostatic charge-discharge curve would remain the same except the calculation would be done for all the components of the SC and not for the EDL

formation at the single electrode. In such a situation, the C_S calculated using CV would be given by $C_S = \left| \int_0^{V_1} Id\varphi \right| / m\nu\Delta\phi,$ where I is the discharge current from scan rate 0 V to V_1, ν is the scan rate, $\Delta\phi$ applied electric field potential difference during the scan, and m is total mass loading on both of the electrodes. While calculating a specific capacitance of an individual electrode for a pseudocapacitor or asymmetric supercapacitor using three electrode systems is necessary because individual electrode contributes differently to the overall capacitance of the device. [329] In order to calculate the capacitance analytically, certainly the Eqs. (4.8) and (4.9) could be very handy for simple calculations, however, they were unable to provide the accurate picture of the charge storage mechanism.

Thus, in order to further prove the hypothesis proposed here, numerical simulations were performed for PPS and CPS configurations to obtain the profiles of E_p and E_h. **Figure 4.9(b)** shows the developing E_h profile near the electrode surface with time (t). The time for EDL formation or dielectric relaxation was around 1 s, which was found to be similar to the experimentally observed frequency of ~1 Hz. **Figure 4.9(c)** shows the steady state profile of concentration of cations (ξ_+) and anions (ξ_-) leading to a net electric potential profile (ψ_{net}) in between the electrodes. The steady state profiles of E_p, E_h and E_{net} (E_p - E_h) have also been shown in **Fig. 4.9.**

Figure 4.9(d) shows the capacitance (C_0) variation with t, which signifies that the C_0 reached maximum value after dielectric relaxation was complete in the electrolyte. The inset of the plot shows the way we numerically evaluated the electric field potential gradient near the electrodes. For lower concentration of electrolyte, we assumed dielectric constant of the Stern layer (ε) to be constant, its value has no effects on the behavior of diffuse layer. [332] However, for the present system since the KOH concentration (ξ_{KOH}) is of high value, we experimentally calculated C_0 for different ξ_{KOH} stimulated values of ε for theoretical C_0 calculation. **Figure 4.9(f)** shows that calculating C_0 while considering the variation in ψ_{net} with κ, can indeed captur the trends observed during our experimental studies.

The numerical solution of the aforementioned coupled system composed of, (i) PNP equation for the electrolyte, (ii) Laplace equation for the applied electric field through the electrodes, (iii) continuity equation, (iv) equations of motion, and (v) ion transport

equations, with the mentioned boundary conditions provided the distribution of ions surrounding the electrodes in the electrolyte.

The Bode diagrams shown in the **Fig. 4.8(c)** helped us tracking the EDL formation experimentally. In this line, numerical simulations were also performed to study the time lag associated with the charge separation in the electrolyte or the EDL formation. **Figure 4.9(b)** shows the profiles for the electric field potential at different time intervals, which were obtained from the numerical analysis. The temporal development of the EDL could also be correlated to the dielectric relaxation of the electrolyte by tracking the variation in dielectric constant ε of the same with time. The dielectric constant of the electrolyte (ε_a) at any time (t_1) can be calculated using the following expression:

$$[\varepsilon_a]_{t=t_1} = [C_o]_{t=t_1} / [C_o]_{t=0}. \quad (4.14)$$

The capacitance at any given time is shown in **Fig.4.9(d)**. **Figure 4.9(c)** shows the variation in ε_a of the electrolyte between the electrode with t. The figure uncovers a typical picture of the dielectric relaxation during the EDL formation near the electrodes of the SC. The figure shows that the magnitude of ε_a increased with time before it became nearly constant at ~1.1 s. From the Eq. (4.10), it is evident that the charge at the electrode also increased with time till t = 1.1 s. The image suggests that the time lag was around 1.1 s after which the capacitance reached a maximum possible value. This time lag was also observed in the experimental data presented before.

4.4.4. Capacitance from TCM and CV analysis:

Capacitance calculation using two capacitance model (TCM) was done by employing the following expression,

$$C_{TCM} = \frac{\varepsilon A}{2d}. \quad (4.15)$$

Where the dielectric permittivity of EDL, $\varepsilon \sim 6\varepsilon_0 \sim 6\times 8.854\times 10^{-12}$ F/m, electrode surface area, $A \sim 0.6$ m^2, considering average surface area of rGO to be ~300 m^2/gm,[7] and EDL thickness, $d \sim 1$ nm.[8] Thus, the capacitance of the device (C_0) with 2 mg/cm^2 mass loading and an electrode surface area of 1 cm^2, was evaluated to be around 15.93 mF. We did an electrochemical CV analysis to measure the specific capacitance of the PPS and CPS, as shown in the **Fig 4.2**. The specific capacitance (C_s) plotted in the **Fig. 4.10**

was calculated from the following expression where '*m*' is the total mass available on the electrode, calculated from by multiplying mass loading (2 mg/cm^2) with the electrode surface area (1 cm^2),

$$C_s = \frac{C_{TCM}}{m}. \tag{4.16}$$

The experimental capacitances were obtained from the cyclic voltammetry analysis as,

$$C_o = \left| \int_0^{V_1} I_o d\phi \right| \left(\nu \Delta\phi\right)^{-1}. \tag{4.17}$$

Where I_0 is the measured discharge current, ν is the scan rate, and $\Delta\phi$ is the applied electrical potential difference between the electrodes.

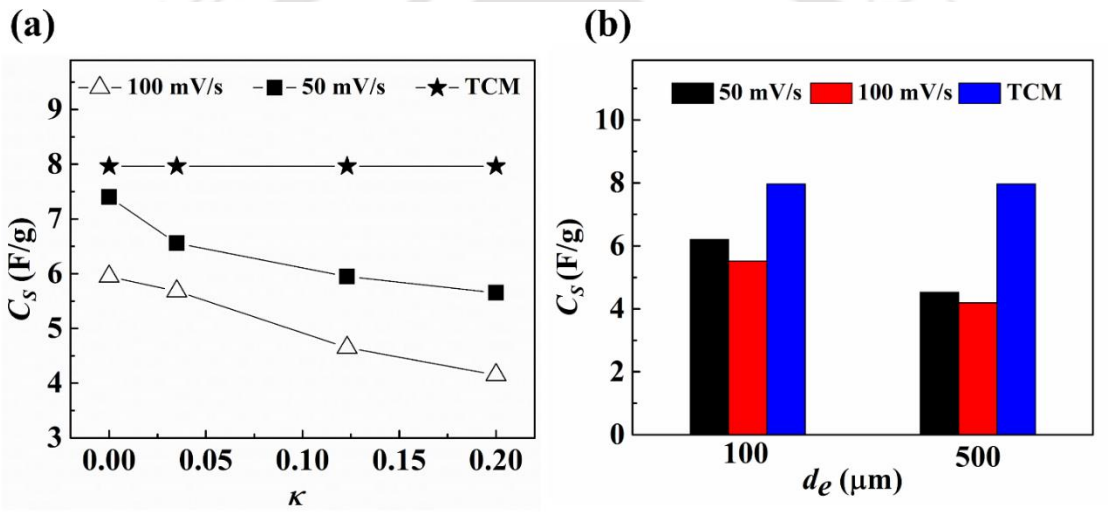

Figure 4.10: Comparison between theoretical and experimental specific capacitance (C_S) values. Image (a) shows the comparison among the experimentally calculated C_S from CV curves of **Fig. 4.6** and the theoretically calculated C_S from TCM using Eqs. (4.16) and (4.17). The line with asterisk symbols represents the values calculated from TCM and the two lines having triangular and box symbols represent experimental values at two different scan rates, 50 mV/s, and 100 mV/s, respectively. The experimental values of C_S were obtained for angles, κ = 0.035 m^{-1}, 0.123 m^{-1}, and 0.2 m^{-1} at scan rates, ν = 50 mV/s and 100 mV/s. Image (b) represents a similar comparison for κ = 0.034 m^{-1} and electrode separations, d_e = 100 μm and 500 μm.

The comparison of C_S evaluated from CV experiments and TCM has been shown in the **Fig. 4.10.** In this regard, we evaluated the specific current, $I_s = I_s/m$, from the **Fig. 4.6** and V_1 was taken as -0.3 V because the CVs were conducted for the voltage sweeps from 0 V to -0.3 V. **Figure 4.10(a)** depicts that C_S remains unchanged with the

bending angle for TCM consideration. However, for both ν = 50 mV/s and 100 mV/s, the capacitances were lower and at the same time, they also reduced with more and more bending (from κ = 0.034 m^{-1} to 0.2 m^{-1}). Thus, TCM was unable to predict the experimental observations. A similar comparison between two CPS with different electrode separations (d_e = 100 μm and 500 μm) at a particular bending (κ = 0.034 m^{-1}) is illustrated in **Fig. 4.10(b)**, which also highlights the limitation of TCM.

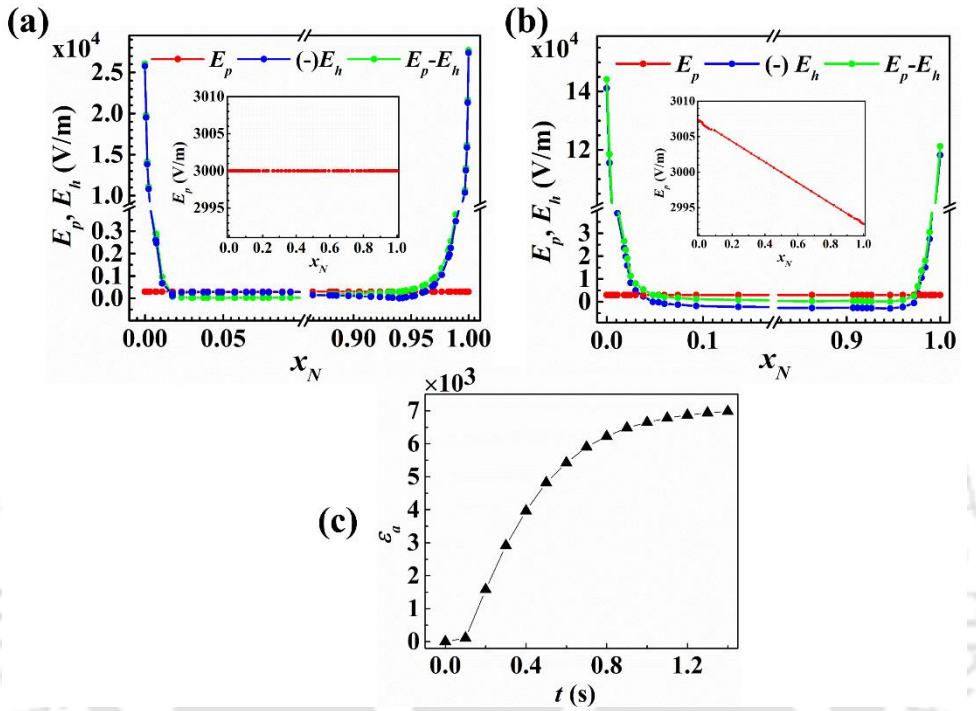

Figure 4.11: Images shows profiles of E_p, E_h, and E_{net} (E_p- E_h) in **(a)** PPS, and **(b)** CPS (for κ = 0.035) configurations. The normalized distance between the electrodes in the x-axis is, $x_N = x/d_e$, where x is the distance from the electrode. The separation distance is 100 μm for PPS and 25 μm for CPS. Image **(c)** shows the variation in dielectric constant (ε) with time (t) for the PPS.

All the equations were solved in a computational fluid dynamic software, COMSOL Multiphysics™, employing the finite element method. The solution domains of CPS and PPS were divided into 60,000 to 90,000 triangular mesh elements before obtaining a grid independent solution. The inbuilt solver direct PARDISO was employed taken to numerically solve the set of unsteady coupled equations along with the boundary conditions. COMSOL Multiphysics™ determined the intermediate time steps (Δt) by Newton's backward time interpolation method. **Figures 4.11(a)** and **4.11(b)** show the profiles for the applied electric field (E_p), the electric field generated in the electrolyte during the EDL formation (E_h) and the net electric field ($E_{net} = E_p - E_h$) for PPS and CPS, respectively. The variations in E_p, E_h, and E_{net} with time have been shown in the

Fig. 4.11. The plots shown here show the steady state profiles, which suggests that there was significantly high E_{net} near the electrodes owing to the presence of surface charges while towards the bulk of the electrolyte the electric field potential progressively diminished to a constant value. Importantly, while E_p for PPS was constant the same for CPS varied linearly, as shown in the insets.

The spatial variation in E_p owing to the change of the geometry led to the variation in the EDL formed around the electrode, which eventually altered the capacitance of CPS. The variations of the capacitance in the simulations were evaluated by initially calculating the charge per unit area on the electrodes as,

for PPS

$$\bar{Q} = \varepsilon\varepsilon_{\circ}\left(\partial\psi_{net}/\partial x\right)_{x=0}, \tag{4.10}$$

and for CPS

$$\bar{Q} = \varepsilon\varepsilon_{\circ}\left(\partial\psi_{net}/\partial r\right)_{r=R_1}. \tag{4.11}$$

Thereafter, the capacitance per unit area was obtained as,

for PPS

$$\bar{C} = \bar{Q}\left[\int_0^{d_e} E_{net}\,dx\right]^{-1}, \tag{4.12}$$

and for CPS

$$\bar{C} = \bar{Q}\left[\int_{R_1}^{R_2} E_{net}\,dr\right]^{-1}. \tag{4.13}$$

Here the symbol $\bar{C}$ signifies overall capacitance of the system and ε represents the dielectric constant of the Stern layer at the electrode surface. It is to be noted that, since for PPS applied electric field potential, φ, doesn't vary with distance. Hence gradient of electric field potential due to ionic charges (ψ_1) can also be used instead of ψ_{net}, as shown in inset of **Fig. 4.9(d)**.

4.4. CONCLUSIONS

Chapter 4

A host of rGO based parallel and curved plate SCs have been fabricated to uncover the unexplored pathways of charge storage. Experiments uncovered electrode polarization at smaller time scales, Stern layer formation at the intermediate ones, and the formation of the diffuse layer at a much larger time scales. A physical model composed of Poisson-Nernst-Plank equations for the electric field in electrolyte and Laplace equation for the electric field in electrodes were coupled with Navier-Stokes equations for the electrolyte was numerically solved with appropriate boundary conditions to corroborate the spatiotemporal experimental behaviors observed for the SCs. The use of net electric field originating from the, (i) electrode polarization due to the applied field and (ii) opposing field in the electrolyte during the EDL formation, during the evaluation of capacitance has been found to be more accurate in explaining the experimental results. The theoretical and experimental results together suggest that charge storage of SCs heavily depend upon electrode geometry, type of electrolyte, electrolyte concentration, electrode separation, separator type, and dielectric relaxation of the electrolyte. The existing physical models were unable to take into account all these parameters while elucidating the performance of an SC. The theoretical model proposed can be a significant step forward in analyzing the performance of the SCs in near future.

Chapter 5

Multimodal Chemo-Magneto-Photo-Taxes of 3G CNT-bots to Power Fuel Cells

ABSTRACT

We report the design and development of a 3G microswimmer, namely CNT-bot, capable of undergoing acid, alkali, magneto and photo taxes inside the acidic or alkaline baths of peroxide fuel and/or water. The use of carboxyl functionalized multi walled carbon nanotubes (MWCNT) facilitated a propulsion of the CNT-bot in the alkaline water by ejecting of carbon-dioxide bubbles. Further, the doping of magnetite nanoparticles (FeONPs), ferrous ions (Fe^{+2}), and titanium dioxide nanoparticles (TiONPs) in the CNT-bot instigate the magnetic, chemical, and photonic handles for propulsions under magnetic field, peroxide fuel, and light, respectively. While the FeONPs stimulated magneto taxis as high as ~10 body lengths per second, the chemotaxis in the peroxide fuel of similar speed was achieved by bubble-propulsion of oxygen gas originating from the Fenton reaction. Further light stimulated Photo-Fenton reaction led to the phototaxy of the CNT-bot. A thin coating of magnesium imparted a half-faced Janus look to the CNT-bot, which helped in the motions inside normal or acidic water mediums through the ejection of hydrogen gas. Further, the chemotaxes could be transformed into pH stimulated directional chemotaxis by establishing a concentration gradient of acid or alkali across the peroxide and/or water baths. The capacity of the CNT-bot to produce oxygen (hydrogen) bubbles in the peroxide (acidic water) fuel was exploited to power a Proton Exchange Membrane (PEM) fuel cell to generate electricity. The pure oxygen and hydrogen gases generated by the CNT-bots in separate chambers were fed directly to the fuel cell in which the incessant motions of the particle facilitated the creation and release of the pure gases for the on-demand electricity generation. The motor could also perform dye degradation through advanced oxidation owing to production of intermediate hydroxyl radicals from Fenton's reaction.

Chapter 5

5.1. INTRODUCTION

The recent advent of biomimetics of diverse natural products and processes inspire the usage of carbonaceous materials for a host of state-of-art applications.[333, 334] For example, the synthesis of artificial self-propelling objects for drug-delivery,[24-26] environmental remediation,[36, 37] or health care[335] applications not only emulate various cellular or subcellular processes[86, 130, 336-339] but often employ carbon derivatives for synthesis.[340, 341] Importantly, the natural processes also motivate the judicious usage of inorganic materials alongside carbon for improved efficiency and functionality. For example, over the past few decades, a host of organic,[342, 343] inorganic,[25, 344-346] and composite self-propellers have shown improved propulsion behaviours under various excitations such as photon,[347] concentration gradient,[348, 349] surface tension gradient,[350, 351] and electric[352, 353] or magnetic[49] or acoustic[354, 355] fields. In this regard, the previous works also suggest that, while the first-generation (1G) motors were synthesized to identify the roles of materials,[356] size reduction, and transport properties[357] on diverse locomotive behaviors, the major focus during the fabrication of second-generation (2G) locomotives has been the functionality, directionality,[358] and biocompatibility.[359] The recent thrust of the design and development of third-generation (3G) motors are directed towards achieving controls over the multimodal directional transports suitable for scalable diverse energy,[360] environmental,[37, 73, 359-361] and health care applications.[86, 362]

For example, a number of previous studies have shown the utility of carbon nanotubes (CNTs), [363, 364] graphene,[365, 366] and their derivatives as 3G self-propellers, which have been employed as proofs-of-concept for dye decomposition, drug delivery,[89, 367] enzymatic propulsions,[368] and healthcare applications.[359, 362] On the other hand, a number of studies have shown the importance of 3G microswimmers for various energy applications. For example, iron (Fe)[71, 369] or magnesium (Mg)[359] based motors have shown their utility in the production of pure hydrogen (H_2) suitable for fuel cell applications. A few seminal contributions have also demonstrated the capacity of the Mg motors to decompose hazardous matters[370] and other *in vivo* applications.[346, 370] It may be noted here that a few previous works have attempted using iron nanoparticles to catalyze the organics such as formic[49] and citric[50] acids to cause bubble-propulsion of motors through hydrogen production. Subsequently, a number of works have also shown that the hydrogen produced from such sources and oxygen produced from the

decomposition of peroxide fuel using iron nanoparticles can directly be fed to fuel cells for real time energy harvesting.[35,47,48,50] However, the prior-art suggests that the use of carbonaceous materials in achieving the multimodal self-propulsion alongside performing a multitude of applications has not been attempted so far. In particular, the alkali-, acid-, and photo-taxes of such self-propellers through the chemical decomposition of water has been considered to be a long standing challenge so far.

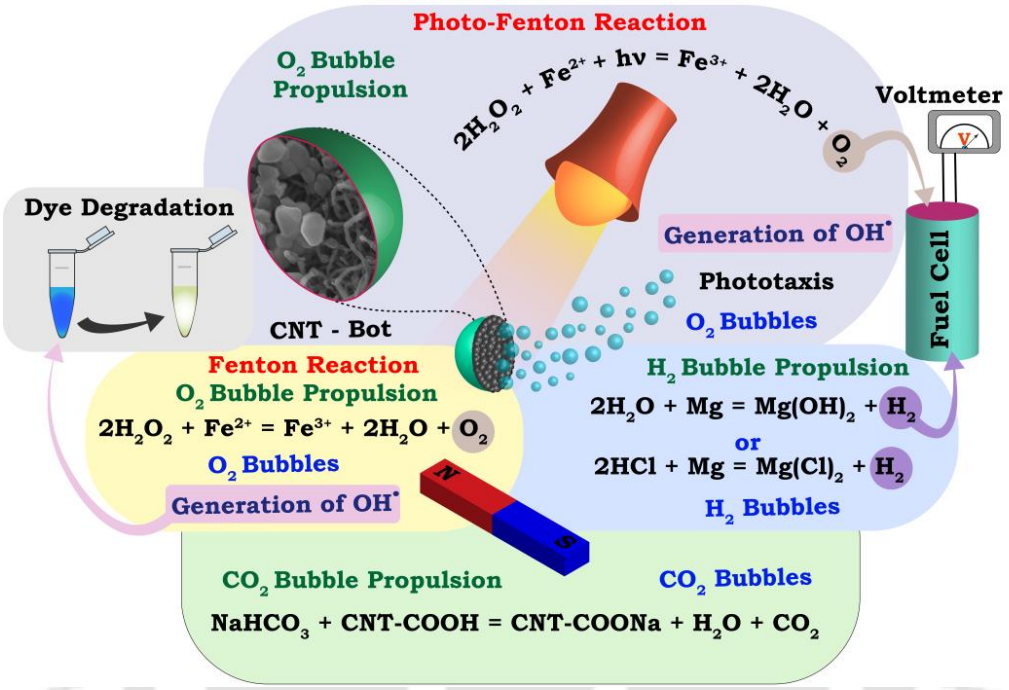

Figure 5.1: Schematically shows a CNT-bot composed of a –COOH functionalized MWCNT cluster doped with a ferrous (Fe^{2+}) salt and magnetite nanoparticle (FeONPs) before coated with a Mg film. The CNT-bot was capable of undergoing two reactions in acidic and alkaline water (e.g. $Mg + H_2O \rightarrow Mg(OH)_2 + H_2$, $Mg + HCl \rightarrow Mg(Cl)_2 + H_2$ and $NaHCO_3$ + MWCNT-COOH → MWCNT-COONa+ $H_2O + CO_2$) and Fenton reaction (in absence of light) and Photo Fenton reaction (in presence of UV light) in the peroxide fuel ($Fe^{+2} + H_2O_2 \rightarrow Fe^{+3} + H_2O + O_2$), as shown on the image. Subsequently, the motor moved by the ejection of hydrogen bubbles in acidic water, carbon-dioxide propulsion in the alkaline water, and oxygen bubbles in the peroxide fuel. The motors could show directionality in the motion under acid and alkali gradients leading to acid- and alkali-taxes, as shown on the images. The scheme also shows that hydrogen and oxygen serve as fuels of PEM Fuel cell and the CNT-bot can also perform dye degradation function.

In view of this background, we report the design and development of a 3G self-propeller, namely CNT-bot. **Figure 5.1** shows that, in a single embodiment, the 3G CNT-bot show multimodal directional propulsion in the form of alkali-, acid-, magneto-, and photo-taxes under chemical, magnetic or photonic stimuli inside multiple fluidic

mediums such as water, bi-carbonate, and hydrogen peroxide solutions. For this purpose, we initially dope the –COOH functionalized multiwall-CNT (MWCNT) with magnetite nanoparticles (FeONP) and ferrous (Fe^{2+}) salt to infuse catalytic and magnetic properties. The presence of FeONPs ensures that the motor can undergo magnetotaxis inside any fluidic medium in presence of a magnet while the presence of Fe^{2+} ensures the motor can undergo chemotaxis inside a peroxide medium through the ejection of O_2 bubbles. Following this, a thin layer of Mg was coated on the FeONP-Fe^{2+} doped CNT-bot to exploit the capacity of Mg to decompose acidic-water and stimulate an acid-taxis through the ejection of H_2 bubbles. Further, the presence of –COOH functionalization on the surface empowers the same CNT-bot to eject carbon-dioxide (CO_2) bubbles in the alkaline-water to stimulate alkali-taxis. Interestingly, the CNT-bot can also show directional acid- and alkali-taxes inside aqueous and peroxide mediums when a pH gradient is established. Further, doping of CNTs with TiO_2 nanoparticles (TiONPs) leads to the formation of photo-active CNT-bots, which show self-propulsion by Photo-Fenton reaction.

Importantly, the production of pure H_2 and O_2 gases from the acidic-water and alkaline-peroxide mediums can directly be fed to a PEM fuel cell for real time power generation. In such a scenario, the incessant self-propulsion of the CNT-bot facilitates the production and release of H_2 and O_2 gases owing to the generation of local turbulence. This helps in the generation ~150 mV in the PEM fuel cells using ~100 mg of CNT-bots. Further, the motor can also perform dye degradation through advanced oxidation owing to production of intermediate hydroxyl radicals from Fenton's reaction. Concisely, the reported phenomena are not only important from the fundamental point of view owing to the capacity of the carbon-based CNT-bots in showing an unprecedented quintuple handles locomotion in a single embodiment but they can also be translated as energy harvester, dye degrader, and pH sensor.

5.2. RESULTS AND DISCUSSION

5.2.1. CNT-bot Locomotion:

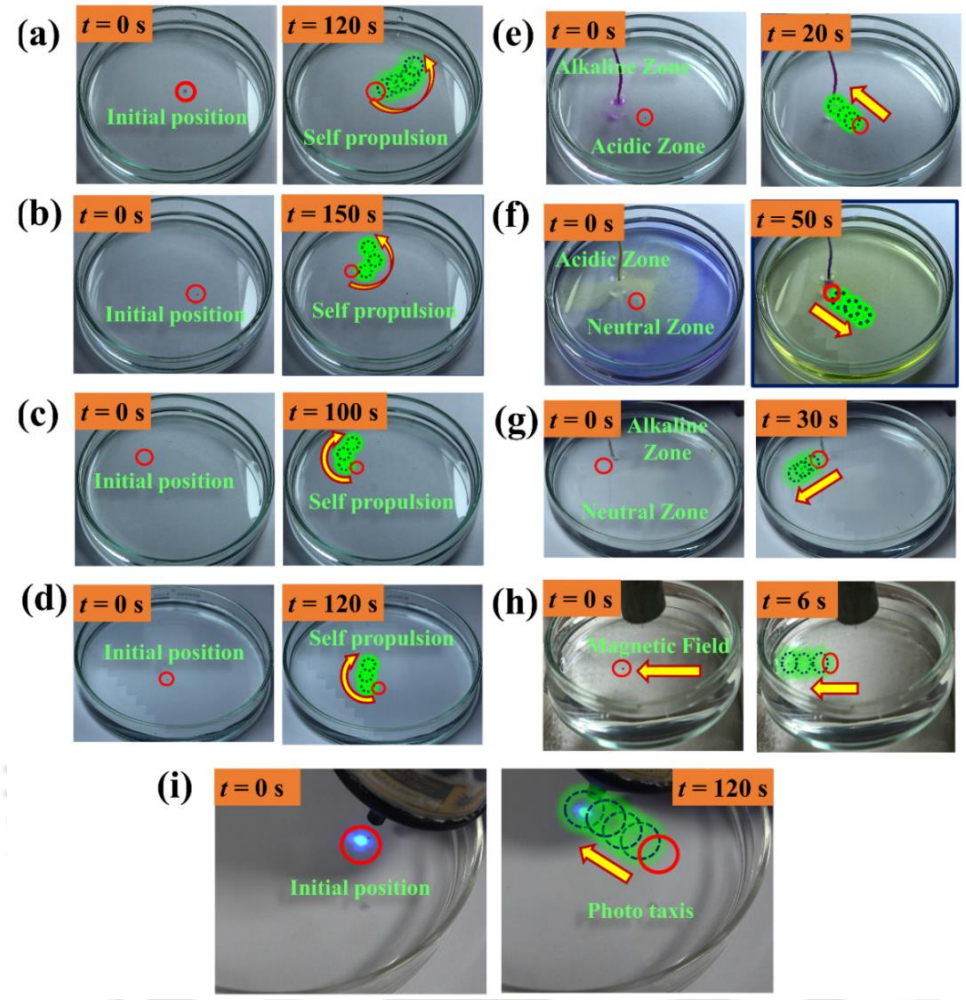

Figure 5.2: Shows the particle locomotion under varied conditions. Image sets (a) – (c) show the trajectory of the random motions of the CNT-bot at different time intervals (shown on the image) in a hydrogen peroxide bath (12%, v/v), water, and 0.5M hydrochloric acid bath, respectively. Image set (d) shows trajectory of the CNT-bot inside a 0.5M aqueous solution of sodium bicarbonate. Image sets (e) - (g) show the trajectory of the directional motion of the CNT-bot at different time intervals when a concentration gradient was established by dripping acid in a water bath, alkali in a peroxide bath, and bicarbonate dripping in a bath of water, respectively. The arrow heads in these images indicate the direction of the movement of the motor. The concentration gradient is indicated by the bromophenol blue, phenolphthalein, and indicators in the image sets (e) – (g), respectively. Image set (h) shows particle trajectory at different time intervals driven by an externally applied magnetic field. In these experiments, the motor size was of ~180 μm to ~300 μm.

The details of the characterizations of such a self-propeller have been discussed in the **sections 5.3**. The experiments uncovered that, in the same embodiment, the 3G

CNT-bot was capable of showing different types of motion in various fuels, such as hydrogen peroxide, acidic or normal water, and aqueous sodium bicarbonate solutions. In addition to these chemotactic behaviors, the motor could show magnetic propulsions owing to the presence of FeONPs in the matrix. In every fuel, the particle underwent a specific reaction, which led to the ejection of the gas bubbles causing the motion of the motor. For example, the CNT-bot was capable of undergoing two reactions in acidic (e.g. $Mg + HCl \rightarrow MgCl_2 + H_2$) or normal water (e.g. $Mg + H_2O \rightarrow Mg(OH)_2 + H_2$) while it could also undergo the following reaction in alkaline water, $NaHCO_3$ + MWCNT-COOH → MWCNT-COONa+ $H_2O + CO_2$. Further, the CNT-bot could also catalytically decompose peroxide fuel, $H_2O_2 + Fe^{+2} \rightarrow Fe^{+3} + H_2O + O_2$ owing to the presence of Fe^{2+}, more popularly known as Fenton's reaction.

In order to establish these facts, we have shown a detailed GC characterization of the gases generated during the course of movement in various fuels in the characterization part later on in **Section 5.3**. The chemotactic motions observed for the CNT-bot was largely due to the ejection of the H_2, O_2, and CO_2 gas-bubbles in acidic water, peroxide fuel, and alkaline water, respectively. A detailed study on the kinetics of the decomposition reactions the hydrogen peroxide, water, acidic water, and alkaline water in presence of the CNT-bots have been presented in the **Section 5.3**. The diverse propulsions achieved for the CNT-bots have been summarized in the **Fig. 5.2**. It may be noted here that in these experiments the particle size was kept in the range of ~180 μm to ~300 μm. Image set (a) shows the random trajectory of the particle moving at an average speed of ~400 μm/s in 12% (v/v) peroxide solution. Image set (b) shows the locus of a CNT-bot in a water bath where the speed was found to be little bit sluggish ~20 μm/s, as compared to the hydrogen peroxide solution. However, in 0.5M HCl solution speed was enhanced by three times to ~ 60 μm/s, as shown in the image set (c). Further, the image set (d) shows the random motion of the CNT-bot in a sodium bicarbonate bath where the speed was found to be ~20 μm/s.

Importantly, the motions shown in the images (a) – (d) were rather random, which could be made directional with the help of establishing a concentration gradient inside the bath, as indicated by the arrows in the image sets (e) – (g). Thus, we dripped aqueous solutions of 1M HCl, 1M NaOH, and 0.5 M $NaHCO_3$ with the help of cotton threads at the center of the petri dish, which established the necessary concentration gradient. The images show the presence of the concentration gradient with the help of the indicators.

The image set (e) shows the trajectory of the directional motion of the CNT-bot when an external concentration gradient was established by dripping acid in a water bath, indicated by the bromophenol blue indicator. Image set (f) shows the trajectory of the directional motion of the CNT-bot when an external concentration gradient was established by dripping alkali in a peroxide bath, which was indicated by the phenolphthalein indicator. Further, the image set (g) shows a directional transport under a $NaHCO_3$ drip.

It is well known that alkali acts as a homogeneous catalyst for the decomposition of H_2O_2. Thus, the dripping of the alkali at the center of the peroxide bath created a peroxide lean zone near the thread as compared to a peroxide rich zone at locations away from the thread. This was indicated by the color gradient of the phenolphthalein. In such a scenario, the depletion of the peroxide on the surface of the CNT-bot was also non-uniform. For example, the surface of the CNT-bot, which was closer to the thread, depleted less peroxide than the surface away from the thread. Subsequently, the difference in the decomposition of peroxide across the surface of the CNT-bot led to the directional transport, as shown in the image set (e). A similar experiment was performed in the water bath when 1M HCl was dripped from thread establishing a pH indicated by the yellow coloration of the bromophenol blue indicator, as shown in the image set (f). In this situation, a lower (higher) pH in the side near (far from) the thread of the CNT-bot could decompose more (less) water into H_2. Subsequently, a larger bubble propulsion on the thread side of the motor led to its movement away from the thread, as indicated by the arrow in the image set (f). Similarly, when dripping of $NaHCO_3$ established an alkali rich zone near the thread as indicated by the phenolphthalein indicator in the image set (g). In this case, a higher (lower) pH in the side near (far from) the thread of the CNT-bot could decompose more (less) $NaHCO_3$ into CO_2. Subsequently, a larger bubble propulsion on the thread side of the motor led to its movement away from the thread, as indicated by the arrow in the image set (g).

The image set (h) shows the magnetic propulsion, which was possible to generate in any of the aforementioned setups. In the case reported, the speed of the CNT-bot was found to be ~2.0 mm/s when the magnetic field was ~155 G. Apart from the remotely guided magnetic propulsion, the photo active CNT-bot loaded with TiONPs could also show propulsion under the remote guidance of the UV light, as shown in the image set

(i). Concisely, the **Fig. 5.2** shows the diverse propulsive behaviors of the CNT-bot synthesized in a single embodiment.

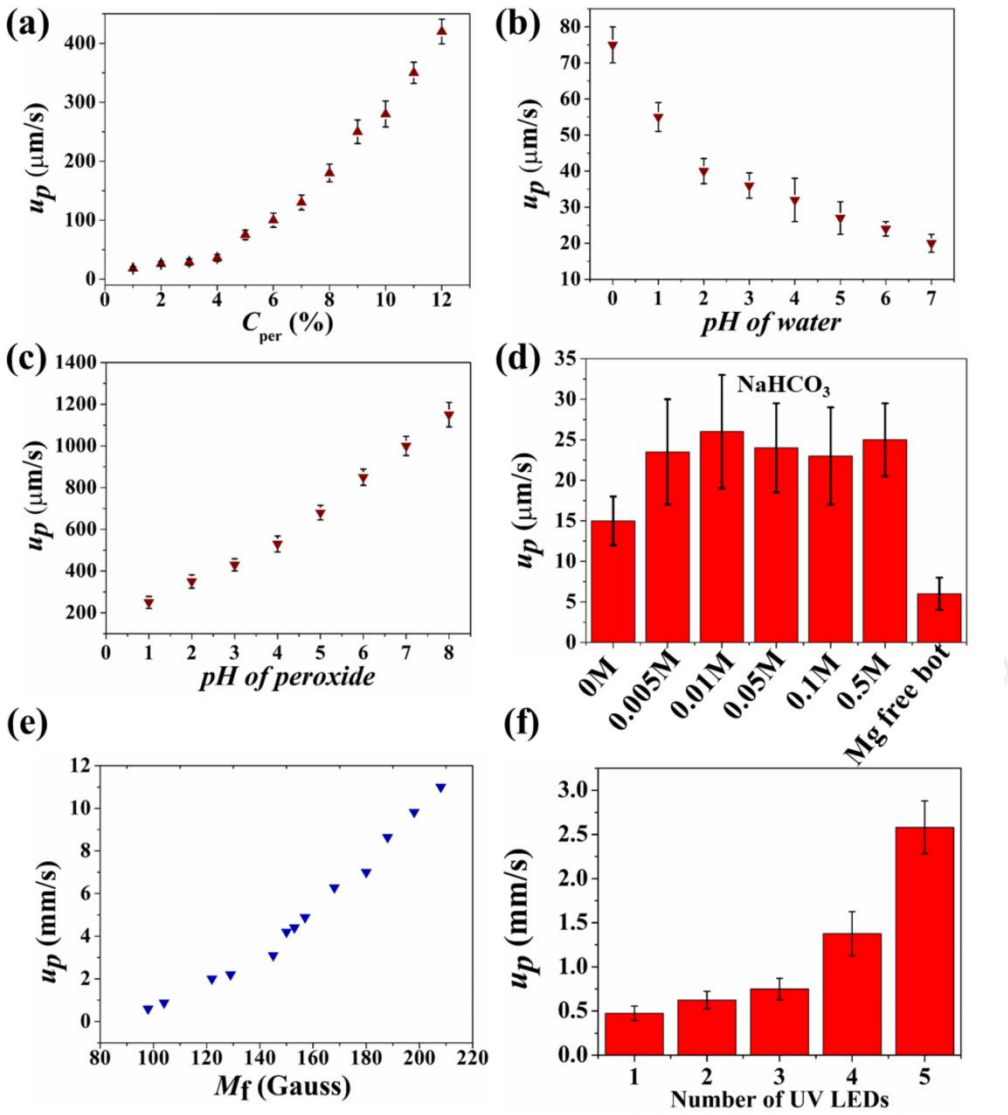

Figure 5.3: Shows the speeds of CNT-bots of size range ~180 to 300 μm under different conditions. Plot (a) shows the variation in the speed of the CNT-bot (u_P) in the aqueous peroxide bath for which the concentration of peroxide (C_{Per}) was increased from 1% (v/v) to 12% (v/v). Plot (b) shows the variation in u_P in a 5% (v/v) peroxide bath when the pH of the bath was varied. Plot (c) shows the variation in u_P when the pH of the water bath was varied. Plot (d) shows the variation in u_P of at different $NaHCO_3$ loading, in pure water, and for a Mg free swimmer. Plot (e) shows variation in u_P with different applied magnetic field strength (H) for a particle of size 220 μm. Plot (f) shows variation in u_P with the intensity of UV LEDs for photo-active CNT-bots.

A parametric study on the speed of the particles under different stimuli has been summarized in the **Fig. 5.3**. The plot (a) shows speeds of the CNT-bots (u_P) in the aqueous peroxide bath of size range ~180 to 300 μm. The plot suggests that u_P

progressively increased from ~60 µm/s to 400 µm/s with an increase of concentration of peroxide (C_{Per}). The plot (b) shows that for a given bath of 5% (v/v) peroxide loading, u_P could increase from ~100 µm/s to ~1100 µm/s when the pH of the bath was increased from 1 to 8. Apart from the peroxide bath we also performed a sensitivity test of u_P in the water bath.

Plot (c) of **Fig. 5.3** shows that u_P shot up from ~20 µm/s to 80 µm/s in a water bath when the pH was reduced from 7 to 0. Interestingly, u_P was found to be higher in bicarbonate solution compared to the speed in normal water. A few previous studies have reported that bicarbonate could remove oxide layers from the top of Mg layer, which may be the reason for this enhancement.[359] In order to find out the probable mechanism for this phenomenon we varied the bicarbonate loading in water. Plot (d) of **Fig. 5.3** shows that the particle speed enhanced almost 1.5 times in the bicarbonate solution as compared to normal water. However, the concentration of bicarbonate had hardly any effect on the particle speed. It may be noted here that the Mg free CNT-bot reported in this plot is the one with Fe^{2+} doped MWCNT in which we did not add any magnesium coating for the H_2 bubble propulsion. This CNT-bot showed u_P ranging between 3 to 6 µm/s, which originated due to the CO_2 bubble propulsion.

Addition of FeONPs in the CNT-bot provided the magnetic handle for the propulsion. Plot (e) of **Fig. 5.3** shows the increase in u_P to as high as ~12 mm/s with the increase in the magnetic field strength (H) for a particle of size ~220 µm. In these experiments, initially, the CNT-bot was placed inside the petri dish between two poles of an electromagnet before the magnetic field was applied. The field strength was evaluated by a built-in Gauss meter while the speed was evaluated from the image analysis of the video recorded. The magnetic and hysteresis properties of the CNT-bot were also studied with the help of the Variable Scanning Magnetometry (VSM), which is summarized in the **Section 5.3**. The photo-active CNT-bots showed a progressive increment in the particle speed with the increase of UV light intensity. An experiment was performed with varying light intensity, as shown in the plot (f) of **Fig. 5.3**. The detailed characterizations of the photo-active CNT-bot have been summarized in the **Section 5.3.** Interestingly, the particle speed went as high as ~ 2.5 mm/s in the presence of UV light source. The lifetime of the CNT-bots is another important aspect to be discussed. In peroxide medium, the CNT-bots could swim ~ 180 s without slowing down whereas the same motor could swim as long as ~500 s in 0.1M HCl with the

reported speed. In water medium, the same CNT-bots showed motion up to ~ 1000 s before it stopped.

5.2.2. Fuel Cell Application:

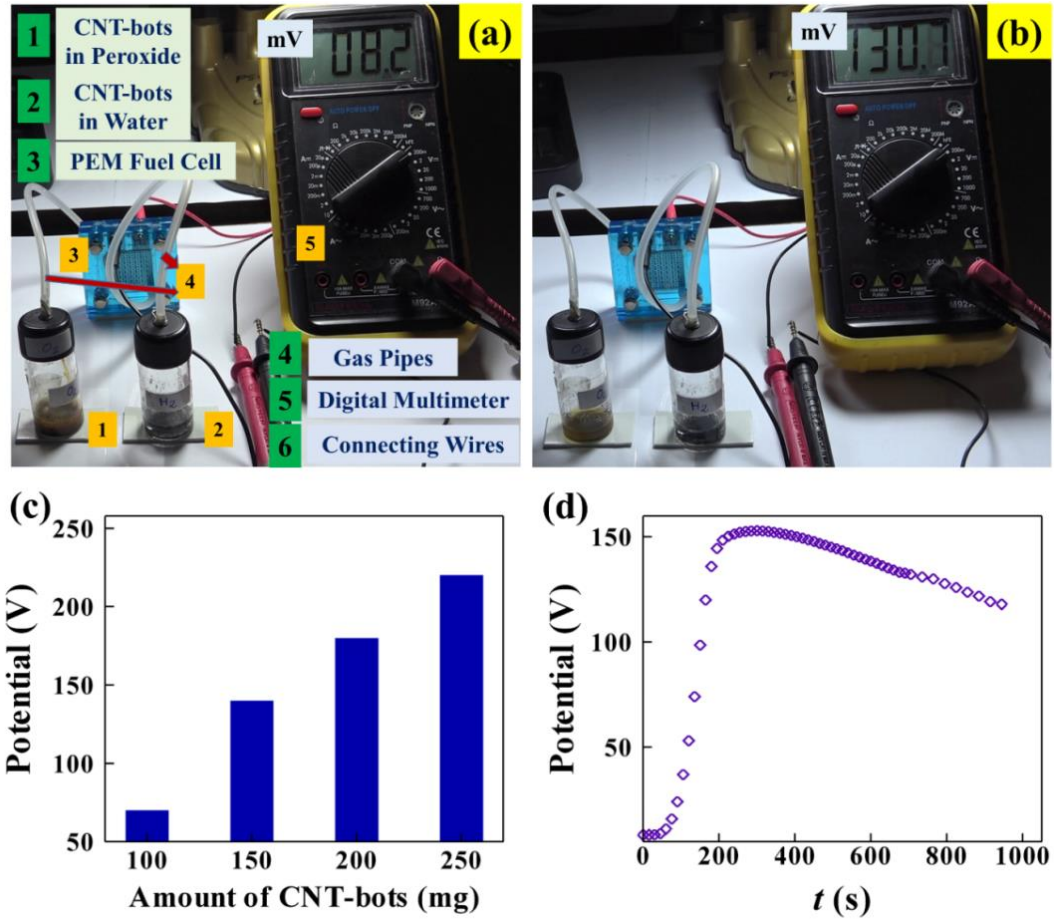

Figure 5.4: Image (a) shows PEM fuel cell set up for electricity generation using the CNT-bots. The containers 1 (filled with CNT-bots and peroxide) and 2 (filled with acidic water and CNT-bots) generated pure O_2 and H_2 gases in real time, which were supplied to the fuel cell (3) through gas tubing (4), as shown. The current generated was measured by a digital multimeter (5). Images (a) and (b) show progressive increase in the potential with time. Image (c) shows the potential developed against amount of CNT-bots fed in the fuels and image (d) shows transient potential output across PEM fuel cell.

The oxygen gas generated due to the Fenton reaction between the CNT-bots and hydrogen peroxide and the hydrogen gas during the reaction between CNT-bots and acidic water medium opened up the opportunity of using them in the fuel cells to produce real time electrical energy. **Figure 5.4** shows the setup having a PEM fuel cell in which the electricity was generated with the help of the CNT-bots. In the container 1, 10% (v/v) peroxide fuel was filled with 50 mg of CNT-bots to generate O_2 gas while

the container 2 was filled with 0.1M aqueous HCl along with 50 mg of CNT-bots to produce H_2 gas. The gases thus generated were fed to the PEM fuel cell (3) through the gas tubing (4) as shown in **Fig. 5.4**. The current generated was measured by a digital multimeter (5). The images show a progressive increase in the electric field potential with time to arrive at a value as high as ~150 mV. The incessant movement of the CNT-bots in the container facilitated the mixing and de-gassing of the liquids, which helped in generating more voltage with time.

The details of the electrochemical characterization of the CNT-bots through a cyclic voltammetry (CV) study have been summarized in the **Section 5.3,** which clearly showed ~ 1.5-fold increase of current when the working electrodes were decorated with the CNT-bots. **Figure 5.4(c)** shows a significant increase in the electric field potential across the PEM fuel cell with the increase in the amount of motor fed in the reservoirs containing hydrogen peroxide and acidic water as fuels. The experiments uncover that when ~100 mg of CNT-bots were fed in each of the reservoirs, containing ~ 10% hydrogen peroxide, and 0.1M HCl, a potential output of ~150 mV was generated. In these experiments, the thickness of magnesium layer on the CNT-bots was ~1 µm and the average size of the bots was ~180 to 300 µm. Roughly, the magnesium content of the motor was ~ 1% to 2%. Thus, with the increase in the amount of CNT-bots, the increment in the production of pure hydrogen and oxygen led to the eventual increase in the potential. However, for a given loading of CNT-bots in the reservoirs, the electric field potential across the fuel cell varied with time, as shown in the **Fig. 5.4(d)**. The plot shows that the potential reached a maximum in short time of ~200 s before started reducing at a much slower rate.

5.2.3. Dye Degradation Application:

The CNT-bots were also capable of producing hydroxyl radicals by Fenton's reaction during the course of their motion, which could also be used for dye degradation and waste water treatment. In order to prove this point, initially in a petri plate, 6 ml of ~50% hydrogen peroxide was mixed with 30 ml of 0.1 mM methylene blue (MB) solution before adding a 20 mg of CNT-bots. The experiments initially uncovered self-propulsion of the CNT-bots before blue color of the solution progressively became colorless to the advanced oxidation reaction by the hydroxyl radicals. **Figure 5.5 (b)** also shows the color of methylene blue dye before and after degradation.

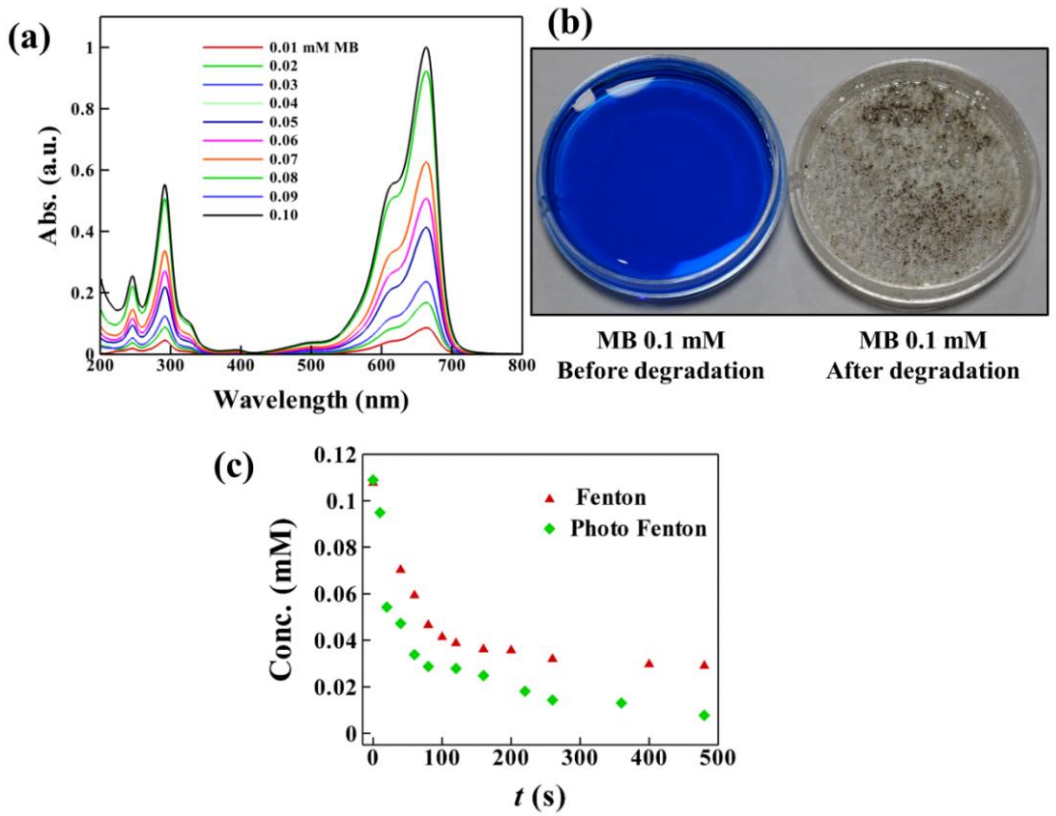

Figure 5.5: Plot (a) shows the UV-Vis absorption of methylene blue solutions of different known concentrations, from 0.01 mM to 0.10 mM. Image (b) shows color of 0.1 mM methylene blue solution before and after degradation using CNT-bot. Image (c) shows the decay of methylene blue solution in peroxide fuel in the presence of CNT-bots (red triangular symbols), and Photo-active CNT-bots (traffic green diamond symbols).

In order to study the dye degradation kinetics, initially, a set of known amounts of MB solutions were prepared in the range of 0.01 mM to 0.1 mM before obtaining the UV-Vis spectra at 675 nm for them, as shown in Figure 5(a). Figure 5 (b) shows the color of methylene blue dye before and the same petri plate after degradation by CNT-bots. Following this, the decay kinetics of 30 ml of 0.1 mM of MB in 50% H2O2 and 20 nm of CNT-bots were studied. For this purpose, a known amount of sample was collected from this bath after every 20 s for a time span of 500 s. The moment CNT-bots were poured into the bath was considered to be 0 s after with the UV-Vis spectra of the pipetted out samples were taken. Figure 5(c) shows the decay of MB solution in peroxide fuel in the presence of CNT-bots (red triangular symbols), and photo-active CNT-bots (traffic green diamond symbols). The photo-active CNT-bots showed a faster degradation because of the possibility of additional Photo-Fenton reaction, which had higher rate kinetics than the ordinary Fenton reaction.

5.3. EXPERIMENTAL SECTION

5.3.1. Materials and methods:

5.3.1.1. Materials:

Carboxylic group substituted multiwall carbon nanotubes (MWCNT, purity 98%, diameter = 6 - 13 nm, length = 2.5 - 20 μm), magnetite nanoparticles (size 50 to 100 nm), ferrous sulphate, magnesium ribbon, hydrogen peroxide (50% v/v), sodium bicarbonate, hydrochloric acid (33% v/v), sodium hydroxide, phenolphthalein, bromothymol blue, potassium iodide, sulphuric acid, and sodium fluoride, were procured from Sigma Aldrich, India. The chemicals were of analytical grade and were used without further purification. Millipore water (resistivity 18.2 MΩ cm and TOC< 5 ppb) was employed to prepare the solutions and wash the products synthesized.

5.3.1.2. Methods:

About 2 mg of carboxylic group (-COOH) substituted MWCNTs and 2 mg of magnetite nanoparticles (FeONPs) were mixed with 1 ml 0.05M ferrous sulphate ($FeSO_4$) solution before it was sonicated for 30 min to make a colloidal suspension. The resulting suspension was dispensed on a glass slide with the help of micropipette before the slide was gently warmed to evaporate water from the suspension. In the process, MWCNTs were doped by FeONP/Fe^{2+} wherein the experimental conditions ensured that the interactions between the FeONP/Fe^{2+} and MWCNT were largely physical. Following this, the glass substrate coated with islands of FeONP/Fe^{2+} doped MWCNTs was coated with magnesium using a thermal evaporator (Make: HHV, India, Model: Lab Coater Auto 500). The deposition was performed for five times to coat a thin layer (~750 nm) of Mg on one side of the FeONP/Fe^{2+} doped MWCNTs. Each time the thermal evaporator deposited ~150 nm thick Mg layer, which eventually led to the thickness of ~750 nm after five stages of coating. The thickness of the film was measured using quartz crystal thickness monitor integrated with the thermal evaporator. The resulting 3G CNT-bots were preserved in an air tight vacuum desiccator. During the experiments, the CNT-bots were lifted by scraping the glass slide surfaces with the help of a sharp needle. Subsequently, the freshly prepared motors were employed to perform the experiments reported in the present study.

For the photo-active CNT-bots, initially, 15 mg CNT and 30 mg TiO_2 were sonicated in 2.5 ml of ~0.05M $FeSO_4$. The sonicated material was then dried at ~60^o C on a pre-cleaned glass slide. After that, Mg was deposited on top of this material using a thermal evaporator. Each deposition in thermal evaporator makes a thickness of around ~200 nm and hence the total thickness of the deposited magnesium layer became ~ 1 µm after 5 repetitions. This deposited material was scrapped out with the help of a sharp needle before using them as microswimmers.

The instruments used to carry out different fabrication and characterization studies are, thermal evaporator (Make: HHV, India, Model: Lab Coater Auto 500), video recorder (Make: Sony, Model: FDR AX40), gas chromatograph (Make: Agilent Model: 7890A & Make: Thermo Fisher Scientific Trace Model: 1110), PEM fuel cell (Vendor: Fuel Cell Store, Product Code: 632000), field-emission scanning electron microscopy (FESEM, Make: JEOL Model: JSM-7610F), energy dispersive x-ray spectroscopy (EDXS, Make: GEMINI 300), XRD (JCPDS 06-0696), Raman spectroscopy (Make: JEOL Moldel: CPX100), vibrating sample magnetometry (VSM, Make: JEOL Model: JES-FA200), UV-Vis spectrophotometer (Make: PerkinElmer Model: Lambda 35), electromagnet (Make: SES Instruments Model: DPS 50), Gauss meter (Make: SES Instruments Model: DGM 102), pH meter (Make: HANNA Model: EDGE pH), Potentiostat (Make: GAMRY, Model: Reference 6000+) and digital multimeter (Make: MASTECH Model: M92A (H)).

Figure 5.6 shows the detailed steps for the fabrication of the CNT-bots. Initially, in the step 1, 15 mg of MWCNT-COOH was mixed with 15 mg of Fe_3O_4 nanoparticles (FeONPs) and/or 30 mg of TiO_2 nanoparticles (TiONPs) before pouring them into ~ 2.5 ml of 0.5M aqueous $FeSO_4$ solution. The solution was then sonicated for around 45 min to disperse the nanoparticles in the CNT matrix. Following this, the sonicated material was spread on a cleaned glass slide before drying at ~60^{o}C for 2 h. Thereafter, the resulting materials on the glass slide were coated with Mg using a thermal evaporator to deposit Magnesium film on the exposed side of the CNT-bots. This procedure imparted ‘Janus’ nature to the CNT-bots fabricated.

5.3.1.3. Synthesis of CNT-bots:

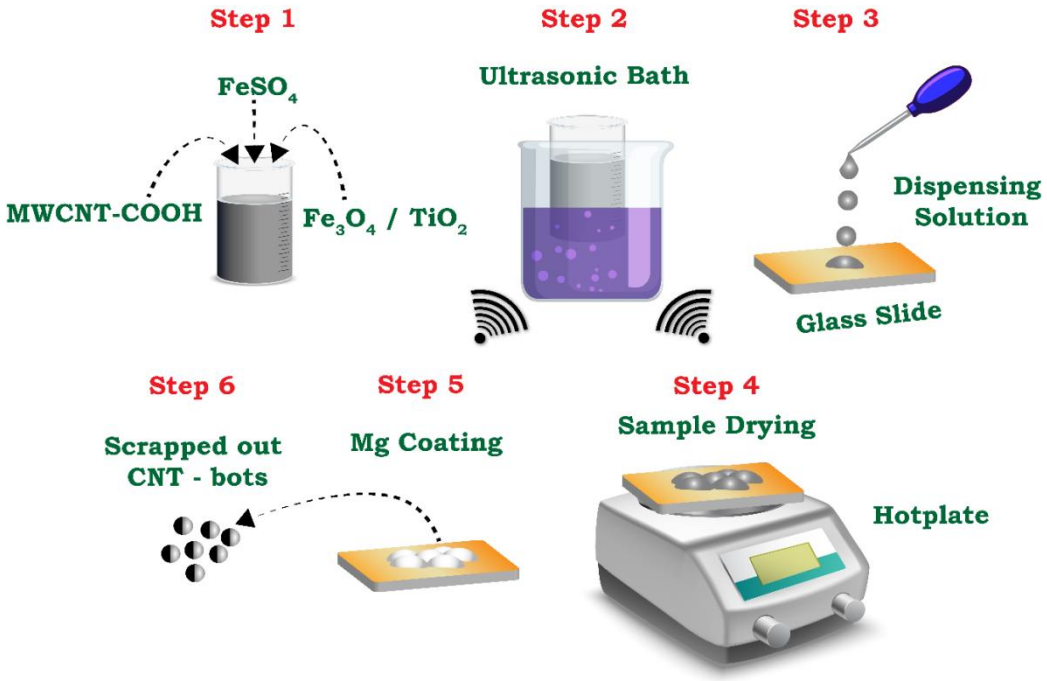

Figure 5.6: Schematically shows different steps of CNT-bot fabrication.

Thereafter, the thin layer was broken into tiny particles with the help of a sharp scraper and stored for the use of CNT-bots. The presence of FeONPs ensured that the motor could undergo magnetotaxis inside any fluidic medium in presence of a magnet while the presence of Fe^{2+} ensured the motor could undergo chemotaxis inside a peroxide medium through the ejection of O_2 bubbles. The coating of Mg facilitated decomposition of acidic-water and stimulated an acid-taxis through the ejection of H_2 bubbles. Further, the presence of –COOH functionalization on the surface empowers the same CNT-bot to eject carbon-dioxide (CO_2) bubbles in the alkaline-water to stimulate alkali-taxis. Interestingly, the CNT-bot could also show directional acid- and alkali-taxes inside aqueous and peroxide mediums when a pH gradient was established. Further, doping of CNTs with TiONPs enabled phototaxy of the CNT-bots through Photo-Fenton reaction.

5.3.2. Characterization:

5.3.2.1. FESEM and Raman Spectroscopy of MWCNT-COOH and Fe^{+2} doped MWCNT-COOH

The doped ferrous ions on the CNT-bot was the major reason behind the motion of the particles inside hydrogen peroxide. In order to confirm the doping, we did Raman

spectroscopy and FESEM characterizations to follow the difference before and after the doping. The images (a) and (c) in the **Fig. 5.7** shows the Raman spectroscopy and FESEM of pristine –COOH functionalized MWCNT. The images (b) and (d) show the Raman spectroscopy and FESEM of Fe^{2+} doped –COOH substituted MWCNTs. The Raman plots show the D (1332 cm^{-1}) and G (1594 cm^{-1}) bands, which were attributed to disorder in sp^2 carbons and sp^2 vibration of carbon atoms. The plots uncover that the ratio of I_D/I_G of Raman spectra increased from 1.290 to 1.401 due to the doping of the MWCNT, which could be because of the loading of the Fe^{2+} ions on the MWCNT matrix. This observation was further verified by the FESEM **Figs. 5.7(c)** and **5.7(d)**, before and after doping of MWCNT matrix. Image (d) clearly shows the presence of the nanocrystals of ferrous sulphate on the MWCNTs. The spot EDXS plots of FESEM shown in the latter part of **Section 5.3** also confirmed the presence of –COOH functionalized MWCNT and their doping with magnetite and ferrous sulphate in the CNT-bot.

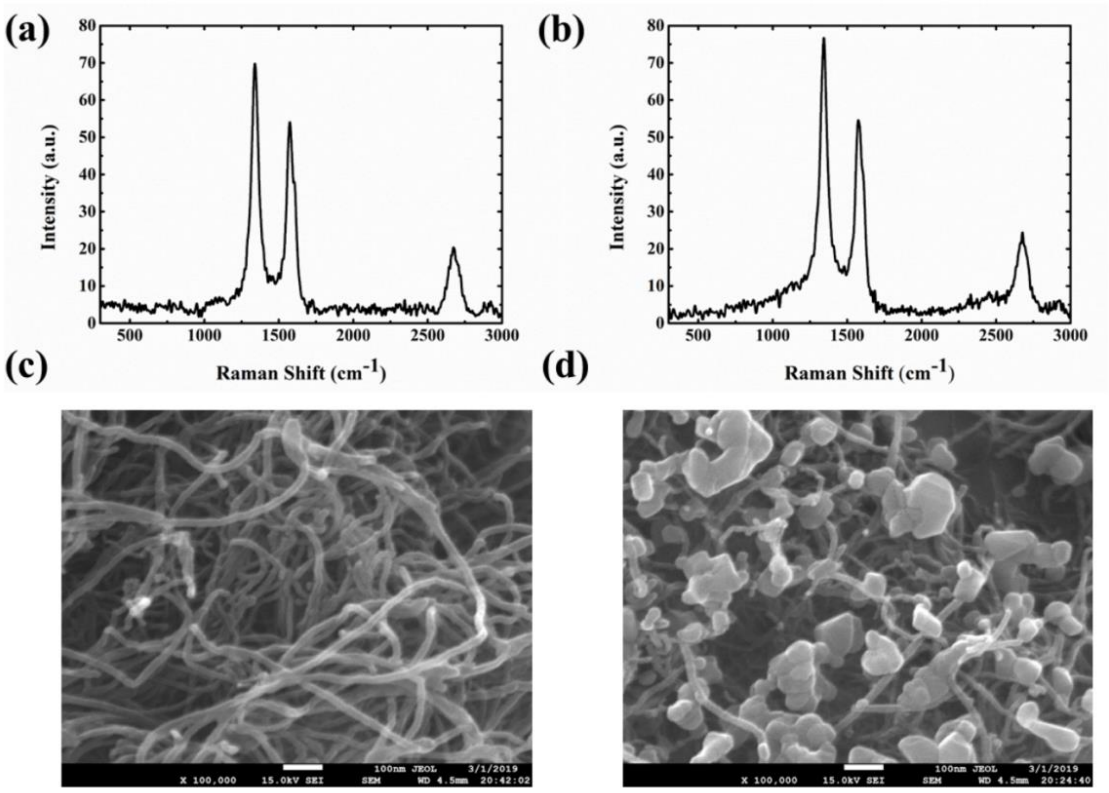

Figure 5.7: Images (a) and (c) show the Raman spectroscopy and FESEM images of pristine –COOH substituted MWCNT. The images (b) and (d) show the same of Fe^{2+} doped –COOH substituted MWCNTs.

5.3.2.2. FESEM images at different stages of synthesis:

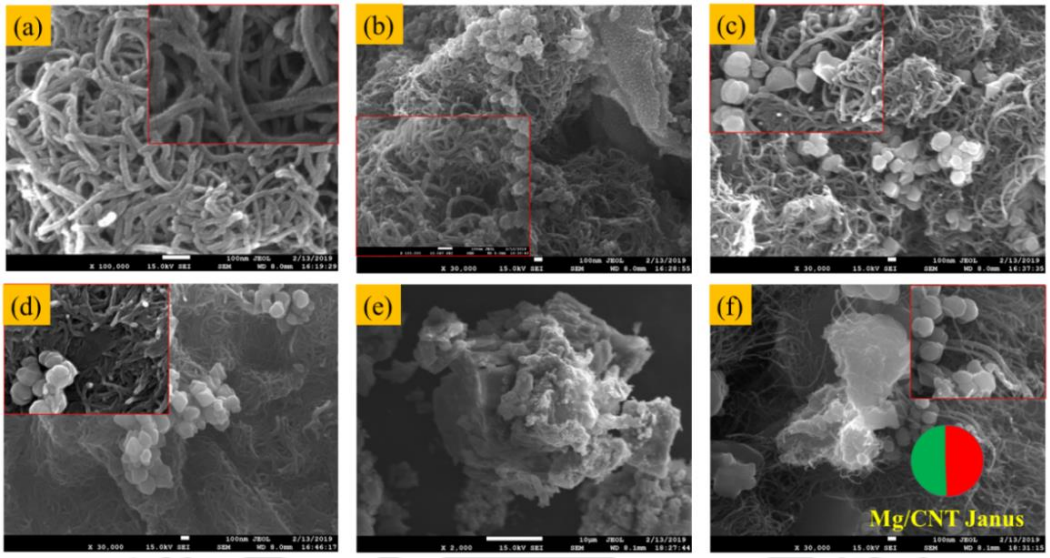

Figure 5.8: Shows the FESEM images of CNT-bot at different stages. Image (a) shows the pristine –COOH functionalized MWCNT at 100 k magnification with the inset showing the same at a higher magnification. Image (b) shows the Fe^{2+} doped MWCNT at 30 k magnification with the inset showing the same at 10^5x. Image (c) shows the FeONP doped MWCNT at 30 k magnification with the inset showing the same at 10^5x. Image (d) shows the FeONP and Fe^{2+} doped MWCNT at 30 k magnification with the inset showing the same at 10^5x. Images (e) and (f) show, at lower magnification, the morphology of the Janus-CNT-bot in which one side was FeONP /Fe^{2+} doped MWCNT while the other side was magnesium coated FeONP /Fe^{2+} doped MWCNTs.

Images (a) to (f) in the **Fig. 5.8** show the FESEM images of the CNT-bot at the different stages of synthesis. Image (a) shows the pristine –COOH functionalized MWCNT, image (b) shows the Fe^{2+} doped MWCNT, image (c) shows the FeONP doped MWCNT, and image (d) shows the composite FeONP-Fe^{2+} doped MWCNT. Images (b) and (c) suggest that ferrous sulphate and magnetite were able to individually penetrate into the MWCNTs matrix (image (a)) due to the electrostatic interactions. Similarly, image (d) shows the morphology of the composite of FeONP-Fe^{2+} doped MWCNTs. The images (e) and (f) show the surface morphology of the CNT-bot, which suggest the morphology of motor somewhat resembled the previously reported Janus motors, as schematically shown on the image In this case, one side of the Janus CNT bot could be imagined as the FeONP-Fe^{2+} doped MWCNT 'red' part while the other 'green' side was magnesium coated FeONP-Fe^{2+} doped MWCNTs, as schematically depicted on the image. It may be noted here the brightest portions in the images were magnesium while the portions having higher contrast was MWCNT composites.

5.3.2.3. Gas Chromatography:

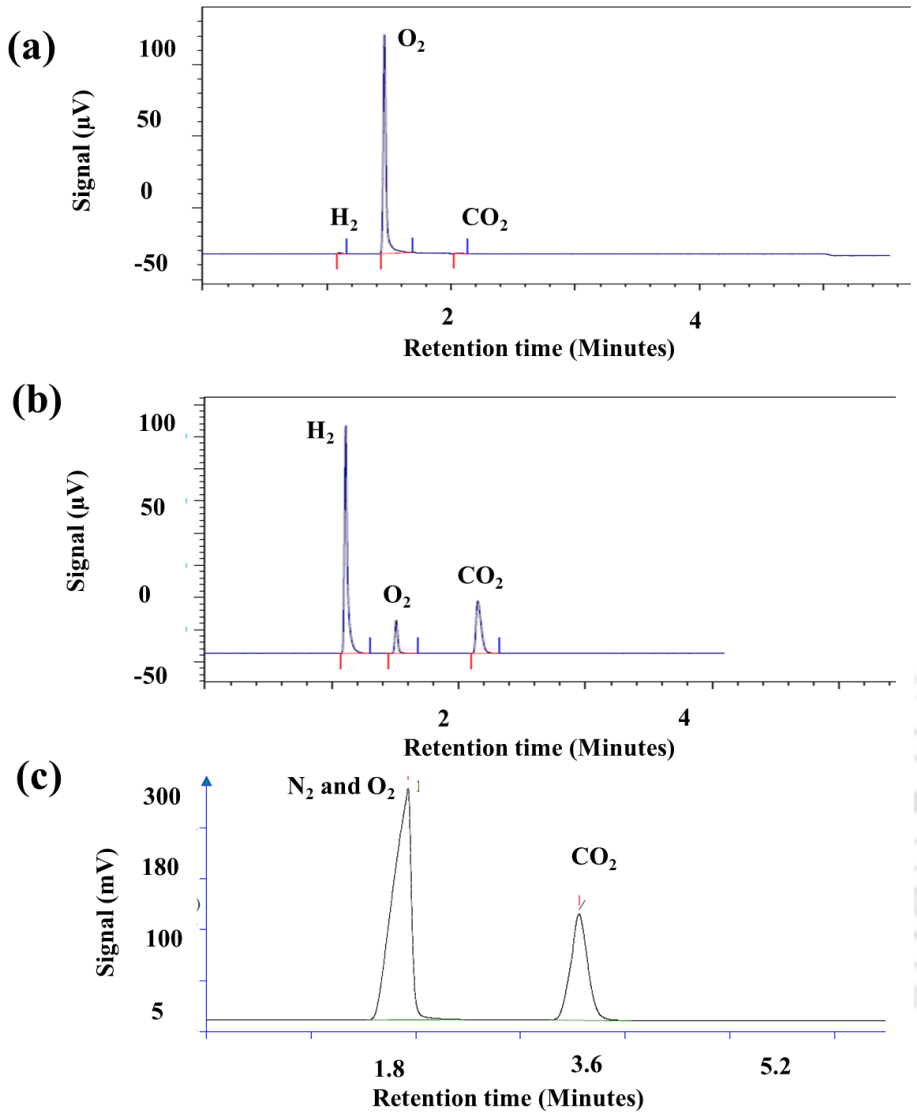

Figure 5.9: Plots (a) – (c) show the gas-chromatographs (GC) of the gases issued out when the CNT-bot reacted with 5% aqueous hydrogen peroxide, 0.05M aqueous HCl, and 0.5M aqueous sodium bicarbonate, respectively.

The gas chromatography (GC) characterization was done to confirm the gases issued out during the bubble propulsion of the CNT-bots. **Figures 5.8(a) – 5.8(c)** show the GC of the gases issued out when the CNT-bot reacted with 5% aqueous hydrogen peroxide, 0.05M aqueous HCl, and 0.5M aqueous sodium bicarbonate, respectively. For these experiments, in three separate stoppered culture tubes, we initially mixed 5 ml of respective fuels and 5 mg of the CNT-bots before the culture tubes were sealed. Following this, the gas accumulated at the empty space of the tube was withdrawn with the help of a GC syringe before injecting the same into the GC column. In the plot

5.8(a), the most intense peak was obtained for the oxygen gas, which was generated due to the Fenton reaction of CNT-bot with peroxide fuel. The presence of a little amount of hydrogen is also indicated in the same plot. This is because, as the hydrogen peroxide decomposed into water, the magnesium coating of the CNT-bot reacted with water to produce hydrogen.

The peak of nitrogen also appeared because we were unable to remove air from the culture tube. The **Fig. 5.9(b)** shows an intense peak of hydrogen when CNT-bots reacted with 0.05M HCl. In this case, the magnesium layer deposited on the CNT-bot reacted with acidic water to produce hydrogen. The plot 5.9(c) shows the peaks of oxygen, nitrogen, and carbon dioxide in which the intensity was high for the carbon dioxide owing to the reaction of carboxylic proton of the -COOH functionalized CNT-bots with sodium bicarbonate.

5.3.2.4 Chemical Kinetics

5.3.2.4.1 Peroxide Decomposition by Fe^{+2} in CNT-bot

The study of the chemical kinetics of the reaction between ferrous ion and hydrogen peroxide was studied iodometrically and with the help of UV spectrophotometry. It is well known that hydrogen peroxide reacts with iodide to give iodine, which can take up excess iodide ions to form triiodide in water. Thus, at the initial stage, known concentrations of aqueous peroxide solutions ranging from 1% to 10% (v/v) were prepared. Following this, we added 1:4 sulphuric acid to each peroxide solution before a stoichiometric excess of potassium iodide was added into the solutions, to facilitate the reaction, $H_2O_2 + H_2SO_4 + 2KI \rightarrow K_2SO_4 + I_2 + 2H_2O$. Thus, addition of potassium iodide in the solution of hydrogen peroxide and potassium iodide liberated iodine. The iodine concentrations were observed to be higher for higher concentration of peroxide, as suggested by the stoichiometric equation. The samples were diluted with the same ratio as it was done for making the calibration curve, as shown with the help of **Figs. 5.10(a) and 5.10(b)**. **Figure 5.10(c)** shows the absorption vs. time plot for reaction between ferrous sulphate and hydrogen peroxide solution, which was obtained from the absorbance values at different time intervals and calibration curve, as shown in **Fig.5.10(d)**.

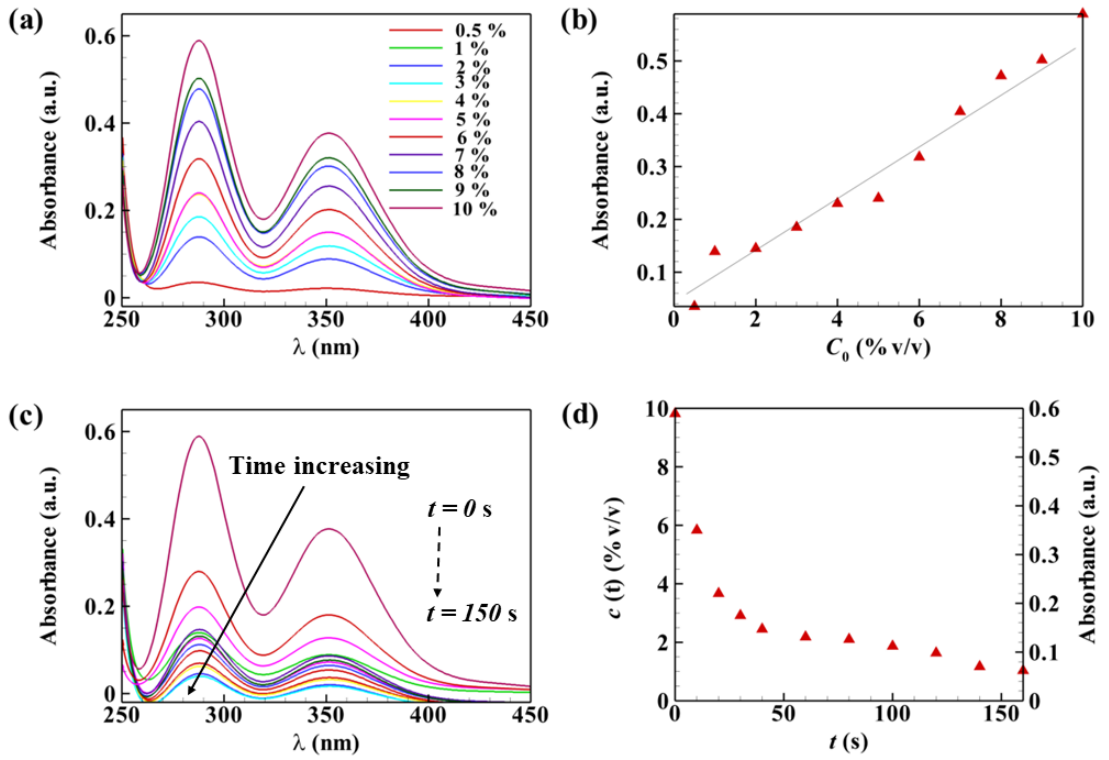

Figure 5.10: Image (a) shows the UV-Vis spectra of different known iodine solutions in the presence of excess iodide. Image (b) shows calibration curve, absorbance vs. peroxide concentration (C_0) for peroxide concentration ranging from 1% (v/v) to 10% (v/v) aqueous peroxide solutions. Plot (c) shows UV-Vis spectra of different iodine solutions generated at different time intervals of reaction. Plot (d) shows C_0 vs. time (t) plot for reaction between ferrous sulphate present in CNT bot and hydrogen peroxide solution.

5.3.2.4.2. Acidic Water Decomposition by Mg in CNT-bot:

The motion of the CNT-bots in water was due to bubble propulsion of hydrogen gas issuing out of the surface of the motor. In order to study the kinetics of this reaction, ~60 mg of CNT-bots was put in a bath of 0.01M HCl containing measured amount (50 ml) of HCl. The reaction started as soon as the CNT-bots were added and we took samples of 500 µl at every 60 s time interval. The concentration of the taken samples was measured by acid base titration method. Thus, an aliquot of 0.002M standard NaOH solution was prepared before the strength of the solution was measured against standard oxalic acid solution. All the samples withdrawn at different time intervals were diluted and titrated against standard 0.002M NaOH. From the titre values, the concentration of acid was calculated at different time intervals. **Figure 5.11** shows the variation of (C_{acid}) with time (t) due to the reaction, $Mg + 2HCl = MgCl_2 + H_2$.

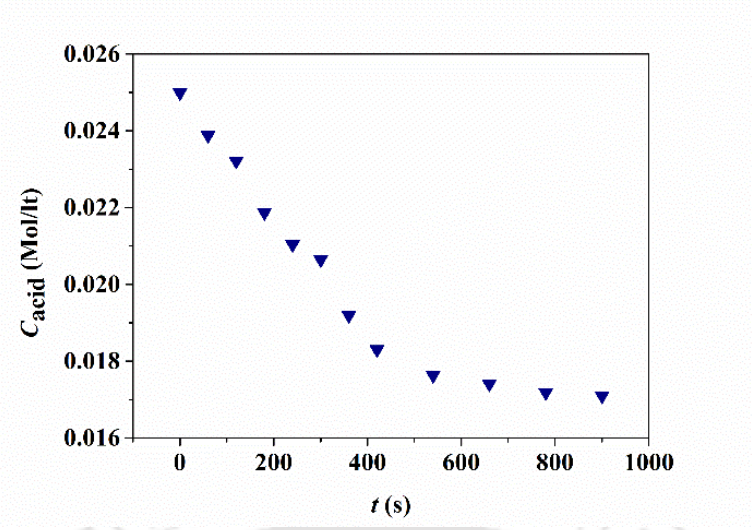

Figure 5.11: The plot shows the variation in the concentration of hydrochloric acid in water (C_{acid}) with time (t) during the reaction of aqueous acid solution with the CNT-bots.

5.3.2.5. Magnetic Hysteresis of CNT-bot:

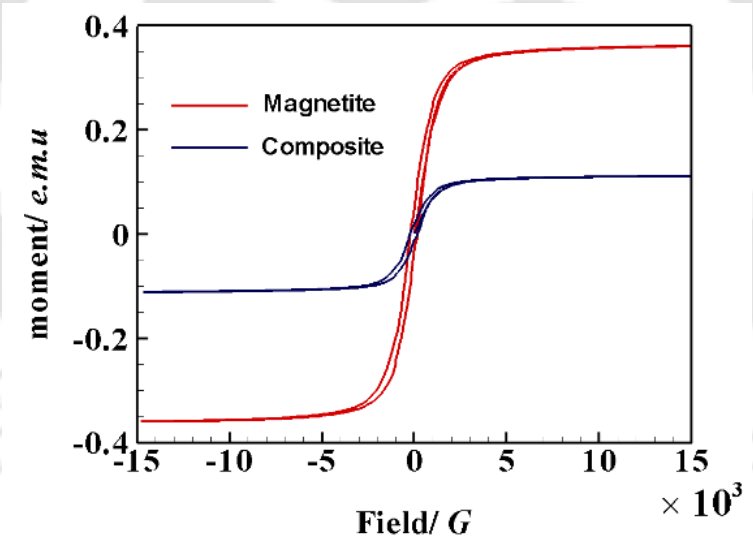

Figure 5.12: Shows magnetic hysteresis loops from vibrational scanning magnetometry (VSM) of pure magnetite (red line) and CNT-bots (blue line), respectively.

The ferromagnetic nature of the CNT-bots was characterized by vibrational scanning magnetometry (VSM). The CNT-bots were made magnetic by doping with magnetite nanoparticles with the MWCNTs in ~1:1 ratio. **Figure 5.12** shows the magnetic hysteresis loop of pure magnetite and CNT-bots. The minimum enclosed area of the loop indicates minimum magnetic loss and acceptable ferromagnetic nature of

magnetite and CNT-bot particles. The plots also indicate that the dipole moment of the CNT-bots was nearly half of the pure magnetite owing to the non-magnetic MWCNTs.

5.3.2.6. Raman Spectroscopy of photo active CNT-bot:

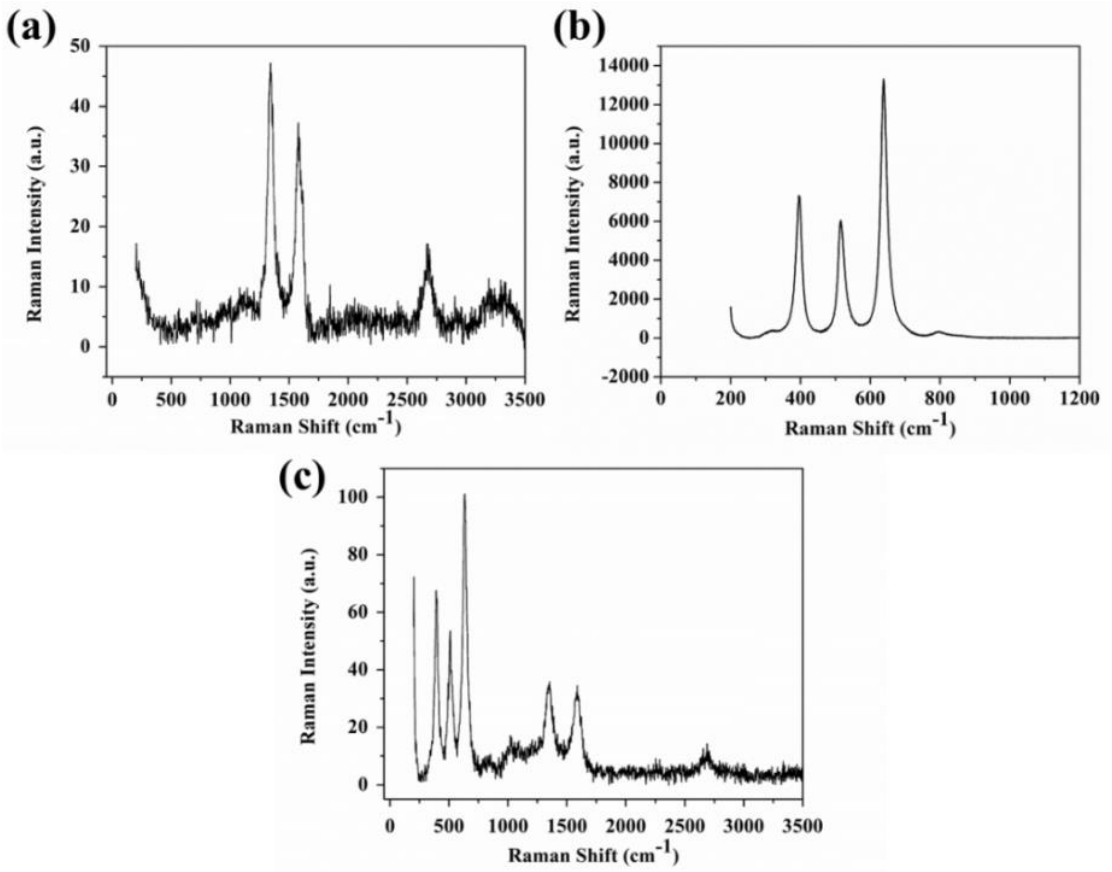

Figure 5.13: Plots (a) to (c) show Raman shifts of pristine MWCNT-COOH, TiONP, and the composite TiONP-$FeSO_4$ doped MWCNT-COOH.

Photo-active CNT-bots were prepared by doping TiONPs and ferrous sulphate in the template of MWCNT. **Figure 5.13** shows Raman spectra of TiO_2, MWCNT-COOH, and the composite material before magnesium deposition. **Figure 5.13(a)** shows the appearance of a prominent peak at 1323 cm^{-1} (D band), which is attributed to disorder in sp^2 carbons available on the surface of MWCNTs. The peak at 1584 cm^{-1} (G band) is corresponding to the sp^2 vibration of carbon atoms on the graphitic surface of MWCNT.[341, 371] Similarly, **Fig. 5.13(b)** show three distinct characteristic peaks of TiONPs at 380 cm^{-1}, 447 cm^{-1} and 612 cm^{-1} indicating rutile structure of TiO_2.[372] **Figure 5.13(c)** shows that, in the composite material all the peaks were present, which also indicate a homogeneous mixture of MWCNT and TiONPs.

5.3.2.7. FESEM of Photo-CNT-bots:

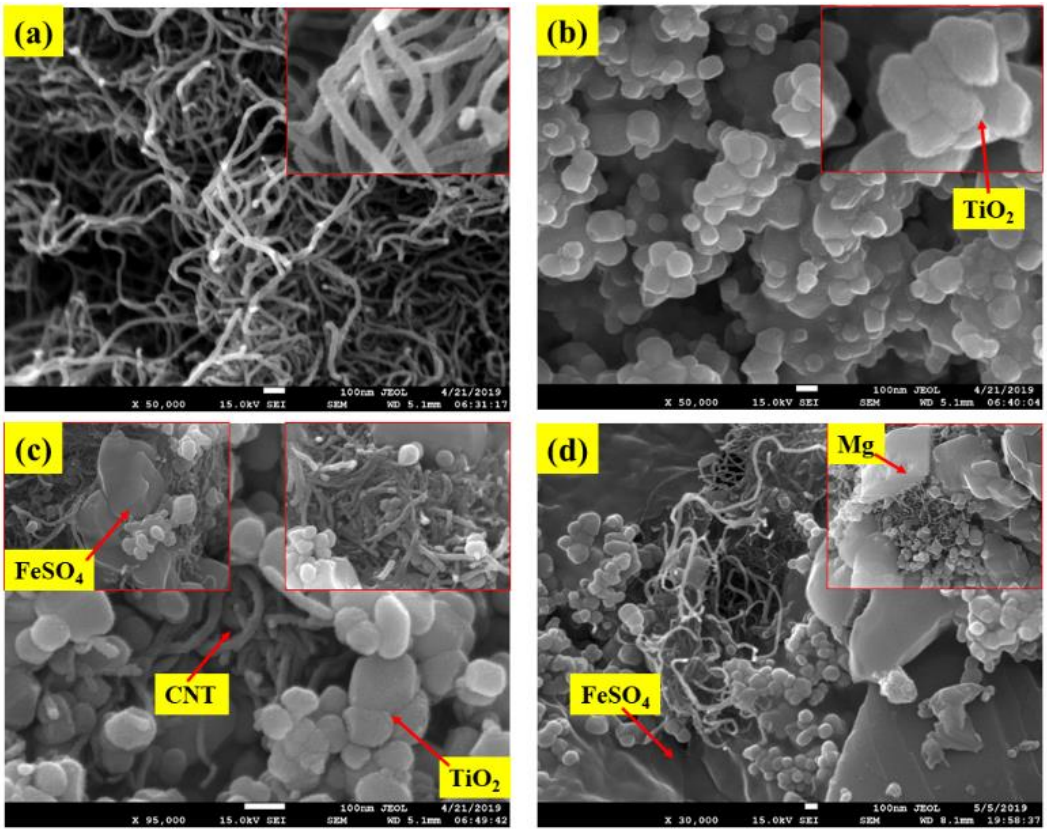

Figure 5.14: Images (a) and (d) show FESEM images of pristine –COOH substituted MWCNT, TiO_2, TiO_2 and ferrous sulphate doped MWCNT-COOH, and the ultimate photo-active CNT-bots after magnesium deposition.

The doped ferrous ions on the photo-active CNT-bot was the major reason behind the motion of the particles inside H_2O_2. FESEM images **5.14(a) – (d)** show COOH substituted MWCNTs, TiONPs, Fe^{+2} and TiONP doped MWCNTs, and photo-active CNT-bots after magnesium deposition. In **Fig. 5.14(c)** presence of all the materials such as MWCNT-COOH, TiO_2, and ferrous sulphate crystals were observed in the composite material. **Figure 5.14(d)** shows the presence of crystals of magnesium in the CNT-bots.

5.3.2.8. Electrochemical Study:

A carbon tape was pasted on an ITO coated glass (1 cm × 2 cm) covering around 80% of the surface area while the rest 20% was kept vacant for connection purposes. Thereafter, the CNT-bots were dispersed on the carbon tape exploiting the presence of the adhesive layer. A cyclic voltammetry (CV) study of this working electrode was made by using ~10% H_2O_2 as electrolyte, Ag/AgCl electrode as reference electrode,

and Pt as counter electrode from -3 V to +3 V with a scan rate of 50 mV/s. The experiments were also performed with the working electrodes of carbon tape without the CNT-bots as a control. **Figure 5.15** clearly shows ~ 1.5-fold increase of current in the case of electrode fabricated with CNT-bots. The reaction of the CNT-bots with ~ 10% H_2O_2 generated excess electrons near the electrode surface and caused an enhancement of current passing through the counter electrode.

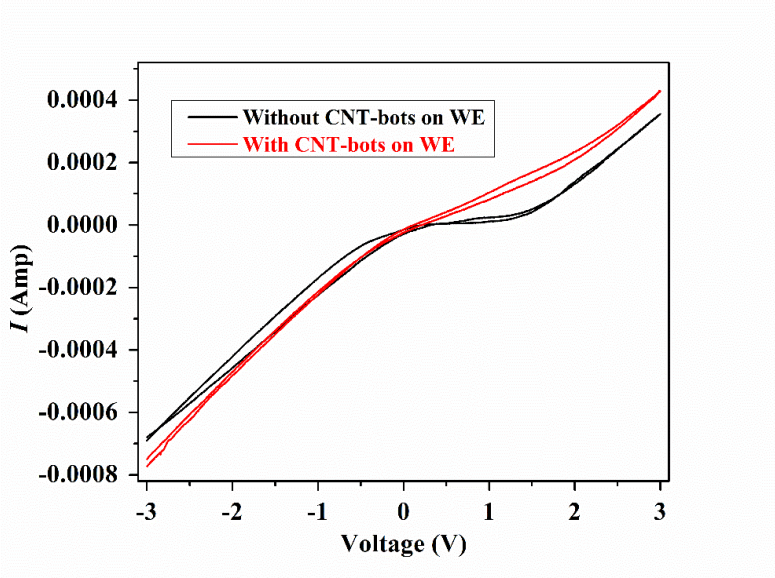

Figure 5.15: Shows the cyclic voltammetry plots of an electrochemical cell having ~ 10% H_2O_2 taking Ag/AgCl and Pt as the reference and counter electrodes while the CNT-bots on carbon tape as the working electrode. The black curve indicates CV of carbon tape electrode without CNT-bots and red curve signifies CV with carbon tape electrode with CNT-bots.

5.3.2.9 EDX Spectroscopy

Presence of different elements in the CNT-bots was confirmed by Electron Dispersive X-ray Spectroscopy (EDXS). **Figures 5.16(a) – 5.16(d)** show the EDXS spectra of pristine carboxylated MWCNT, magnetite doped MWCNTs, ferrous sulphate treated and magnetite doped MWCNTs, and CNT-bots after final magnesium coating, respectively. The plot (a) shows the peaks of carbon and oxygen. The plots (b) and (c) show the peaks of carbon, oxygen, iron, and sulphur, which indicated magnetite and ferrous sulphate doping. Plot (d) shows the presence of all carbon, oxygen, iron, sulphur, and magnesium on the CNT-bot.

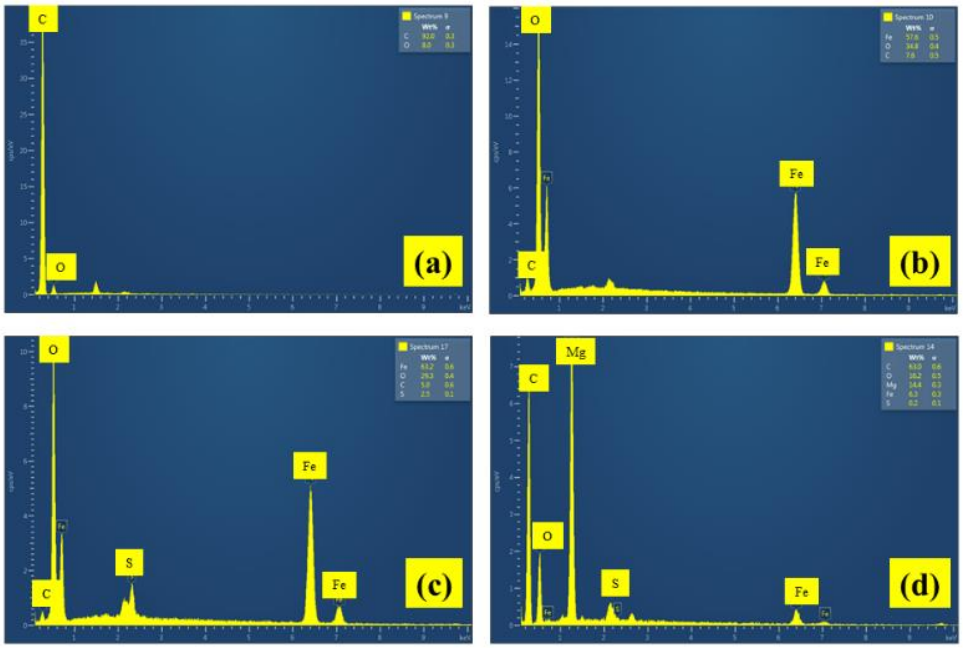

Figure 5.16: Images (a) – (d) show the EDXS spectra of pristine carboxylated MWCNT, magnetite doped MWCNTs, ferrous sulphate treated and magnetite doped MWCNTs, and CNT-bots after final magnesium coating, respectively.

5.3.2.10. XRD Analysis:

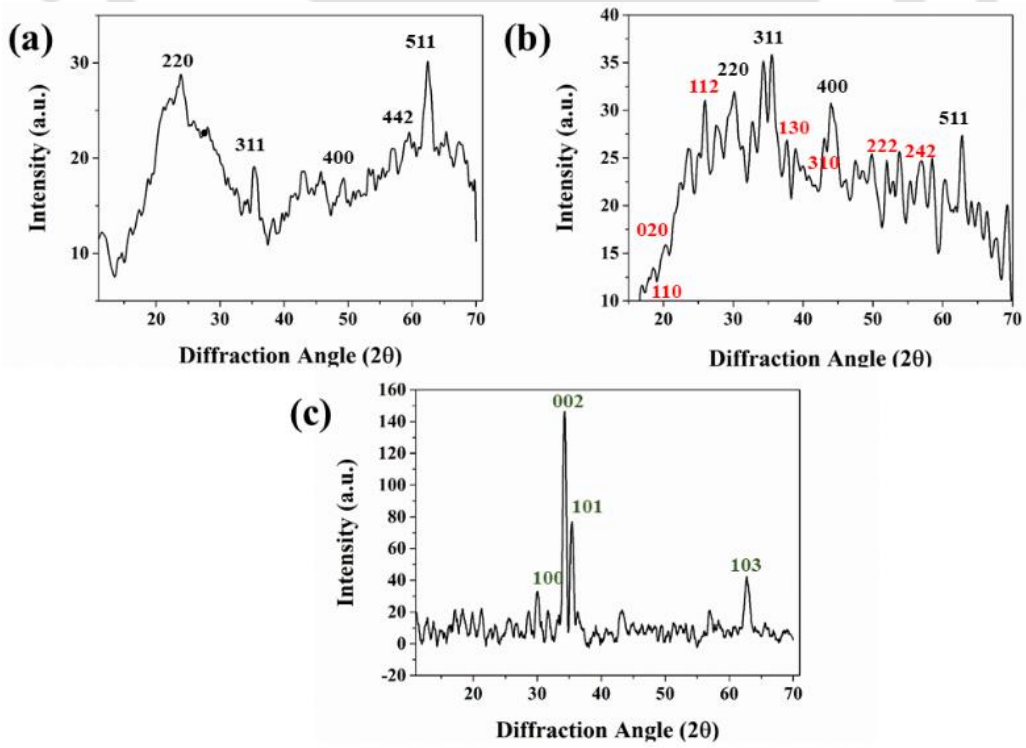

Figure 5.17: Image (a) shows XRD spectra of pristine magnetite nanoparticles. Image (b) shows magnetite doped and ferrous sulphate treated MWCNTs. Image (c) shows XRD spectra of the CNT-bots after the deposition of magnesium layer.

The XRD spectra of the pristine magnetite and MWCNT and subsequent composites after doping and depositions were also performed. **Figure 5.17(a)** shows the XRD pattern of pristine magnetite nanoparticles with the characteristic peaks at, 220, 311, 400, 442, and 511 for magnetite. **Figure 5.17(b)** shows the XRD spectra of magnetite doped and ferrous sulphate treated MWCNTs before deposition of magnesium. In this case, both the peaks for magnetite and ferrous sulphate were observed at 220, 311, 400, 442, and 511 for magnetite[1] and ferrous sulphate[373] at 110, 020, 112, 130,310, 222, and 242. The **Fig. 5.17(c)** shows the XRD spectra of the CNT-bot after the addition of the layer. In addition to the previous peaks, we observed the presence of peaks at, 100, 002, 101, and 103, corresponding to magnesium.

5.4. CONCLUSIONS

We report the design and development of a 3G CNT-bot capable of showing four different types of acid and alkali taxes inside peroxide and water baths in a single embodiment. The movement of the motor could also be remotely controlled with the help of the magnetic field. The Janus type CNT-bots were fabricated by doping magnetite and ferrous ions on the carboxyl functionalized MWCNTs before coating one side of them with a thin magnesium layer. While the Fenton reaction facilitated the motion of the CNT-bot inside the acidic and alkaline peroxide mediums through the ejection of the oxygen bubbles, the motor could decompose in both normal or acidic water to produce bubble propulsion by issuing out hydrogen gas. The motor could also show carbon-dioxide bubble propulsion in an alkaline bicarbonate solution. The motor movement could be enhanced by increasing the concentration and pH of the peroxide fuel whereas the speed of the motor increased in the water bath by reducing the pH. The chemotaxis in the peroxide medium was found to be as high as ~10 body lengths per second at an optimal pH and peroxide loading while the same was found to be ~1 body length per second in water at a very low pH. The movement of the motors could be remotely guided at a speed of as high as ~10 body length per second with the help of a bar magnet. Establishing a gradient of alkali in the peroxide bath, acid in the water bath, and alkali in the water bath, the movement of the motors could be made directional. In the process, the CNT-bots showed directional acid and alkali taxes emulating the movements of the cellular and subcellular processes.[20-26,] A proof-of-concept prototype for real time energy harvesting has been demonstrated in which the CNT-bots have

been employed to generate pure oxygen and hydrogen gases for a PEM fuel cell to generate an electric field potential as high as ~150 mV. The self-propelling CNT-bots facilitated the mixing and de-gassing of the liquids, suitable for a real-time voltage generation as demonstrated. Concisely, the study highlights the potential of the multimodal carbon based 3G CNT-bots for energy harvesting when functionalized with some inorganic materials in meager amount.

Chapter 6

Chemotaxis of a Janus micro-swimmer undergoing differential catalytic reactions on the surfaces

ABSTRACT

We computationally explore the chemotaxis of a Janus particle capable of undergoing a second order chemical reaction, $aA+bB \rightarrow cC+dD$, on the surface at different rates at the sides, when flown inside a microfluidic channel. Such motions are simulated considering the full descriptions of hydrodynamic equations, reaction-convection-diffusion equations, and fluid-structure interaction equations with appropriate boundary conditions. The simulations under a finite element framework uncover that the differential rate kinetics on the surfaces of a Janus particle helps in building up an osmotic pressure gradient across the particle owing to the variations in the concentrations of the reactants and products, which eventually helps in driving the motor. The simulations uncover that the mass diffusivities of the reactants and products play a crucial role in determining the speed and direction of motion of the particle. Interestingly, for reactions with no stoichiometric change, i.e. $a + b = c + d$, the difference in diffusivities could generate self-propulsion while the increase in the rate of reaction leads to the accelerated motion. However, when the overall stoichiometric change follows the trend, $a + b > c + d$, the particle exhibit motion with or without any difference in diffusivity of the reactants and products. In the process, the conditions for the direction of the particle motion have also been identified.

Stands for	Symbol
Cartesian coordinate directions	x, y
x component speed of fluid	u
Particle speed	u_p
Stands for different components	i
Concentration of the ith reactant	c_{ri}
Concentration of the ith product	c_{pi}
Diffusivity of the ith reactant	D_{ri}
Diffusivity of the ith product	D_{pi}
Average diffusivity of all the reactants	D_r
Average diffusivity of all the reactants	D_p
Reaction rate constant in the left half of the particle	k_L
Reaction rate constant in the right half of the particle	k_R
Symbolize two reactants	A, B
Stoichiometric coefficients of reactants A and B	a, b
Symbolize two products	C, D
Stoichiometric coefficients of products A and B	c, d
The density of the fluid medium	ρ
Viscosity of the fluid medium	μ
Density of the solid particle	ρ_s
Diameter of the channel	d_c
Length of the channel	l_c
Length of the semi-major axis of the elliptical particle	a_p
Length of the semi-minor axis of the elliptical particle	b_p
Distance measured from the particle surface	l
Osmotic pressure	π

Table 6.1: List of symbols and parameters which are used in this chapter.

Chapter 6

6.1. INTRODUCTION

The motion of a microscopic particle inside channels or biological systems[130, 374-379] have been under significant research attention due to their substantial technological and scientific importance. For example, pinocytosis[380, 381] or phagocytosis of biological cells,[382, 383] charge transfer during ATP synthesis[384, 385] or the diffusion of biological particles through the cell membrane are some of the chemical potential driven locomotion. The autonomous motions of bacteria by flagella[388, 389] or the motion of spermatozoa[390] have also inspired the scientists and technologists for synthesizing the self-motile objects. Of late, motivated by these natural processes, a wide range of micro and nanoscale self-propelling artificial objects have been synthesized, which are capable of doing various functions on their own. Such migrations of particles are found to take place under various applied fields e.g. electric field,[43-46] magnetic field,[47-49] chemical potential gradient,[50, 51] acoustic field,[52, 53] photon intensity field,[54] surface tension gradient field[55-57] and are known as electrophoresis, magnetophoresis, chemophoresis, sono-taxis, photo-taxis, Marangoni flow, respectively. Further, the Janus particles[386, 387] capable of showing motions with the help of the different chemical responses at the sides have gained considerable attention over the years. Such autonomous and field-driven find various futuristic mesoscale applications ranging from separation,[20, 21] transport and delivery, surgery,[23] and mixing.

In particular, motions of flagella or bacteria are all chemical concentration driven, which are also termed as chemotaxis. These naturally occurring motions inspired scientists to develop synthetic self-propelling micro/nanobots undergoing chemotaxis. For example, nanoscale bimetallic rods[391, 392] show chemotactic motions inside a peroxide fuel and the speed of such motor increases with H_2O_2 concentration in the fuel. The time scale of the process depends on the diffusivity values of the components. If the time scale is very short, say $1/D_r$ where D_r is the rotational Brownian diffusion coefficient, the motion is found to be unidirectional. For a higher time scale longer than $1/D_r$, the motion of the particle becomes random.[393] The monotonic relationship between the concentration and speed of the bimetallic colloidal rods reveals some very interesting fact of such chemotaxis.[394] A number of previous works observed that the tubular microbots and Janus motors show a directional motion toward the higher H_2O_2 concentration.[395] Further, the effects of alkali concentration on the motion of a microsphere in a peroxide solution have also been explored recently.[396]

Importantly, a number of previous studies show that the motors driven by chemical gradient can also be directed remotely by application of external magnetic[397] or electric fields.[398] Such synthetically developed motors have the capacity of loading cargo, essentially a drug, and delivering it to a specific location. Since the malignant tumor cells generate more hydrogen peroxide compared to normal cells, such motors can move in such a peroxide rich environment near the tumor cells and deliver drugs[335, 399, 400] to the specific location. Alongside chemotaxis, in a wide number of phenomena in biological systems, it is seen that the microorganism or the cell can itself generate chemical attractant/repellent inside or on the surface of its body.[378, 379, 401] Uneven distribution of this chemical concentration over the microorganism or cell surface generates a chemical potential gradient, which leads to the self-propulsion of the microorganism or the cell. Such locomotions are observed in amoeba, *Dictyostelium discoideum* as well as the intestinal bacterium, *Escherichia coli*.[402, 403]Mimicking these motions, there are recent developments of synthetic auto-chemotactic motors.[404]

However, despite the availability of fairly huge literature, the origins of such motions as well as the variations of speed and direction of such motions with the various internal and external parameters are still a very important area for research. In particular, the contributions of various kinetic and dynamic parameters i.e. reaction rate constants and diffusion coefficients in the determination of the particle speed and direction are not very well understood so far. Thus, in this chapter, we focus on the motion of Janus motors having different kinetics of reaction at the sides of the particle in the presence of an imposed external concentration gradient. Such motions are simulated considering the full descriptions of hydrodynamic equations, reaction-convection-diffusion equations, and fluid-structure interaction equations with appropriate boundary conditions. The simulations under a finite element framework uncover that the differential rate kinetics on the surfaces of a Janus particle helps in building up an osmotic pressure gradient across the particle owing to the variations in the concentrations of the reactants and products, which eventually helps in driving the motor. The simulations disclose that the particle speed depends on various parameters ranging from fluid viscosity, fluid density, the bulk concentration of the components in the fluid, reaction kinetics, diffusivity of the reactants and products, channel confinement, and the particle size and shape. The simulated results are found to successfully predict the particle speed available with the experimental results.

6.2. PROBLEM FORMULATION

6.2.1. Governing Equations:

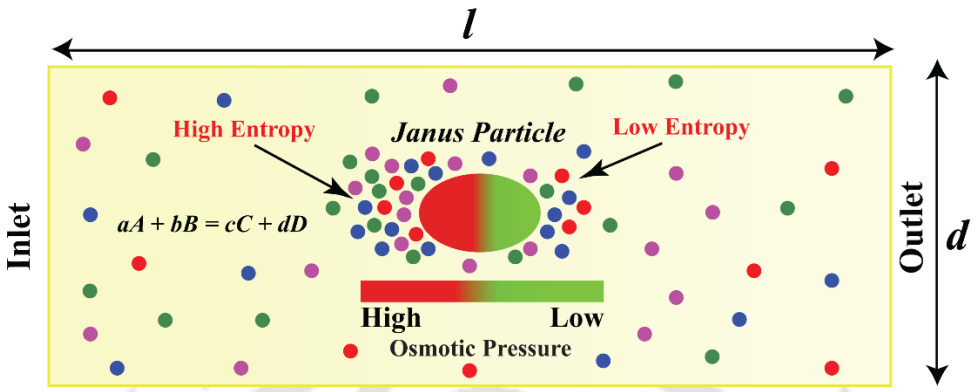

Figure 6.1: Schematically shows chemophoretic movement of an elliptical particle inside a liquid filled microchannel as a result of local osmotic pressure imbalance. An asymmetric catalytic chemical reaction is taking place on the particle surface with different reaction kinetics at the two different halves of the particle. There are two reactants, which give two products following reaction stoichiometry, $aA+bB\rightarrow cC+dD$.

The theoretical model for both chemophoretic and auto-chemophoretic motion of an elliptical particle is done taking a particle inside a microfluidic channel, which is filled with fluid. The liquid inside microfluidic channel contains four different components and undergoing chemical reactions. A mixed coordinate system is employed in order to model the problem. Near the particle surface, polar coordinate is taken mentioning the center of the particle as, $r = 0$. The channel is a 2D rectangular, and hence a Cartesian coordinate system is used in order to solve hydrodynamics and transport equations. The fluid inside the channel is considered to be Newtonian and incompressible. In this problem formulation, the bold variables indicate vectors, the bold variables with double overbars indicate tensors, partial derivative of a variable is denoted by the symbol ∂, the notation ∇ is the gradient operator, the letter 'I' denotes identity tensor, and the superscript T stands for transpose of a tensor.

The components of a vector are symbolized by keeping those components inside a box bracket after the bold vector variable, e.g., $\mathbf{u}[u,v]$ and $\mathbf{u}_s[u_s, v_s]$ denote fluid velocity and displacement vector of the solid particle. The concentration of the i^{th} component is shown by c_i. The symbols t, ρ, ε, ρ_s, μ, and D_i represents time, the density of electrolyte, the permittivity of the electrolyte, the density of the solid particle, the viscosity of

electrolyte, the diffusivity of i^{th} component, respectively. The letter 'M' represents molar concentration, i.e. mol/m^3. Transport equation for the concentration of reactants and the products along with the hydrodynamic equations for the fluid flow inside the channel are employed. The concentration of reactants in general term the i^{th} component (c_{ri}) surrounding the particle where the reaction is going on in the near vicinity governed by the following scalar transport equations,

$$\partial c_{ri} / \partial t + u_i \cdot \nabla c_{ri} = D_{ri} \nabla^2 c_{ri} - k \prod c_{ri} \,. \tag{6.1}$$

Here i ranges from 1 to n and n is the molecularity of the reaction. The term $\prod c_{ri}$ represents multiplication of all the reactants. The concentration of the products is governed by the following reaction-convection-diffusion equation

$$\partial c_{pi} / \partial t + u_i \cdot \nabla c_{pi} = D_{pi} \nabla^2 c_{pi} + k \prod c_{ri} \,, \tag{6.2}$$

where c_{pi} denotes the concentration of the product components. The last term in both Eq. (6.1) and (6.2) appears for the reaction near the particle surface. These two sets of equations are mutually coupled and these equations are also coupled with the hydrodynamic equation by the convective term. For the fluid flow, the following continuity equation along with Navier-Stokes equations are solved,

$$\nabla \cdot \mathbf{u} = 0, \tag{6.3}$$

$$\rho \frac{D\mathbf{u}}{Dt} = -\nabla p + \mu\left(\nabla^2 \mathbf{u}\right) - \nabla \pi \,. \tag{6.4}$$

The last term in Eq. (6.4) appears for the body force, which is evolved as osmotic pressure imbalance due to the chemical reaction, the external chemical concentration gradient, or as an effect of both the things as an osmotic pressure difference ($\Delta\pi$). Osmotic pressure is calculated from the equation,

$$\pi = RT \sum c_i \,. \tag{6.5}$$

Here, $\sum c_i$ represents the summation of the concentration of all the components (including both the reactants and products). Osmotic pressure being a colligative property, the pressure can be expressed as a function of the concentrations of the components. The fluid-structure interaction (FSI) has been considered to track the motion of the particle, which migrates under osmotic pressure gradient during the

chemophoretic/auto-chemophoretic phenomenon. The equations associated with the FSI are,

$$\rho_s\left(\partial^2\mathbf{u}_s/\partial t^2\right)-\nabla\cdot\bar{\bar{\boldsymbol{\sigma}}}=0, \tag{6.6}$$

$$\bar{\bar{\boldsymbol{\sigma}}}=-p\bar{\bar{\mathbf{I}}}+\mu\left(\nabla\mathbf{u}+\nabla\mathbf{u}^T\right). \tag{6.7}$$

Here the symbols, ρ_s and $\bar{\bar{\boldsymbol{\sigma}}}$ represent the density of the solid and stress tensor of a Newtonian fluid, respectively.

6.2.2. Boundary Conditions:

The boundary conditions for Eq. (6.1) and Eq. (6.2) are different for the imposed and auto chemophoretic motion of the particle. For the imposed chemophoretic motion, Dirichlet boundary condition at the inlet and outlet of the channel are used. At the one end, either at $x = 0$ or at $x = l$, $c_{ri} = c_{ri0}$ is maintained, whereas initially the concentration of the product (c_{pi}) is kept zero at both the ends of the channel. On the other end i.e. either at $x = l$ or at $x = 0$ normal flux boundary conditions $-\mathbf{n}\cdot\nabla D_i c_{ri}=0$ for the reactants (c_{ri}) are maintained. For the auto-chemophoretic motion of the particle, constant concentration (c_{ri}) at the beginning of the simulation i.e. at $t = 0$ without no inflow and no flux at any of the ends of the channel are deployed.

The continuity and Navier-Stokes Eqs. (6.3) and (6.4) have been solved by taking the no slip and impermeable boundary conditions ($u = v = 0$ at $y = 0, d$) at the walls of the microchannel. To ensure that the motion of the particle along with the fluid inside the channel happens due to the chemical gradient only, no pressure gradient across the channel is taken and both the ends of the channel are kept at atmospheric pressure. For the fluid-structure interaction, the two-way coupling is enforced along with the particle. For this purpose, continuity of velocity boundary condition, $\mathbf{u} = \dot{\mathbf{u}}_s$, have been enforced on the particle surface while a no-slip condition is enforced along the inner wall of the tube. Zero displacement ($\mathbf{u_s} = 0$) and zero speed ($\dot{\mathbf{u}}_s = 0$) of the particle at initial time ($t = 0$) have been enforced to meet the two boundary conditions necessary to solve the Eq. (6.6)**.** The hydrodynamic stress, which is being imparted on the particle surface is taken from the coupled momentum equations.

6.3. NUMERICAL METHODOLOGY

Finite element method (FEM) of commercial CFD simulation software, COMSOL Multiphysics™, is outsourced for discretization and solution of the coupled set of Eqs. (6.1) – (6.7) with the aforementioned boundary conditions. The software uses the Galerkin least-square (GLS) method along with the second order elements for speed calculations and first-order elements to discretize the equations. The velocity and pressure profile calculations are done using the segregated predictor-corrector method with incremental pressure correction. Consistent initialization and time-marching are taken care of by the software using a second-order backward difference method with a suitable time step size of ~10^{-4} s. The data, thus obtained from numerical simulations, are exported and further post-processing is made for proper representation.

6.4. VALIDATION

6.4.1. Analytical Model:

A simple analytical model has been suggested to validate the results obtained from computational fluid dynamics simulations. The particle is assumed to be spherical in shape and hence in order to model it analytically, a three-dimensional spherical (r, θ, φ) coordinate system is taken. In the present study, for the purpose of simplicity of the analytical calculations, it is assumed that all the derivatives with respect to polar coordinates are zero. Hence, the radial direction in space and time coordinate survive for the purpose of all the calculations of this part. A simple set of unsteady reaction-diffusion equations are taken for individual reactant and product. For this validation, a first-order elementary reaction following the stoichiometry, $R \rightarrow S$ *is* used. The reaction kinetics of the stated reaction follows the rate equation, $-dC_R/dt = dC_p/dt = kC_R$ .The values of the reaction rate constants are varied with position to incorporate differential rates at two different ends of the particle. The reaction and diffusion equation, which determine the concentration profiles as a function of space and time for both reactant and product are,

$$\partial c_R/\partial t = D_R \nabla^2 c_R - k c_R, \tag{6.8}$$

$$\partial c_P/\partial t = D_P \nabla^2 c_P + k c_R. \tag{6.9}$$

6.4.2. Boundary Conditions:

In order to solve Eqs. (6.8) and (6.9), boundary conditions that describe the physical system and the underlying phenomenon are set. The solution space, which is assumed for the present study is [R, $R+l_a$]. Here, l_a is the active distance measured from the particle surface ($r = R$), up to which the effect of reaction-diffusion does not reach and the concentration beyond which, can safely assume to be constant. The boundary conditions pertinent to the physical system are,

$$c_R\left(R,t\right) = c_{RS},$$

$$c_R\left(r,0\right) = c_{RS},$$

$$\nabla c_R\left(l_c,0\right) = 0;$$

and for the product the boundary conditions are,

$$c_P\left(R,t\right) = c_{PS} = 0,$$

$$c_P\left(r,0\right) = c_{RS},$$

$$\nabla c_R\left(l,0\right) = 0.$$

Here, c_{RS} and c_{PS} are steady concentrations of the reactant and product on the particle surface and also everywhere at the initial time ($t = 0$).

6.4.3. Comparison of Semi-Analytical and Simulation Results:

In order to prove the validity of the numerical CFD code, the concentration profiles obtained by CFD simulation and the proposed analytical model are compared in this section. Fluid-structure interactions and moving deforming mesh, employed in the numerical simulations to emulate the particle motion as a result of local osmotic pressure build-up, actually affect the concentration profiles around the particle with time. Analytical solutions taking moving reference frame are a little bit cumbersome and also beyond the scope of the present study. Hence, a simple static reference frame is taken for the concentration profile calculations.

The differential Eqs. (6.8) and (6.9) are solved using commercial package MATHEMATICA™ to evaluate the concentration profiles around the sphere. Different kinetic parameters based on differential reaction rate kinetics at two different sides of the particle are employed. **Figures 6.2 (a)** and **6.2(b)** show the comparison of profiles at the left and right halves of the particle, where the reaction rate constants are k_R = 8.5

$s^{-1}$and k_L = 1.7 s^{-1}. The figures show a good match between numerical and analytical profiles near the particle surface and it deviates as we move away from the surface. Non-linearity of the CFD simulation, associated fluid flow, particle motion affects the concentration profile and those might be the reasons for slight mismatch of simulation and analytical profiles, especially away from the particle surface. However, the asymptotic match obtained from this study establishes the authenticity of further calculations using these sets of equations and numerical methodologies involved in COMSOL Multiphysics™. Analytical calculations of the particle speed are very cumbersome as set of Eqs. 6.1 to 6.7 are mostly nonlinear and coupled with an additional complexity of particle movement and hence all the particle speed calculations are done numerically.

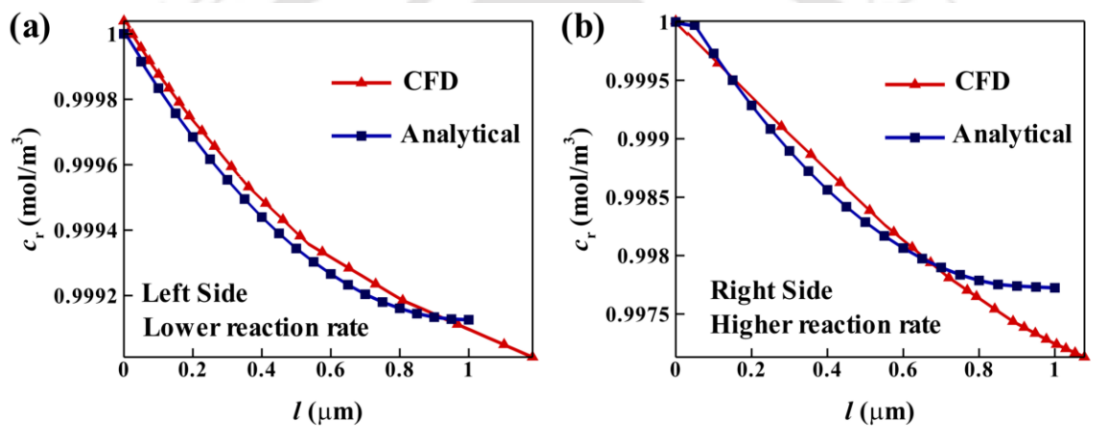

Figure 6.2: Image (a) shows the comparison of concentration profile of reactant, at the left side of the moving particle, obtained from CFD numerical simulation and analytical solution. Image (b) shows a similar comparison for the right side of the moving particle. A first-order reaction is undergoing having rate constants k_L = 1.75 and k_R = 8.9 s^{-1} in the left and right halves of the particle, respectively. The diffusivity of the reactant (D_r) is kept constant as 3 ×10^{-9} m^2/s.

6.5. RESULTS & DISCUSSION

In this chapter, a Janus particle has been considered, which has chemical dissimilarities on the surface. Thus, the particle shows different reaction rates at its two different ends to generate an osmotic pressure gradient across the surface. In the process, the particle acquires motion by converting the chemical energy into the mechanical one. In order to theoretically model such a system, we consider a second-order reaction with the stoichiometry, $aA+bB \rightarrow cC+dD$, with different rate constants at the chemically heterogeneous sides of a Janus particle. Thereafter, initially, we study the motion of a Janus particle, which moves in a confined microchannel of diameter 5 μm and length 15 μm. In this situation, the propulsion is originated from an imposed concentration field along the channel as well as the thrust generated by local osmotic pressure gradient due to the differential chemical reactions across the surface. Further, we study the motion of a freely floating Janus particle undergoing self-phoretic motion in a relatively less confined microchannel of diameter 250 μm and length 500 μm owing to the sole influence of the local osmotic pressure gradient.

6.5.1. Influence of Shape:

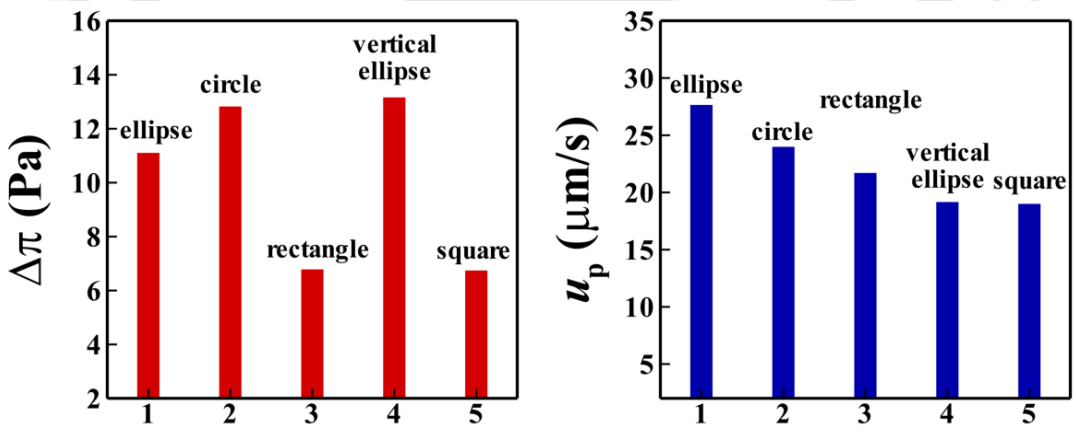

Figure 6.3: Shows automated chemophoretic motions of particles with different shapes inside a channel of diameter (d) 250 μm and length (l_c) 500 μm. For all the cases perimeter of the particle is kept 56 μm. Plot (a) shows developed average osmotic pressure difference across the particle, taking the average along with a line extended up to 10 μm both sides from the particle surface. Plot (b) compares and contrasts the speed of the particles with different shapes.

In this regard, a Janus particle is taken considered a microchannel of diameter 250 μm and a length 500 μm. We assume that, over a period of time, an osmotic pressure

gradient builds up across the particle owing to differential rate kinetics at different portions of the particle, which eventually drives the particle. A set of simulations have been performed with particles of different shapes, such as elliptical, circular, rectangular, or square, keeping all other simulation parameters unchanged. The particle geometries are considered in such a manner that all the particles have equal perimeters of ~56 μm in order to ensure similar reaction effects for all the cases. The initial reactant concentrations of both the reactants are taken as 1 mol/m^3 while the products are assumed to be absent. For this particular section, the rate constant of the reaction is varied from ~ 0.88 to 8.8 M^{-1} s^{-1}. The model also assumes that the left-hand side of the particle offers higher reaction kinetics (k_L = 8.8 M^{-1} s^{-1}) compared to the right-hand side (k_R = 0.88 M^{-1} s^{-1}). In such a scenario, higher diffusivity for the products (D_p = 4×10^{-9} m^2/s) compared to the diffusivity of reactants (D_r = 2×10^{-9} m^2/s) drives the particle in the positive *x*-direction (left side to the right side). One important thing related to the current problem is that there are two different time scales, which govern the entire process. The reaction time scale is in the order of c_0^n/k for nth order reaction, whereas the diffusion time scale is defined as $t = l^2/D$. Here, c_0 and n signify initial concentration of a component present in the system and order of the reaction, respectively.

The present simulation parameters make the diffusion time scale (order of ms) smaller compared to the reaction time scale (order of μs) and hence diffusion time scale dominates in determining the fate of the entire particle motion. The developed osmotic pressure across the particle stimulates a very weak flow around the particle. Although the drag force varies with the shape of the particle owing to the variation in the projected area, the effect of drag is very negligible for a particle of such a small size, at a significantly small Reynold's number. **Figure 6.3(a)** shows profile of $\Delta\pi$ across the particle, which manifests a weak laminar flow across the entire channel. The plots suggest that the shapes have a significant influence on the osmotic pressure drop around the particle. In this case, we also observe that the particle speed increases with $\Delta\pi$, as shown in **Fig. 6.3(b)**, with an exception for circular and elliptical particle. The plot suggests that although the elliptical particle generates less osmotic pressure drop across the surface, a lower drag force helps them attaining maximum speed. Thus, we perform rest of the simulations considering the elliptical particles.

6.5.2. Influence of External concentration gradient:

In the previous case, with differently shaped particles, the motion is a self-phoretic motion, which is happening due to differential rate kinetics at different ends. However, one of the interests of the present study lies in exploring the fate of this moving particle, as discussed in the previous section, when an additional external concentration gradient is imposed along the channel horizontal axis.

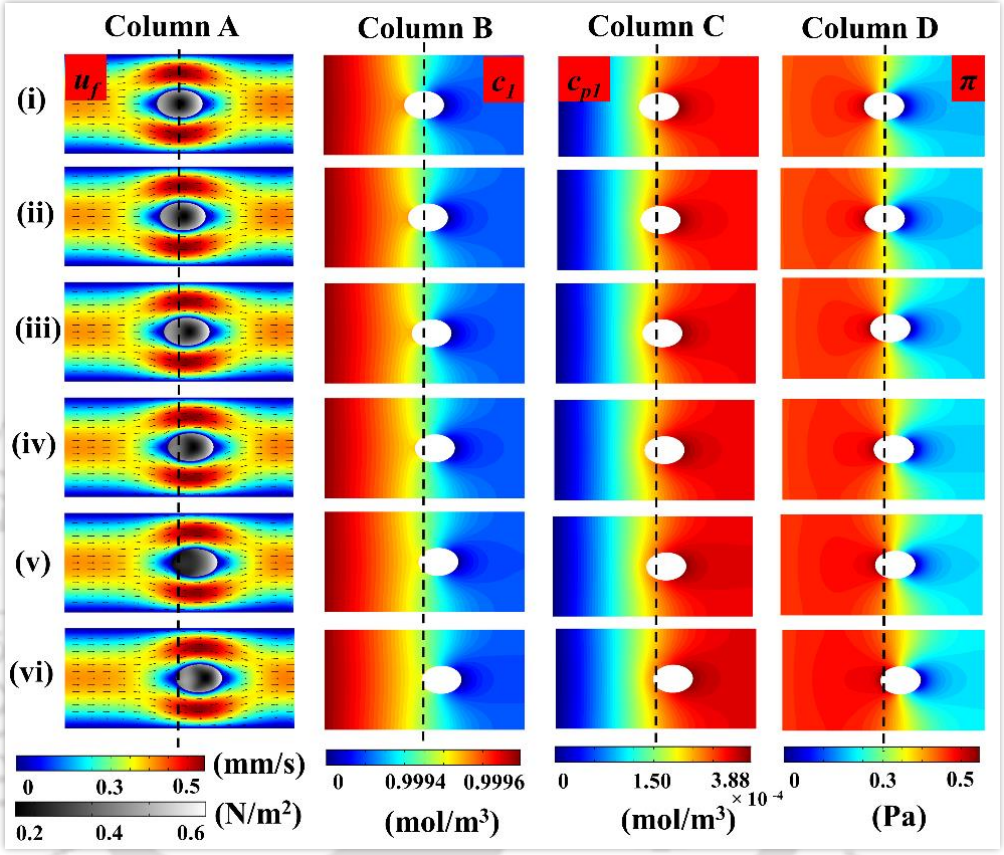

Figure 6.4: Shows the chemophoretic motion of a Janus particle moving inside a microfluidic channel of diameter (d_p) 5 μm and length of the channel (l_c) 15 μm in presence of a constant concentration Dirichlet condition at the left side of the channel. The semi-major and semi-minor axis length of the elliptical particle is 1 μm and 0.7 μm, respectively. Image set (i) to (vi) of column A show the position of the particle inside the channel at different time intervals. Image sets of column B show a reactant concentration (c_{r1}) at all the respective frames. Image set of column C represents the concentration profile of a product (c_{p1}) around the particle at respective time intervals. Images (i) to (vi) of column D show the osmotic pressure profile around the particle, across the channel.

Many of the biological processes show such kind of motion, which are mainly guided by external concentration gradient. For example, the motions of microorganisms towards a food rich zone or the chemo-repellent motion of the same away from zone of a specific chemical. **Figure 6.4** shows the motion of an elliptical Janus particle inside

a microfluidic channel of diameter, d_p = 5 μm and length, l = 15 μm. A second order catalytic reaction is considered around the particle wherein the right-hand side of the particle has a higher reaction rate compared to the left-hand side. The product components have a higher diffusivity (D_{pi} = 4×10^{-9} m^2/s) compared to the reactant components (D_{ri} = 2×10^{-9} m^2/s). In this case, an additional constant concentration (c_{ri} = 1 mol/m^3) condition is given at the left side of the channel.

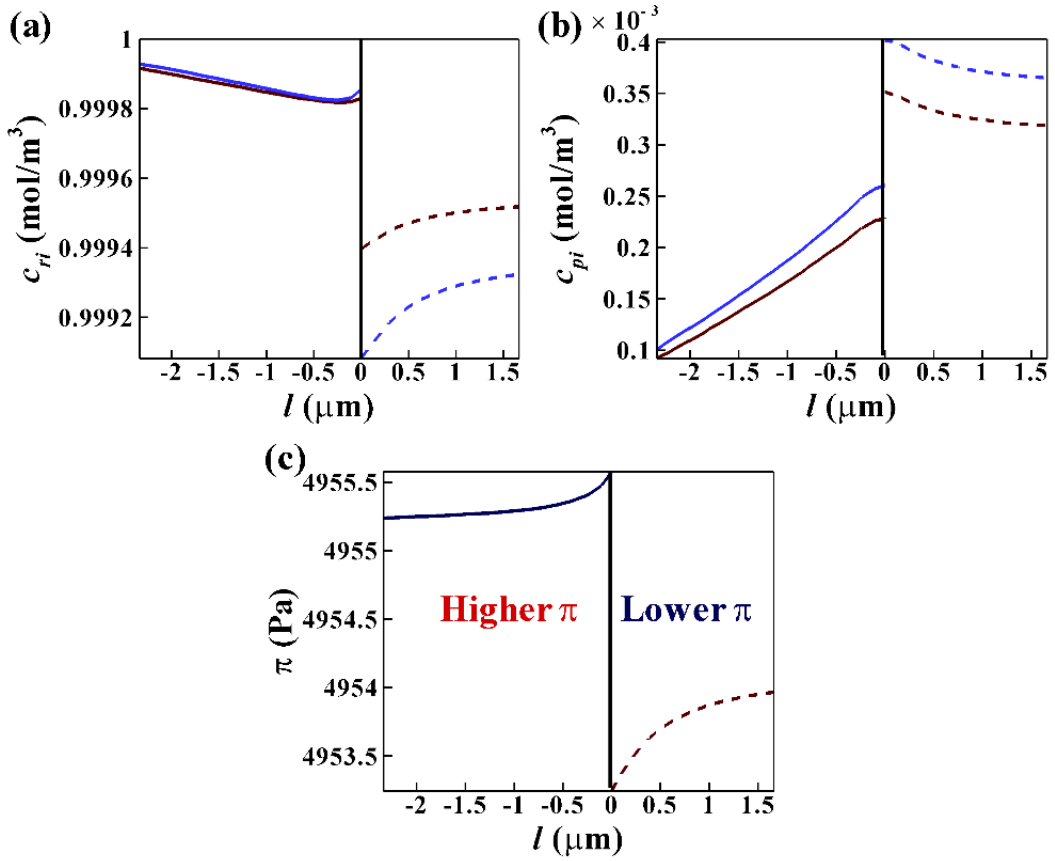

Figure 6.5: Shows the concentration profile along the channel axis of reactants taken in the right and left-hand side of the particle. Blue lines (lighter shade) represent concentration of the reactant A, whereas grey (darker shade) denotes concentration of reactant B. Image (b) shows the concentration of the products, again blue (lighter shade) represents the concentration of product C and grey (darker shade) shows concentration of product D. Plot (c) shows the osmotic pressure profiles in the right and left half of the particle. Particle surfaces are taken as the starting point and from the particle $-l$, and $+l$ represents left and right distance along the axis. Solid lines denote for left side profiles and the dotted lines denote the right-side profiles.

We consider a reaction, $aA+bB\rightarrow cC+dD$ with a second order reaction rate. Concentrations of *A*, *B*, *C*, and *D* are represented as c_{r1}, c_{r2}, c_{p1}, and c_{p2}, respectively. In the present case, along with the external concentration gradient a catalytic reaction also takes place with two different rate kinetics in the left and right half of the particle.

However, we also impose an external concentration gradient, which develops as additional pressure drop along the channel axis of the channel alongside the pressure drop due to the different rate of chemical reaction around the particle. In this section, we quantify the magnitude of the forces generated from external concentration gradient and due to the differential chemical reactions around the particle.

The pressure gradient across the particle due to the external concentration field is indeed higher compared to the one generated solely due to the difference in reaction kinetics. Hence, the particle moves from left to the right-hand side of the channel while guided by the externally imposed concentration field. However, the particle velocity is also found to be significantly affected by the differential catalytic reactions on the surface, which is further investigated in the later part of this article.

Figure 6.5 represents the profiles of concentrations and osmotic pressure around the moving particle as shown in **Fig. 6.4**. **Figure 6.5(a)** shows that the concentration of the reactants decreases as one moves to the particle surface as the reaction is occurring near the particle surface. **Fig. 6.4(b)** shows that the product profiles have higher values near the particle surface while the same diminishes away from the particle. The reaction and diffusion near the particle surface along with the imposed concentration gradient inside the channel creates an imbalance of osmotic pressure across the particle. **Fig. 6.5(c)** shows that the left side of the particle shows higher osmotic pressure as a combined effect of reaction-diffusion for the present scenario. As a result, the particle moves from the left to right side of the channel.

In order to quantify the effect of channel length, few simulations are also performed with varying the same from 15 μm to 60 μm, as shown in **Fig. 6.6(a)**. In this case, the reaction kinetics in the right-hand (k_R = 2.1 M^{-1} s^{-1}) side is higher compared to the reaction kinetics in the left-hand side (k_L = 0.8 M^{-1} s^{-1}). The diffusivity of the product components (D_{pi} = 3×10^{-9} m^2/s) is also higher compared to the diffusivity of the reactants (D_{ri} = 2×10^{-9} m^2/s). Such set of parameters generates higher component accumulation in the left-hand side compared to the right-hand side to facilitate self-chemophoretic motion in the positive *x*-direction (left to the right). The local osmotic pressure generated across the particle is shown in **Fig. 6.6(b)**. The simulations suggest that with the increase in the channel length the effect of the external concentration decreases. Subsequently, the osmotic pressure drop across the particle also decreases with concurrent decrease of particle speed.

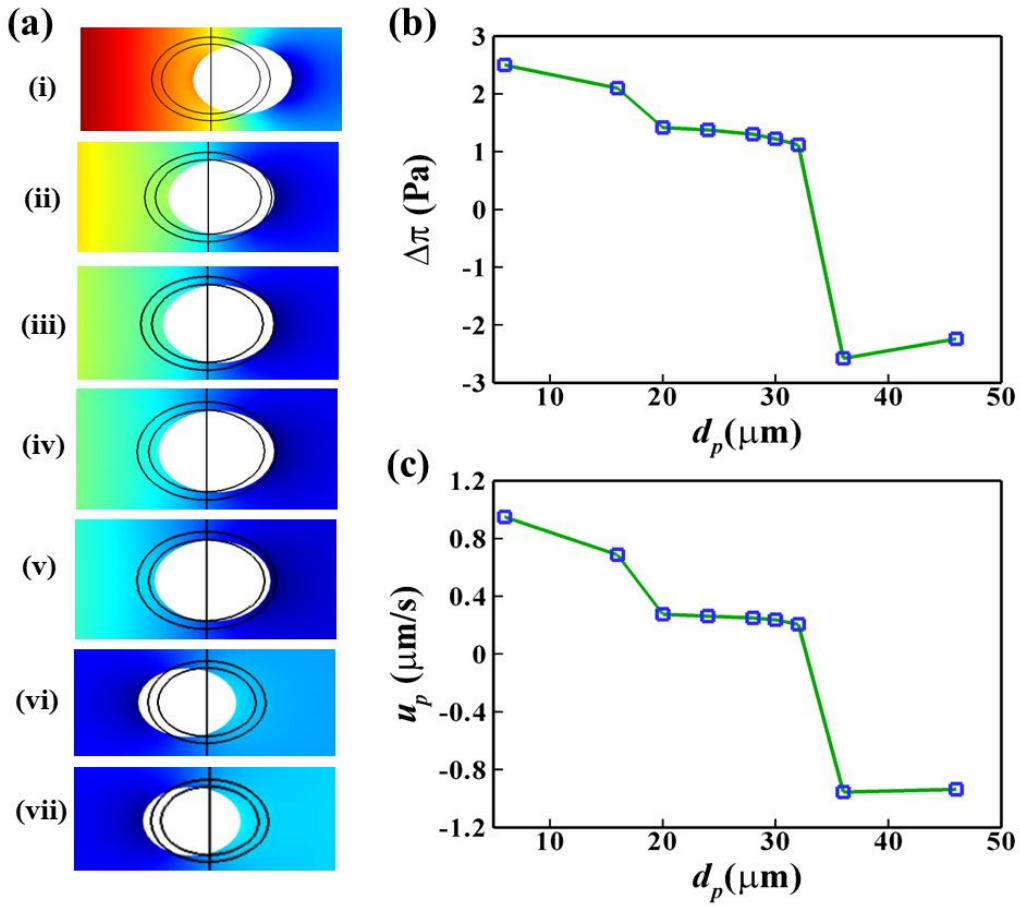

Figure 6.6: Image set (i) to (vii) of plot (a) represent motion of the particle inside a microchannel having diameter (d_p) 5 μm with varying length (l) 20, 24, 28, 30, 32, 36, 46 μm respectively. Plot (b) shows average pressure drop ($\Delta\pi$) across the particle for different channel lengths. Plot (c) shows particle velocity for different channel lengths.

Interestingly, after a critical channel length of 32 μm, as shown in **Fig. 6.6(a),** the $\Delta\pi$ becomes negative and the particle flows in the opposite direction (right to left). The respective particle velocity is shown in **Fig. 6.6(c)**. In this situation, different reaction kinetics across the particle makes a higher π in the right-hand side, which facilitates the particle to move towards the left-hand side. However, due to the presence of an external concentration source on the left-hand side, it increases the overall concentration on the left-hand side. However, for the larger length of the channel, the effect diminishes and the particle moves as a result of different reaction kinetics across the channel. In such a scenario, the particle moves towards the opposite direction. For the simulations, it can be concluded that the major advantage of putting an external concentration is that it can be used to guide the particle motion as a controller.

6.5.3. Influence of Zero concentration gradient:

Importantly, one of the major objectives of the present study lies in the exploration of the different aspects of self-phoretic motion of the 'Janus' particle. In order to capture the autonomous motion of the particle, a channel with larger diameter (d_p = 250 µm) is taken with a particle, which has different catalytic activities at two different sides of it. The size of the particle is also larger compared to the previous one with 10 µm semi-major axis and 7 µm semi-minor axis.

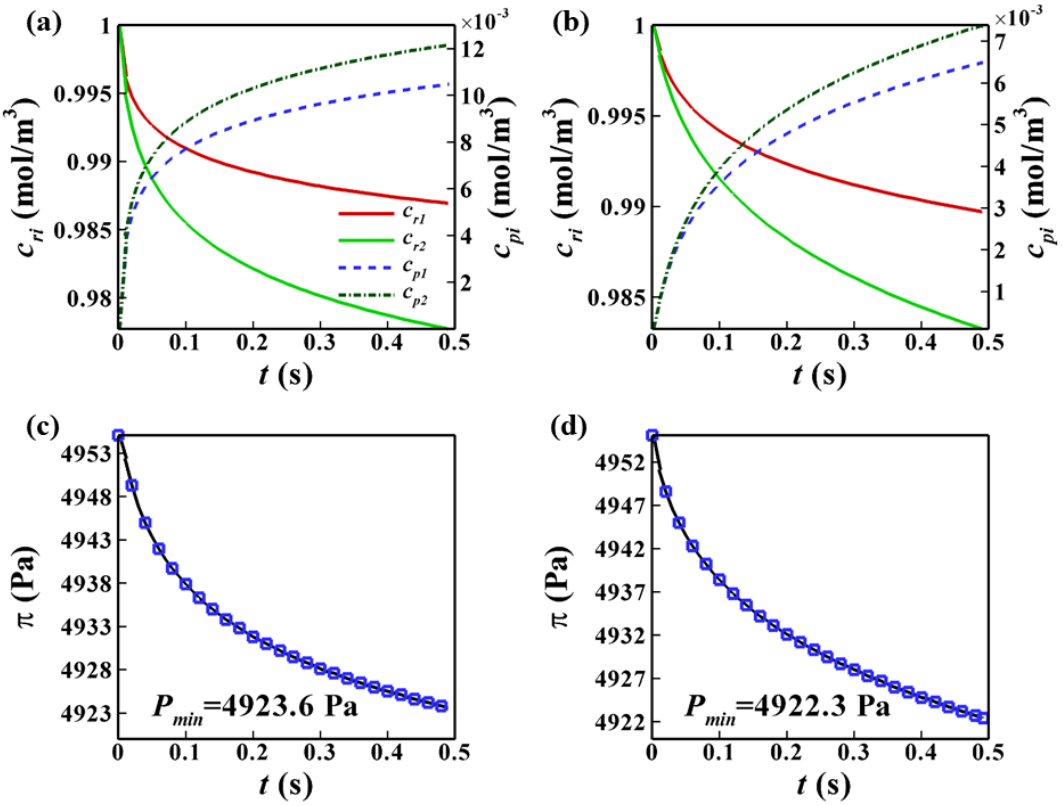

Figure 6.7: Shows the average concentration vs time profile (taken across a line along the axis away from the particle surface) of the reactants (c_{ri}) and products (c_{pi}) at the left-hand side of the particle. Plot (b) shows the same average concentration of reactants (c_{ri}) and products (c_{pi}) at the right-hand side of the particle. Plots (c) and (d) show the developed osmotic pressure (π) vs time profile for the left and right side of the particle respectively.

In this case, no external concentration gradient is considered and the particle is driven by the sole influence of the local osmotic pressure imbalance. The entire channel is filled with the solution having an equal concentration (1 mol/m^3) of reactants. When the particle is placed in the middle of the channel, the reactants decompose on the particle surface because of the catalytic activity. However, owing to the differential catalytic activities at the sides of the Janus particle, inhomogeneous concentration of the reactants and products are found to be set in as time progresses. As a result, the

particle experiences a $\Delta\pi$ to achieve the motion. The direction and magnitude of motion depend on reaction kinetics as well as on the diffusivities of the components. The osmotic pressure-drop, although very small in nature, can eventually move the micron-sized particle in the channel. The phenomenon takes place is found to be purely transient in nature. Again, in this case, also there are two competing time scales, diffusive and reactive. However, the rate limiting diffusive time scale actually governs the phenomenon.

Figure 6.7 describes the development of the concentration profiles due to the reaction as time progresses and hence the development of the osmotic pressure around the particle. **Figs. 6.7(a)** and 6.**7(c)** show profiles for the left-hand side of the particle whereas **Figs. 6.7(b)** and 6.**7(d)** show profiles for the right-hand side of the particle. In this case, the left-hand side has a higher reaction rate (k_L = 8.8 $M^{-1}s^{-1}$) compared to the reaction rate of right-hand side (k_L = 0.88 $M^{-1}s^{-1}$) and hence it incurs consumptions of more reactants and yield of more products compared to the consumption and yield of the other side. The concentration of the reactants (products) reaches up to 0.975 mol/m^3 (0.012 mol/m^3) on the left-hand side whereas it goes up to 0.984 mol/m^3 (0.007 mol/m^3) on the right-hand side. **Figures 6.7(c)** and **6.7(d)** show the decrease in the absolute value of the average osmotic pressure as time progresses along with the effective $\Delta\pi$, which drives the particle. In this case, reaction and diffusion kinetics determine the absolute value of the osmotic pressure.

It is observed that with changing the particle orientation, the particle actually changes its direction. **Figure 6.8** shows two different particles, one has a higher reaction rate on the right-hand side (k_R = 8.8 M^{-1} s^{-1}), as shown in **Fig. 6.8(a),** of the particle and the other, has opposite nature (k_L = 8.8 M^{-1} s^{-1}), as shown in **Fig. 6.8(d)**. The diffusivities of the components are kept unchanged for both kinds. In this study, diffusivity of the products ($D_p = 3\times10^{-9}$) is kept higher compared to the diffusivity of the reactants ($D_r = 1.5\times10^{-9}$).

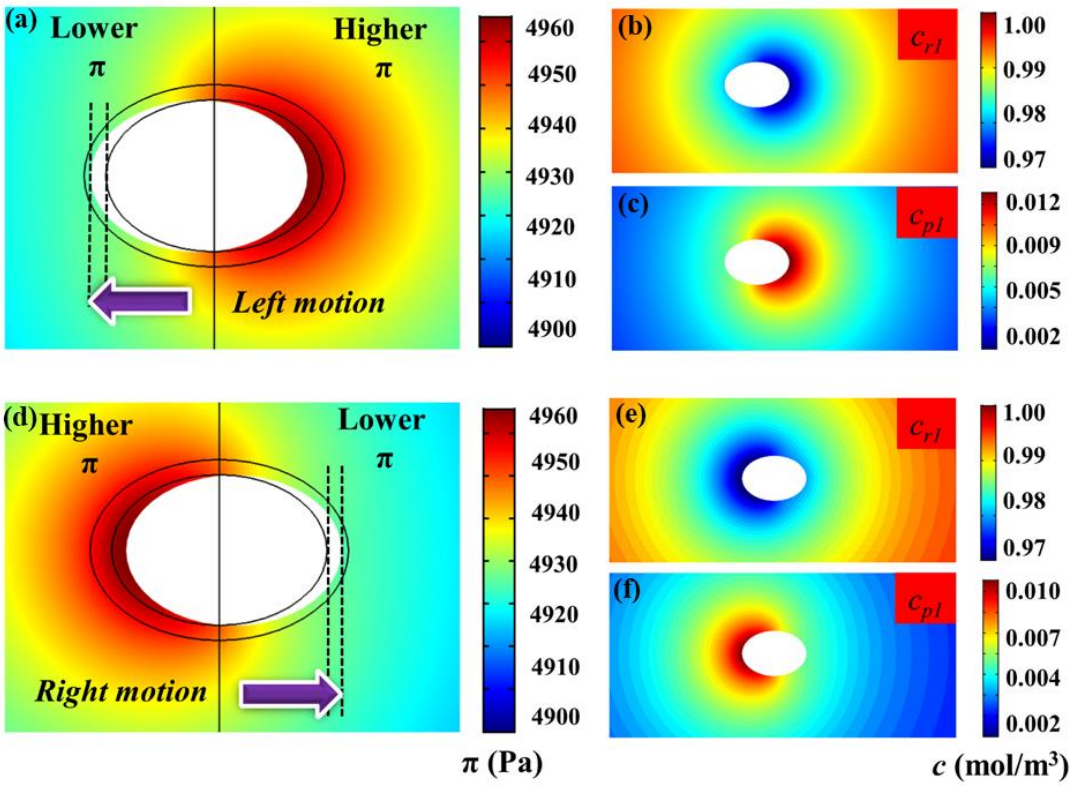

Figure 6.8: Plot (a) shows the contour of the osmotic pressure, surrounding a particle having a higher reaction rate (k_R) at the right-hand side, with a particle moving from right to the left-hand side. Images (b) and (c) show contours of concentration of a reactant and a product. Plot (d) shows the contour of osmotic pressure, surrounding a particle having a higher reaction rate (k_L) at the left-hand side, with a particle moving left to right. Plots (e) and (f) show the concentration of contours of a reactant and a product surrounding the particle, respectively.

For the first particle, **Fig. 6.8(a)**, the higher reaction rate at the right-hand side gives rise to a lower concentration of the reactant in the right-hand side and a higher concentration of the product in the left-hand side of the particle, as shown in **Fig. 6.8(b)** and **6.8(c)**, respectively. Distribution of these components around the particle makes an inhomogeneous scenario to create a $\Delta\pi$ across the particle, as shown in **Fig. 6.8(a)**. The higher osmotic pressure develops at the right half of the particle facilitates the particle motion towards the left side. **Figure 6.8(d)** shows a particle having similar arrangements but the orientation is opposite, i.e. the left half of the particle offers higher reaction rate constant (k_L). The contour profiles of the reactant and the product are as shown in **Fig. 6.8(e)** and **6.8(f)**, respectively. The figure shows opposite nature owing to the opposite orientation of the particle.

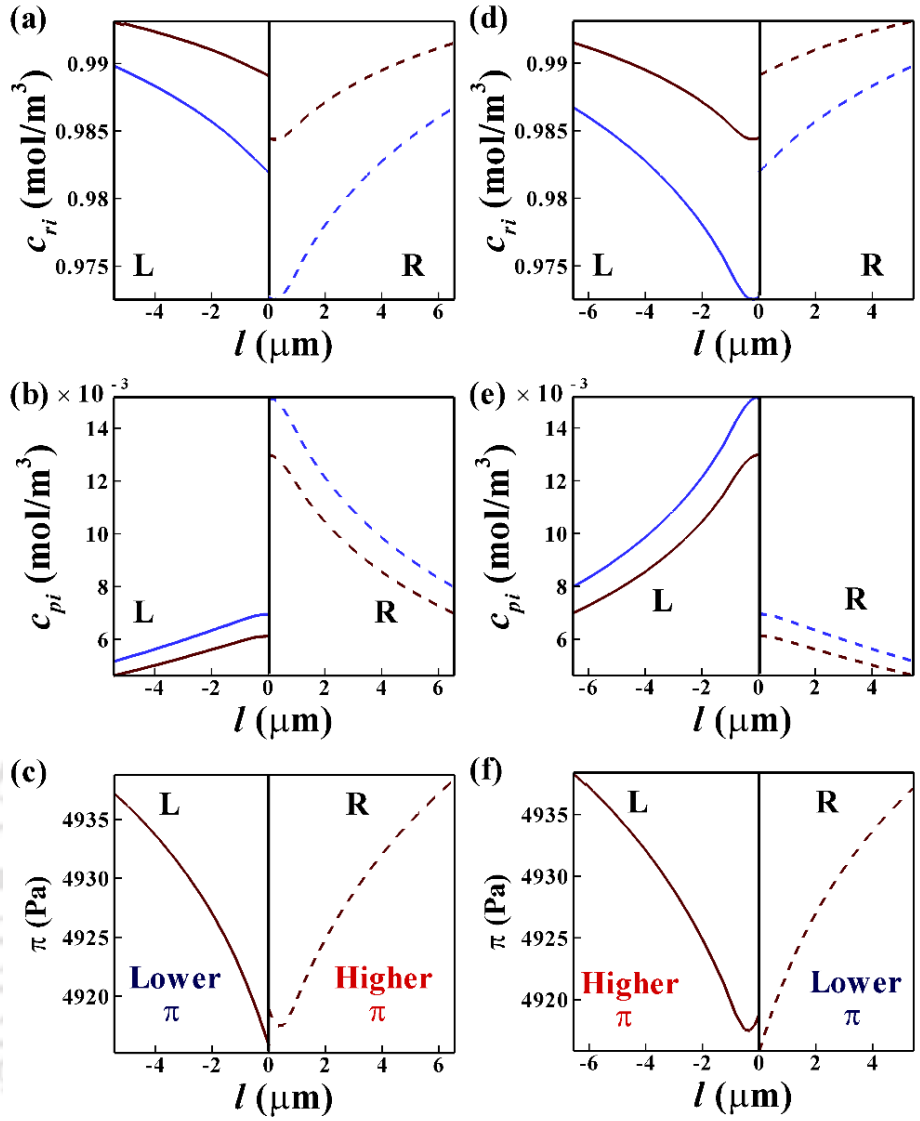

Figure 6.9: Images (a) to (c) show the reactant concentration, product concentration, and osmotic pressure vs distance from the particle surface (*l*) plots for a particle having a higher reaction kinetics on the right half of the particle. Images (d) to (f) show the reactant concentration, product concentration, and osmotic pressure vs distance from the particle surface (*l*) profiles for a particle having higher reaction rate constant on the left half of the particle.

Figure 6.9 shows the concentration plots of different reactants, products and also the osmotic pressure plots taken along the axis of the channel in the vicinity of the particle surface. For the purpose of representation, the coordinate of the particle surface is taken as '0' on both the ends of the particle. Distance from the right-hand side of the particle surface is taken as positive (+*l*) and distance from the left surface is taken as negative (-*l*). **Figure 6.9(a)** shows that the reactants diminish as we move away from the particle surface, whereas the concentration of the products increases away from the

particle surface as shown in **Fig. 6.9(b)**. **Figure 6.9(c)** shows the corresponding osmotic pressure profiles along a line taken from the particle surface and it shows a slight difference of ~ 1-2 Pa across the particle. Despite being a very small $\Delta\pi$, this meager pressure difference is capable of moving the particle ahead. **Figure 6.9(d)** to **6.9(f)** show exactly mirror images of the plots in **Fig. 6.9(a)** to **6.8(c)**. As all the other parameters are kept constant except change in the orientation of the particle, the profiles show an exact mirror image of the previous profiles. In this case, the particle moves from left to right, as discussed in the previous section, because the osmotic pressures build up is more on the left-hand side as compared to the right side.

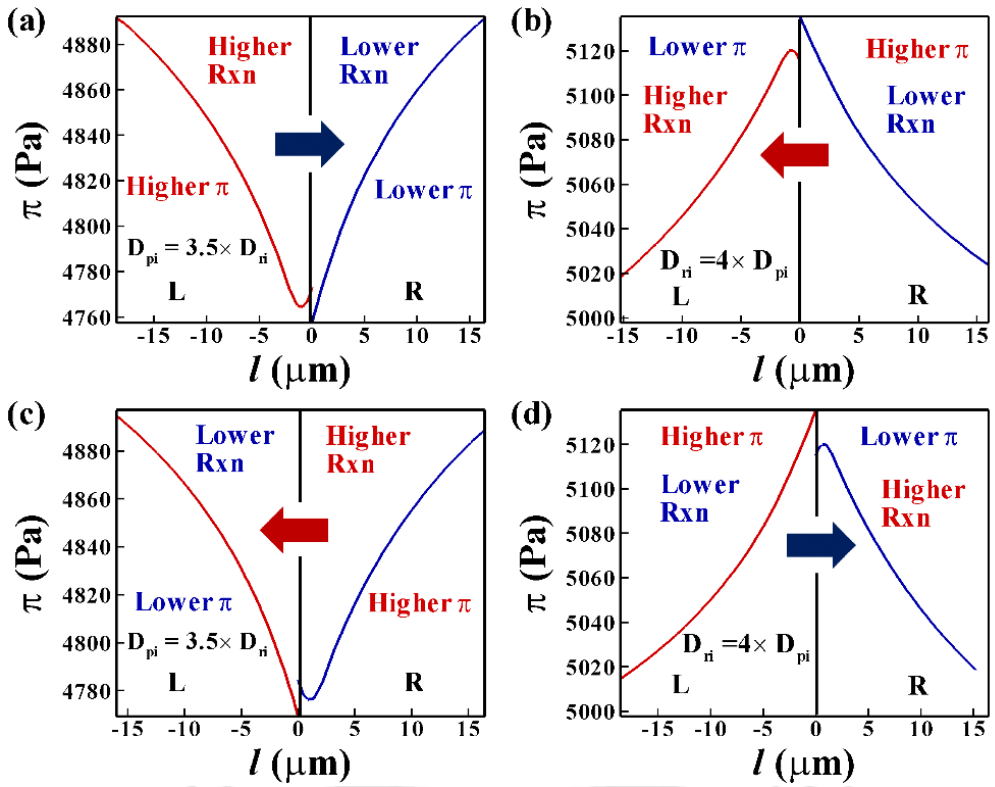

Figure 6.10: Images (a) to (d) show the osmotic pressure distribution taken on a line along the axis of the channel near the particle. The distance '*l*' is measured from the surface of the particle. Images (a) and (c) have higher diffusivity of product components (D_{pi}) than reactant components (D_{ri}) with alternating reaction rates at both sides as commented in the images. Images (b) and (d) have higher diffusivity of the reactant components (D_{ri}) than product components (D_{pi}) with alternating higher and lower reaction rates as indicated in the diagrams.

The development of the concentration profile for the components depends mainly on the reaction kinetics. However, the development of the $\Delta\pi$ across the particle is also determined by the component diffusivities. Component diffusivities actually make the

difference in cumulative concentration across the particle and hence it develops inhomogeneity of osmotic pressure across the channel. An inhomogeneity of concentration across the particle essentially means the development of $\Delta\pi$, which actually drives the particle. In the following section, four different situations are taken, as shown in **Fig. 6.10.** For simplicity and proper understanding, diffusivities of both the reactants and products are separately kept at constant values making different values for reactants and products. Two different orientations of the particle can be taken (one having a higher reaction rate constant on the left-hand side and another having a higher rate constant on the right side of the particle). For each situation, two different combinations are possible (diffusivities of reactants higher and diffusivities of products higher). As a whole, four different situations are taken for analysis.

In the present study, the reaction rates are tuned in different sides of the particle along with the diffusivities of the reactant and product components. Four different combinations can be made as shown in **Fig. 6.10**. Keeping the reaction rate higher on the right-hand side, we tuned diffusivities of the reactants and the products (**Fig. 6.10(a)** and **(b))** and vice versa (**Fig. 6.10(c)** and **6.10(d)**). Reaction rate constant having higher rate kinetics is kept at 8.80 $M^{-1}s^{-1}$ whereas the lower rate constant is kept at 0.88 $M^{-1}s^{-1}$. The osmotic pressure builds up as per the parameters taken for simulation. In **Fig. 6.10(a)** and **(c)** the diffusivity ratio is kept at 3.5 whereas in the case of **Fig. 6.10(b)** and **6.10(d)** the diffusivity ratio is made 4.0. It is evident from **Fig. 6.10(b)** and **6.10(d)** show that more the diffusivity ratio more is the osmotic pressure and also the $\Delta\pi$ builds up around the particle. Interestingly, **Fig. 6.10(a)** and **6.10(c)** differ from the **Figs. 6.10(b)** and **6.10(d)**. **Figure 6.10(b)** and **6.10(d)** show exactly the opposite trend than that of **Fig. 6.10(a)** and **6.10(c)**.

In the case of **Fig. 6.10(a)** and **6.10(c)**, where reactants have higher diffusivity, the osmotic pressure is lower at the particle surface and it increases away from the particle surface. However, in **Fig. 6.10(b)** and **6.10(d)**, where the product has higher diffusivities, the opposite trend is found, i.e. the osmotic pressure is higher near the particle surface and it diminishes with distance from particle surface. In fact, when the product components have higher diffusivity then those product components tend to go away from the surface making the outside more entropy zone (**Fig. 6.10(a)** and **6.10(c)**). In the case, where product components have lower diffusivities, the product molecules tend to stay near the particle making the zone with a higher osmotic pressure. In each

plot, we have shown the direction of the particle motion by arrows. A blue arrow signifies left to right motion and red arrow denotes motion from right to the left-hand side of the particle. The plot summarizes the fact of anomalous particle motion for this kind of chemophoretic automated motion.

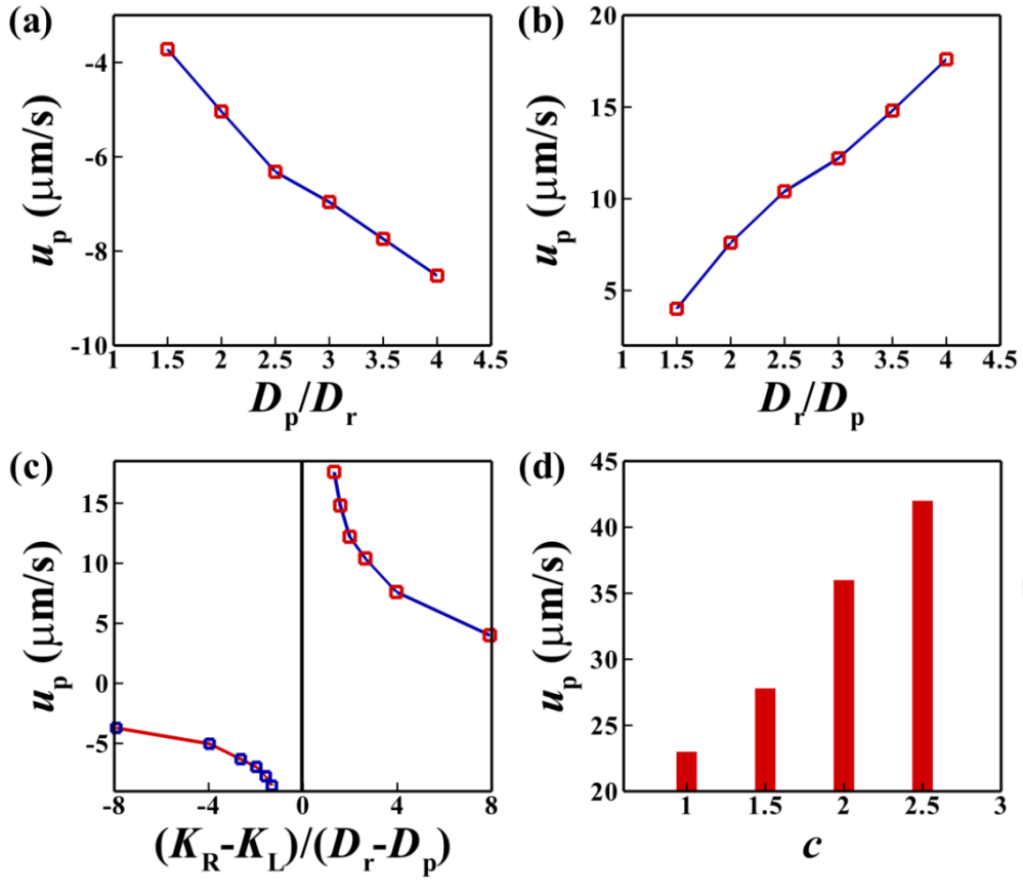

Figure 6.11: Plot (a) and (b) show the particle velocity against the ratio of (D_p/D_r) and (D_r/D_p) respectively. The right-hand side of the particle has a higher reaction rate (k_R = 8.80 $M^{-1}s^{-1}$) compared to the left-hand side (k_L = 0.88 $M^{-1}s^{-1}$) of the particle. Image (c) shows the particle velocity against a coefficient defined as ($[k_L-k_R]/[D_r-D_p]$). Image (d) shows the variation of particle velocity for a reaction where there is an increase of entropy with respect to stoichiometric coefficient c. The stoichiometry of the reaction is $aA+bB \rightarrow cC+dD$.

Diffusivities of the components determine the direction of the particle motion as it develops the opposite $\Delta\pi$ on tuning the diffusivities of the reactants and products. The reaction rate constants are kept constant on both sides. In this case, higher reaction rate is considered on the right-hand side (k_R = 8.8 $M^{-1}s^{-1}$) and lower reaction rate on the left-hand side (k_L = 0.88 $M^{-1}s^{-1}$). **Figure 6.11(a)** shows particle velocity variations with the change of the ratio of product to reactant diffusivity (D_p/D_r). In this case, such a $\Delta\pi$ is developed where the right-hand side develops higher osmotic pressure to move the

particle moves towards the left-hand side of the channel. This is expressed by negative velocity in the figure. As the product to reactant diffusivity (D_p/D_r) increases the particle shows the higher magnitude of the velocity.

Figure 6.11(b) shows the opposite case, where the reactants have higher diffusivities compared to the products. In this scenario, the osmotic pressure builds up more in the left-hand side and hence it drives the particle from left to right side of the channel and the same is shown as positive velocity in the **Fig. 6.11(b)**. It has been observed that the fate of the particle, that is both the direction and the magnitude of velocity of the particle, actually depends on both differences in rate constants and difference in diffusivity values. We have defined a coefficient ($[k_L\text{-}k_R]/[D_r\text{-}D_p]$, on which the particle velocity depends. Here, D_r and D_p denote the average of diffusivities of the reactant components and product components respectively. The positive value of the coefficient shows velocity in the positive direction whereas the negative valued coefficient shows velocity in the left-hand direction. However, the magnitude of velocity differs for the equal magnitude of the coefficient having different signs. In addition to the difference in diffusivities and reaction kinetics, the stoichiometric ratios also determine the motion of the particle. In this case, we have defined such a reaction, where the number of components increases with the reaction. We have defined a reaction, where one of the products (C) increases in number as reaction propagates. The more the formation of the product the more is the osmotic pressure build up around the particle. **Figure 6.11(d)** shows a linear increment of the particle velocity as we increase the stoichiometric coefficient 'c'.

6.6. CONCLUSIONS

In this study, we performed a comprehensive analysis of the motions of a Janus particle moving under the effect of the developed $\Delta\pi$ across the particle. The $\Delta\pi$ across the particle is developed as a result of combined effects of inhomogeneous catalytic reaction near the particle surface, externally applied concentration gradient. Self-propulsions due to the differential chemical reaction have also been studied in detail. Such motions are simulated considering the full descriptions of hydrodynamic equations, reaction-convection-diffusion equations, and fluid-structure interaction equations with appropriate boundary conditions. The key findings of this study are,

(i) The numerical simulations under a finite element framework uncover that the differential rate kinetics on the surfaces of a Janus particle helps in building up an osmotic pressure gradient across the particle owing to the variations in the concentrations of the reactants and products, which eventually helps in driving the motor. Presence of an imposed chemical potential gradient across the Janus particle can facilitate as well as reverse the motion of the particle. This happens based on the strength of concentration gradient imposed near the particle to tune the net osmotic pressure imbalance.

(ii) Reaction kinetics and the diffusivity of the components together steer the motion of the particle for a situation where the physical properties of the reacting medium, as well as the other simulation parameters are kept constant.

(iii) A coefficient $[k_L\text{-}k_R]/[D_r\text{-}D_p]$ has been defined, which can be employed to correlate the speed of the particle with the magnitudes of the diffusivities and rate constants of the entire chemotactic system considered.

(iv) A change in overall stoichiometric numbers of the products with respect to the number of reactants can actually have a significant influence on the motion of the particle. A reaction generating more stochiometric products can actually impart higher velocity to the particle.

Concisely, the present study uncovers many interesting facts about a particle moving under $\Delta\pi$ around a Janus particle having different reaction kinetics at different end.

Chapter 7

Conclusions and Future Scopes

In summary, the present thesis explores, (i) the dependence of electrophoretic migration speed and direction of a uniformly charged or 'Janus', with respect to heterogeneous surface charge, motor under the application of external electric field.; (ii) initiation and enhancement of micromixing in the electroosmotic flows inside rigid, flexible, and physicochemically heterogeneous microchannels; (iii) effect of various parameters on the charge storage capacity of EDL supercapacitors; (iv) development of a multimodal 3G CNT bots based on carbon nanotube composite material, which is capable of showing chemo-, magneto- and photo-taxis motion and performing energy harvesting, and dye degradation duties; and (v) study of the dependence of chemotactic motion of a 'Janus' particle, which respect to different catalytic reaction activities on particle surface, on reaction kinetics, component diffusivities, and reaction stoichiometry. The major conclusions drawn from each technical chapter are as follows,

(i) In the second chapter, electrophoresis of a charged particle inside a microfluidic channel has been explored in detail. With the help of CFD simulations, Poisson–Nernst–Planck equations, mass and momentum balance equations along with fluid structure interaction employing moving–deforming–mesh is solved to uncover the most accurate picture of electrophoretic motions. The study reveals that dynamic and unsteady EDL formation and its distortion affect the electrophoretic migration and also uncovers the time scale of EDL formation and steady electrophoretic migration. The particle size, fluid viscosity, drag on the particle and the fluid, applied field intensity, and surface potential and most importantly chemical heterogeneity on particle surface are found to influence the speed of the particles significantly, which has not been explored so far.

(ii) In the third chapter, electroosmotic motion of weak electrolyte inside physico-chemically patterned channels has been explored in detail with the help of CFD simulations. The simulations uncover a host of steady and unsteady flow profiles of EO flow profiles inside chemically, physicochemically, and flexible surfaces. Further, the strategic use of periodic patches of chemical and physicochemical patterns on the surface of the channel shows the emergence of the localized back flows, which in turn facilitates the formation of the zone of recirculation inside the channel. It has been observed that the strength of the recirculation can be increased by enhancing the intensity of the applied field, reducing the channel diameter, and imparting flexibility to the channel walls. Interestingly, the variation in the current density in the EDL near

the chemical or physicochemical patches is found to be useful in the measurement of the variations in the ζ-potentials of the biological surfaces.

(iii) In the fourth chapter, we explored charge storage capacities of parallel and curved plate supercapacitors, which are based on graphene oxide. Experiments uncovered electrode polarization at smaller time scales, Stern layer formation at the intermediate ones, and the formation of the diffuse layer at much larger time scales. A physical model composed of the Poisson−Nernst−Planck equations for the electric field in electrolyte and the Laplace equation for the electric field in electrodes was coupled with the Navier−Stokes equations for the electrolyte numerically solved with appropriate boundary conditions to corroborate the spatiotemporal experimental behaviors observed for the SCs. The use of net electric field originating from the (i) electrode polarization due to the applied field and (ii) opposing field in the electrolyte during the EDL formation during the evaluation of capacitance has been found to be more accurate in explaining the experimental results. The theoretical and experimental results together suggest that charge storage of SCs heavily depends on electrode geometry, type of electrolyte, electrolyte concentration, electrode separation, separator type, and dielectric relaxation of the electrolyte.

(iv) In fifth chapter, an experimental work on 3G micromotor based on carbon nanotubes uncovers multimodal motion with multiple controls. Such micromotors are capable of showing energy harvesting in fuel cell and dye degradation applications. A 3G CNT-bot capable of showing four different types of acid and alkali taxes inside peroxide and water baths in a single embodiment. The bot is also capable of showing magneto taxis and photo taxis motion. A single embodiment of the CNT-bot could show three different types of bubble propulsions, ejection of hydrogen bubble in acidic or normal water, ejection of oxygen in a peroxide fuel, and ejection of carbon dioxide bubbles in an alkaline solution. The motor could perform dye degradation job via advanced oxidation process owing to appearance of hydroxyl radical during the course of its motion. A proof-of-concept prototype for real time energy harvesting has been demonstrated in which the CNT-bots have been employed to generate pure oxygen and hydrogen gases for a PEM fuel cell to generate an electric field potential as high as ~150 mV.

(v) In the sixth chapter, self-propulsion or external chemical concentration driven propulsions of micro motors have been explored theoretically with similar CFD

simulations. Generation of local osmotic pressure imparts motion to the particle. This is basically a Janus kind of particle, which is capable of hosting two different rate kinetics, can undergo chemophoretic motion by exploiting chemical energy stored in the reactants. An external chemical gradient near to the Janus particle can affect the particle motion as well as it can reverse the motion of the particle based on the strength of concentration gradient present near the particle. Reaction kinetics, the diffusivity of the components together steers the motion of the particle for a situation where the physical properties of the reacting medium, as well as the other simulation parameters are kept constant. A coefficient $[k_L\text{-}k_R]/[D_r\text{-}D_p]$ has been defined, which guides the particle velocity, both the magnitude and reaction. A change in entropy, with respect to the stoichiometry of the reaction, can actually tune the motion of the particle. A reaction, which generates more randomness to the system, can actually impart higher velocity to the particle.

Future Scopes

The present thesis opens up various possibilities of future studies in both theoretical and experimental fonts. For example,

(i) in the second chapter, we explored different aspects of electrophoretic migration of a charged particle inside microscale channels. However, the present thesis did not explore the effect of induced charge, particle deformability, channel deformability, migration of charged liquid droplets, and effect of fluid structure interactions on non-uniform and alternating electric fields.

(ii) In the third chapter, we explored combined effect of physical, chemical heterogeneity, and channel deformability on micromixing in the case of electroosmotic flows inside microfluidic channels. However, there are more opportunities to be explored in the same line as the present thesis does not elaborate electroosmotic mixing in the cases of nanochannels, where EDLs interfere with each other and develop a different kind of electrokinetic environment.

(iii) In the fourth chapter, we explored charged storage capacities for PPS, and CPS geometries. The chapter also explored different time scales of EDL formation, effect of uniform and nonuniform external fields and many more. However, there are many other scopes that remain unexplored, for example, effects of different materials on CPS

model, surface patterning of the plates, or material modifications and replacements, among others.

(iv) The fifth chapter attempts to develop a multimodal and multifunctional 3G micromotors, to power fuel cell and doing environmental cleaning job. However, there are possibilities of making these 3G micromotors more suitable for human body. i.e. biocompatible, in order to exploit them as microsurgery robots, drug delivery agents. The efficiency of energy generation by these motors also needs further research.

(vi) The sixth chapter theoretically explores chemophoretic migration of 'Janus' kinds of micromotors. It takes care of the osmotic pressure imbalance force and it was considered that the speed of the motor generates from osmotic pressure only. However, the motion of a 'Janus' particles in reacting environment is more complex in nature. There are various factors, such as Brownian motion, surface tension imbalance, temperature imbalance, generation of local electric field in case of ionic environment, and these factors affect the speed and direction of the motion. Thus, theoretical modelling of all these aspects is expected to provide a more most accurate picture of a particle motion in a reacting medium.

LIST OF PUBLICATIONS

1. Journal Publications

1.1 From Thesis:

1. A. Dixit, S. Middya, **S. Mitra**, S. Maity, M. Bhattacharjee, D. Bandyopadhyay, Unexplored Pathways to Charge Storage in Supercapacitors, *J. Phys. Chem. C*, **2018**, 123, (1), 195-204.DOI: 10.1021/acs.jpcc.8b10326

2. **S. Mitra**, S. Mukherjee, A. Ghosh, D. Bandyopadhyay, Effects of Fluid-Structure-Interaction and Surface Heterogeneity on the Electrophoresis of Microparticles, *Ind. Eng. Chem. Res.*, **2019**, DOI: 10.1021/acs.iecr.8b06345

3. **S. Mitra**, N. Roy, S. Maity, Multimodal Chemo-Magneto-Photo-Taxes of 3G CNT-bots to Power Fuel Cells, *J. Microsys. Nano Eng.* (Under minor Review)

4. **S. Mitra**, S. Maity, S. Sutradhar, Electrosmosis with Augmented Mixing in Rigid to Flexible Microchannels with Surface Patterns, *Ind. Eng. Chem. Res.*

5. **S. Mitra**, A. Pashupalak, D. Bandyopadhyay, S. Majumdar, A CFD simulation study on behaviors of micro swimmers under external chemical gradient and self-propulsion (Manuscript under preparation)

1.2 From Collaboration:

6. S. Thakur, S. Rarotra, M. Bhattacharjee, **S. Mitra**, Gayatri Natu, T. K. Mandal, A. K. Dasmahapatra, and D. Bandyopadhyay, Self-Organized Large-Scale Integration of Mesoscale-Ordered Heterojunctions for Process-Intensified Photovoltaics, *Phys. Rev. Appl.*, **2018**, 10, (6), 064012 DOI: 10.1103/PhysRevApplied.10.064012

7. B. Ravi, S. Chakraborty, M. Bhattacharjee, **S. Mitra**, A. Ghosh, P. S. G. Pattader, and D. Bandyopadhyay, Pattern-Directed Ordering of Spin-Dewetted Liquid Crystal Micro- or Nanodroplets as Pixelated Light Reflectors and Locomotives, *ACS Appl. Mater. Interfaces*, **2016**, 9, (1), 1066-1076. DOI: 10.1021/acsami.6b12182

8. E. A. Shevchenko, **S. Mitra**, S. A. Ermakov, A. G. Titov, A. A. Ermakov, P. S. G. Pattader, Joint mass transfer of two components associated with the spontaneous interfacial convection in the liquid-liquid extraction system, *Chem. Eng. Sci.*, **2018**, 195, 301-311DOI: 10.1016/j.ces.2018.09.018

9. S. Maity, J. Chaudhuri, **S. Mitra**, S. Rarotra and D. Bandyopadhyay, Electric Field Assisted Multicomponent Reaction in a Microfluidic Reactor for Superior Conversion and Yield, *Electrophoresis*, **2018**, 40, (3), 401-409 DOI: 10.1002/elps.201800377

10. N. Mandal, **S. Mitra**, D. Bandyopadhyay, Paper-Sensors for Point-of-Care Monitoring of Drinking Water Quality, *IEEE Sens. J.*, **2019**, DOI: 10.1109/JSEN.2019.2919269

11. N. Roy, **S. Mitra,** N. Das, N. Mandal, H. B. Nemade, D. Bandyopadhyay, T. K. Mandal, Paper Based Enzymatic Chemiresistor for POC Detection of Ethanol in Human Breath, *IEEE Sens. J.* (Under Review)

12. **S. Mitra**, E. Shevchenko, S. Singh, M. Sachan, A. Ghosh, M. Basak, P.S.G. Pattader, Efficient Micro Extraction Process Exploiting Spontaneous Interfacial Convection Driven By Marangoni And Electric Field Instability: A Computational Fluid Dynamics Study (Manuscript Submitted)

13. **S.Mitra**, E. Shevchenko, S. A. Ermakov, P.S.G. Pattader, Multicomponent Counter Mass Transfer in Liquid-Liquid Extraction in Presence of Spontaneous Interfacial Convection, *Solvent Extr. Ion Exch.* (Under Review)

2. Conference Publications

1. A Computational Study on the Periodic Drop Formation Employing the Electric Field Lithography, **S. Mitra**, A. Ghosh, S. Maity and D. Bandyopadhyay, 4th *International Conference on Advanced Nanomaterial and Nanotechnology (ICANN – 2015)*, IIT Guwahati, Guwahati, India, 2015. (Poster)

2. Motion of a Particle to Achieve Mixing Inside a Micro-Channel Exploiting Lorentz Force: A Computational Study, **S. Mitra** and D. Bandyopadhyay, *2nd International Conference on Material Science (ICMS – 2017)*, Tripura University, Suryamaninagar, Tripura West, Agartala, Tripura, 2017. (Poster)

3. Mathematical Modelling of Reactive-diffusion Phenomenon Involving Higher Order Reaction, **S. Mitra**, A. Ghosh, S. Maity and D. Bandyopadhyay, *CHEMCON – 2015*, IIT Guwahati, Guwahati, India, 2015. (Presentation)

4. A Computational Study on Travelling Wave Periodic Column/Hole Formation Employing Electric Field Lithography, **S. Mitra,** A. Ghosh, and D. Bandyopadhyay, *International Conference on Emerging Trends in Nanoscience and Nanotechnology*

(ICETINN – 2017), Sikkim Manipal Institute of Technology, Majitar, Sikkim, India, 2017. (Presentation)

5. MWCNT, AuNP nanocomposite based POCT sensor for quantitative detection of urea in biological samples, Nirmal Roy, **S. Mitra** and T. K. Mandal, *Research Conclave*, IIT Guwahati, 2018, Indian Institute of Technology, Guwahati, Assam, India. (Poster)

6. Magnesium Coated Thiol-Functionalized Carbon-Nanotubes as Microswimmers for efficient Arsenic Capture and Sensing, **S. Mitra**, N. Roy, D. Bandyopadhyay, Carbon MEMS, 2018, IIT Hyderabad, Hyderabad, India. (Poster)

7. Magnesium Coated Thiol-Functionalized Carbon-Nanotubes as Microswimmers for efficient Arsenic Capture and Sensing, **S. Mitra**, N. Roy, D. Bandyopadhyay, CompFlu, 2018, IIT Roorkee, Roorkee, India. (Poster)

8. Efficient Micro Extraction Process Exploiting Spontaneous Interfacial Convection Driven by Marangoni and Electric Field Instability: A Computational Fluid Dynamics Study, **S. Mitra**, P.S.G. Pattader, CompFlu, 2018, IIT Roorkee, Roorkee, India. (Poster)

9. Effects of Fluid-Structure-Interaction and Surface Heterogeneity on the Electrophoresis of Microparticles, **S. Mitra**, S. Mukherjee, A. Ghosh, CompFlu, 2018, IIT Roorkee, Roorkee, India. (Presentation)

10. Multimodal Chemo-Magneto-Photo-Taxes of 3G CNT-bots to Power Fuel Cells, **S. Mitra**, N. Roy, S. Maity, Lab on a Chip, Mumbai 2019, India. (Presentation)

11 Multicomponent Counter Mass Transfer in Liquid-Liquid Extraction in Presence of Spontaneous Interfacial Convection, **S.Mitra**, E. Shevchenko, S. A. Ermakov, P.S.G. Pattader, Alumni Symposium, Calcutta University, 2019, India. (Presentation)

3. Patents

1. N. Roy, **S. Mitra,** N. Das, N. Mandal, H. B. Nemade, D. Bandyopadhyay, T. K. Mandal, Paper Based Enzymatic Chemiresistor for POC Detection of Ethanol in Human Breath (Patent under preparation)

2. M. Basak, **S. Mitra,** A. Vyas, S. Maity, D. Bandyopadhyay, M. Sachdev, Portable Device for Colorimetric Detection of Cervical Cancer Biomarker (Patent under preparation)

References

(1) Elgeti, J.; Winkler, R. G.; Gompper, G., Physics of microswimmers—single particle motion and collective behavior: a review. *Rep. Prog. Phys.* **2015,** *78*, (5), 056601.

(2) Zheng, X.; ten Hagen, B.; Kaiser, A.; Wu, M.; Cui, H.; Silber-Li, Z.; Löwen, H., Non-Gaussian statistics for the motion of self-propelled Janus particles: Experiment versus theory. *Phys. Rev. E* **2013,** *88*, (3), 032304.

(3) Renn, M. J.; Pastel, R.; Lewandowski, H. J., Laser guidance and trapping of mesoscale particles in hollow-core optical fibers. *Phys. Rev. Lett.* **1999,** *82*, (7), 1574.

(4) Baraban, L.; Harazim, S. M.; Sanchez, S.; Schmidt, O. G., Chemotactic behavior of catalytic motors in microfluidic channels. *Angew. Chem., Int. Ed.* **2013,** *52*, (21), 5552-5556.

(5) Gangwal, S.; Cayre, O. J.; Bazant, M. Z.; Velev, O. D., Induced-charge electrophoresis of metallodielectric particles. *Phys. Rev. Lett.* **2008,** *100*, (5), 058302.

(6) Keh, H.-J.; Anderson, J., Boundary effects on electrophoretic motion of colloidal spheres. *J. Fluid Mech.* **1985,** *153*, 417-439.

(7) Lee, C.-Y.; Chang, C.-L.; Wang, Y.-N.; Fu, L.-M., Microfluidic mixing: a review. *Int. J. Mol. Sci.* **2011,** *12*, (5), 3263-3287.

(8) Li, F.-C.; Kinoshita, H.; Li, X.-B.; Oishi, M.; Fujii, T.; Oshima, M., Creation of very-low-Reynolds-number chaotic fluid motions in microchannels using viscoelastic surfactant solution. *Experimental Thermal and Fluid Science* **2010,** *34*, (1), 20-27.

(9) Sudarsan, A. P.; Ugaz, V. M., Fluid mixing in planar spiral microchannels. *Lab on a Chip* **2006,** *6*, (1), 74-82.

(10) Yang, R.-J.; Fu, L.-M.; Lin, Y.-C., Electroosmotic flow in microchannels. *J. Colloid Interface Sci.* **2001,** *239*, (1), 98-105.

(11) TermehYousefi, A.; Bagheri, S.; Adib, N., Integration of biosensors based on microfluidic: a review. *Sens. Rev.* **2015,** *35*, (2), 190-199.

(12) Han, K. N.; Li, C. A.; Seong, G. H., Microfluidic chips for immunoassays. *Annu. Rev. Anal. Chem.* **2013,** *6*, 119-141.

(13) Cui, F.; Rhee, M.; Singh, A.; Tripathi, A., Microfluidic sample preparation for medical diagnostics. *Annu. Rev. Biomed. Eng.* **2015,** *17*, 267-286.

(14) Malek, C. G. K., Laser processing for bio-microfluidics applications (part II). *Anal. Bioanal. Chem.* **2006,** *385*, (8), 1362-1369.

(15) Domachuk, P.; Tsioris, K.; Omenetto, F. G.; Kaplan, D. L., Bio-microfluidics: biomaterials and biomimetic designs. *Adv. Mater.* **2010,** *22*, (2), 249-260.

(16) Exchangers, M. H., *Microreactors: new technology for modern chemistry*. Weinheim: Wiley/VCH: 2000.

(17) Wang, X.; Cheng, C.; Wang, S.; Liu, S., Electroosmotic pumps and their applications in microfluidic systems. *Microfluid. Nanofluid.* **2009,** *6*, (2), 145-162.

(18) Yamamoto, D.; Shioi, A., Self-propelled nano/micromotors with a chemical reaction: Underlying physics and strategies of motion control. *KONA Powder Part. J.* **2015**, 2015005.

(19) Moo, J. G. S.; Pumera, M., Chemical energy powered nano/micro/macromotors and the environment. *Chemistry–A European Journal* **2015,** *21*, (1), 58-72.

(20) Saville, D.; Palusinski, O., Theory of electrophoretic separations. Part I: Formulation of a mathematical model. *AIChE J.* **1986,** *32*, (2), 207-214.

(21) Lin, C.-H.; Wang, J.-H.; Fu, L.-M., Improving the separation efficiency of DNA biosamples in capillary electrophoresis microchips using high-voltage pulsed DC electric fields. *Microfluid. Nanofluid.* **2008,** *5*, (3), 403-410.

(22) Malek, C. G. K., Laser processing for bio-microfluidics applications (part I). *Anal. Bioanal. Chem.* **2006,** *385*, (8), 1351-1361.

(23) Nelson, B. J.; Kaliakatsos, I. K.; Abbott, J. J., Microrobots for minimally invasive medicine. *Annu. Rev. Biomed. Eng.* **2010,** *12*, 55-85.

(24) Patra, D.; Sengupta, S.; Duan, W.; Zhang, H.; Pavlick, R.; Sen, A., Intelligent, self-powered, drug delivery systems. *Nanoscale* **2013,** *5*, (4), 1273-1283.

(25) Xuan, M.; Shao, J.; Lin, X.; Dai, L.; He, Q., Self-propelled janus mesoporous silica nanomotors with sub-100 nm diameters for drug encapsulation and delivery. *ChemPhysChem* **2014,** *15*, (11), 2255-2260.

(26) Jeong, B.; Bae, Y. H.; Lee, D. S.; Kim, S. W., Biodegradable block copolymers as injectable drug-delivery systems. *Nature* **1997,** *388*, (6645), 860.

(27) Gao, W.; Kagan, D.; Pak, O. S.; Clawson, C.; Campuzano, S.; Chuluun-Erdene, E.; Shipton, E.; Fullerton, E. E.; Zhang, L.; Lauga, E., Cargo-towing fuel-free magnetic nanoswimmers for targeted drug delivery. *small* **2012,** *8*, (3), 460-467.

(28) Baraban, L.; Makarov, D.; Streubel, R.; Monch, I.; Grimm, D.; Sanchez, S.; Schmidt, O. G., Catalytic Janus motors on microfluidic chip: deterministic motion for targeted cargo delivery. *ACS nano* **2012,** *6*, (4), 3383-3389.

(29) Ma, X.; Hahn, K.; Sanchez, S., Catalytic mesoporous Janus nanomotors for active cargo delivery. *J. Am. Chem. Soc.* **2015,** *137*, (15), 4976-4979.

(30) Kwon, S.-H.; Park, J.; Kim, W. K.; Yang, Y.; Lee, E.; Han, C. J.; Park, S. Y.; Lee, J.; Kim, Y. S., An effective energy harvesting method from a natural water motion active transducer. *Energy Environ. Sci.* **2014,** *7*, (10), 3279-3283.

(31) Dhiman, P.; Yavari, F.; Mi, X.; Gullapalli, H.; Shi, Y.; Ajayan, P. M.; Koratkar, N., Harvesting energy from water flow over graphene. *Nano Lett.* **2011,** *11*, (8), 3123-3127.

(32) He, Y.; Huang, Z.; Chen, B.; Tsutsui, M.; Miao, X. S.; Taniguchi, M., Electrokinetic Analysis of Energy Harvest from Natural Salt Gradients in Nanochannels. *Sci. Rep.* **2017,** *7*, (1), 13156.

(33) Mou, F.; Chen, C.; Ma, H.; Yin, Y.; Wu, Q.; Guan, J., Self-Propelled Micromotors Driven by the Magnesium–Water Reaction and Their Hemolytic Properties. *Angew. Chem., Int. Ed.* **2013,** *52*, (28), 7208-7212.

(34) Yánez-Sedeño, P.; Campuzano, S.; Pingarrón, J., Janus particles for (bio) sensing. *Applied Materials Today* **2017,** *9*, 276-288.

(35) Li, J.; Singh, V. V.; Sattayasamitsathit, S.; Orozco, J.; Kaufmann, K.; Dong, R.; Gao, W.; Jurado-Sanchez, B.; Fedorak, Y.; Wang, J., Water-driven micromotors for rapid photocatalytic degradation of biological and chemical warfare agents. *ACS nano* **2014,** *8*, (11), 11118-11125.

(36) Sánchez, S.; Soler, L.; Katuri, J., Chemically powered micro-and nanomotors. *Angew. Chem., Int. Ed.* **2015,** *54*, (5), 1414-1444.

(37) Gao, W.; Wang, J., The environmental impact of micro/nanomachines: a review. *Acs Nano* **2014,** *8*, (4), 3170-3180.

(38) Kuntaegowdanahalli, S. S.; Bhagat, A. A. S.; Kumar, G.; Papautsky, I., Inertial microfluidics for continuous particle separation in spiral microchannels. *Lab Chip* **2009,** *9*, (20), 2973-2980.

(39) Di Carlo, D., Inertial microfluidics. *Lab on a Chip* **2009,** *9*, (21), 3038-3046.

(40) Tsutsui, H.; Ho, C.-M., Cell separation by non-inertial force fields in microfluidic systems. *Mech. Res. Commun.* **2009,** *36*, (1), 92-103.

(41) Yang, R.-J.; Hou, H.-H.; Wang, Y.-N.; Fu, L.-M., Micro-magnetofluidics in microfluidic systems: A review. *Sens. Actuators, B* **2016,** *224*, 1-15.

(42) Cho, C.-C., Electrokinetically driven flow mixing utilizing chaotic electric fields. *Microfluid. Nanofluid.* **2008,** *5*, (6), 785-793.

(43) Davison, S.; Sharp, K., Transient electrophoretic motion of cylindrical particles in capillaries. *Nanoscale and microscale thermophysical engineering* **2007,** *11*, (1-2), 71-83.

(44) Lee, T. C.; Keh, H. J., Electrophoretic motion of a charged particle in a charged cavity. *European Journal of Mechanics-B/Fluids* **2014,** *48*, 183-192.

(45) Wu, Z.; Gao, Y.; Li, D., Electrophoretic motion of ideally polarizable particles in a microchannel. *Electrophoresis* **2009,** *30*, (5), 773-781.

(46) Ye, C.; Sinton, D.; Erickson, D.; Li, D., Electrophoretic motion of a circular cylindrical particle in a circular cylindrical microchannel. *Langmuir* **2002,** *18*, (23), 9095-9101.

(47) Wang, M.; He, L.; Yin, Y., Magnetic field guided colloidal assembly. *Mater. Today* **2013,** *16*, (4), 110-116.

(48) Fan, W.-T. L.; Pak, O. S.; Sandoval, M., Ellipsoidal Brownian self-driven particles in a magnetic field. *Phys. Rev. E* **2017,** *95*, (3), 032605.

(49) Yamane, Y.; Hemmatiyan, S.; Ieda, J. i.; Maekawa, S.; Sinova, J., Spinmotive force due to motion of magnetic bubble arrays driven by magnetic field gradient. *Sci. Rep.* **2014,** *4*, 6901.

(50) Yoshikawa, K., Spontaneous Mode Selection of Self-Motile Object under Chemical Noneqilibricity. *Procedia IUTAM* **2012,** *5*, 240-243.

(51) Brady, J. F., Particle motion driven by solute gradients with application to autonomous motion: continuum and colloidal perspectives. *J. Fluid Mech.* **2011,** *667*, 216-259.

(52) Shigematsu, T.; Kurosawa, M.; Asai, K. In *Investigation of surface acoustic wave motor's motion resolution determinant*, Proc. Wold Cong. on Acoustics 2003, 2003; 2003.

(53) Du, X.; Swanwick, M.; Fu, Y. Q.; Luo, J.; Flewitt, A.; Lee, D.-S.; Maeng, S.; Milne, W., Surface acoustic wave induced streaming and pumping in 128 Y-cut LiNbO3 for microfluidic applications. *J. Micromech. Microeng.* **2009,** *19*, (3), 035016.

(54) Nedev, S.; Carretero-Palacios, S.; Kühler, P.; Lohmüller, T.; Urban, A. S.; Anderson, L. J.; Feldmann, J., An optically controlled microscale elevator using plasmonic Janus particles. *ACS Photonics* **2015,** *2*, (4), 491-496.

(55) Keller, J. B.; Miksis, M. J., Surface tension driven flows. *SIAM J. Appl. Math.* **1983,** *43*, (2), 268-277.

(56) Cira, N. J.; Benusiglio, A.; Prakash, M., Dancing droplets: Autonomous surface tension-driven droplet motion. *Phys. Fluids* **2014,** *26*, (9), 091113.

(57) Suematsu, N. J.; Sasaki, T.; Nakata, S.; Kitahata, H., Quantitative estimation of the parameters for self-motion driven by difference in surface tension. *Langmuir* **2014,** *30*, (27), 8101-8108.

(58) Jong, W.; Kuo, T.; Ho, S.; Chiu, H.; Peng, S., Flows in rectangular microchannels driven by capillary force and gravity. *Int. Commun. Heat Mass Transfer* **2007,** *34*, (2), 186-196.

(59) Tachibana, H.; Saito, M.; Tsuji, K.; Yamanaka, K.; Tamiya, E., Self-propelled continuous-flow PCR in capillary-driven microfluidic device: Microfluidic behavior and DNA amplification. *Sens. Actuators, B* **2015,** *206*, 303-310.

(60) Jäggi, R. D.; Sandoz, R.; Effenhauser, C. S., Microfluidic depletion of red blood cells from whole blood in high-aspect-ratio microchannels. *Microfluid. Nanofluid.* **2007,** *3*, (1), 47-53.

(61) Datta, M.; McMaster, M.; Brewer, R.; Zhou, P.; Tsao, P.; Upadhaya, G.; Munch, M., Method of fabricating high surface to volume ratio structures and their integration in microheat exchangers for liquid cooling system. In Google Patents: 2010.

(62) Krishnan, M.; Burke, D. T.; Burns, M. A., Polymerase chain reaction in high surface-to-volume ratio SiO2 microstructures. *Anal. Chem.* **2004,** *76*, (22), 6588-6593.

(63) Ting, T. W.; Hung, Y. M.; Guo, N., Field-synergy analysis of viscous dissipative nanofluid flow in microchannels. *Int. J. Heat Mass Transfer* **2014,** *73*, 483-491.

(64) Sanaei, A.; Jamili, A.; Callard, J., Effects of Non-Darcy flow and pore proximity on gas condensate production from nanopore unconventional resources. **2014**.

(65) Khanikar, V.; Mudawar, I.; Fisher, T., Effects of carbon nanotube coating on flow boiling in a micro-channel. *Int. J. Heat Mass Transfer* **2009,** *52*, (15-16), 3805-3817.

(66) Hung, T.-C.; Yan, W.-M., Enhancement of thermal performance in double-layered microchannel heat sink with nanofluids. *Int. J. Heat Mass Transfer* **2012,** *55*, (11-12), 3225-3238.

(67) Chen, H.; Ran, T.; Gan, Y.; Zhou, J.; Zhang, Y.; Zhang, L.; Zhang, D.; Jiang, L., Ultrafast water harvesting and transport in hierarchical microchannels. *Nat. Mater.* **2018,** *17*, (10), 935.

(68) Keißner, A.; Brücker, C., Directional fluid transport along artificial ciliary surfaces with base-layer actuation of counter-rotating orbital beating patterns. *Soft Matter* **2012,** *8*, (19), 5342-5349.

(69) Bhuyan, T.; Bhattacharjee, M.; Singh, A. K.; Ghosh, S. S.; Bandyopadhyay, D., Boolean-chemotaxis of logibots deciphering the motions of self-propelling microorganisms. *Soft matter* **2018,** *14*, (16), 3182-3191.

(70) Bhuyan, T.; Singh, A. K.; Dutta, D.; Unal, A.; Ghosh, S. S.; Bandyopadhyay, D., Magnetic field guided chemotaxis of imushbots for targeted anticancer therapeutics. *ACS Biomater. Sci. Eng.* **2017,** *3*, (8), 1627-1640.

(71) Singh, A. K.; Dey, K. K.; Chattopadhyay, A.; Mandal, T. K.; Bandyopadhyay, D., Multimodal chemo–magnetic control of self-propelling microbots. *Nanoscale* **2014,** *6*, (3), 1398-1405.

(72) Capretto, L.; Cheng, W.; Hill, M.; Zhang, X., Micromixing within microfluidic devices. In *Microfluidics*, Springer: 2011; pp 27-68.

(73) Singh, V. V.; Soto, F.; Kaufmann, K.; Wang, J., Micromotor-Based Energy Generation. *Angew. Chem., Int. Ed.* **2015,** *54*, (23), 6896-6899.

(74) Ji, H.; Zhao, X.; Qiao, Z.; Jung, J.; Zhu, Y.; Lu, Y.; Zhang, L. L.; MacDonald, A. H.; Ruoff, R. S., Capacitance of carbon-based electrical double-layer capacitors. *Nat. Commun.* **2014,** *5*, 3317.

(75) Davis, J. A.; James, R. O.; Leckie, J. O., Surface ionization and complexation at the oxide/water interface: I. Computation of electrical double layer properties in simple electrolytes. *J. Colloid Interface Sci.* **1978,** *63*, (3), 480-499.

(76) Guldbrand, L.; Jönsson, B.; Wennerström, H.; Linse, P., Electrical double layer forces. A Monte Carlo study. *The Journal of chemical physics* **1984,** *80*, (5), 2221-2228.

(77) Grahame, D. C., The electrical double layer and the theory of electrocapillarity. *Chem. Rev.* **1947,** *41*, (3), 441-501.

(78) Oldham, K. B., A Gouy–Chapman–Stern model of the double layer at a (metal)/(ionic liquid) interface. *J. Electroanal. Chem.* **2008,** *613*, (2), 131-138.

(79) Stigter, D., Micelle formation by ionic surfactants. I. Two phase model, Gouy-Chapman model, hydrophobic interactions. *J. Colloid Interface Sci.* **1974,** *47*, (2), 473-482.

(80) González, A.; Goikolea, E.; Barrena, J. A.; Mysyk, R., Review on supercapacitors: technologies and materials. *Renewable Sustainable Energy Rev.* **2016,** *58*, 1189-1206.

(81) Wang, G.; Zhang, L.; Zhang, J., A review of electrode materials for electrochemical supercapacitors. *Chem. Soc. Rev.* **2012,** *41*, (2), 797-828.

(82) Vangari, M.; Pryor, T.; Jiang, L., Supercapacitors: review of materials and fabrication methods. *J. Energy Eng.* **2012,** *139*, (2), 72-79.

(83) Liu, H.-Y.; Wang, K.-P.; Teng, H., A simplified preparation of mesoporous carbon and the examination of the carbon accessibility for electric double layer formation. *Carbon* **2005,** *43*, (3), 559-566.

(84) Ivaništšev, V.; O'Connor, S.; Fedorov, M., Poly (a) morphic portrait of the electrical double layer in ionic liquids. *Electrochem. Commun.* **2014,** *48*, 61-64.

(85) Ai, Y.; Zeng, Z.; Qian, S., Direct numerical simulation of AC dielectrophoretic particle–particle interactive motions. *J. Colloid Interface Sci.* **2014,** *417*, 72-79.

(86) Peng, F.; Tu, Y.; Wilson, D. A., Micro/nanomotors towards in vivo application: cell, tissue and biofluid. *Chem. Soc. Rev.* **2017,** *46*, (17), 5289-5310.

(87) Sattayasamitsathit, S.; Kou, H.; Gao, W.; Thavarajah, W.; Kaufmann, K.; Zhang, L.; Wang, J., Fully loaded micromotors for combinatorial delivery and autonomous release of cargoes. *Small* **2014,** *10*, (14), 2830-2833.

(88) Gao, W.; Dong, R.; Thamphiwatana, S.; Li, J.; Gao, W.; Zhang, L.; Wang, J., Artificial micromotors in the mouse's stomach: A step toward in vivo use of synthetic motors. *ACS nano* **2015,** *9*, (1), 117-123.

(89) Gao, W.; Wang, J., Synthetic micro/nanomotors in drug delivery. *Nanoscale* **2014,** *6*, (18), 10486-10494.

(90) Lewis, R. W.; Humpheson, C.; Bruch Jr, J. C., Applications of Electro-Osmosis to Ground-Water Flow Problems. *Groundwater* **1975,** *13*, (6), 484-491.

(91) Kim, D.-S.; Park, J.-E.; Shin, J.-K.; Kim, P. K.; Lim, G.; Shoji, S., An extended gate FET-based biosensor integrated with a Si microfluidic channel for detection of protein complexes. *Sens. Actuators, B* **2006,** *117*, (2), 488-494.

(92) Choi, K.; Kim, J.-Y.; Ahn, J.-H.; Choi, J.-M.; Im, M.; Choi, Y.-K., Integration of field effect transistor-based biosensors with a digital microfluidic device for a lab-on-a-chip application. *Lab Chip* **2012,** *12*, (8), 1533-1539.

(93) Chen, J. K.; Yang, R. J., Electroosmotic flow mixing in zigzag microchannels. *Electrophoresis* **2007,** *28*, (6), 975-983.

(94) Gregersen, M. M.; Andersen, M. B.; Soni, G.; Meinhart, C.; Bruus, H., Numerical analysis of finite Debye-length effects in induced-charge electro-osmosis. *Phy. Rev. E* **2009,** *79*, (6), 066316.

(95) Herr, A.; Molho, J.; Santiago, J.; Mungal, M.; Kenny, T.; Garguilo, M., Electroosmotic capillary flow with nonuniform zeta potential. *Anal. Chem.* **2000,** *72*, (5), 1053-1057.

(96) Mirbozorgi, S.; Niazmand, H.; Renksizbulut, M., Electro-osmotic flow in reservoir-connected flat microchannels with non-uniform zeta potential. *J. Fluids Eng.* **2006,** *128*, (6), 1133-1143.

(97) Na, R.; Jian, Y.; Chang, L.; Su, J.; Liu, Q., Transient electro-osmotic and pressure driven flows through a microannulus. *Open J. Fluid Dyn.* **2013,** *3*, (02), 50.

(98) Yao, S.; Hertzog, D. E.; Zeng, S.; Mikkelsen Jr, J. C.; Santiago, J. G., Porous glass electroosmotic pumps: design and experiments. *J. Colloid Interface Sci.* **2003,** *268*, (1), 143-153.

(99) Levitan, J. A.; Devasenathipathy, S.; Studer, V.; Ben, Y.; Thorsen, T.; Squires, T. M.; Bazant, M. Z., Experimental observation of induced-charge electro-osmosis around a metal wire in a microchannel. *Colloids Surf., A* **2005,** *267*, (1-3), 122-132.

(100) Guy, R. H.; Kalia, Y. N.; Delgado-Charro, M. B.; Merino, V.; López, A.; Marro, D., Iontophoresis: electrorepulsion and electroosmosis. *J. Controlled Release* **2000,** *64*, (1-3), 129-132.

(101) Arulanandam, S.; Li, D., Liquid transport in rectangular microchannels by electroosmotic pumping. *Colloids Surf., A* **2000,** *161*, (1), 89-102.

(102) Dasgupta, P. K.; Liu, S., Electroosmosis: a reliable fluid propulsion system for flow injection analysis. *Anal. Chem.* **1994,** *66*, (11), 1792-1798.

(103) Perrett, D., 200 years of Electrophoresis. *Chromatog. Today* **2010**, 4-7.

(104) Abramson, H. A.; Gorin, M. H., Skin Reactions. VII. Relationship of Skin Permeability to Electrophoresis of Biologically Active Materials into the Living Human Skin. *J. Phys. Chem.* **1939,** *43*, (3), 335-346.

(105) Sadeghi, A.; Saidi, M. H.; Mozafari, A. A., Heat transfer due to electroosmotic flow of viscoelastic fluids in a slit microchannel. *International Journal of Heat and Mass Transfer* **2011,** *54*, (17-18), 4069-4077.

(106) Zhu, Z.; Lu, J. J.; Liu, S., Protein separation by capillary gel electrophoresis: a review. *Anal. Chim. Acta* **2012,** *709*, 21-31.

(107) Gordon, A. H.; Work, T. S.; Work, E., *Electrophoresis of proteins in polyacrylamide and starch gels*. North-Holland: 1969.

(108) Zoetendal, E. G.; Akkermans, A. D.; De Vos, W. M., Temperature gradient gel electrophoresis analysis of 16S rRNA from human fecal samples reveals stable and host-specific communities of active bacteria. *Appl. Environ. Microbiol.* **1998,** *64*, (10), 3854-3859.

(109) Muyzer, G.; De Waal, E. C.; Uitterlinden, A. G., Profiling of complex microbial populations by denaturing gradient gel electrophoresis analysis of polymerase chain reaction-amplified genes coding for 16S rRNA. *Appl. Environ. Microbiol.* **1993,** *59*, (3), 695-700.

(110) Pan, B.-f.; Gao, F.; Gu, H.-c., Dendrimer modified magnetite nanoparticles for protein immobilization. *J. Colloid Interface Sci.* **2005,** *284*, (1), 1-6.

(111) Zhang, Y.; Yang, M.; Portney, N. G.; Cui, D.; Budak, G.; Ozbay, E.; Ozkan, M.; Ozkan, C. S., Zeta potential: a surface electrical characteristic to probe the interaction of nanoparticles with normal and cancer human breast epithelial cells. *Biomed. Microdevices* **2008,** *10*, (2), 321-328.

(112) Bhattacharjee, S., DLS and zeta potential–what they are and what they are not? *J. Controlled Release* **2016,** *235*, 337-351.

(113) Tantra, R.; Schulze, P.; Quincey, P., Effect of nanoparticle concentration on zeta-potential measurement results and reproducibility. *Particuology* **2010,** *8*, (3), 279-285.

(114) Uskoković, V.; Castiglione, Z.; Cubas, P.; Zhu, L.; Li, W.; Habelitz, S., Zeta-potential and particle size analysis of human amelogenins. *J. Dent. Res.* **2010,** *89*, (2), 149-153.

(115) Xu, R., Progress in nanoparticles characterization: Sizing and zeta potential measurement. *Particuology* **2008,** *6*, (2), 112-115.

(116) Berne, B. J.; Pecora, R., *Dynamic light scattering: with applications to chemistry, biology, and physics*. Courier Corporation: 2000.

(117) Pecora, R., *Dynamic light scattering: applications of photon correlation spectroscopy*. Springer Science & Business Media: 2013.

(118) Brown, W., *Dynamic light scattering: the method and some applications*. Clarendon press Oxford: 1993; Vol. 313.

(119) Chen, S. B.; Keh, H. J., Axisymmetric electrophoresis of multiple colloidal spheres. *J. Fluid Mech.* **1992,** *238*, 251-276.

(120) Velev, O. D.; Bhatt, K. H., On-chip micromanipulation and assembly of colloidal particles by electric fields. *Soft Matter* **2006,** *2*, (9), 738-750.

(121) Chang, Y. C.; Keh, H. J., Diffusiophoresis and electrophoresis of a charged sphere perpendicular to two plane walls. *J. Colloid Interface Sci.* **2008,** *322*, (2), 634-653.

(122) Keh, H. J.; Chiou, J. Y., Electrophoresis of a colloidal sphere in a circular cylindrical pore. *AIChE J.* **1996,** *42*, (5), 1397-1406.

(123) Gascoyne, P. R.; Vykoukal, J., Particle separation by dielectrophoresis. *Electrophoresis* **2002,** *23*, (13), 1973-1983.

(124) Morgan, H.; Hughes, M. P.; Green, N. G., Separation of submicron bioparticles by dielectrophoresis. *Biophys. J.* **1999,** *77*, (1), 516-525.

(125) Sahoo, Y.; Goodarzi, A.; Swihart, M. T.; Ohulchanskyy, T. Y.; Kaur, N.; Furlani, E. P.; Prasad, P. N., Aqueous ferrofluid of magnetite nanoparticles: fluorescence labeling and magnetophoretic control. *The Journal of Physical Chemistry B* **2005,** *109*, (9), 3879-3885.

(126) Krack, M.; Hohenberg, H.; Kornowski, A.; Lindner, P.; Weller, H.; Förster, S., Nanoparticle-loaded magnetophoretic vesicles. *J. Am. Chem. Soc.* **2008,** *130*, (23), 7315-7320.

(127) Potoček, B.; Gaš, B.; Kenndler, E.; Štědrý, M., Electroosmosis in capillary zone electrophoresis with non-uniform zeta potential. *J. Chromatogr. A* **1995,** *709*, (1), 51-62.

(128) Kłodzińska, E.; Szumski, M.; Dziubakiewicz, E.; Hrynkiewicz, K.; Skwarek, E.; Janusz, W.; Buszewski, B., Effect of zeta potential value on bacterial behavior during electrophoretic separation. *Electrophoresis* **2010,** *31*, (9), 1590-1596.

(129) Schwer, C.; Kenndler, E., Electrophoresis in fused-silica capillaries: the influence of organic solvents on the electroosmotic velocity and the. zeta. potential. *Anal. Chem.* **1991,** *63*, (17), 1801-1807.

(130) Alon, U.; Surette, M. G.; Barkai, N.; Leibler, S., Robustness in bacterial chemotaxis. *Nature* **1999,** *397*, (6715), 168.

(131) Adler, J., Chemotaxis in bacteria. *Annu. Rev. Biochem.* **1975,** *44*, (1), 341-356.

(132) Piazza, R.; Parola, A., Thermophoresis in colloidal suspensions. *Journal of Physics: Condensed Matter* **2008,** *20*, (15), 153102.

(133) Talbot, L.; Cheng, R.; Schefer, R.; Willis, D., Thermophoresis of particles in a heated boundary layer. *J. Fluid Mech.* **1980,** *101*, (4), 737-758.

(134) McNab, G.; Meisen, A., Thermophoresis in liquids. *J. Colloid Interface Sci.* **1973,** *44*, (2), 339-346.

(135) Gao, W.; Feng, X.; Pei, A.; Gu, Y.; Li, J.; Wang, J., Seawater-driven magnesium based Janus micromotors for environmental remediation. *Nanoscale* **2013,** *5*, (11), 4696-4700.

(136) Wang, H.; Zhao, G.; Pumera, M., Beyond platinum: Bubble-propelled micromotors based on Ag and MnO2 catalysts. *J. Am. Chem. Soc.* **2014,** *136*, (7), 2719-2722.

(137) Gao, W.; D'Agostino, M.; Garcia-Gradilla, V.; Orozco, J.; Wang, J., Multi-fuel driven janus micromotors. *Small* **2013,** *9*, (3), 467-471.

(138) Xu, T.; Soto, F.; Gao, W.; Garcia-Gradilla, V.; Li, J.; Zhang, X.; Wang, J., Ultrasound-modulated bubble propulsion of chemically powered microengines. *J. Am. Chem. Soc.* **2014,** *136*, (24), 8552-8555.

(139) Shao, J.; Xuan, M.; Zhang, H.; Lin, X.; Wu, Z.; He, Q., Chemotaxis-Guided Hybrid Neutrophil Micromotors for Targeted Drug Transport. *Angew. Chem., Int. Ed.* **2017,** *56*, (42), 12935-12939.

(140) Wang, J.; Manesh, K. M., Motion control at the nanoscale. *Small* **2010,** *6*, (3), 338-345.

(141) Sen, A.; Ibele, M.; Hong, Y.; Velegol, D., Chemo and phototactic nano/microbots. *Faraday Discuss.* **2009,** *143*, 15-27.

(142) Gao, W.; Sattayasamitsathit, S.; Uygun, A.; Pei, A.; Ponedal, A.; Wang, J., Polymer-based tubular microbots: role of composition and preparation. *Nanoscale* **2012,** *4*, (7), 2447-2453.

(143) Delezuk, J. A.; Ramírez-Herrera, D. E.; de Ávila, B. E.-F.; Wang, J., Chitosan-based water-propelled micromotors with strong antibacterial activity. *Nanoscale* **2017,** *9*, (6), 2195-2200.

(144) Wu, Z.; Li, J.; de Ávila, B. E. F.; Li, T.; Gao, W.; He, Q.; Zhang, L.; Wang, J., Water-Powered Cell-Mimicking Janus Micromotor. *Adv. Funct. Mater.* **2015,** *25*, (48), 7497-7501.

(145) Ibele, M. E.; Wang, Y.; Kline, T. R.; Mallouk, T. E.; Sen, A., Hydrazine fuels for bimetallic catalytic microfluidic pumping. *J. Am. Chem. Soc.* **2007,** *129*, (25), 7762-7763.

(146) Ma, X.; Wang, X.; Hahn, K.; Sánchez, S., Motion control of urea-powered biocompatible hollow microcapsules. *ACS nano* **2016,** *10*, (3), 3597-3605.

(147) Schattling, P.; Thingholm, B.; Stadler, B., Enhanced diffusion of glucose-fueled Janus particles. *Chem. Mater.* **2015,** *27*, (21), 7412-7418.

(148) Luo, C.; Li, H.; Liu, X., Propulsion of microboats using isopropyl alcohol as a propellant. *J. Micromech. Microeng.* **2008,** *18*, (6), 067002.

(149) Adamczyk, J. J., Applications of self-organizing map for patterning macrofungal diversity of xerothermic swards. *Ecological research* **2011,** *26*, (3), 547-554.

(150) Angelani, L.; Di Leonardo, R.; Ruocco, G., Self-starting micromotors in a bacterial bath. *Phys. Rev. Lett.* **2009,** *102*, (4), 048104.

(151) Soler, L.; Magdanz, V.; Fomin, V. M.; Sanchez, S.; Schmidt, O. G., Self-propelled micromotors for cleaning polluted water. *Acs Nano* **2013,** *7*, (11), 9611-9620.

(152) Lehman, A. C.; Berg, K. A.; Dumpert, J.; Wood, N. A.; Visty, A. Q.; Rentschler, M. E.; Platt, S. R.; Farritor, S. M.; Oleynikov, D., Surgery with cooperative robots. *Computer Aided Surgery* **2008,** *13*, (2), 95-105.

(153) Li, J.; de Avila, B. E.-F.; Gao, W.; Zhang, L.; Wang, J., Micro/nanorobots for biomedicine: Delivery, surgery, sensing, and detoxification. *Science Robotics* **2017,** *2*, (4).

(154) Idowu, S. O.; Capaldi, N.; Fifka, M. S.; Zu, L.; Schmidpeter, R., *Dictionary of corporate social responsibility*. Springer: 2015.

(155) Rothschild, A.; Dotan, H., Beating the efficiency of photovoltaics-powered electrolysis with tandem cell photoelectrolysis. *ACS Energy Lett.* **2016,** *2*, (1), 45-51.

(156) Bergqvist, J.; Österberg, T.; Melianas, A.; Aguirre, L. E.; Tang, Z.; Cai, W.; Ma, Z.; Kemerink, M.; Gedefaw, D.; Andersson, M. R., Asymmetric photocurrent extraction in semitransparent laminated flexible organic solar cells. *npj Flexible Electronics* **2018,** *2*, (1), 4.

(157) Lewis, N. S.; Nocera, D. G., Powering the planet: Chemical challenges in solar energy utilization. *Proc. Natl. Acad. Sci.* **2006,** *103*, (43), 15729-15735.

(158) Kang, M.; Kim, J.; Jang, B.; Chae, Y.; Kim, J.-H.; Ahn, J.-H., Graphene-based three-dimensional capacitive touch sensor for wearable electronics. *ACS nano* **2017,** *11*, (8), 7950-7957.

(159) Stoller, M. D.; Park, S.; Zhu, Y.; An, J.; Ruoff, R. S., Graphene-based ultracapacitors. *Nano Lett.* **2008,** *8*, (10), 3498-3502.

(160) Liu, Y.-W.; Pennathur, S.; Meinhart, C. D., Electrophoretic mobility of a spherical nanoparticle in a nanochannel. *Phys. Fluids* **2014,** *26*, (11), 112002.

(161) Hu, N.; Ai, Y.; Qian, S., Field effect control of electrokinetic transport in micro/nanofluidics. *Sens. Actuators, B* **2012,** *161*, (1), 1150-1167.

(162) Mukherjee, S.; Goswami, P.; Dhar, J.; Dasgupta, S.; Chakraborty, S., Ion-size dependent electroosmosis of viscoelastic fluids in microfluidic channels with interfacial slip. *Phys. Fluids* **2017,** *29*, (7), 072002.

(163) Na, R.; Jian, Y.; Long, C.; Su, J.; Liu, Q., Transient Electro-Osmotic and Pressure Driven Flows through a Microannulus. *Open J. Fluid Dyn.* **2013,** *3*, (2), 50.

(164) Choi, W.; Sharma, A.; Qian, S.; Lim, G.; Joo, S. W., On steady two-fluid electroosmotic flow with full interfacial electrostatics. *J. Colloid Interface Sci.* **2011,** *357*, (2), 521-526.

(165) Anderson, J. L.; Prieve, D. C., Diffusiophoresis caused by gradients of strongly adsorbing solutes. *Langmuir* **1991,** *7*, (2), 403-406.

(166) Shin, S.; Ault, J. T.; Warren, P. B.; Stone, H. A., Accumulation of Colloidal Particles in Flow Junctions Induced by Fluid Flow and Diffusiophoresis. *Phys. Rev. X* **2017,** *7*, (4), 041038.

(167) Lauffer, M. A.; Gortner, R. A., Electrokinetics. XXI. Electrokinetic Theory. Streaming Potential and the Electroösmotic Counter Effect. *J. Phys. Chem.* **1939,** *43*, (6), 721-732.

(168) Erickson, D.; Li, D., Streaming potential and streaming current methods for characterizing heterogeneous solid surfaces. *J. Colloid Interface Sci.* **2001,** *237*, (2), 283-289.

(169) Luong, D.; Sprik, R., Streaming potential and electroosmosis measurements to characterize porous materials. *ISRN Geophysics* **2013,** *2013*.

(170) Chun, M.-S.; Lee, T. S.; Choi, N. W., Microfluidic analysis of electrokinetic streaming potential induced by microflows of monovalent electrolyte solution. *J. Micromech. Microeng.* **2005,** *15*, (4), 710.

(171) Cann, J. R.; Oates, D. C., Theory of electrophoresis and sedimentation for some kinetically controlled interactions. *Biochemistry* **1973,** *12*, (6), 1112-1119.

(172) Andersch, M. A.; Wilson, D. A.; Menten, M. L., Sedimentation constants and electrophoretic mobilities of adult and fetal carbonylhemoglobin. *J. Biol. Chem.* **1944,** *153*, (1), 301-305.

(173) Suss, M. E.; Mani, A.; Zangle, T. A.; Santiago, J. G., Electroosmotic pump performance is affected by concentration polarizations of both electrodes and pump. *Sens. Actuators, A* **2011,** *165*, (2), 310-315.

(174) Weber, K.; Osborn, M., The reliability of molecular weight determinations by dodecyl sulfate-polyacrylamide gel electrophoresis. *J. Biol. Chem.* **1969,** *244*, (16), 4406-4412.

(175) Korohoda, W.; Wilk, A., Cell electrophoresis—a method for cell separation and research into cell surface properties. *Cell. Mol. Biol. Lett.* **2008,** *13*, (2), 312-326.

(176) Shields IV, C. W.; Reyes, C. D.; López, G. P., Microfluidic cell sorting: a review of the advances in the separation of cells from debulking to rare cell isolation. *Lab Chip* **2015,** *15*, (5), 1230-1249.

(177) Campuzano, S.; Orozco, J.; Kagan, D.; Guix, M.; Gao, W.; Sattayasamitsathit, S.; Claussen, J. C.; Merkoçi, A.; Wang, J., Bacterial isolation by lectin-modified microengines. *Nano Lett.* **2011,** *12*, (1), 396-401.

(178) Jagannadh, S. N.; Muralidhara, H., Electrokinetics methods to control membrane fouling. *Ind. Eng. Chem. Res.* **1996,** *35*, (4), 1133-1140.

(179) Ray, B.; Reddy, P. D. S.; Bandyopadhyay, D.; Joo, S. W.; Sharma, A.; Qian, S.; Biswas, G., Surface instability of a thin electrolyte film undergoing coupled electroosmotic and electrophoretic flows in a microfluidic channel. *Electrophoresis* **2011,** *32*, (22), 3257-3267.

(180) Song, L.; Yu, L.; Zhou, Y.; Antao, A. R.; Prabhakaran, R. A.; Xuan, X., Electrokinetic instability in microchannel ferrofluid/water co-flows. *Sci. Rep.* **2017,** *7*.

(181) Škvarla, J., Hard versus soft particle electrokinetics of silica colloids. *Langmuir* **2007,** *23*, (10), 5305-5314.

(182) Yariv, E., Migration of ion-exchange particles driven by a uniform electric field. *J. Fluid Mech.* **2010,** *655*, 105-121.

(183) Yariv, E.; Brenner, H., The electrophoretic mobility of an eccentrically positioned spherical particle in a cylindrical pore. *Phys. Fluids* **2002,** *14*, (9), 3354-3357.

(184) Chen, G. Z., Understanding supercapacitors based on nano-hybrid materials with interfacial conjugation. *Prog. Nat. Sci.: Mater. Int.* **2013,** *23*, (3), 245-255.

(185) Napoli, M.; Atzberger, P.; Pennathur, S., Experimental study of the separation behavior of nanoparticles in micro-and nanochannels. *Microfluid. Nanofluid.* **2011,** *10*, (1), 69-80.

(186) Ge, L.; Wang, S.; Ge, S.; Yu, J.; Yan, M.; Li, N.; Huang, J., Electrophoretic separation in a microfluidic paper-based analytical device with an on-column wireless electrogenerated chemiluminescence detector. *Chem. Commun.* **2014,** *50*, (43), 5699-5702.

(187) Xu, C.; Lin, W.; Cai, L., Demonstrating Electrophoretic Separation in a Straight Paper Channel Delimited by a Hydrophobic Wax Barrier. *J. Chem. Educ.* **2016,** *93*, (5), 903-905.

(188) Zipper, H.; Glantz, M. D., The paper electrophoretic separation of phosphatides. *J. Biol. Chem.* **1958,** *230*, 621-624.

(189) Stellwagen, N. C., Electrophoresis of DNA in agarose gels, polyacrylamide gels and in free solution. *Electrophoresis* **2009,** *30*, (S1), S188-S195.

(190) Magnusdottir, S.; Aakerman, B.; Jonsson, M., DNA electrophoresis in agarose gels: three regimes of DNA migration identified and characterized by the electrophoretic orientational behavior of DNA. *J. Phys. Chem.* **1994,** *98*, (10), 2624-2633.

(191) Stellwagen, N. C., Electrophoresis of DNA in agarose gels, polyacrylamide gels and in free solution. *Electrophoresis* **2009,** *30*, (S1).

(192) Paxton, W. F.; Baker, P. T.; Kline, T. R.; Wang, Y.; Mallouk, T. E.; Sen, A., Catalytically induced electrokinetics for motors and micropumps. *J. Am. Chem. Soc.* **2006,** *128*, (46), 14881-14888.

(193) Kagan, D.; Calvo-Marzal, P.; Balasubramanian, S.; Sattayasamitsathit, S.; Manesh, K. M.; Flechsig, G.-U.; Wang, J., Chemical sensing based on catalytic nanomotors: motion-based detection of trace silver. *J. Am. Chem. Soc.* **2009,** *131*, (34), 12082-12083.

(194) Zhang, M.; Ai, Y.; Sharma, A.; Joo, S. W.; Kim, D. S.; Qian, S., Electrokinetic particle translocation through a nanopore containing a floating electrode. *Electrophoresis* **2011,** *32*, (14), 1864-1874.

(195) Allen, G. M.; Mogilner, A.; Theriot, J. A., Electrophoresis of cellular membrane components creates the directional cue guiding keratocyte galvanotaxis. *Curr. Biol.* **2013,** *23*, (7), 560-568.

(196) Jaffe, L. F., Electrophoresis along cell membranes. *Nature* **1977,** *265*, (5595), 600-602.

(197) Huang, Y.-J.; Schiapparelli, P.; Kozielski, K.; Green, J.; Lavell, E.; Guerrero-Cazares, H.; Quinones-Hinojosa, A.; Searson, P., Electrophoresis of cell membrane heparan sulfate regulates galvanotaxis in glial cells. *J Cell Sci* **2017**, jcs. 203752.

(198) Kłodzińska, E.; Jaworski, M.; Kupczyk, W.; Jackowski, M.; Buszewski, B., A study of interactions between bacteria and antibiotics by capillary electrophoresis. *Electrophoresis* **2012,** *33*, (19-20), 3095-3100.

(199) Simon, B.; Hancu, G.; Gyéresi, Á., Application of capillary electrophoresis to the simultaneous determination and stability study of four extensively used penicillin derivatives. *Braz. J. Pharm. Sci.* **2014,** *50*, (3), 521-527.

(200) Schellman, J. A.; Stigter, D., Electrical double layer, zeta potential, and electrophoretic charge of double-stranded DNA. *Biopolymers* **1977,** *16*, (7), 1415-1434.

(201) Lim, J.; Whitcomb, J.; Boyd, J.; Varghese, J., Transient finite element analysis of electric double layer using Nernst–Planck–Poisson equations with a modified Stern layer. *J. Colloid Interface Sci.* **2007,** *305*, (1), 159-174.

(202) Verwey, E., Theory of the electric double layer of stabilized emulsion. *Proc. Konink. Nederland. Akad. Wetenschap* **1950,** *53*, 375.

(203) Egorova, E. M., The validity of the Smoluchowski equation in electrophoretic studies of lipid membranes. *Electrophoresis* **1994,** *15*, (1), 1125-1131.

(204) Morrison, F.; Stukel, J., Electrophoresis of an insulating sphere normal to a conducting plane. *J. Colloid Interface Sci.* **1970,** *33*, (1), 88-93.

(205) Delgado, Á. V.; González-Caballero, F.; Hunter, R.; Koopal, L.; Lyklema, J., Measurement and interpretation of electrokinetic phenomena. *J. Colloid Interface Sci.* **2007,** *309*, (2), 194-224.

(206) Levine, S.; Mingins, J.; Bell, G., The discrete-ion effect in ionic double-layer theory. *J. Electroanal. Chem.* **1967,** *13*, (3), 280-329.

(207) Schnitzer, O.; Yariv, E., Nonlinear electrophoresis at arbitrary field strengths: small-Dukhin-number analysis. *Phys. Fluids* **2014,** *26*, (12), 122002.

(208) O'Brien, R., The solution of the electrokinetic equations for colloidal particles with thin double layers. *J. Colloid Interface Sci.* **1983,** *92*, (1), 204-216.

(209) Yariv, E.; Brenner, H., The electrophoretic mobility of an eccentrically positioned spherical particle in a cylindrical pore. *Physics of Fluids* **2002,** *14*, (9), 3354-3357.

(210) Keh, H.; Anderson, J., Boundary effects on electrophoretic motion of colloidal spheres. *J. Fluid Mech.* **1985,** *153*, 417-439.

(211) Loewenberg, M.; Davis, R. H., Near-contact electrophoretic particle motion. *J. Fluid Mech.* **1995,** *288*, 103-122.

(212) Ye, C.; Xuan, X.; Li, D., Eccentric electrophoretic motion of a sphere in circular cylindrical microchannels. *Microfluid. Nanofluid.* **2005,** *1*, (3), 234-241.

(213) Chiu, H. C.; Keh, H. J., Electrophoresis of a colloidal sphere with double-layer polarization in a microtube. *Microfluid. Nanofluid.* **2016,** *20*, (4), 64.

(214) Liu, W., One-dimensional steady-state Poisson–Nernst–Planck systems for ion channels with multiple ion species. *Journal of Differential Equations* **2009,** *246*, (1), 428-451.

(215) Zheng, Q.; Wei, G.-W., Poisson–Boltzmann–Nernst–Planck model. *J. Chem. Phys.* **2011,** *134*, (19), 194101.

(216) Saville, D. A.; Palusinski, O. A., Theory of electrophoretic separations. Part I: Formulation of a mathematical model. *AIChE J.* **1986,** *32*, (2), 207-214.

(217) Urbanski, J. P.; Thorsen, T.; Levitan, J. A.; Bazant, M. Z., Fast ac electro-osmotic micropumps with nonplanar electrodes. *Appl. Phys. Lett.* **2006,** *89*, (14), 143508.

(218) Bazant, M. Z.; Kilic, M. S.; Storey, B. D.; Ajdari, A., Towards an understanding of induced-charge electrokinetics at large applied voltages in concentrated solutions. *Adv. Colloid Interface Sci.* **2009,** *152*, (1-2), 48-88.

(219) Urbanski, J. P.; Levitan, J. A.; Burch, D. N.; Thorsen, T.; Bazant, M. Z., The effect of step height on the performance of three-dimensional ac electro-osmotic microfluidic pumps. *J. Colloid Interface Sci.* **2007,** *309*, (2), 332-341.

(220) Storey, B. D.; Edwards, L. R.; Kilic, M. S.; Bazant, M. Z., Steric effects on ac electro-osmosis in dilute electrolytes. *Phys. Rev. E* **2008,** *77*, (3), 036317.

(221) Zheng, M.; Xiaoxia, D.; Hu, Y.; ZHANG, B.; Changying, X.; Yansheng, L., Effect of Ionic Liquids on Organic Reactions Based on Activity Coefficients at Infinite Dilution. *Chin. J. Chem. Eng.* **2013,** *21*, (12), 1370-1375.

(222) Zittle, C. A.; Schmidt, C. L., Heats of solution, heats of dilution, and specific heats of aqueous solutions of certain amino acids. *J. Biol. Chem.* **1935,** *108*, (1), 161-185.

(223) Diedenhofen, M.; Eckert, F.; Klamt, A., Prediction of infinite dilution activity coefficients of organic compounds in ionic liquids using COSMO-RS. *J. Chem. Eng. Data* **2003,** *48*, (3), 475-479.

(224) McKee, R., A generalization of the nernst-Einstein equation for self-diffusion in high defect concentration solids. *Solid State Ionics* **1981,** *5*, 133-136.

(225) Hsu, J.-P.; Yeh, L.-H.; Ku, M.-H., Evaluation of the electric force in electrophoresis. *J. Colloid Interface Sci.* **2007,** *305*, (2), 324-329.

(226) Bhattacharyya, S.; De, S., Gel electrophoresis and size selectivity of charged colloidal particles in a charged hydrogel medium. *Chem. Eng. Sci.* **2016,** *141*, 304-314.

(227) Makino, K.; Ohshima, H., Electrophoretic mobility of a colloidal particle with constant surface charge density. *Langmuir* **2010,** *26*, (23), 18016-18019.

(228) Klymenko, O. V.; Amatore, C.; Sun, W.; Zhou, Y.-L.; Tian, Z.-W.; Svir, I., Theory and computational study of electrophoretic ion separation and focusing in microfluidic channels. *Nonlinear Anal.* **2012,** *17*, (4), 431-447.

(229) Jones, T. B., Basic theory of dielectrophoresis and electrorotation. *IEEE Engineering in medicine and Biology Magazine* **2003,** *22*, (6), 33-42.

(230) Yamada, K.; Shibata, H.; Suzuki, K.; Citterio, D., Toward practical application of paper-based microfluidics for medical diagnostics: state-of-the-art and challenges. *Lab on a Chip* **2017,** *17*, (7), 1206-1249.

(231) Liu, S.; Su, W.; Ding, X., A review on microfluidic paper-based analytical devices for glucose detection. *Sensors* **2016,** *16*, (12), 2086.

(232) Yang, Y.; Noviana, E.; Nguyen, M. P.; Geiss, B. J.; Dandy, D. S.; Henry, C. S., based microfluidic devices: emerging themes and applications. *Anal. Chem.* **2016,** *89*, (1), 71-91.

(233) Luka, G.; Ahmadi, A.; Najjaran, H.; Alocilja, E.; DeRosa, M.; Wolthers, K.; Malki, A.; Aziz, H.; Althani, A.; Hoorfar, M., Microfluidics integrated biosensors: A leading technology towards lab-on-a-chip and sensing applications. *Sensors* **2015,** *15*, (12), 30011-30031.

(234) Konwarh, R.; Gupta, P.; Mandal, B. B., Silk-microfluidics for advanced biotechnological applications: A progressive review. *Biotechnology advances* **2016,** *34*, (5), 845-858.

(235) Novikov, V.; Shved, O.; Chervetsova, V.; Lobur, I.; Matviykiv, S. In Microfluidic lab-chip devices for biotechnological applications, Perspective Technologies and Methods in MEMS Design, 2011; IEEE: 2011; pp 227-229.

(236) Juang, Y. J.; Chang, J. S., Applications of microfluidics in microalgae biotechnology: A review. *Biotech. J.l* **2016,** *11*, (3), 327-335.

(237) Akyazi, T.; Basabe-Desmonts, L.; Benito-Lopez, F., Review on microfluidic paper-based analytical devices towards commercialisation. *Anal. Chim. Acta* **2018,** *1001*, 1-17.

(238) Almeida, M. I. G.; Jayawardane, B. M.; Kolev, S. D.; McKelvie, I. D., Developments of microfluidic paper-based analytical devices (μPADs) for water analysis: A review. *Talanta* **2018,** *177*, 176-190.

(239) Maria, M. S.; Rakesh, P.; Chandra, T.; Sen, A., Capillary flow-driven microfluidic device with wettability gradient and sedimentation effects for blood plasma separation. *Scientific reports* **2017,** *7*, 43457.

(240) Sarkar, A.; Hou, H. W.; Mahan, A. E.; Han, J.; Alter, G., Multiplexed affinity-based separation of proteins and cells using inertial microfluidics. *Sci. Rep.* **2016,** *6*, 23589.

(241) Patankar, N. A.; Hu, H. H., Numerical simulation of electroosmotic flow. *Anal. Chem.* **1998,** *70*, (9), 1870-1881.

(242) Rice, C.; Whitehead, R., Electrokinetic flow in a narrow cylindrical capillary. *The Journal of Physical Chemistry* **1965,** *69*, (11), 4017-4024.

(243) O'Farrell, P. H., High resolution two-dimensional electrophoresis of proteins. *J. Biol. Chem.* **1975,** *250*, (10), 4007-4021.

(244) Ohshima, H., Electrophoresis of soft particles. *Adv. Colloid Interface Sci.* **1995,** *62*, (2-3), 189-235.

(245) Ebel, J.; Anderson, J. L.; Prieve, D., Diffusiophoresis of latex particles in electrolyte gradients. *Langmuir* **1988,** *4*, (2), 396-406.

(246) Tang, C. Y.; Kwon, Y.-N.; Leckie, J. O., Probing the nano-and micro-scales of reverse osmosis membranes—A comprehensive characterization of physiochemical

properties of uncoated and coated membranes by XPS, TEM, ATR-FTIR, and streaming potential measurements. *J. Membr. Sci.* **2007,** *287*, (1), 146-156.

(247) Peeters, J.; Mulder, M.; Strathmann, H., Streaming potential measurements as a characterization method for nanofiltration membranes. *Colloids Surf., A* **1999,** *150*, (1-3), 247-259.

(248) Booth, F., Sedimentation potential and velocity of solid spherical particles. *The J. Chem. Phys.* **1954,** *22*, (12), 1956-1968.

(249) Ohshima, H.; Healy, T. W.; White, L. R.; O'Brien, R. W., Sedimentation velocity and potential in a dilute suspension of charged spherical colloidal particles. *J. Chem. Soc., Faraday Trans. 2* **1984,** *80*, (10), 1299-1317.

(250) Leinweber, F. C.; Eijkel, J. C.; Bomer, J. G.; van den Berg, A., Continuous flow microfluidic demixing of electrolytes by induced charge electrokinetics in structured electrode arrays. *Anal. Chem.* **2006,** *78*, (5), 1425-1434.

(251) Van der Heyden, F. H.; Bonthuis, D. J.; Stein, D.; Meyer, C.; Dekker, C., Electrokinetic energy conversion efficiency in nanofluidic channels. *Nano Lett.* **2006,** *6*, (10), 2232-2237.

(252) Guo, W.; Cao, L.; Xia, J.; Nie, F. Q.; Ma, W.; Xue, J.; Song, Y.; Zhu, D.; Wang, Y.; Jiang, L., Energy harvesting with single-ion-selective nanopores: a concentration-gradient-driven nanofluidic power source. *Adv. Funct. Mater.* **2010,** *20*, (8), 1339-1344.

(253) Garcia, A. L.; Ista, L. K.; Petsev, D. N.; O'Brien, M. J.; Bisong, P.; Mammoli, A. A.; Brueck, S. R.; López, G. P., Electrokinetic molecular separation in nanoscale fluidic channels. *Lab Chip* **2005,** *5*, (11), 1271-1276.

(254) Yuan, Z.; Garcia, A. L.; Lopez, G. P.; Petsev, D. N., Electrokinetic transport and separations in fluidic nanochannels. *Electrophoresis* **2007,** *28*, (4), 595-610.

(255) Acar, Y. B.; Alshawabkeh, A. N.; Gale, R. J., Fundamentals of extracting species from soils by electrokinetics. *Waste Manage.* **1993,** *13*, (2), 141-151.

(256) Nguyen, N.-T.; Wu, Z., Micromixers—a review. *J. Micromech. Microeng.* **2004,** *15*, (2), R1.

(257) Dukhin, A. S., Biospecific mechanism of double layer formation and peculiarities of cell electrophoresis. *Colloids and Surfaces A: Physicochemical and Engineering Aspects* **1993,** *73*, 29-48.

(258) Kim, J. U., Electrical double layer: revisit based on boundary conditions. *arXiv preprint physics/0511007* **2005**.

(259) Moya, A., Theory of the formation of the electric double layer at the ion exchange membrane–solution interface. *Phys. Chem. Chem. Phys.* **2015,** *17*, (7), 5207-5218.

(260) Horwitz, W., The theory of electrokinetic phenomena. *Journal of Chemical Education* **1939,** *16*, (11), 519.

(261) Ross, S.; Long, R., Electrophoresis as method of investigating electric double layer. *Ind. Eng. Chem. Res.* **1969,** *61*, (10), 58-71.

(262) Chandra, A., Dynamics of electrical double layer formation at a charged solid surface. *Journal of Molecular Structure: THEOCHEM* **1998,** *430*, 105-111.

(263) Schellman, J. A.; Stigter, D., Electrical double layer, zeta potential, and electrophoretic charge of double-stranded DNA. *Biopolymers: Original Research on Biomolecules* **1977,** *16*, (7), 1415-1434.

(264) Payne, R., The electrical double layer: Problems and recent progress. *J. Electroanal. Chem. Interfacial Electrochem.* **1973,** *41*, (2), 277-309.

(265) Yalcin, S. E.; Lee, S. Y.; Joo, S. W.; Baysal, O.; Qian, S., Electrodiffusiophoretic motion of a charged spherical particle in a nanopore. *The Journal of Physical Chemistry B* **2010,** *114*, (11), 4082-4093.

(266) Anderson, J. L., Effect of nonuniform zeta potential on particle movement in electric fields. *J. Colloid Interface Sci.* **1985,** *105*, (1), 45-54.

(267) Hu, Y.; Werner, C.; Li, D., Electrokinetic transport through rough microchannels. *Analytical Chemistry* **2003,** *75*, (21), 5747-5758.

(268) Choi, W.; Sharma, A.; Qian, S.; Lim, G.; Joo, S. W., Is free surface free in micro-scale electrokinetic flows? *J. Colloid Interface Sci.* **2010,** *347*, (1), 153-155.

(269) Gao, Y.; Wong, T. N.; Yang, C.; Ooi, K. T., Two-fluid electroosmotic flow in microchannels. *J. Colloid Interface Sci.* **2005,** *284*, (1), 306-314.

(270) Ngoma, G. D.; Erchiqui, F., Pressure gradient and electroosmotic effects on two immiscible fluids in a microchannel between two parallel plates. *J. Micromech. Microeng.* **2005,** *16*, (1), 83.

(271) Gao, Y.; Wong, T. N.; Yang, C.; Ooi, K. T., Transient two-liquid electroosmotic flow with electric charges at the interface. *Colloids and Surfaces A: Physicochemical and Engineering Aspects* **2005,** *266*, (1-3), 117-128.

(272) Gao, Y.; Wang, C.; Wong, T. N.; Yang, C.; Nguyen, N.-T.; Ooi, K. T., Electro-osmotic control of the interface position of two-liquid flow through a microchannel. *J. Micromech. Microeng.* **2007,** *17*, (2), 358.

(273) Liu, M.; Liu, Y.; Guo, Q.; Yang, J., Modeling of electroosmotic pumping of nonconducting liquids and biofluids by a two-phase flow method. *J. Electroanal. Chem.* **2009,** *636*, (1-2), 86-92.

(274) Sotowa, K.-I.; Yamamoto, A.; Nakagawa, K.; Sugiyama, S., Indentations and baffles for improving mixing rate in deep microchannel reactors. Chem. Eng. J. **2011,** *167*, (2-3), 490-495.

(275) Wätzig, H.; Kaupp, S.; Graf, M., Inner surface properties of capillaries for electrophoresis. *TrAC Trends in Analytical Chemistry* **2003,** *22*, (9), 588-604.

(276) Hu, Y.; Werner, C.; Li, D., Influence of the three-dimensional heterogeneous roughness on electrokinetic transport in microchannels. *J. Colloid Interface Sci.* **2004,** *280*, (2), 527-536.

(277) Zhou, B.; Xu, W.; Syed, A. A.; Chau, Y.; Chen, L.; Chew, B.; Yassine, O.; Wu, X.; Gao, Y.; Zhang, J., Design and fabrication of magnetically functionalized flexible micropillar arrays for rapid and controllable microfluidic mixing. *Lab Chip* **2015,** *15*, (9), 2125-2132.

(278) Sharp, K. V.; Adrian, R. J., Transition from laminar to turbulent flow in liquid filled microtubes. *Experiments in fluids* **2004,** *36*, (5), 741-747.

(279) Deng, S.; Jian, Y.; Bi, Y.; Chang, L.; Wang, H.; Liu, Q., Unsteady electroosmotic flow of power-law fluid in a rectangular microchannel. *Mech. Res. Commun.* **2012,** *39*, (1), 9-14.

(280) Dutta, P.; Beskok, A., Analytical solution of time periodic electroosmotic flows: analogies to Stokes' second problem. *Anal. Chem.* **2001,** *73*, (21), 5097-5102.

(281) Sadr, R.; Yoda, M.; Zheng, Z.; Conlisk, A., An experimental study of electro-osmotic flow in rectangular microchannels. *J. Fluid Mech.* **2004,** *506*, 357-367.

(282) Horiuchi, K.; Dutta, P., Joule heating effects in electroosmotically driven microchannel flows. *Int. J. Heat Mass Transfer* **2004,** *47*, (14-16), 3085-3095.

(283) Sims, S. M.; Higuchi, W. I.; Srinivasan, V.; Peck, K., Ionic partition coefficients and electroosmotic flow in cylindrical pores: Comparison of the predictions of the Poisson-Boltzmann equation with experiment. *J. Colloid Interface Sci.* **1993,** *155*, (1), 210-220.

(284) Sun, Y.; Lim, C.; Liu, A.; Ayi, T.; Yap, P., Design, simulation and experiment of electroosmotic microfluidic chip for cell sorting. *Sensors and Actuators A: Physical* **2007,** *133*, (2), 340-348.

(285) Sze, A.; Erickson, D.; Ren, L.; Li, D., Zeta-potential measurement using the Smoluchowski equation and the slope of the current–time relationship in electroosmotic flow. *J. Colloid Interface Sci.* **2003,** *261*, (2), 402-410.

(286) Dutta, P.; Beskok, A., Analytical solution of combined electroosmotic/pressure driven flows in two-dimensional straight channels: finite Debye layer effects. *Anal. Chem.* **2001,** *73*, (9), 1979-1986.

(287) Erickson, D.; Li, D., Influence of surface heterogeneity on electrokinetically driven microfluidic mixing. *Langmuir* **2002,** *18*, (5), 1883-1892.

(288) Biddiss, E.; Erickson, D.; Li, D., Heterogeneous surface charge enhanced micromixing for electrokinetic flows. *Anal. Chem.* **2004,** *76*, (11), 3208-3213.

(289) Ilic, B.; Czaplewski, D.; Zalalutdinov, M.; Schmidt, B.; Craighead, H., Fabrication of flexible polymer tubes for micro and nanofluidic applications. *Journal of Vacuum Science & Technology B: Microelectronics and Nanometer Structures Processing, Measurement, and Phenomena* **2002,** *20*, (6), 2459-2465.

(290) Noori, A.; Selvaganapathy, P. R.; Wilson, J., Microinjection in a microfluidic format using flexible and compliant channels and electroosmotic dosage control. *Lab Chip* **2009,** *9*, (22), 3202-3211.

(291) Thonart, P.; Custinne, M.; Paquot, M., Zeta potential of yeast cells: application in cell immobilization. *Enzyme and Microbial Technology* **1982,** *4*, (3), 191-194.

(292) Wilson, W. W.; Wade, M. M.; Holman, S. C.; Champlin, F. R., Status of methods for assessing bacterial cell surface charge properties based on zeta potential measurements. *J. Microbiol. Methods* **2001,** *43*, (3), 153-164.

(293) Xu, X.; Li, S.; Zhang, H.; Shen, Y.; Zakeeruddin, S. M.; Graetzel, M.; Cheng, Y.-B.; Wang, M., A power pack based on organometallic perovskite solar cell and supercapacitor. *ACS nano* **2015,** *9*, (2), 1782-1787.

(294) Xu, J.; Chen, Y.; Dai, L., Efficiently photo-charging lithium-ion battery by perovskite solar cell. *Nat. Commun.* **2015,** *6*, 8103.

(295) Scalia, A.; Bella, F.; Lamberti, A.; Bianco, S.; Gerbaldi, C.; Tresso, E.; Pirri, C. F., A flexible and portable powerpack by solid-state supercapacitor and dye-sensitized solar cell integration. *J. Energy Power Sources* **2017,** *359*, 311-321.

(296) Alotto, P.; Guarnieri, M.; Moro, F., Redox flow batteries for the storage of renewable energy: A review. *Renewable Sustainable Energy Rev.* **2014,** *29*, 325-335.

References

(297) Kalyani, V.; Mondal, S.; Saha, J.; Subramaniam, C., Electrochemical, top-down nanostructured pseudocapacitive electrodes for enhanced specific capacitance and cycling efficiency. *Nanoscale* **2018,** *10*, (8), 3663-3672.

(298) Kim, B. M.; Qian, S.; Bau, H. H., Filling carbon nanotubes with particles. *Nano Lett.* **2005,** *5*, (5), 873-878.

(299) Yang, S.; Lohe, M. R.; Müllen, K.; Feng, X., New-generation graphene from electrochemical approaches: production and applications. *Adv. Mater.* **2016,** *28*, (29), 6213-6221.

(300) Hwang, J. Y.; Li, M.; El-Kady, M. F.; Kaner, R. B., Next-Generation Activated Carbon Supercapacitors: A Simple Step in Electrode Processing Leads to Remarkable Gains in Energy Density. *Adv. Funct. Mater.* **2017,** *27*, (15), 1605745.

(301) Liu, L.; Niu, Z.; Chen, J., Unconventional supercapacitors from nanocarbon-based electrode materials to device configurations. *Chem. Soc. Rev.* **2016,** *45*, (15), 4340-4363.

(302) Liu, C.; Yu, Z.; Neff, D.; Zhamu, A.; Jang, B. Z., Graphene-based supercapacitor with an ultrahigh energy density. *Nano Lett.* **2010,** *10*, (12), 4863-4868.

(303) Stoller, M. D.; Ruoff, R. S., Best practice methods for determining an electrode material's performance for ultracapacitors. *Energy Environ. Sci.* **2010,** *3*, (9), 1294-1301.

(304) Ren, H.; Gu, C.; Joo, S. W.; Zhao, J.; Sun, Y.; Huang, J., Effective hydrogen gas sensor based on NiO@ rGO nanocomposite. *Sens. Actuators, B* **2018,** *266*, 506-513.

(305) Zhu, J.; Xu, Y.; Wang, J.; Lin, J.; Sun, X.; Mao, S., The effect of various electrolyte cations on electrochemical performance of polypyrrole/RGO based supercapacitors. *Phys. Chem. Chem. Phys.* **2015,** *17*, (43), 28666-28673.

(306) Yu, G.; Hu, L.; Vosgueritchian, M.; Wang, H.; Xie, X.; McDonough, J. R.; Cui, X.; Cui, Y.; Bao, Z., Solution-processed graphene/MnO2 nanostructured textiles for high-performance electrochemical capacitors. *Nano Lett.* **2011,** *11*, (7), 2905-2911.

(307) Xia, J.; Chen, F.; Li, J.; Tao, N., Measurement of the quantum capacitance of graphene. *Nat. Nanotechnol.* **2009,** *4*, (8), 505.

(308) Conway, B.; Supercapacitors, E., Scientific fundamentals and technological applications. *Electrochem. Supercapacitors* **1999**, 417-477.

(309) Lai, L.; Yang, H.; Wang, L.; Teh, B. K.; Zhong, J.; Chou, H.; Chen, L.; Chen, W.; Shen, Z.; Ruoff, R. S., Preparation of supercapacitor electrodes through selection of graphene surface functionalities. *ACS nano* **2012,** *6*, (7), 5941-5951.

(310) Taberna, P.; Simon, P.; Fauvarque, J.-F., Electrochemical characteristics and impedance spectroscopy studies of carbon-carbon supercapacitors. *J. Electrochem. Soc.* **2003,** *150*, (3), A292-A300.

(311) Yao, H. B.; Ge, J.; Wang, C. F.; Wang, X.; Hu, W.; Zheng, Z. J.; Ni, Y.; Yu, S. H., A flexible and highly pressure-sensitive graphene–polyurethane sponge based on fractured microstructure design. *Adv. Mater.* **2013,** *25*, (46), 6692-6698.

(312) Schmidt, O.; Hawkes, A.; Gambhir, A.; Staffell, I., The future cost of electrical energy storage based on experience rates. *Nat. Energy* **2017,** *2*, (8), 17110.

(313) Zhang, L. L.; Zhao, X., Carbon-based materials as supercapacitor electrodes. *Chem. Soc. Rev.* **2009,** *38*, (9), 2520-2531.

(314) Dey, K. K.; Das, S.; Poyton, M. F.; Sengupta, S.; Butler, P. J.; Cremer, P. S.; Sen, A., Chemotactic separation of enzymes. *ACS nano* **2014,** *8*, (12), 11941-11949.

(315) Stern, O., Zur theorie der elektrolytischen doppelschicht. *Zeitschrift für Elektrochemie und angewandte physikalische Chemie* **1924,** *30*, (21-22), 508-516.

(316) Vatamanu, J.; Borodin, O.; Olguin, M.; Yushin, G.; Bedrov, D., Charge storage at the nanoscale: understanding the trends from the molecular scale perspective. *J. Mater. Chem. A* **2017,** *5*, (40), 21049-21076.

(317) Fedorov, M. V.; Kornyshev, A. A., Towards understanding the structure and capacitance of electrical double layer in ionic liquids. *Electrochim. Acta* **2008,** *53*, (23), 6835-6840.

(318) Mei, B.-A.; Munteshari, O.; Lau, J.; Dunn, B.; Pilon, L., Physical interpretations of Nyquist plots for EDLC electrodes and devices. *The Journal of Physical Chemistry C* **2017,** *122*, (1), 194-206.

(319) Drüschler, M.; Huber, B.; Roling, B., On Capacitive Processes at the Interface between 1-Ethyl-3-methylimidazolium tris (pentafluoroethyl) trifluorophosphate and Au (111). *The Journal of Physical Chemistry C* **2011,** *115*, (14), 6802-6808.

(320) Wohde, F.; Balabajew, M.; Roling, B., Li+ transference numbers in liquid electrolytes obtained by very-low-frequency impedance spectroscopy at variable electrode distances. *J. Electrochem. Soc.* **2016,** *163*, (5), A714-A721.

(321) Choi, N. S.; Chen, Z.; Freunberger, S. A.; Ji, X.; Sun, Y. K.; Amine, K.; Yushin, G.; Nazar, L. F.; Cho, J.; Bruce, P. G., Challenges facing lithium batteries and electrical double-layer capacitors. *Angew. Chem., Int. Ed.* **2012,** *51*, (40), 9994-10024.

(322) Pandolfo, A.; Hollenkamp, A., Carbon properties and their role in supercapacitors. *J. Power Sources* **2006,** *157*, (1), 11-27.

(323) Schuster, R.; Kirchner, V.; Xia, X.; Bittner, A.; Ertl, G., Nanoscale electrochemistry. *Phys. Rev. Lett.* **1998,** *80*, (25), 5599.

(324) Cesiulis, H.; Tsyntsaru, N.; Ramanavicius, A.; Ragoisha, G., The study of thin films by electrochemical impedance spectroscopy. In *Nanostructures and thin films for multifunctional applications*, Springer: 2016; pp 3-42.

(325) Frackowiak, E.; Beguin, F., Carbon materials for the electrochemical storage of energy in capacitors. *Carbon* **2001,** *39*, (6), 937-950.

(326) Li, Y.; Li, Z.; Shen, P. K., Simultaneous formation of ultrahigh surface area and three-dimensional hierarchical porous graphene-like networks for fast and highly stable supercapacitors. *Adv. Mater.* **2013,** *25*, (17), 2474-2480.

(327) Iroh, J. O.; Levine, K., Capacitance of the polypyrrole/polyimide composite by electrochemical impedance spectroscopy. *Journal of Power Sources* **2003,** *117*, (1-2), 267-272.

(328) Bazant, M. Z.; Thornton, K.; Ajdari, A., Diffuse-charge dynamics in electrochemical systems. *Physical review E* **2004,** *70*, (2), 021506.

(329) Kortschot, R.; Philipse, A.; Erné, B., Debye length dependence of the anomalous dynamics of ionic double layers in a parallel plate capacitor. *J. Phy. Chem. C* **2014,** *118*, (22), 11584-11592.

(330) Macdonald, J. R., Theory of ac space-charge polarization effects in photoconductors, semiconductors, and electrolytes. *Physical Review* **1953,** *92*, (1), 4.

(331) Borenstein, A.; Hanna, O.; Attias, R.; Luski, S.; Brousse, T.; Aurbach, D., Carbon-based composite materials for supercapacitor electrodes: a review. *Journal of Materials Chemistry A* **2017,** *5*, (25), 12653-12672.

(332) Nagy, T.; Henderson, D.; Boda, D., Simulation of an electrical double layer model with a low dielectric layer between the electrode and the electrolyte. *The Journal of Physical Chemistry B* **2011,** *115*, (39), 11409-11419.

(333) Sun, Z.; Yuan, H.; Liu, Z.; Han, B.; Zhang, X., A highly efficient chemical sensor material for H2S: α-Fe2O3 nanotubes fabricated using carbon nanotube templates. *Adv. Mater.* **2005,** *17*, (24), 2993-2997.

(334) Musameh, M.; Notivoli, M. R.; Hickey, M.; Kyratzis, I. L.; Gao, Y.; Huynh, C.; Hawkins, S. C., Carbon nanotube webs: a novel material for sensor applications. *Adv. Mater.* **2011,** *23*, (7), 906-910.

(335) Parmar, J.; Ma, X.; Katuri, J.; Simmchen, J.; Stanton, M. M.; Trichet-Paredes, C.; Soler, L.; Sanchez, S., Nano and micro architectures for self-propelled motors. *Sci. Technol. Adv. Mater.* **2015,** *16*, (1), 014802.

(336) Nicholls, D.; DeVerse, A.; Esplin, R. S.; Castañeda, J.; Loyd, Y.; Nair, R.; Voinescu, R.; Zhou, C.; Wang, W.; Gibbs, J. G., Shape-dependent motion of structured photoactive microswimmers. *ACS Appl. Mater. Interfaces* **2018,** *10*, (21), 18050-18056.

(337) Wang, H.; Pumera, M., Emerging materials for the fabrication of micro/nanomotors. *Nanoscale* **2017,** *9*, (6), 2109-2116.

(338) Wang, J.; Gao, W., Nano/microscale motors: biomedical opportunities and challenges. *ACS nano* **2012,** *6*, (7), 5745-5751.

(339) Guix, M.; Mayorga-Martinez, C. C.; Merkoçi, A., Nano/micromotors in (bio) chemical science applications. *Chem. Rev.* **2014,** *114*, (12), 6285-6322.

(340) Chandrasekaran, A.; Ellett, F.; Jorgensen, J.; Irimia, D., Temporal gradients limit the accumulation of neutrophils toward sources of chemoattractant. *Microsyst. Nanoeng.* **2017,** *3*, 16067.

(341) Abdulla, S.; Mathew, T. L.; Pullithadathil, B., Highly sensitive, room temperature gas sensor based on polyaniline-multiwalled carbon nanotubes (PANI/MWCNTs) nanocomposite for trace-level ammonia detection. *Sens. Actuators, B* **2015,** *221*, 1523-1534.

(342) Jurado-Sánchez, B.; Sattayasamitsathit, S.; Gao, W.; Santos, L.; Fedorak, Y.; Singh, V. V.; Orozco, J.; Galarnyk, M.; Wang, J., Self-Propelled Activated Carbon Janus Micromotors for Efficient Water Purification. *Small* **2015,** *11*, (4), 499-506.

(343) Liu, L.; Dong, Y.; Sun, Y.; Liu, M.; Su, Y.; Zhang, H.; Dong, B., Motion-based pH sensing using spindle-like micromotors. *Nano Res.* **2016,** *9*, (5), 1310-1318.

(344) Gao, W.; Pei, A.; Dong, R.; Wang, J., Catalytic iridium-based Janus micromotors powered by ultralow levels of chemical fuels. *J. Am. Chem. Soc.* **2014,** *136*, (6), 2276-2279.

(345) Dong, R.; Zhang, Q.; Gao, W.; Pei, A.; Ren, B., Highly efficient light-driven TiO2–Au Janus micromotors. *ACS nano* **2015,** *10*, (1), 839-844.

(346) Mou, F.; Chen, C.; Zhong, Q.; Yin, Y.; Ma, H.; Guan, J., Autonomous motion and temperature-controlled drug delivery of Mg/Pt-poly (N-isopropylacrylamide) Janus micromotors driven by simulated body fluid and blood plasma. *ACS Appl. Mater. Interfaces* **2014,** *6*, (12), 9897-9903.

(347) Dong, R.; Hu, Y.; Wu, Y.; Gao, W.; Ren, B.; Wang, Q.; Cai, Y., Visible-light-driven BiOI-based Janus micromotor in pure water. *J. Am. Chem. Soc.* **2017,** *139*, (5), 1722-1725.

(348) Peng, F.; Tu, Y.; van Hest, J. C.; Wilson, D. A., Self-Guided Supramolecular Cargo-Loaded Nanomotors with Chemotactic Behavior towards Cells. *Angew. Chem., Int. Ed.* **2015,** *54*, (40), 11662-11665.

(349) Dey, K. K.; Sen, A., Chemically propelled molecules and machines. *J. Am. Chem. Soc.* **2017,** *139*, (23), 7666-7676.

(350) Schmitt, M.; Stark, H., Marangoni flow at droplet interfaces: Three-dimensional solution and applications. *Phys. Fluids* **2016,** *28*, (1), 012106.

(351) Savino, R.; Cecere, A.; Di Paola, R., Surface tension-driven flow in wickless heat pipes with self-rewetting fluids. *Int. J. Heat Fluid Flow* **2009,** *30*, (2), 380-388.

(352) Gao, W.; Pei, A.; Feng, X.; Hennessy, C.; Wang, J., Organized self-assembly of Janus micromotors with hydrophobic hemispheres. *J. Am. Chem. Soc.* **2013,** *135*, (3), 998-1001.

(353) Yang, F.; Qian, S.; Zhao, Y.; Qiao, R., Self-diffusiophoresis of Janus catalytic micromotors in confined geometries. *Langmuir* **2016,** *32*, (22), 5580-5592.

(354) Garcia-Gradilla, V.; Orozco, J.; Sattayasamitsathit, S.; Soto, F.; Kuralay, F.; Pourazary, A.; Katzenberg, A.; Gao, W.; Shen, Y.; Wang, J., Functionalized ultrasound-propelled magnetically guided nanomotors: Toward practical biomedical applications. *ACS nano* **2013,** *7*, (10), 9232-9240.

(355) Ahmed, D.; Lu, M.; Nourhani, A.; Lammert, P. E.; Stratton, Z.; Muddana, H. S.; Crespi, V. H.; Huang, T. J., Selectively manipulable acoustic-powered microswimmers. *Sci. Rep.* **2015,** *5*, 9744.

(356) Liu, R.; Sen, A., Autonomous nanomotor based on copper–platinum segmented nanobattery. *J. Am. Chem. Soc.* **2011,** *133*, (50), 20064-20067.

(357) Maloney, J. M.; Schreiber, D. S.; DeVoe, D. L., Large-force electrothermal linear micromotors. *J. Micromech. Microeng.* **2003,** *14*, (2), 226.

(358) Guckel, H.; Skrobis, K.; Christenson, T.; Klein, J.; Han, S.; Choi, B.; Lovell, E.; Chapman, T., Fabrication and testing of the planar magnetic micromotor. *J. Micromech. Microeng.* **1991,** *1*, (3), 135.

(359) Chen, C.; Karshalev, E.; Guan, J.; Wang, J., Magnesium-Based Micromotors: Water-Powered Propulsion, Multifunctionality, and Biomedical and Environmental Applications. *Small* **2018**, 1704252.

(360) Orozco, J.; Cheng, G.; Vilela, D.; Sattayasamitsathit, S.; Vazquez-Duhalt, R.; Valdés-Ramírez, G.; Pak, O. S.; Escarpa, A.; Kan, C.; Wang, J., Micromotor-Based High-Yielding Fast Oxidative Detoxification of Chemical Threats. *Angew. Chem., Int. Ed.* **2013,** *52*, (50), 13276-13279.

(361) Guix, M.; Meyer, A. K.; Koch, B.; Schmidt, O. G., Carbonate-based Janus micromotors moving in ultra-light acidic environment generated by HeLa cells in situ. *Sci. Rep.* **2016,** *6*, 21701.

(362) de Ávila, B. E.-F.; Angsantikul, P.; Li, J.; Lopez-Ramirez, M. A.; Ramírez-Herrera, D. E.; Thamphiwatana, S.; Chen, C.; Delezuk, J.; Samakapiruk, R.; Ramez, V., Micromotor-enabled active drug delivery for in vivo treatment of stomach infection. *Nat. Commun.* **2017,** *8*, (1), 272.

(363) Bhirde, A. A.; Patel, S.; Sousa, A. A.; Patel, V.; Molinolo, A. A.; Ji, Y.; Leapman, R. D.; Gutkind, J. S.; Rusling, J. F., Distribution and clearance of PEG-single-walled carbon nanotube cancer drug delivery vehicles in mice. *Nanomedicine* **2010,** *5*, (10), 1535-1546.

(364) Laocharoensuk, R.; Burdick, J.; Wang, J., Carbon-nanotube-induced acceleration of catalytic nanomotors. *ACS nano* **2008,** *2*, (5), 1069-1075.

(365) Hu, C.; Zhao, Y.; Cheng, H.; Wang, Y.; Dong, Z.; Jiang, C.; Zhai, X.; Jiang, L.; Qu, L., Graphene microtubings: controlled fabrication and site-specific functionalization. *Nano Lett.* **2012,** *12*, (11), 5879-5884.

(366) Vilela, D.; Parmar, J.; Zeng, Y.; Zhao, Y.; Sánchez, S., Graphene-based microbots for toxic heavy metal removal and recovery from water. *Nano Lett.* **2016,** *16*, (4), 2860-2866.

(367) Wu, Y.; Lin, X.; Wu, Z.; Möhwald, H.; He, Q., Self-propelled polymer multilayer Janus capsules for effective drug delivery and light-triggered release. *ACS Appl. Mater. Interfaces* **2014,** *6*, (13), 10476-10481.

(368) Orozco, J.; Vilela, D.; Valdés-Ramírez, G.; Fedorak, Y.; Escarpa, A.; Vazquez-Duhalt, R.; Wang, J., Efficient Biocatalytic Degradation of Pollutants by Enzyme-Releasing Self-Propelled Motors. *Chemistry–A European Journal* **2014,** *20*, (10), 2866-2871.

(369) Draz, M. S.; Kochehbyoki, K. M.; Vasan, A.; Battalapalli, D.; Sreeram, A.; Kanakasabapathy, M. K.; Kallakuri, S.; Tsibris, A.; Kuritzkes, D. R.; Shafiee, H., DNA engineered micromotors powered by metal nanoparticles for motion based cellphone diagnostics. *Nat. Commun.* **2018,** *9*, (1), 4282.

(370) Singh, A. K.; Rarotra, S.; Pasumarthi, V.; Mandal, T. K.; Bandyopadhyay, D., Formic acid powered reusable autonomous ferrobots for efficient hydrogen generation under ambient conditions. *J. Mater. Chem. A* **2018,** *6*, (19), 9209-9219.

(371) Machado, F. M.; Bergmann, C. P.; Lima, E. C.; Adebayo, M. A.; Fagan, S. B., Adsorption of a textile dye from aqueous solutions by carbon nanotubes. *Mater. Res.* **2014,** *17*, 153-160.

(372) Ohsaka, T.; Izumi, F.; Fujiki, Y., Raman spectrum of anatase, TiO2. *J. Raman Spectrosc.* **1978,** *7*, (6), 321-324.

(373) Zhang, L.; Yu, X.; Hu, H.; Li, Y.; Wu, M.; Wang, Z.; Li, G.; Sun, Z.; Chen, C., Facile synthesis of iron oxides/reduced graphene oxide composites: application for electromagnetic wave absorption at high temperature. *Sci. Rep.* **2015,** *5*, 9298.

(374) Perrone, J. A., Model for the computation of self-motion in biological systems. *JOSA A* **1992,** *9*, (2), 177-194.

(375) Yim, M.; Shen, W.-M.; Salemi, B.; Rus, D.; Moll, M.; Lipson, H.; Klavins, E.; Chirikjian, G. S., Modular self-reconfigurable robot systems [grand challenges of robotics]. *IEEE Robotics & Automation Magazine* **2007,** *14*, (1), 43-52.

(376) D'Orsogna, M. R.; Chuang, Y.-L.; Bertozzi, A. L.; Chayes, L. S., Self-propelled particles with soft-core interactions: patterns, stability, and collapse. *Phys. Rev. Lett.* **2006,** *96*, (10), 104302.

(377) Nandi, N.; Bhattacharyya, K.; Bagchi, B., Dielectric relaxation and solvation dynamics of water in complex chemical and biological systems. *Chem. Rev.* **2000,** *100*, (6), 2013-2046.

(378) Defranco, A. L.; Parkinson, J. S.; Koshland, D., Functional homology of chemotaxis genes in Escherichia coli and Salmonella typhimurium. *J. Bacteriol.* **1979,** *139*, (1), 107-114.

(379) Berg, H. C., Feature Article Site Index Motile Behavior of Bacteria. *Phys. Today* **2001,** *9*, 25.

(380) Kruth, H. S., Receptor-independent fluid-phase pinocytosis mechanisms for induction of foam cell formation with native LDL particles. *Curr. Opin. Lipidol.* **2011,** *22*, (5), 386.

(381) Burgdorf, S.; Kurts, C., Endocytosis mechanisms and the cell biology of antigen presentation. *Curr. Opin. Immunol.* **2008,** *20*, (1), 89-95.

(382) Patriarca, P.; Dri, P.; Kakinuma, K.; Rossi, F., Studies on the mechanism of metabolic stimulation in polymorphonuclear leukocytes during phagocytosis. Activators and inhibitors of the granule bound NADPH oxidase. *J. Cell. Biochem.* **1976,** *12*, (3), 137-146.

(383) Griffin, F. M.; Griffin, J. A.; Leider, J. E.; Silverstein, S. C., Studies on the mechanism of phagocytosis. I. Requirements for circumferential attachment of particle-bound ligands to specific receptors on the macrophage plasma membrane. *J. Exp. Med.* **1975,** *142*, (5), 1263-1282.

(384) Mitchell, P., Chemiosmotic coupling in oxidative and photosynthetic phosphorylation. *Biol. Rev.* **1966,** *41*, (3), 445-501.

(385) Kasumov, E. A.; Kasumov, R. E.; Kasumova, I. V., A mechano-chemiosmotic model for the coupling of electron and proton transfer to ATP synthesis in energy-transforming membranes: a personal perspective. *Photosynth. Res.* **2015,** *123*, (1), 1-22.

(386) Yi, Y.; Sanchez, L.; Gao, Y.; Yu, Y., Janus particles for biological imaging and sensing. *Analyst* **2016,** *141*, (12), 3526-3539.

(387) Granick, S.; Jiang, S.; Chen, Q., Janus particles. *Phys. Today* **2009,** *62*, (7), 68-69.

(388) Riedel-Kruse, I. H.; Hilfinger, A.; Howard, J.; Jülicher, F., How molecular motors shape the flagellar beat. *HFSP J.* **2007,** *1*, (3), 192-208.

(389) Minamino, T.; Imada, K.; Namba, K., Molecular motors of the bacterial flagella. *Curr. Opin. Struct. Biol.* **2008,** *18*, (6), 693-701.

(390) Roberts, A., Motion of spermatozoa in fluid streams. *Nature* **1970,** *228*, (5269), 375.

(391) Hong, Y.; Velegol, D.; Chaturvedi, N.; Sen, A., Biomimetic behavior of synthetic particles: from microscopic randomness to macroscopic control. *Phys. Chem. Chem. Phys.* **2010,** *12*, (7), 1423-1435.

(392) Sengupta, S.; Dey, K. K.; Muddana, H. S.; Tabouillot, T.; Ibele, M. E.; Butler, P. J.; Sen, A., Enzyme molecules as nanomotors. *J. Am. Chem. Soc.* **2013,** *135*, (4), 1406-1414.

(393) Erdmann, U.; Ebeling, W.; Schimansky-Geier, L.; Schweitzer, F., Brownian particles far from equilibrium. *The European Physical Journal B-Condensed Matter and Complex Systems* **2000,** *15*, (1), 105-113.

(394) Howse, J. R.; Jones, R. A.; Ryan, A. J.; Gough, T.; Vafabakhsh, R.; Golestanian, R., Self-motile colloidal particles: from directed propulsion to random walk. *Phys. Rev. Lett.* **2007,** *99*, (4), 048102.

(395) Baraban, L.; Harazim, S. M.; Sanchez, S.; Schmidt, O. G., Chemotactic behavior of catalytic motors in microfluidic channels. *Angew. Chem.* **2013,** *125*, (21), 5662-5666.

(396) Dey, K. K.; Bhandari, S.; Bandyopadhyay, D.; Basu, S.; Chattopadhyay, A., The pH taxis of an intelligent catalytic microbot. *Small* **2013,** *9*, (11), 1916-1920.

(397) Kline, T. R.; Paxton, W. F.; Mallouk, T. E.; Sen, A., Catalytic nanomotors: remote-controlled autonomous movement of striped metallic nanorods. *Angew. Chem.* **2005,** *117*, (5), 754-756.

(398) Calvo-Marzal, P.; Manesh, K. M.; Kagan, D.; Balasubramanian, S.; Cardona, M.; Flechsig, G.-U.; Posner, J.; Wang, J., Electrochemically-triggered motion of catalytic nanomotors. *Chem. Commun.* **2009**, (30), 4509-4511.

(399) Wang, L.; Chen, J.; Feng, X.; Zeng, W.; Liu, R.; Lin, X.; Ma, Y.; Wang, L., Self-propelled manganese oxide-based catalytic micromotors for drug delivery. *RSC Adv.* **2016,** *6*, (70), 65624-65630.

(400) Lagzi, I., Chemical robotics—chemotactic drug carriers. *Cent. Eur. J. Med.* **2013,** *8*, (4), 377-382.

(401) Zhuang, J.; Park, B. W.; Sitti, M., Propulsion and Chemotaxis in Bacteria-Driven Microswimmers. *Adv. Sci.* **2017,** *4*, (9).

(402) Mittal, N.; Budrene, E. O.; Brenner, M. P.; Van Oudenaarden, A., Motility of Escherichia coli cells in clusters formed by chemotactic aggregation. *Proceedings of the National Academy of Sciences* **2003,** *100*, (23), 13259-13263.

(403) King, J. S.; Insall, R. H., Chemotaxis: finding the way forward with Dictyostelium. *Trends Cell Biol.* **2009,** *19*, (10), 523-530.

(404) Taktikos, J.; Zaburdaev, V.; Stark, H., Modeling a self-propelled autochemotactic walker. *Phys. Rev. E* **2011,** *84*, (4), 041924.

References